In-orbit Stability Analysis of the LISA Pathfinder Optical Metrology: Photoreceivers and Polarisation

Der Fakultät für Mathematik und Physik
der Gottfried Wilhelm Leibniz Universität Hannover

zur Erlangung des akademischen Grades
Doktorin der Naturwissenschaften
Dr. rer. nat.

genehmigte Dissertation von

MSc Brigitte Kaune

Hannover 2021

Referent:	Prof. Dr. Gerhard Heinzel
Korreferent:	Prof. Dr. Benno Willke
Korreferent:	Prof. Dr. William Joseph Weber
Tag der Promotion:	19.03.2021

Abstract

The Laser Interferometer Space Antenna (LISA) is a space mission, planned to be launched in 2034, to observe gravitational waves in the highly promising frequency band between 100 µHz and 0.1 Hz. To demonstrate its technical feasibility, the LISA Pathfinder (LPF) space mission was operated from December 2015 until July 2017. LPF successfully showed that a Test Mass (TM) can be set into free fall and that its displacement to another suspended TM can be measured with laser interferometers, both sensitive enough to be applicable for LISA. Further questions and technical challenges, however, need to be addressed on the path towards LISA.

One difference between the two missions is their duration. The much longer LISA mission will have to cope with a higher dose of cosmic radiation. Hence, the long-term stability of radiation sensitive components is an important parameter under test. For LPF, the photoreceivers, InGaAs Photodiodes (PDs), were expected to significantly decrease in responsivity by 17%. As a consequence, the stabilities of the actual in-flight PD responsivities were monitored, to compare with the pre-flight estimates, as described in this thesis.
The responsivity measurement experiment used an independent optical power measurement to calibrate the PDs. The signal was generated by a power modulation of the laser beam, inducing a radiation pressure modulation at the TMs. The corresponding differential TM displacement was measured with the precise interferometric readout, thus giving a calibration of the laser power. It was found that the PDs on LPF did not degrade within the statistical errors of 1% during the full monitoring duration of one year. Therefore, in a simplified linear extrapolation to a 6 year LISA mission, a decrease in the antenna sensitivity of more than $\approx 6\%$, as consequence of less detected power, is not expected.

The analysis of individual beam powers revealed an unexpected low frequency power noise that became the second main research question of this thesis. With a dedicated model of the optical interferometer paths, the noise source could be identified as an unstable polarisation state with up to 4.5% off-nominal polarised power. Nominally, the polarisation on LPF was cleaned with a Polarising Beam Splitter (PBS). However, a laboratory analysis of flight spare PBSs showed a decrease in the polarisation purity, which originated from slow out-gassing of water when exposed to vacuum for three weeks. An extrapolation of the observed effect for a longer exposure to vacuum, in combination with a degraded incident polarisation state to the PBS were found to be the best explanation for the in-flight polarisation instabilities.
The impact of the unexpected noise on LPF's scientific results was found to be negligible, with the exception of the induced radiation pressure to the TMs below 0.1 mHz. For the longest noise run in February 2017, the best estimate of the radiation pressure contribution to the differential TM acceleration noise amplitude was found to be up to $26\,(+6-2)\,\%$ at 74 µHz.
As a consequence for LISA, the sensitivity to polarization should be considered during the selection process of optical components and their long-term performance in a space environment should be tested.

Keywords: LISA Pathfinder, Photodiode Responsivity, Polarisation.

Contents

List of Figures

List of Boxes

List of Acronyms

ADC	Analogue-to-Digital Converter
AEI	Albert Einstein Institut
AOM	Acusto Optical Modulator
ASD	Amplitude Spectral Density
BS	Beam Splitter
CL	Control Loop
DC	Direct Current
DFACS	Drag Free and Attitude Control System
DFT	Discrete Fourier Transformation
DMU	Data Management Unit
DOP	Degree Of Polarisation
DRS	Disturbance Reduction System
DWS	Differential Wavefront Sensing
FIOS	Fibre Injector Optical Subassembly
FSU	Fibre Switching Unit
GaAs	Gallium Arsenide
GRS	Gravitational Reference Sensor
GW	Gravitational Wave
InGaAs	Indium Gallium Arsenide
KAGRA	Kamioka Gravitational Wave Detector
LEOP	Low Earth Orbit Phase
LIGO	Laser Interferometer Gravitational-Wave Observatory
LISA	Laser Interferometer Space Antenna
LPF	LISA Pathfinder
LTP	LISA Technology Package
MB	Modulation Bench

NIEL Non-Ionizing Energy Loss

OB Optical Bench

OMS Optical Metrology System

OPD Optical Path-length Difference

OW Optical Window

PBS Polarising Beam Splitter

PD Photodiode

PER Polarisation Extinction Ratio

P-pol Power with Parallel Polarisation

PTA Pulsar Timing Array

QPD Quadrant Photodiode

RF Radio Frequency

RIN Relative Intensity Noise

SC Spacecraft

SEP Solar Energetic Particles

SNR Signal-to-Noise Ratio

S-pol Power with Orthogonal Polarisation

TM Test Mass

USO Ultra-Stable Oscillator

List of Symbols

Table 0.1.: List of the used LPF telemetry parameters and quantities that are directly derived from them (compare to Appendix A and Table 2.2).

Parameter	Unit	Description
DC_{ij}	$[A \cdot \Omega/V = 1]$	Photocurrent at a PD in port j = A, B of the interferometer i = x1, x12, R, F, converted to a voltage and sampled with an ADC.
Σ_i	$[A \cdot \Omega/V = 1]$	Average of the summed DC_{ij} parameters of the four QPD segments, for the j = A and j = B PD in the interferometer i.
$P_{\text{Pwr-mon}m}$	$[\mu A]$	Photocurrent at the Power monitor PDA1 or PDA2.
x_1	[m]	Displacement of TM1 with respect to the OB.
x_{12}	[m]	Differential displacement of TM1 and TM2.
φ_1, φ_2 ,η_1, η_2	[rad]	TM angles, either derived by the DWS signal or the DC signal of a QPD.
ϕ_{12}	[rad]	Longitudinal phase of the x12 interferometer.
$P_{RF,m}$	[V]	Monitor of the RF Power amplifier, linearly mapped to a 10V reference voltage.
Δ_g	$[m/s^2]$	Differential acceleration of TM1 and TM2.
C	[W/W]	Interferometric contrast.
a_{het}	[W]	Power of the heterodyne signal, corresponding to the heterodyne amplitude.

Table 0.2.: List of further parameters that are used in this thesis

Parameter	Unit	Description
P_m	[W]	Optical power of a laser beam m.
$P_{\mathrm{TM}i}$	[W]	Optical power at TMi.
η_i	[A/W]	Responsivity of PDi.
C_{CL}	[1/W]	Control coefficient, equivalent to the LPF fast amplitude CL.
φ_{PBS}	[°]	Rotation of the Polarising Beam Splitter (PBS) around its vertical axis in the LPF design.
φ_{pol}	[°]	Angle of linear input polarisation against the nominal orthogonal polarisation axis.

Table 0.3.: List of constants that are used in this thesis

Constant	Unit	Description
$\lambda_{i,\,m}$	no units	Dimensionless propagation factor of beam m to a parameter i, see Appendix B.
$\mathrm{R_i}$	no units	Reflectivity of a component i.
$\mathrm{T_i}$	no units	Transmissivity of a component i.
$\mathrm{m_i}$	[kg]	Mass of a TMi.
$\mathrm{R_{TI}}$	[Ω]	Trans-impedance resistance.
$\mathrm{U_{ADC}}$	[V]	ADC range.
η_{het}, η_{hom}	no units	Heterodyne/ homodyne efficiency.
n_{fs}	no units	Refractive index of fused silica.
G_i	[W]	G-coefficient, converting the Σ_i parameters to optical power.
A_{BD}	[m^2]	Surface of a beam dump.

1. Introduction

1.1. Gravitational waves and their detection

Gravitational Waves (GWs) are tiny ripples in spacetime, emitted by asymmetric acceleration of heavy masses. They travel at the speed of light almost without attenuation while periodically shrinking and stretching the spacetime on their way through the universe [1]. As depicted in Figure 1.1, the period lengths of these waves range by orders of magnitude, depending on their source. Fast spinning neutron stars with a non-spherical mass distribution for example emit GWs at kilohertz frequencies, whereby waves from a non-symmetric expansion of the early universe are expected at period lengths corresponding to the age of the universe. However, although the sources of GW are heavy stellar objects, their effect on the curvature of spacetime is tiny. Even a strong GW from a neighbouring galaxy changes the absolute distance, L, between two separate points by no more than $\Delta L = 5 \cdot 10^{-22}\, L$ (for example for a GW from a supernova in a neighbouring galaxy with the so-called GW strain of $h = 10^{-21}$, [2]) .

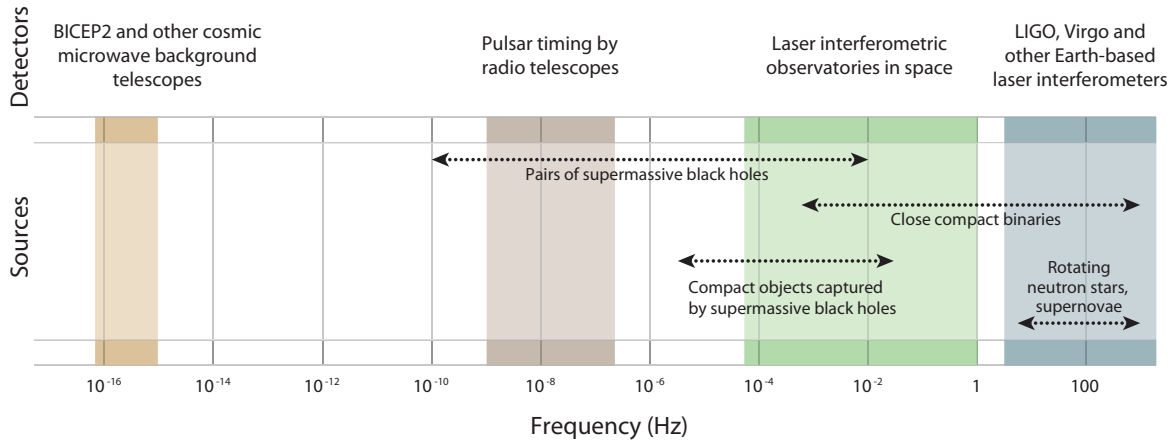

Figure 1.1.: The specific frequency range of gravitation waves from different sources is shown together with the corresponding existing and planned detectors. A gravitational background from cosmic inflation is present at the entire frequency spectrum [3]. The picture is a reprint from Reference [3].

Nevertheless, in 1974 the first experimental evidence on the existence of these tiny variations in the curvature of space-time was found by Russell Hulse and Joseph Taylor. They discovered a binary pulsar, whose decrease of orbital frequency fit the theoretical prediction of the energy-loss by the emission of GWs [4].

Fanned by this first indirect detection, the development of a novel experimental technique for the direct detection of GWs — the so-called laser interferometry — progressed.

Both, the first indirect and the first direct detection of GWs, were awarded with the Nobel Prize in 1993 and 2017, underlining the importance of these discoveries for the future astronomy. The GW astronomy unveils a completely new way to observe the universe with a complementary medium to the electro-magnetic spectrum.

1.2. Current detectors and their constraints

The currently most used measurement principle for GW detectors is the concept of laser interferometry that allows the ultra-sensitive measurement of relative length changes between two distant test bodies. Besides the two Laser Interferometer Gravitational-Wave Observatory (LIGO) detectors, there are several more earth-based detectors, of which at least the Virgo detector close to Pisa has already proven enough sensitivity for GW detection ([5]). The results of the first observation run of the Kamioka Gravitational Wave Detector (KAGRA) in Japan using cryogenic mirrors are eagerly anticipated [6].

The basic concept of these ground-based detectors is a Michelson interferometer with kilometre-long arms. It converts a GW induced length-change into a measurable optical power [7]. Therefore, a laser beam is split at a BS into two perpendicular beams, the so-called interferometer arms, as depicted in Figure 1.2. Each of these arms has a mirror at the end that reflects the beam back to the BS for interference. A change of one interferometer arm length also changes the relative phase between the two beams of the interference signal. The resulting change in optical power at the interferometer output can be measured with a photo detector. Therefore, a passing GW induces a signal by stretching one interferometer arm while shrinking the other. The induced signal strength depends on the length of the arms and the orientation of the detector with respect to the GW source. To reach the required sensitivity for detecting a GW signal, the interferometer arms need to be protected from all non-gravitational disturbing forces by reduction of the environmental noise and sophisticated control mechanisms.

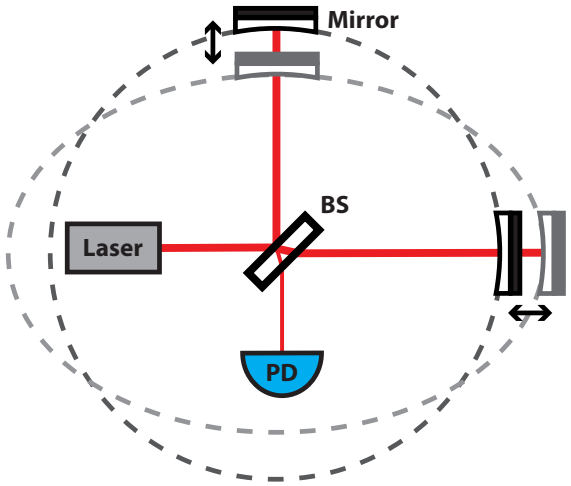

Figure 1.2.: Basic concept of a Michelson interferometer: A laser beam is split into two arms with a Beam Splitter (BS). After reflection at the end-mirrors, the beams are interfered at the BS and detected with a Photodiode (PD). The effect of a passing GW is illustrated with high exaggeration by the elliptic deformation of the arm lengths [7, 8].

In general, the interferometric measurement principle is not restricted to a specific GW frequency. However, the frequency range with sufficient sensitivity is limited. On the one hand, the earth-based detectors are restricted by their arm-length. GWs with frequencies below 1 Hz have wavelengths longer than several hundred thousands of kilometres. The induced displacement signal could therefore be increased by much longer interferometer arms which is

restricted by cost and the curvature of Earth's surface. On the other hand, noise sources limit the range with sufficient signal to noise ratio. Towards higher frequencies, quantum effects are dominating the detector sensitivity. At low frequencies, the sensitivity is restricted by environmental noise from seismic activity and gradient-noise in the local gravity field. For the LIGO detectors the resulting frequency band with sufficient sensitivity for GW detections is between 10 Hz and 10 kHz [9, 10]. At these frequencies signals from compact binary mergers and core collapse supernovae are expected, as shown in Figure 1.1.

For the very low GW frequencies below 10^{-6} Hz, a different measurement principle can be used. The signals from several pulsars in a so-called Pulsar Timing Array (PTA) are analysed for slow variations in their arrival-time that are induced by a passing GW. The expected signals originate from a background of GWs from massive black hole binaries in the centres of merging galaxies, as can be seen in Figure 1.1.

However, a great amount of scientifically very interesting events emit GWs in the frequency band between the sensitive range of the existing interferometer detectors and the PTAs. For example, compact binaries emit low frequency GWs, long before they get close enough, to finally merge at higher frequencies. Also, a merger of heavier black holes (intermediate and supermassive), or a stellar compact object closely orbiting a supermassive black hole (a so-called EMRI) are emitting GWs at lower frequencies than detectable with the current interferometric detectors and above sensitive frequencies of a PTA.

To access this highly promising frequency band (depicted in Figure 1.1) with the well established laser interferometer technique, much longer interferometer arms are needed in a very long-term stable and quiet environment. The most reasonable solution to this is: the interferometer must be brought into space. Therefore, the so-called Laser Interferometer Space Antenna mission is aiming to detect GWs in space at frequencies between 100 µHz and 0.1 Hz [11], as described in the following.

1.3. The future of GW detection in space: LISA

For more than two decades, a space-based GW observatory, the so-called Laser Interferometer Space Antenna (LISA), was designed to fill the scientific gap between the ground-based detectors, sensitive to very high frequencies, and the PTAs, observing the very low-frequency GWs. In 2017, the mission concept was accepted by the ESA as their L3 mission to be launched in 2034 [11].

LISA consists of three Spacecraft (SC) in a giant triangular formation, as shown in Figure 1.3. Its centre of mass is orbiting the Sun at the same radius as the Earth. Each SC houses two free-falling solid cubes made of a gold–platinum alloy - the so-called Test Masses (TMs). The distance between these geodesic reference points at different SC, millions of kilometres apart, is changing by low frequency GWs. However, even strong GWs

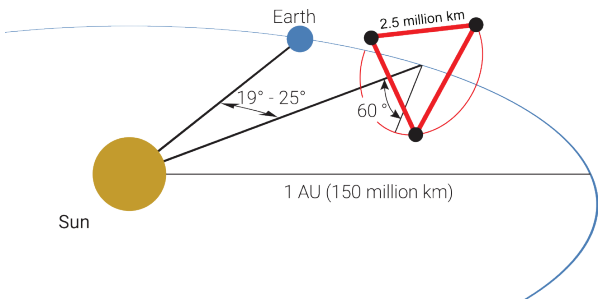

Figure 1.3.: The LISA configuration and orbits. Reprint from Reference [12].

imply only pico-metre changes between the TMs.

For the measurement of these tiny displacements, laser light will be exchanged by the SC to build an interferometer. Due to divergence, the laser beam diameter after travelling millions of kilometres, is huge even for a well-collimated beam. Therefore, the transmitted power reaching the distant spacecraft only has a remaining low intensity of some hundreds of pico-Watts. As a consequence, the light cannot be reflected off a TM, back to the emitting SC. As the solution to this, the emitted light is collected with a telescope and interfered with a local laser, being a part of the so-called split interferometer scheme. The optics needed to build the interferometers are mounted on an ultra-stable optical desk, the so-called Optical Bench (OB). The final measurement of relative TM displacement therefore is a combination of three split interferometers measuring the distance between the OB of one SC to the one of the distant SC and the distance of the two OBs to their geodesic reference points, the TMs.

The SC will have relative velocities to each other, adding Doppler shifts to the emitted laser frequencies. The different laser frequencies produce time-dependent beat note frequencies in the interferometric signals that need to be analysed by a dedicated phasemeter.

Furthermore, the inter-SC interferometer has highly unequal arm lengths, because only one beam travels the million-kilometre distance while the other one is locally travelling. Therefore, the resulting beat note is highly affected by frequency noise that needs to be removed by a dedicated algorithm in the post processing of the data, the so-called time delay interferometry [13].

For being able to detect the tiny differential length changes from GWs, the metrology systems have to fulfil several requirements that have never been reached before. First, the displacement of two test bodies, millions of kilometres apart, needs to be detected with a precision of an atomic radius. This can be specified by a requirement on the remaining total noise in the measurement of differential TM displacement in one interferometer link between two LISA satellites, given by the amplitude spectral density:

$$\tilde{s}^{\mathrm{LISA}}_{\mathrm{disp.}} \leq 10\frac{\mathrm{pm}}{\sqrt{\mathrm{Hz}}} \cdot \sqrt{1+\left(\frac{2\,\mathrm{mHz}}{f}\right)^4}, \tag{1.1}$$

within the measurement band of $100\,\mu\mathrm{Hz} < f < 0.1\,\mathrm{Hz}$ [11, 14].

Secondly, it is fundamentally important to the mission that all forces acting on the TMs are strongly suppressed and minimized. Therefore, a control system needs to be implemented, that effectively keeps a TM in geodesic motion along its sensitive axis with the distant TM, without adding noise above the desired sensitivity level. The resulting requirement on the amplitude spectral density in stray acceleration of the TM in the LISA measurement band is specified by the requirement:

$$\tilde{s}^{\mathrm{LISA}}_{\mathrm{acc.}} \leq 3\,\frac{\mathrm{fm}}{\mathrm{s}^2\sqrt{\mathrm{Hz}}}\sqrt{1+\left(\frac{0.4\,\mathrm{mHz}}{f}\right)^2} \cdot \sqrt{1+\left(\frac{f}{8\,\mathrm{mHz}}\right)^4}, \tag{1.2}$$

as described in Reference [11].

Several technical challenges for LISA's metrology systems were overcome by many years of laboratory research. However, the actual feasibility of some systems like the drag-free control of the SC could only be demonstrated in the absence of Earths gravity field. Therefore, a space-based technical demonstrator mission — the so-called LISA Pathfinder — was designed.

1.4. LPF: demonstrating new metrology horizons

LISA Pathfinder (LPF) was a technical demonstrator with the scientific objective to prove the feasibility of crucial technology components for LISA without the need of being sensitive to GWs. It was launched in December 2015 and with great success operated until end of June 2017.

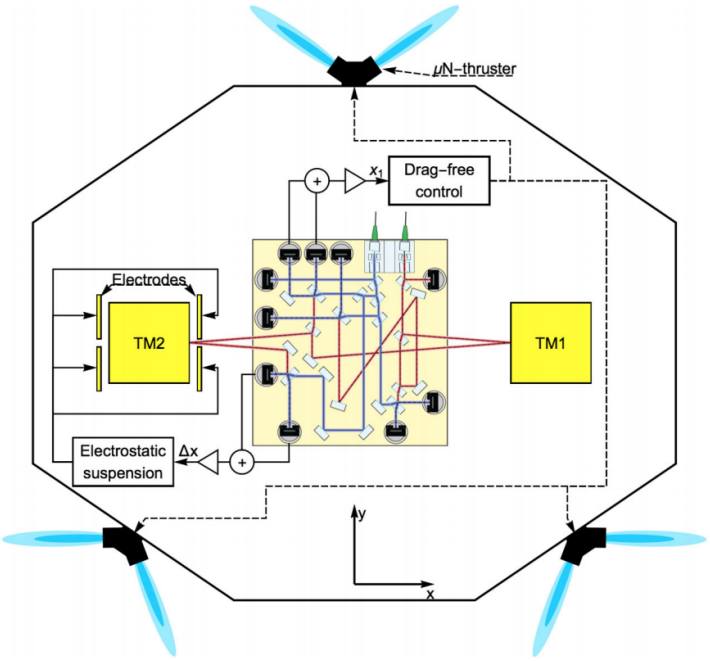

Figure 1.4.: Schematic of the LPF satellite. Two TMs are housed inside a SC. The displacement of TM1 to the OB is measured interferometrically for drag free control of the SC with micro-Newton thrusters. Furthermore, the measurement of differential displacement between TM1 and TM2 is used to force TM2 to follow the drag-free TM1 with capacitive actuation. Reprint from Reference [15]

The concept of LPF is comparable to one interferometer link between two LISA satellites, shrunk to a distance that fits into only one SC. Hence, the LPF satellite houses two TMs along one sensitive axis, whose relative distance is measured interferometrically, as depicted in Figure 1.4. The two TMs could not both float free in all dimensions, due to the finiteness of their housings. However, the basic metrology concepts of a SC following a free-floating TM and measuring its displacement to another suspended reference TM could be demonstrated.

In contrast to LISA, the small separation between the two TMs, together with the mission operation point — the first Earth-Sun Lagrange point L1 — provided nominally negligible

deviations of the TM geodesic paths. Of course, there were several non-gravitational forces like reflected particles, electrostatic and magnetic forces or radiation pressure that act on the TMs. Moreover, also the geodesic paths itself were changed by the gravitationally coupled system of the satellite and the two TMs. All these interactions needed to be minimised, controlled, measured and modelled to retrieve the final parameter: The remaining differential acceleration, Δ_g, between the two free falling TMs. The requirement was specified with a relaxation in the measurement band and a factor 10 in comparison to LISA (compare to Requirement 1.2), to:

$$\tilde{s}_{\mathrm{acc}}^{\mathrm{LPF}} \leqq 30\,\frac{\mathrm{fm}}{\mathrm{s}^2\sqrt{\mathrm{Hz}}}\sqrt{1+\left(\frac{f}{3\,\mathrm{mHz}}\right)^4} \tag{1.3}$$

within the measurement band of $1\,\mathrm{mHz} < f < 30\,\mathrm{mHz}$ [15, 16, 17, 18].

The second mission observable was the interferometric readout of the differential TM displacement with a specified requirement [17, 18, 19] in the measurement band of:

$$\tilde{s}_{\mathrm{disp.}}^{\mathrm{LPF}} \leqq 9\,\frac{\mathrm{pm}}{\sqrt{\mathrm{Hz}}}\cdot\sqrt{1+\left(\frac{3\,\mathrm{mHz}}{f}\right)^4}, \tag{1.4}$$

The so-called Optical Metrology System (OMS) is the instrument under investigation in this thesis and therefore described in Chapter 2 in more detail.

The free-fall was realised by the so-called Drag Free and Attitude Control System (DFACS), as shown in Figure 1.4. The relative displacement of the two TMs with respect to the SC was measured in all degrees of freedom by capacitive readout with the so-called Gravitational Reference Sensor (GRS). Along the sensitive axis, the displacements were furthermore measured with higher sensitivity by the OMS. The corresponding displacement signals were then input to the DFACS controller. The capacitive housing was also used to actuate the suspended TM2, such that it follows the motion of the drag free TM1.

The tremendous technical challenges of the mission underline the importance of the LPF in-flight results that excelled the mission requirements by more than an order of magnitude and therefore already demonstrated enough sensitivity for LISA. The differential acceleration noise between the TMs above 2 mHz was found to be lower than $(1.74 \pm 0.05)\,\mathrm{fm\,s^{-2}/\sqrt{Hz}}$. At the desired lowest frequency of 20 µHz of the LISA band, it was still at $(60 \pm 10)\,\mathrm{fm\,s^{-2}/\sqrt{Hz}}$ (corresponding to a noise measurement of ≈ 13 days at 11 °C in February 2017 [15]). The OMS exceeded the mission requirements even by more than a factor of a hundred, with a readout noise of $s_{\mathrm{disp.}}^{1/2} = (34.8 \pm 0.3)\,\mathrm{fm/\sqrt{Hz}}$ at frequencies above 30 mHz, where the TM motion is not limiting the performance [16, 19].

1.5. This thesis: Long-term monitoring of the PD responsivity during flight of LPF.

The LPF mission was a huge success that clearly paved the way towards LISA and the GW detection in space. However, although LPF demonstrated the feasibility of the basic concepts needed for LISA, there are still major differences in the mission concepts.

One obvious difference is the much longer duration of the LISA mission with a proposed extension up to 10 years. The stability of the metrology systems must resist the environmental influences and guarantee a functionality for at least six years with a four-years nominal mission duration and an approximately two-years transfer and commission phase to final LISA orbits [11].

In consideration of the OMS, the long-term stability of one component is of special interest: the optical sensors detecting the laser radiation at the outputs of the interferometers. The main science measurement is processed from this interferometric readout. The detectors are planned to be Indium Gallium Arsenide (InGaAs) PDs. As electro-optical components, they are expected to be sensitive to cosmic radiation. The exposure to high energy particles can lead to radiation-induced conductivity or a decrease of the detected power by displacement of the atoms in the semiconductor. However, the measured power is a relevant parameter for LISA, because the received beams in the inter-spacecraft interferometers have only little remaining power. Therefore the sensitivity of these interferometers is limited by shot noise. As a consequence, the detected power affects the sensitivity of the whole antenna towards higher frequencies [3, 14].

Shot noise scales by the square root of the detected power at a photo receiver. The ratio of detected power at a PD to the applied optical power is described by the so-called PD responsivity, η. A loss in PD responsivity by a factor ϵ would therefore lead to a decrease in the signal to noise ratio of the interferometer signal by a factor $\sqrt{1-\epsilon}$, due to shot noise.

For the LPF mission, InGaAs PDs were used, as it is planned for LISA. Radiation tests for flight preparation showed that they will suffer from damage by atom displacement with an average decrease in responsivity of 17% for the full expected mission duration including the transport to L1 (Reference [20, 21], detailed radiation test results are discussed in Section 2.5). For LPF this was of minor relevance since shot noise is not a significant noise contribution in the LPF interferometers. However, a simple linear extrapolation of the PD radiation tests to an at least three times longer LISA like mission duration would lead to a notable decrease in sensitivity of the shot noise limited antenna. Nevertheless, the radiation tests on ground have a different composition of particles and energies than the actual cosmic radiation environment. Therefore, the in-flight performance of LPF's PDs under realistic conditions is an important parameter with regard to LISA. It was the main objective of the performed experiments presented in the first part of this thesis.

Part I begins with the experimental planning for the long-term monitoring of LPF's PD responsivities, described in Chapter 3. The experiment design is based on a reference power measurement via radiation pressure. However, the radiation pressure estimation required a further monitoring experiment: the TM reflectivity monitoring.

The resulting in-flight long-term stability of the TM reflectivity is detailed in Chapter 4 and in Chapter 5 for the PD responsivity.

Due to the extremely good performance of LPF's OMS, the planned investigations went beyond their initial question. Tiny effects below the expected noise level became visible and analysable. Therefore, the observation of a tiny power-to-phase coupling, below the expected sensitivity, is further described in Chapter 6. Although several properties of the coupling could be identified, the underlying mechanism is still a subject under investigation.

The analysis of the TM reflectivity monitoring experiments started the research on another unexpected observation, as focused on in Part II: The beam powers are affected by low frequency power noise, induced by the beam polarisation. The chronological path to the polarisation theory, is outlined in Chapter 7.

The description of the observed power fluctuations by a dedicated model of the interferometric beam paths, regarding polarisation, is described in Chapter 8. A corresponding analysis of equivalent pre-flight measurements with the flight OB is detailed in Chapter 9 .

A discussion on the possible origin of the polarisation fluctuations can be found in Chapter 10. The resulting first best theory of stress induced effects at the polarisation cleaner on the LPF OB was investigated experimentally in Chapter 11. A rejection of the first theory led to measurements with the spare OB at the University of Glasgow, as detailed in Chapter 12. A subsequent laboratory analysis of the flight spare PBSs after vacuum baking is described in Chapter 13.

The impact of the instable polarisation state on the LPF science is detailed in Chapter 14.

In the last Part III, possible impacts of the different findings in this thesis on LISA, especially on the OB design are outlined. Furthermore, the results of the thesis are summarised and discussed and a conclusion is made.

A note on the use of boxes:
To improve readability, the logical structure of argumentative steps in this thesis is supported by summary boxes (coloured petrol blue) that can typically be found at the end of a chapter. The boxes summarise the main findings and state subsequent questions.
Besides the summary boxes, auxiliary calculations that are directly used in the current analysis, are separated in sunny yellow coloured boxes for clarity.

2. LISA Pathfinder instrument description: The optical metrology system

The LPF mission was a joined project of the ESA and NASA [18]. The Disturbance Reduction System (DRS) controls the satellite with Micro-Newton thrusters. It is the NASA contribution and described with more detail in [22, 23]. The sensors for the DRS, measuring the relative displacement of satellite and the the drag-free TM however, are part of the LISA Technology Package (LTP) provided by the ESA.
The LTP consists of two sub-systems: The inertial sensor, comprising the TMs and all subsystems directly interacting with them, and the OMS — providing the high-precision interferometric readout of the TM displacement. The OMS is the main instrument under investigation in this thesis and therefore described in this chapter with further detail.
First, the instruments generating and modulating the laser light are described in Section 2.1. In the next Section 2.2, the beam paths of the different interferometers on the OB are described.
The heterodyne interference signals at the interferometer output and their processing in the phasemeter is detailed in Section 2.3. The resulting OMS parameters, as well as some further LPF parameters, used in this thesis, are summarized in 2.4. With regard to the long-term monitoring, LPFs PDs and the results of the applied radiation tests, previous to flight, are described in the last Section 2.5.

2.1. The laser assembly

LPFs laser assembly comprises the laser and all instruments used for modulating and controlling the properties of the light. The laser itself is a diode pumped Nd:YAG crystal with a nonplanar ring oscillator design [24]. It generates a beam with about 35 mW in a single transverse TEM00 mode with linear polarisation at a wavelength of 1064 nm.
The laser frequency is actuated with a piezo that directly changes the crystal length and, on longer time scales, also by heating the crystal. The control signal is provided from the frequency-sensitive so-called frequency interferometer on the OB, as described Section 2.2.
Furthermore, slow changes in the laser power reaching the OB can be controlled by the laser pump current. Besides this slow power control loop, acting directly on the laser, there is also a control mechanism, as described in Box 2.1.1. During flight, only the fast control loop was used to avoid changes in the laser temperature.
The laser output light is fibre-coupled to the so-called Modulation Bench (MB).

The MB is designed to modulate the laser output light in frequency, power and phase, before it is transmitted to the OB for interference.
At first, the light is split with a 50:50 BS into two beams of equivalent power that travel

different paths before recombination at the optical bench. Then, the two beams are shifted in frequency with two Acusto Optical Modulators (AOMs) by $\Delta f = 80\,\mathrm{MHz} \pm 0.5\,\mathrm{kHz}$. The AOMs further allow for fast actuation of the output beam power with analogue loops, as described in Box 2.1.1.
Besides the beam power, the relative phase between the beams is also controlled at the MB. Therefore the output beams of the AOMs are guided through two so-called Optical Path-length Difference (OPD) actuators. They are able to balance differential changes in the path-length of the two beams by piezo-actuated displacement of a retroreflector in the beam path. The control signal is generated by the path length difference of the two beams between the BS on the MB and the recombination at the OB, measured by the so-called reference interferometer, described Section 2.2. More details on the OPD Control Loop (CL) can be found in Reference [24]. The output of the OPD actuators is coupled with polarisation maintaining optical fibres to the OB.

Box 2.1.1: Fast power control loop:

On LPF the transmitted beam powers to the OB are controlled individually with two identically constructed fast controllers, one for each beam. The loops needed to be fast enough, to control the power around the heterodyne frequency and thus reduce the effect of relative intensity noise. Therefore, the loops were implemented to work with analogue signals, in contrast to all other CLs of the OMS.

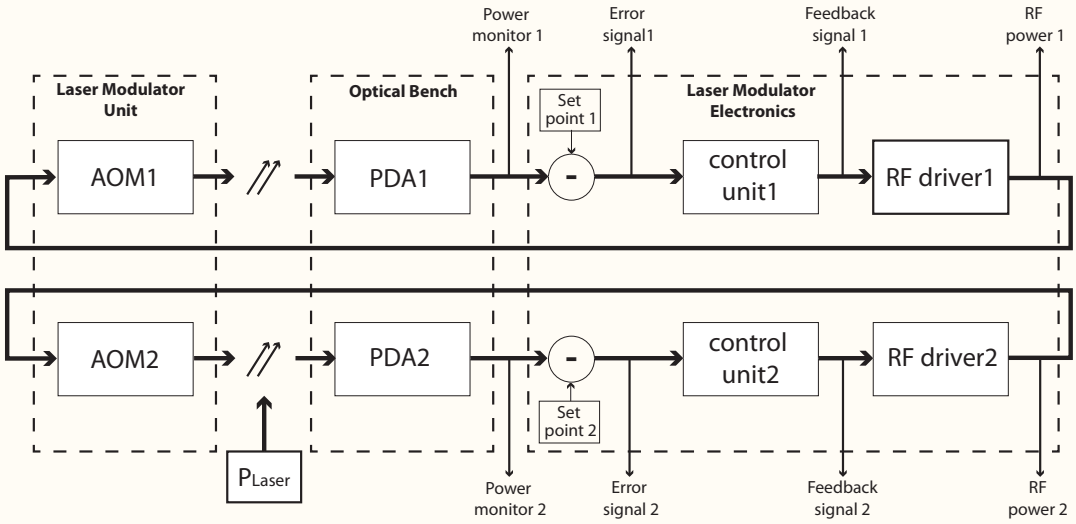

The laser power is split at the modulation bench into two beams, which are both shifted in frequency with an AOM. The AOM output powers are then transmitted to the OB, where they are detected with two power monitor diodes (PDA1 and PDA2, compare to Figure 2.1). For this, the beams are reflected towards PDA1 and PDA2 directly after the corresponding Fibre Injector Optical Subassemblys (FIOSs) with uncoated BSs. The reflected beam powers therefore derive to $\approx 7.87\%$, by the Fresnel formulas for fused silica, orthogonal polarisation and an 45° angle of incidence (Reference [25], page 234 and following).
The power monitor signals are then converted to a voltage with a trans-impedance

amplifier and subtracted from defined control set-points. The corresponding error signals are then input to the control units which derive the feedback signals for the AOM Radio Frequency (RF) drivers. The output of the RF drivers is an electrical power, amplifying the RF power that is fed back to the AOMs. Finally, the RF power actuates the beam power, being diffracted at the AOM crystal into the first order, which is then transmitted to the OB. For further details on the power CL, see References [26, 24].

The analogue implementation of the loop does not allow to apply any guidance signals. Only the set-points of the loop can be accessed with a corresponding command.
In contrast, several signals from within the loops are downloadable from the satellite: The power monitor signals, the error signals, the feedback signals and the RF powers. In this thesis the RF powers are used at different points. The parameter that monitors the RF powers is a 16-bit word that is linearly mapped to a 10 V reference voltage.

2.2. The optical bench

The OB is the core system of the OMS. The beams are guided to the TMs and recombined for interference. Furthermore, its design is of particular interest for the analysis of the beam polarisation, as described in Part II.

A block of Zerodur with $\approx 200\,\text{mm} \times 200\,\text{mm} \times 45\,\text{mm}$ [27] provides an ultra stable optical desk with a high stiffness and ultra low thermal expansion coefficient. The optical components are quasi-monolithically mounted on that plate [28], forming four interferometers. The layout of the OB is shown in Figure 2.1.
The two fibre-coupled beams from the MB are converted to a collimated free beam, parallel to the baseplate, with the so-called FIOSs, as shown in Figure 2.2.

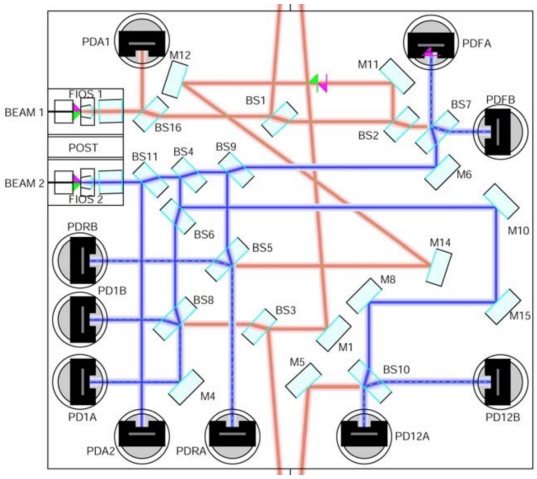

Figure 2.1.: The LPF-OB Layout with a 2 dimensional CAD drawing, reprint from Reference [29].

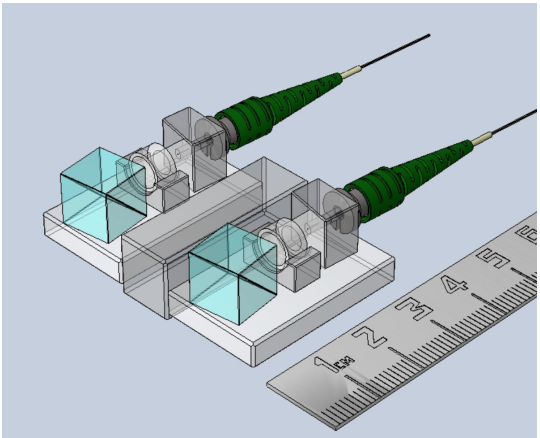

Figure 2.2.: A 3D CAD drawing of the twin pair FIOSs with their mount for coupling the two beams onto the OB together, reprint from Reference [30].

The FIOS consists of a fused silica baseplate that carries the fibre, a collimating lens and a polarisation cleaner. The baseplate is sidelong mounted to an adapter made of Zerodur that itself acts as a mount to the OB. The fibres are glued to a close fitting silica micro-capillary tube that is further glued in a hole of a silica block. Also the collimating lens is glued to a fused silica block. The fibre and lens carrier were then bonded to the baseplate. At the end of the fibre out-coupling system a cubic PBS is glued to clean the output polarisation state. The cube is intentionally rotated to 2° to avoid back reflection into the fibre. The measured rotation angles of the PBSs on the two flight FIOSs are $2° \pm 2°$ for FIOS1 and $3° \pm 2°$ for FIOS2 [31] and [32]. FIOS1 here corresponds to the so-called "measurement beam", which hits the TMs and FIOS2 to the "reference beam" that travels only on the OB without hitting any TM. The unequal path-length of the two beams on the OB is compensated with different lengths of the fibres. The reference beam fibre is approximately 38.2 ± 0.1cm longer, than the measurement beam one [33]).

At the front of the OB, a small part of the beam power is picked off at BS16 and BS11 and detected at the power monitor diodes PDA1 and PDA2 (see Figure 2.1) for power control, as described in Box 2.1.1. After the power pick-off, each beam is further divided into four beams that form four interferometers. In correspondence, three 50:50 BS are used, producing four equally strong output beams, each with two BSs in its beam path. Each of the four measurement beams is in the end combined at another BS - the recombination BS - with one of the four reference beams. In total, $3 + 3 + 4 = 10$ BSs are needed to form the four interferometers.

The difference between the four interferometers are their beam paths. The particular paths, that the beams travel until they are recombined, corresponds to different physical quantities, measured by this interferometer. The LPF interferometers are named after the quantity they intend to observe. Therefore, the particular beam paths are described in the following.

Reference interferometer:

The reference interferometer is, as its name suggests, a reference to the other interferometer paths. The two beams from the MB travel its way through the AOMs and fibres to the OB and are brought to interference without hitting the TMs. The retrieved phase of this interferometer is therefore containing all differential path-length changes from the MB, for example induced by the AOMs or the fibres, but no TM displacements.
On the one hand, this interferometer allows to subtract these disturbing path-length fluctuations, but on the other hand it also serves as the sensor for the active OPD control loop. For this, the retrieved phase of the reference interferometer is fed back to the actuators, located on the MB.

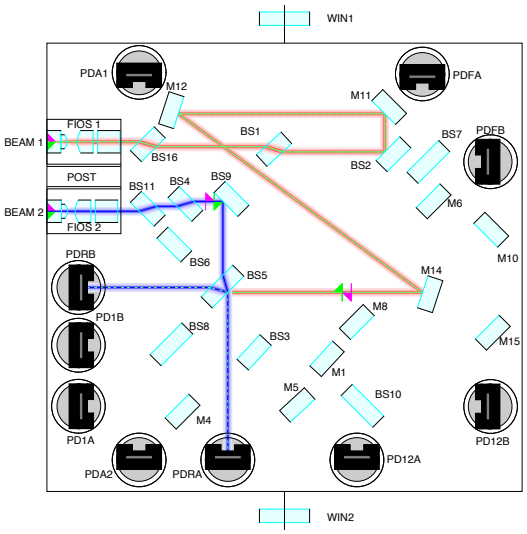

Figure 2.3.: Beam paths of the **reference interferometer**, image: E. D. Fitzsimmons.

Frequency interferometer:

Besides the reference interferometer, there is a second one, travelling exclusively on the OB without hitting any TM: the so-called frequency interferometer. In contrast to the reference interferometer, the measurement and the reference beam of the frequency interferometer travel about the same path-length on the OB. However, as mentioned before, the fibre of the reference beam is about 38 cm longer than the one of the measurement beam. As a consequence, the arm lengths of the frequency interferometer are unequal. This property leads to the feature of this interferometer: it is sensitive to frequency fluctuations of the laser light, because they translate to path-length fluctuations via the arm length mismatch. As for the optical path length difference fluctuations, also for the frequency fluctuations there is an active control mechanism implemented (more details can be found in Reference [24]). Hence, the phase signal of the frequency interferometer is fed back to a slow and a fast operating laser frequency actuator.

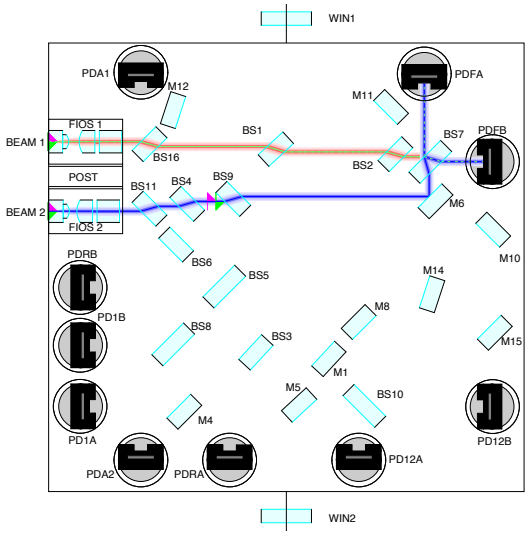

Figure 2.4.: Beam paths of the **frequency interferometer**, image: E. D. Fitzsimmons.

TM1 (x1-)interferometer:

The TM1- or shortened the x1-interferometer is measuring the displacement of the drag-free TM1 to the OB, along the sensitive axis. Therefore, the measurement beam is reflected off TM1 before being recombined with the reference beam. A subtraction of the reference interferometer leaves the desired longitudinal displacement of TM1 and the OB. The retrieved longitudinal and angular displacement can be used as an input signal to the drag-free attitude control system of the sensitive axis.

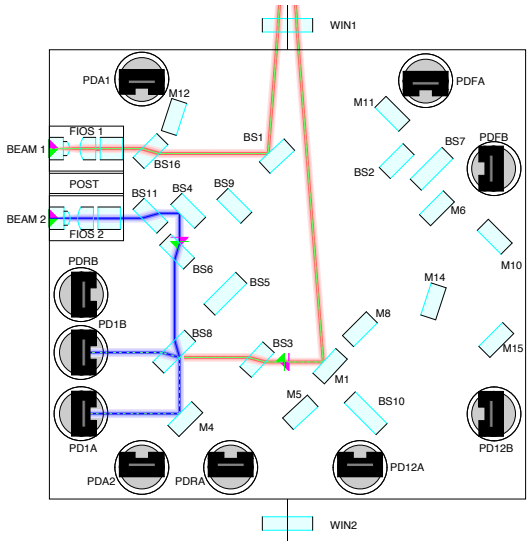

Figure 2.5.: Beam paths of the **x1 interferometer**, image: E. D. Fitzsimmons.

The beam is reflected off the TM with a steep angle of 4.5°. This minimizes lateral displacement of the beam for a TM displacement along the sensitive axis while sufficiently separating incoming and outgoing beam. As a consequence, some OB components are mounted with an offset to the nominal 45° angle to guide the beam to the TMs. The TMs are isolated in an extra vacuum tank to reduce Brownian noise from remaining out-gassing. Therefore,

optical windows are implemented into the tank, allowing the transmission to and from the TMs.

Differential TM (x12-)interferometer:

The differential TM interferometer, or shortly, the x12 interferometer, is the main science interferometer. The measurement beam is reflected off both TMs before recombination with the reference beam. A subtraction of the reference interferometer, therefore, leaves the differential displacement of the two TMs along their sensitive axis. The retrieved displacement can be used in the TM control mechanism, keeping TM2 following TM1 along the sensitive axis.

Furthermore, the differential displacement is used to derive the differential TM acceleration, as described in Section 2.4.

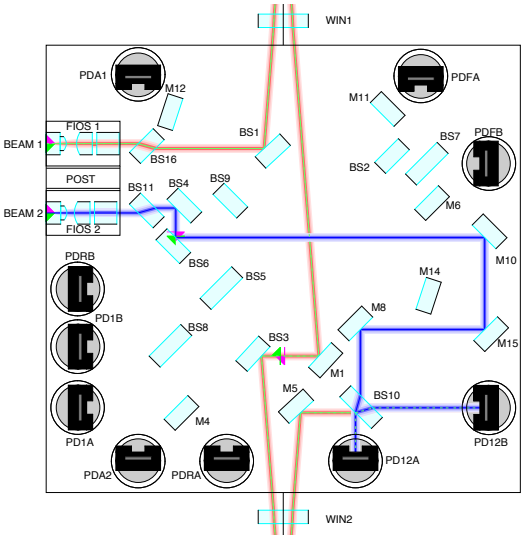

Figure 2.6.: Beam paths of the **x12 interferometer**, image: E. D. Fitzsimmons.

2.3. Heterodyne readout and balanced detection

The recombination of the two frequency shifted beams produces an interference signal at the heterodyne frequency of 1 kHz in both output ports of the recombination BS. Both of these ports are detected with a Quadrant Photodiode (QPD). Besides redundancy, the advantage of detecting both ports is the so-called balanced detection, as described in the following. The interference signal of one part of the measurement beam, $P_{\mathrm{MB,\,PD}} = \frac{1}{8} \cdot P_{\mathrm{MB}}$, with one part of the reference beam, $P_{\mathrm{RB,\,PD}} = \frac{1}{8} \cdot P_{\mathrm{RB}}$, in one of the interferometer ports, denoted as A-port, can be written as:

$$P_{\mathrm{A}} = P_{\mathrm{RB,\,A}} + P_{\mathrm{MB,\,A}} \pm 2 \cdot \sqrt{\eta_{\mathrm{het}} \cdot P_{\mathrm{RB,\,A}} \cdot P_{\mathrm{MB,\,A}}} \cdot \cos(\omega_{\mathrm{het}} \cdot t - \phi)\,, \tag{2.1}$$

with the heterodyne frequency, ω_{het}, a differential phase, ϕ, of the two beams and the heterodyne efficiency, η_{het}. With Equation 2.1 it can easily be seen that Relative Intensity Noise (RIN) at the heterodyne frequency is indistinguishable from the interference signal itself and therefore adds a spurious phase noise.

Because of energy conservation, the sign of the heterodyne part in Equation 2.1 is inverse in the other port, the so-called B-port [7].

$$P_{\mathrm{B}} = P_{\mathrm{RB,\,B}} + P_{\mathrm{MB,\,B}} \mp 2 \cdot \sqrt{\eta_{\mathrm{het}} \cdot P_{\mathrm{RB,\,B}} \cdot P_{\mathrm{MB,\,B}}} \cdot \cos(\omega_{\mathrm{het}} \cdot t - \phi)\,. \tag{2.2}$$

With a 50:50 splitting ratio of the recombination BS, $P_{\mathrm{RB,\,A}} = P_{\mathrm{RB,\,B}}$ and $P_{\mathrm{MB,\,A}} = P_{\mathrm{MB,\,B}}$ the differential power of the two ports, $P_{\mathrm{A}} - P_{\mathrm{B}}$, removes the static power and the corresponding

RIN at the heterodyne frequency, while superposing the heterodyne part of the interference signal.

$$P_{\mathrm{A}} - P_{\mathrm{B}} = 4 \cdot \sqrt{\eta_{\mathrm{het}} \cdot P_{\mathrm{RB,\ A/B}} \cdot P_{\mathrm{MB,A/B}}} \cdot \cos(\omega_{\mathrm{het}} \cdot t - \phi)\,. \tag{2.3}$$

Since the interference signal is detected with a QPD, the four quadrants from A and B port are balanced individually.

For the measurement of the phase in the interference signal, the so-called phasemeter is used. It retrieves the amplitude and phase of the detected heterodyne signal, described by the real and imaginary part of the so-called complex vector $\vec{F}$, by demodulation at the heterodyne frequency. The data processing in the phasemeter is described in the Appendix A with further detail.

2.4. OMS parameters and the differential TM acceleration

The detected powers at the QPDs of the OB interferometers are the source for all derived OMS parameters. They are processed with the phasemeter, as described in Appendix A, and combined in such a way to yield a longitudinal and an angular displacement of the TMs. The signal processing of the phasemeter output in the so-called data management unit is described in the following.

The normalised phasemeter output is given by:

- $Re\{\vec{F}_{ij}^{k}\}$ and $Im\{\vec{F}_{ij}^{k}\}$: the normalised real and imaginary part of the complex vector
- DC_{ij}^{k}: the normalised Direct Current (DC) component

for $i = \mathrm{R}, \mathrm{F}, 1, 12$ referring to the particular interferometer, $j = \mathrm{A}$, B, referring to the interferometer port and $k = \mathrm{A}$, B, C, D, referring to the particular quadrant .

At first, the parameters from A and B diode are averaged individually for the four quadrants, with the balanced detection scheme, described in 2.3. Afterwards, the sum of all quadrants of a balanced QPD and the one sided QPD parameters are calculated, as described in Table 2.1.

The average phase of the four balanced quadrants in one interferometer provides the desired length measurement. Besides this average longitudinal phase, the differential phase between the left and the right quadrants, or the upper and the lower quadrants provides further information of a tilt between the two beams. This measurement principle is called the Differential Wavefront Sensing (DWS) [34, 35]. The corresponding LPF parameters summarised in Table2.2.

The so-called g_i-coefficients in Table 2.2 are used to further scale the derived angular signals, the DWS phase and the DC signal, to angular displacement of the TMs. In contrast to the longitudinal displacement, where the conversion to TM displacement is given by $\mathrm{g}_{\mathrm{TM}} = \frac{\lambda}{4\pi \cdot \cos(\alpha_{\mathrm{TM}})}$, the g_i-coefficients for angular TM displacement are a result of system calibration previous to flight. The derived values can be found in [36]. Furthermore, the set-points of the DWS parameters need to be found via a system calibration during flight. The set-points are

	$\vec{F}$	DC
average A and B	$\vec{F}_i^k = \frac{1}{2} \cdot \left(\vec{F}_{i\mathrm{A}}^k + \vec{F}_{i\mathrm{B}}^k\right)$	$\mathrm{DC}_i^k = \frac{1}{2} \cdot \left(\mathrm{DC}_{i\mathrm{A}}^k + \mathrm{DC}_{i\mathrm{B}}^k\right)$
full QPD	$\vec{F}_i = \sum_k^4 \vec{F}_i^k$	$\Sigma_i = \sum_k^4 \mathrm{DC}_i^k$
one sided	$\vec{F}_i^{\mathrm{left}} = \vec{F}_i^{\mathrm{A}} + \vec{F}_i^{\mathrm{C}}$ $\vec{F}_i^{\mathrm{right}} = \vec{F}_i^{\mathrm{B}} + \vec{F}_i^{\mathrm{D}}$ $\vec{F}_i^{\mathrm{up}} = \vec{F}_i^{\mathrm{A}} + \vec{F}_i^{\mathrm{B}}$ $\vec{F}_i^{\mathrm{down}} = \vec{F}_i^{\mathrm{C}} + \vec{F}_i^{\mathrm{D}}$	$\mathrm{DC}_i^{\mathrm{left}} = \mathrm{DC}_i^{\mathrm{A}} + \mathrm{DC}_i^{\mathrm{C}}$ $\mathrm{DC}_i^{\mathrm{right}} = \mathrm{DC}_i^{\mathrm{B}} + \mathrm{DC}_i^{\mathrm{D}}$ $\mathrm{DC}_i^{\mathrm{up}} = \mathrm{DC}_i^{\mathrm{A}} + \mathrm{DC}_i^{\mathrm{B}}$ $\mathrm{DC}_i^{\mathrm{down}} = \mathrm{DC}_i^{\mathrm{C}} + \mathrm{DC}_i^{\mathrm{D}}$

Table 2.1.: Computation of A-B-average, full QPD and one sided QPD parameters, for $\vec{F}$ and DC as processed by the Data Management Unit (DMU).

Parameter	Estimation
longitudinal phase	$\phi_i = \arg(\vec{F}_i) + n \cdot 2\pi$, with phase tracking $\Phi_i = \phi_i - \phi_{\mathrm{R}} = \mathrm{PT}\left(\arg\left(\frac{\vec{F}_i}{\vec{F}_{\mathrm{R}}}\right)\right)$
TM displacement	$x_1 = \frac{\lambda}{4\pi \cdot \cos(\alpha_{\mathrm{TM}})}\Phi_1$, with $\alpha_{\mathrm{TM}} = 4.5°$ $x_{12} = \frac{\lambda}{4\pi \cdot \cos(\alpha_{\mathrm{TM}})}\Phi_{12}$
DWS phase	$\mathrm{DWS}_i^{\varphi} = \arg\left(\frac{\vec{F}_i^{\mathrm{left}}}{\vec{F}_i^{\mathrm{right}}}\right)$ $\mathrm{DWS}_i^{\eta} = \arg\left(\frac{\vec{F}_i^{\mathrm{up}}}{\vec{F}_i^{\mathrm{down}}}\right)$
DWS angle	$\varphi_1^{\mathrm{DWS}} = \mathrm{g}_1\mathrm{DWS}_1^{\varphi}$ $\eta_1^{\mathrm{DWS}} = \mathrm{g}_2\mathrm{DWS}_1^{\eta}$ $\varphi_2^{\mathrm{DWS}} = \mathrm{g}_3\mathrm{DWS}_1^{\varphi} + \mathrm{g}_4\mathrm{DWS}_{12}^{\varphi}$ $\eta_2^{\mathrm{DWS}} = \mathrm{g}_5\mathrm{DWS}_1^{\eta} + \mathrm{g}_6\mathrm{DWS}_{12}^{\eta}$
DC signal	$\mathrm{DC}_i^{\varphi} = \frac{\Sigma_i^{\mathrm{left}} - \Sigma_i^{\mathrm{right}}}{\Sigma_i}$ $\mathrm{DC}_i^{\eta} = \frac{\Sigma_i^{\mathrm{up}} - \Sigma_i^{\mathrm{down}}}{\Sigma_i}$
DC angle	$\varphi_1^{\mathrm{DC}} = \mathrm{g}_{11}\mathrm{DC}_1^{\varphi}$ $\eta_1^{\mathrm{DC}} = \mathrm{g}_{12}\mathrm{DC}_1^{\eta}$ $\varphi_2^{\mathrm{DC}} = \mathrm{g}_{13}\mathrm{DC}_1^{\varphi} + \mathrm{g}_{14}\mathrm{DC}_{12}^{\varphi}$ $\eta_2^{\mathrm{DC}} = \mathrm{g}_{15}\mathrm{DC}_1^{\eta} + \mathrm{g}_{16}\mathrm{DC}_{12}^{\eta}$

Table 2.2.: List of the relevant LPF parameters as output of the DMU.

the DWS signals, measured with the optimal aligned TM. They are commonly referred to, as DWS offsets.

Besides the OMS output parameters, the differential TM acceleration Δ_g, as well as diagnostic parameters like temperatures and control loop signals were also used in this thesis.
The differential TM acceleration, $\Delta_g(t)$, can be derived from the displacement time series $x_{12}(t)$ as follows:

$$\Delta_g(t) = \ddot{x}_{12}(t) + \omega_2^2 x_{12}(t) + \left(\omega_2^2 - \omega_1^2\right) \cdot x_1(t) - g_c(t) - g_\Omega(t)\,, \tag{2.4}$$

with the second derivative of the differential displacement, $\ddot{x}_{12}(t)$. Therefore, the applied control forces on TM2, $g_c(t)$, the stiffness parameters of the two TMs, ω_1 and ω_2, and a centrifugal force correction, $g_\Omega(t)$, need to be taken into account. Details on these parameters and their calibration can be found in Reference [37, 15, 16, 38].

2.5. LPF's PDs and the expected effects of cosmic radiation

On LPF all interferometer diodes are InGaAs QPDs, operated with 0 V bias. Also the fast power control loops use InGaAs QPDs, where only one quadrant is utilised. For the fast operating loop, a bias voltage of 5 V is used.

PDs are electro-optical components and therefore known to be sensitive to cosmic radiation. Two different basic interaction mechanisms can be distinguished. On the one hand ionizing radiation can create electron hole pairs in the semiconductor and thus lead to radiation-induced conductivity. On the other hand the non-ionizing radiation can lead to the so-called displacement damage in a PD. It describes the displacement of atoms by an incident particle and can be quantified with the Non-Ionizing Energy Loss (NIEL) [39]. The NIEL describes the energy that a specific particle transfers to a certain solid by non-ionizing mechanisms like Coulombic interaction or nuclear interaction (elastic and inelastic) with the lattice atom of the solid. It depends on the particle, its energy and the properties of the solid.

Therefore, In preparation to the LPF mission two different radiation tests were applied to the QPDs. The first one was a mission-equivalent total ionising dose of gamma rays and the second one addressed the displacement damage with a mission-equivalent fluence of high energy particles. The performance of the diodes after radiation was tested in terms of two critical parameters: The PD responsivity and the dark current.

The expected mission dose was calculated for Gallium Arsenide (GaAs) (equivalent to InGaAs) and an equivalent shielding of 4.96 mm Aluminium (for the PDs in place on the OB), as described in Reference [40]. Both tests were applied with a safety factor of 2 for the total expected dose or fluence.

Results of the ionizing radiation test:
The corresponding expected total ionizing dose was computed to 3.27 krad. The radiation tests for the ionizing radiation were performed with Co60, as described in Reference [41]. All tested devices showed negligible impact of gamma rays on responsivity and dark current, even within the safety margin.

Results of displacement damage test:
The average particle fluxes for the launch, the low earth orbiting, the transfer and the on-orbit phase were summed. The equivalent fluence was computed for a bombardment with 35 MeV protons, which was the maximum particle energy, available with the capabilities of the cyclotron at the University in Birmingham. The expected equivalent fluence with a shielding of 5 mm Aluminium was computed to $1.27 \cdot 10^{10} \frac{\text{particles}}{\text{cm}^2}$ (for 35 MeV protons). For this analysis the NIEL for protons in GaAs was used. In contrast to the applied gamma radiation, the proton bombardment, clearly showed an effect on the two relevant parameters — the responsivity and dark current — as described in Reference [20]. For a fluence of $3 \cdot 10^{10} \frac{35\,\text{MeV}}{\text{cm}^2}$ the responsivity decreased up to 35%. But, even without the safety margin, still an average decrease of 17.5% is expected (for the mission equivalent fluence, [21]). Nevertheless, even for the maximum measured decrease in responsivity the phasemeter still meets its performance requirements (as described with more detail in Reference [20]). Also the dark current of the biased PDs strongly increased with a factor of about 100 for the fluence of $3 \cdot 10^{10} \frac{35\,\text{MeV}}{\text{cm}^2}$. Nevertheless, the final maximum value of 450 nA is still small enough to fulfil the requirements of 2 µA. Furthermore, the increase in noise from dark current is negligible for the phasemeter processing, due to the 0 V bias.

Part I.

Long-term monitoring of the photodiode responsivity and the test mass reflectivity

The LPF mission allowed to monitor the PD responsivity in a satellite environment, similar to the one in LISA. The retrieval of the parameter from the LPF data set however, implicated the need for two experiments. In the first one, changes in the TM reflectivity are monitored with single beam power measurements and in the second one, the PD responsivity is derived from a power modulation.
The experimental planning of the two experiments is described in Chapter 3. The in-flight single beam power measurements are detailed in Chapter 4 and the changes in TM reflectivity over the mission duration are derived.
Chapter 5 describes the power modulations and its characterisation during flight of LPF. Furthermore, the PD responsivity and its changes during flight are derived.
Within power modulation characterisation measurements, a spurious tiny power-to-phase coupling was observed. This effect is investigated in Chapter 6 for further LPF data and possible origins are discussed.

3. Experimental planning

The long-term stability of LPFs PDs is an important parameter under test, as described in Section 1.5. The observable power measurement however, depends on several parameters that need to be disentangled.
Therefore, a reference power measurement via radiation pressure and a monitoring of the TM reflectivity are used, as described in Section 3.1.
The design of the corresponding two experiments are detailed in Section 3.2 for the TM reflectivity and in Section 3.3 for the PD responsivity.

3.1. Disentangling the photodiode responsivity and optical power with the LPF data sets

The measured power on a PD linearly depends on the PD responsivity and on the applied optical power. Therefore, it is impossible to distinguish between these two quantities by only the detected power at the PD. Even if there are many measurements, like the eight OB PDs on LPF, the changes in responsivity could only be monitored in comparison to one reference diode. As an example, a decrease in the responsivity of one of OB PDs leads to less detected power at that particular diode. However, this measured decrease in power could have also been induced by a change of the applied laser power. Usually a change in laser power would be common mode to all PDs, whereas a change in the responsivity only affects one particular diode. An overall slow decrease in the PD responsivity, due to a similar relevant dose of cosmic radiation however, would be indistinguishable from a slow change in laser power. On the other hand, a spatially restricted change in the laser power, induced for example by changes in the alignment of a particular beam path, could look like a change in PD responsivity.

As a consequence, a reference measurement of the laser power — independent on any PD responsivity — is needed to break the linear degeneracy and isolate the parameters.
At the time of experimental planning, the satellite was already built up and on its way for flight preparation. Therefore, the design of the long-term monitoring experiments, described here, had to be restricted to the existing hardware and data management infrastructure. The essential question therefore was: Is there any possibility to measure the laser power independently on LPF? Luckily there is one: The applied radiation pressure to the TMs can be used to retrieve the applied beam power.

LPF's main instrument, the LTP, is by design a high-precision accelerometer. The laser beam is reflected off the TMs for interferometric readout of their position. Thereby, it applies a force to the TMs via radiation pressure, proportional to the beam power. The force induces a differential TM displacement that can be measured independently of the applied optical power by the highly precise interferometric readout.

The radiation pressure is given by impulse conservation. For each reflected photon, almost twice their impulse is transferred to the TM $|\vec{p}_{\mathrm{TM}}| = 2 \cdot |\vec{p}_{\mathrm{photon}}| \cdot \cos(4.5°) \approx 2 \cdot \frac{\hbar\omega}{c}$. The resulting force therefore depends on the energy of a photon, given by its wavelength, and the number of reflected photons. This number scales with the desired parameter, the applied beam power, but also with the reflectivity of the TMs, R_{TM}. To ensure that a measured decrease in the radiation pressure is actually induced by the beam power and not by a decrease in the TM reflectivity, a second experiment — monitoring the TM reflectivity — is needed.

Therefore, two experiments were designed to finally retrieve a power reference for the PD calibration: A measurement of the radiation pressure with a beam power modulation, described in Section 3.3, and a TM reflectivity measurement by a combination of single beam powers, as described in 3.2.

3.2. Test mass reflectivity — experiment design

The TM reflectivity at the beam spot position directly influences the induced radiation pressure. Besides its relevance for the reference power measurement, the TM reflectivity itself is an important observable, since it contributes to direct force noise via radiation pressure.

It can be measured by the ratio of reflected to incident power. On LPF the reflected power off the TMs is detected at the four QPDs in the TM interferometers. The beam is furthermore detected at the diodes of the rigid interferometers, without hitting any TM. This measurement, therefore, corresponds to the incident power. However, the measurements are performed with different PDs. The dependency on the PD responsivity therefore needs to be removed in another step. The corresponding experiment design is described in the following, using a simplified model of the OB, as depicted in Figure 3.1.

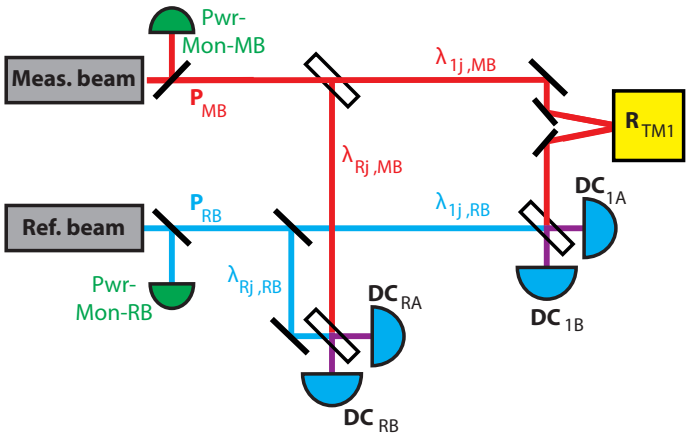

Figure 3.1.: Simplified representation of the OB, with a combined factor for transmission, reflection and losses at the optical bench components, λ_i.

The incident measurement and reference beam travel different paths along the OB , until they are recombined at a BS and detected with two PDs, A and B. In two of the four interferometers, the measurement beam also hits at least one of the TMs before it is combined with the reference beam.

The measured power at a PD is given by the sum of the DC parameters from the four segments: $\mathrm{DC}_{ij} = \sum_k^4 \mathrm{DC}_{ij}^k$. The eight power measurements, DC_{ij}, can then be written as follows:

$$\mathrm{DC}_{ij} = (P_{\mathrm{MB}} \cdot \lambda_{ij,\,\mathrm{MB}}^{\mathrm{OB}} \cdot R_i + P_{\mathrm{RB}} \cdot \lambda_{ij,\,\mathrm{RB}}^{\mathrm{OB}}) \cdot \eta_{ij}. \tag{3.1}$$

with the measurement and reference beam power, P_{MB} and P_{RB}, the combined TM reflectivity and optical window transmittance, R_i, the PD responsivity, η_{ij} and a constant term, $\lambda_{ij,m}^{\mathrm{OB}}$, describing the transmitted power in that particular beam path. It therefore accounts for the reflection and transmission coefficients of the remaining OB components (at BSs and mirrors), and the sum of all losses, L_i, in that beam path with, $\lambda_i = 1 - \mathrm{L}_i$. The indices correspond to:

$$\begin{Bmatrix} i \\ j \end{Bmatrix} = \begin{Bmatrix} \mathrm{R}, \mathrm{F}, 1, 12 \\ \mathrm{A}, \mathrm{B} \end{Bmatrix} \text{ , and} \tag{3.2}$$

$$\begin{Bmatrix} R_{\mathrm{R}} \\ R_{\mathrm{F}} \\ R_1 \\ R_{12} \end{Bmatrix} = \begin{Bmatrix} 1 \\ 1 \\ R_{\mathrm{TM1}} \\ R_{\mathrm{TM1}} \cdot R_{\mathrm{TM2}} \end{Bmatrix}. \tag{3.3}$$

The TM reflectivity can then be isolated from the laser power and PD responsivity by an appropriate combination of single beam power measurements, as described by Figure 3.2 and the following equations.

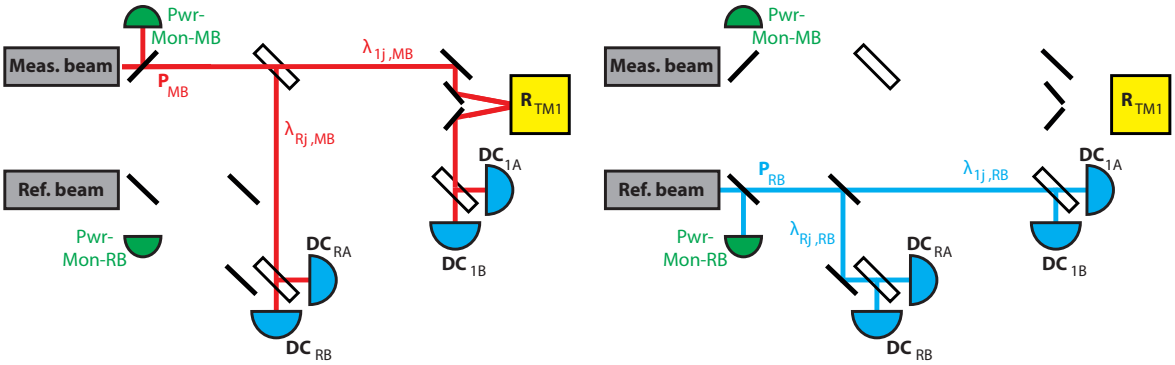

Figure 3.2.: Measurement of single beam powers in the simplified OB representation.

If one beam is turned off, the power on the different diodes 3.1 reduces to:

$$\mathrm{DC}_{ij}(P_{\mathrm{MB}} = 0) = P_{\mathrm{RB}} \cdot \lambda_{ij,\,\mathrm{RB}}^{\mathrm{OB}} \cdot \eta_{ij} \tag{3.4}$$

$$\mathrm{DC}_{ij}(P_{\mathrm{RB}} = 0) = P_{\mathrm{MB}} \cdot \lambda_{ij,\,\mathrm{MB}}^{\mathrm{OB}} \cdot R_i \cdot \eta_{ij}. \tag{3.5}$$

The measurement beam power on the diodes of the TM interferometers $\mathrm{DC}_{1j}(P_{\mathrm{RB}} = 0)$ and $\mathrm{DC}_{12j}(P_{\mathrm{RB}} = 0)$ includes the reflectivity $R_{\mathrm{TM}i}$. To eliminate the PD responsivity η_{ij} the measurements need to be combined with the power of the reference beam on that particular diode $\mathrm{DC}_{ij}(P_{\mathrm{MB}} = 0)$. For the TM1 interferometer this combination is given by :

$$\frac{\mathrm{DC}_{1j}(P_{\mathrm{RB}}=0)}{\mathrm{DC}_{1j}(P_{\mathrm{MB}}=0)} = \frac{P_{\mathrm{MB}} \cdot \lambda^{\mathrm{OB}}_{1j,\,\mathrm{MB}} \cdot R_{\mathrm{TM}i}}{P_{\mathrm{RB}} \cdot \lambda^{\mathrm{OB}}_{1j,\,\mathrm{RB}}}. \tag{3.6}$$

In the next step, the laser power of reference beam and measurement beam are removed. This is done with a power measurement in a different interferometer without TMs, for example the reference interferometer. Of course, also for this interferometer the PD responsivity needs to be eliminated, first:

$$\frac{\mathrm{DC}_{\mathrm{R}j}(P_{\mathrm{RB}}=0)}{\mathrm{DC}_{\mathrm{R}j}(P_{\mathrm{MB}}=0)} = \frac{P_{\mathrm{MB}} \cdot \lambda^{\mathrm{OB}}_{\mathrm{R}j,\,\mathrm{MB}}}{P_{\mathrm{RB}} \cdot \lambda^{\mathrm{OB}}_{\mathrm{R}j,\,\mathrm{RB}}}. \tag{3.7}$$

Division of Equation 3.6 with Equation 3.7 leaves the TM1 reflectivity:

$$R_{\mathrm{TM1}} = \frac{\mathrm{DC}_{1j}(P_{\mathrm{RB}}=0) \cdot \mathrm{DC}_{\mathrm{R}j}(P_{\mathrm{MB}}=0)}{\mathrm{DC}_{1j}(P_{\mathrm{MB}}=0) \cdot \mathrm{DC}_{\mathrm{R}j}(P_{\mathrm{RB}}=0)} \cdot \frac{\lambda^{\mathrm{OB}}_{1j,\,\mathrm{RB}} \cdot \lambda^{\mathrm{OB}}_{\mathrm{R}j,\,\mathrm{MB}}}{\lambda^{\mathrm{OB}}_{1j,\,\mathrm{MB}} \cdot \lambda^{\mathrm{OB}}_{\mathrm{R}j,\,\mathrm{RB}}}. \tag{3.8}$$

For TM2 the correspondingly derived combinations are given as follows:

$$R_{\mathrm{TM2}} = \frac{\mathrm{DC}_{12j}(P_{\mathrm{RB}}=0) \cdot \mathrm{DC}_{1j}(P_{\mathrm{MB}}=0)}{\mathrm{DC}_{12j}(P_{\mathrm{MB}}=0) \cdot \mathrm{DC}_{1j}(P_{\mathrm{RB}}=0)} \cdot \frac{\lambda^{\mathrm{OB}}_{12j,\,\mathrm{RB}} \cdot \lambda^{\mathrm{OB}}_{1j,\,\mathrm{MB}}}{\lambda^{\mathrm{OB}}_{12j,\,\mathrm{MB}} \cdot \lambda^{\mathrm{OB}}_{1j,\,\mathrm{RB}}}, \tag{3.9}$$

$$= \frac{\mathrm{DC}_{12j}(P_{\mathrm{RB}}=0) \cdot \mathrm{DC}_{\mathrm{R}j}(P_{\mathrm{MB}}=0)}{\mathrm{DC}_{12j}(P_{\mathrm{MB}}=0) \cdot \mathrm{DC}_{\mathrm{R}j}(P_{\mathrm{RB}}=0) \cdot R_{\mathrm{TM1}}} \cdot \frac{\lambda^{\mathrm{OB}}_{12j,\,\mathrm{RB}} \cdot \lambda^{\mathrm{OB}}_{\mathrm{R}j,\,\mathrm{MB}}}{\lambda^{\mathrm{OB}}_{12j,\,\mathrm{MB}} \cdot \lambda^{\mathrm{OB}}_{\mathrm{R}j,\,\mathrm{RB}}}. \tag{3.10}$$

Equation 3.8 to 3.10 are now only dependent on the measurements of the single beam powers and the transmission coefficients of the remaining OB components $\lambda^{\mathrm{OB}}_{ij,\,m}$. The OB components are all multilayer-coated fused silica blocks, which are expected to be very weakly sensitive to cosmic rays. As a consequence, it is assumed that the transmission coefficients are stationary, so that the TM reflectivities can be monitored during mission with high accuracy. For the comparison of different monitoring measurement samples, the laser power fluctuations and PD responsivities cancel by design. The only remaining statistical measurement noise, affecting Equation 3.8 to 3.10, is uncorrelated electronic read-out noise of the different channels, dominated by the Analogue-to-Digital Converter (ADC).
However, the stationary transmission coefficients are only known within errors. Therefore, the measurements of the TM reflectivities are affected by systematic errors. Prior to flight, the optical properties of the OB components were measured with an uncertainty of 0.49% for the BSs and 0.24% for the mirrors (see Reference [42]) Propagation of the uncertainty-boundaries to $R_{\mathrm{TM}i}$ gives a comparably big systematic error of 2.62% for TM1 and 2.78% for TM2.
Nevertheless, the changes in the TM reflectivity can be monitored with high accuracy, so that its impact on the radiation pressure is distinguishable from the applied power.
Therefore, the second step on the path to the PD responsivity monitoring is described in the following — the measurement of applied radiation pressure.

3.3. Photodiode responsivity — experiment design

LPF uses interferometry to precisely measure the differential TM acceleration. The measurement beam is reflected off the two TMs, to measure their differential optical path-length.

Thereby, it applies a force via radiation pressure to the TMs, which can be used as a power reference, as described in the following.

A beam with power $P_{\mathrm{TM}i}$, being reflected off the two TMs, applies a static differential force, $F_{\mathrm{TM1}} + F_{\mathrm{TM2}}$, to them, given by the following equation:

$$F_{\mathrm{TM1}} + F_{\mathrm{TM2}} = (1 + R_{\mathrm{TM1}}) \cdot \frac{P_{\mathrm{TM1}}}{\mathrm{c}} + (1 + R_{\mathrm{TM2}}) \cdot \frac{P_{\mathrm{TM2}}}{\mathrm{c}} \text{ , with} \tag{3.11}$$

$$P_{\mathrm{TM2}} = P_{\mathrm{TM1}} \cdot \lambda^{\mathrm{OB}}_{\mathrm{TM1\,-\,TM2,\ MB}} \cdot R_{\mathrm{TM1}} \,. \tag{3.12}$$

The power at TM2 is linear dependent on the reflectivity of TM1, because the beam is at first reflected off TM1 before it is guided to TM2. The coefficient $\lambda^{\mathrm{OB}}_{\mathrm{TM1\,-\,TM2,\ MB}}$ therefore describes the transmission and reflection coefficients and losses at the OB components between TM1 and TM2.

Apart from the radiation pressure there are more sources of static forces acting on the TMs. Therefore, a constant force is applied via the capacitive actuators to the suspended TM2, keeping the TM centred within its housing [18]. To determine the desired contribution from the radiation pressure the power of the measurement beam, P_{MB}, is modulated, so that the induced force is isolated in frequency. The power modulation combined with the constant voltage then results in a back and forth displacement of the TMs, as described by the following equation:

$$x_{\mathrm{TM1}} + x_{\mathrm{TM2}} = \left((1 + R_{\mathrm{TM1}}) \cdot \frac{P_{\mathrm{TM1}}}{\mathrm{m_{TM1}}} + (1 + R_{\mathrm{TM2}}) \cdot \frac{P_{\mathrm{TM2}}}{\mathrm{m_{TM2}}} \right) \cdot \frac{a_{\mathrm{mod}}}{\mathrm{c} \cdot (\omega_{\mathrm{m}}^2 - \omega_{\mathrm{stiff}}^2)} \,. \tag{3.13}$$

Here, a_{mod} describes the power modulation depth at the modulation frequency ω_{m}. The stiffness term ω_{stiff}, corresponds to the gravitationally coupled system of TMs and satellite, as described in Reference [43, 24].

With the measured differential TM displacement $x_{\mathrm{TM1}} + x_{\mathrm{TM2}}$ and the applied forces F_{sus} for suspension control, the resulting differential TM acceleration, Δg, can be retrieved, as described with more detail in Reference [15] and [16].

The desired power reference is then given by the following Equation 3.14:

$$\Delta_g|_{\omega_{\mathrm{m}}} = (1 + R_{\mathrm{TM1}}) \cdot \frac{P_{\mathrm{TM1}}|_{\omega_{\mathrm{m}}}}{\mathrm{c} \cdot m_{\mathrm{TM1}}} + (1 + R_{\mathrm{TM2}}) \cdot \frac{P_{\mathrm{TM2}}|_{\omega_{\mathrm{m}}}}{\mathrm{c} \cdot m_{\mathrm{TM2}}}. \tag{3.14}$$

For the implementation of the power modulation on LPF, a square wave modulation had to be used, since the analogue power control loop only allowed to change the set-point. Conveniently, a square wave modulation also provides signal at higher frequencies — the several odd harmonics of the modulation frequency. A simplified scheme of the induced TM displacement is illustrated in Figure 3.3.

As the next step, the relation between the PD measurements, containing the relevant responsivities, and the reference power needs to be determined.
The applied power modulation is detected by the power monitor diodes of each individual beam and the eight QPDs at the interferometer output ports. In principle each of these diodes can be calibrated by the reference power, with one exception — the reference beam power monitor diode that is not detecting any light of the measurement beam. For this diode only

an indirect calibration by comparing a reference beam modulation between a calibrated QPD and the reference beam power monitor diode is possible.

The PD responsivity η, describes how much photocurrent I is induced by the optical power, P, hitting the diode:

$$I = P \cdot \eta_i. \tag{3.15}$$

On LPF the induced photocurrent is further processed before it is downloadable from the satellite as the so-called Σ parameter.

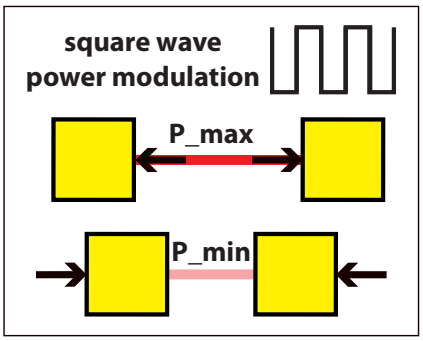

Figure 3.3.: Illustration of TM displacement induced by radiation pressure modulation

A QPD basically consist of 4 individual PDs, the so-called segments with index k, detecting about one quarter of the beam surface. The induced photocurrent, I^k, of each segment is individually converted to a voltage with a trans-impedance amplifier, with resistance, $\mathrm{R_{TI}}$, and sampled with an ADC of range $\mathrm{U_{ADC}}$. This results in a sampled signal, DC^k, for each quadrant of:

$$\mathrm{DC}^k = I^k \cdot \frac{\mathrm{R}^k_{\mathrm{TI}}}{\mathrm{U}^k_{\mathrm{ADC}}} = P^k \eta^k \cdot \frac{\mathrm{R}^k_{\mathrm{TI}}}{\mathrm{U}^k_{\mathrm{ADC}}} \tag{3.16}$$

with units of $\left[\mathrm{A} \cdot \frac{\Omega}{\mathrm{V}} = 1\right]$.

The DC signals are usually not available, because of the high data-rate. They are further processed to the so-called Σ parameters. These are given by the sum of all four quadrants and averaging with the neighbouring diode in that interferometer (index i):

$$\Sigma_i = \frac{1}{2} \cdot \left(\sum_{k=1}^{4} \mathrm{DC}^k_{i\mathrm{A}} + \sum_{k=1}^{4} \mathrm{DC}^k_{i\mathrm{B}}\right). \tag{3.17}$$

Assuming the agreement of all trans-impedance amplifier resistances and ADC ranges within errors, and an equal splitting of the laser power between the A and B ports, the Σ parameters can be written as:

$$\Sigma_i = \frac{1}{2} \cdot P_i \cdot (\eta_{i\mathrm{A}} + \eta_{i\mathrm{B}}) \cdot \frac{\mathrm{R}^k_{\mathrm{TI}}}{\mathrm{U}^k_{\mathrm{ADC}}} = P_i \cdot \eta_i \cdot \frac{\mathrm{R_{TI}}}{\mathrm{U_{ADC}}}, \tag{3.18}$$

with the virtually combined responsivity of A and B diode in one interferometer:

$$\eta_i = \frac{1}{2} \cdot (\eta_{i\mathrm{A}} + \eta_{i\mathrm{B}}). \tag{3.19}$$

The optical power P_i will be estimated from radiation pressure measurement, as described by Equation 3.14.

But, the reference power is estimated from the force, applied to the TMs by the incident beam. However, this power is measured at the TMs. To compare with the Σ parameters, the share of the measurement beam power at the diodes needs to be determined. Since the radiation pressure is estimated via a measurement beam modulation, a demodulation of the

Σ parameter at that frequency directly refers to the modulated measurement beam power at the diode. The propagation of this power back to the TMs can be done via the propagation factors $\lambda^{\perp}_{\Sigma_i\text{-TM1, MB}}$, described in Appendix B.

$$P_{\text{TM1}}|_{\omega_\text{m}} = P_i|_{\omega_\text{m}} \cdot \lambda^{\perp}_{\Sigma_i\text{-TM1, MB}} \,. \tag{3.20}$$

Of course, the transmission coefficients differ along the four interferometer beam paths. The power at TM1 can therefore be written with the available Σ_i parameters of the four interferometers, following Equation 3.18:

$$P_{\text{TM1}}|_{\omega_\text{m}} = \Sigma_i|_{\omega_\text{m}} \cdot \lambda^{\perp}_{\Sigma_i\text{-TM1, MB}} \cdot \frac{1}{\eta_i} \cdot \frac{\text{U}_\text{ADC}}{\text{R}_\text{TI}} \,. \tag{3.21}$$

Combined with the reference power (Equation 3.14), the PD responsivity, η_i, can finally be retrieved from the differential acceleration, Δ_g, and the measured power, Σ_i, at the modulation frequency by:

$$\eta_i = \frac{\Sigma_i(@\,\omega_\text{m})}{\Delta_g(@\,\omega_\text{m})} \cdot \left(\lambda^{\perp}_{\Sigma_i\text{-TM1, MB}} \cdot \frac{1 + R_\text{TM1}}{\text{c} \cdot \text{m}_\text{TM1}} + \lambda^{\perp}_{\Sigma_i\text{-TM2, MB}} \cdot \frac{1 + R_\text{TM2}}{\text{c} \cdot \text{m}_\text{TM2}} \right) \cdot \frac{\text{U}_\text{ADC}}{\text{R}_\text{TI}} \,. \tag{3.22}$$

With regard to LISA, the modulation parameters were chosen as follows: a degradation of 50 % in PD responsivity leads to a decrease of $\sqrt{2}$ in sensitivity for a shot noise limited observatory. Therefore, the PD responsivity should be monitored with an accuracy that, when linearly extrapolated, at least excludes a decrease of 50 % in a planned LISA duration of 6 years. Within a monitoring period of one year LPF nominal mission duration, the accuracy must therefore be better than 8.5 %. To be able to temporally resolve effects on a timescale of months an accuracy of 1 % was targeted with resulting parameters of 0.1 % peak-to-peak modulation depth at 1.67 mHz with a duration of 10 000 s.

Furthermore, three characterisation measurements for the power modulation were planned, to investigate possible noise sources affecting the measurement.
The first one is a reference power modulation without modulation of the radiation pressure. Therefore, the reference beam is used, to modulate the power at the PDs without applying differential acceleration to the TMs.
In the second one, the modulation depth is increased to check the linearity between modulated power and observed differential acceleration.
The last measurement estimates the impact of the temperature gradient at the PDs. Therefore, the two beams are counter modulated to keep the average optical power at the PDs and in consequence its temperature stable, while modulating the radiation pressure.

4. Test mass reflectivity monitoring during flight

During the flight of LPF, the reflectivity of the two TMs at the beam spot positions was monitored with an experimental concept using single beam powers, as described in Section 3.2. The following Chapter describes the performed single beam power measurements in Section 4.1 and analyses the noise in the individual time series. The changes in TM reflectivity between the individual investigations are finally retrieved in Section 4.3. The estimates are further compared to a reference measurement, to estimate realistic errors to the long-term monitor.

4.1. Measurement of single beam powers

For the measurement of the single beam powers, the beams were turned off one after another. Of course, this procedure could only be executed in satellite operating modes with GRS control, since there is no interferometric read-out with only one beam. Therefore, most of these investigations were run during station keeping manoeuvres, so that no other experiments were disturbed.

The single beam powers are also part of another long-term monitoring experiment: the spot positions of the single beams on the PDs that can be used to monitor the OB stability. The shared use of the data increased the outcome of the experiment and thus helped to justify several executions of the procedure.

During the so-called cool down phase the temperature of the whole satellite was reduced by several degrees. A change in temperature is of special interest for the OB stability monitoring. Therefore, the single beam powers were measured frequently during that time.

Almost all investigations could be used for the estimation of TM reflectivity. Figure 4.1 shows the schedule of all single beam power measurements, having the full set of data, which means: The power of both beams on all quadrants of A and B diodes in each interferometer. Therefore, a total monitoring duration of 392 days is reached with this data set. However, the gaps in between two individual investigations last from an hour up to several days. Hence, the index of measurement (vertical axis in Figure 4.1) is used throughout this thesis instead of the actual date of execution, to avoid indistinguishable clusters of data points.

For the computation of the beam spot positions the individual quadrant powers were needed. The experiment also required a higher sampling rate of 10 Hz data, which increased the desired data to be downloaded by an additional 320 samples per second (8 diodes times 4 quadrants times 10 samples per second). However, it was not possible to download 32 channels with 10 Hz in addition to the basic LPF data set at once. Therefore, the power on all 8 quadrants of

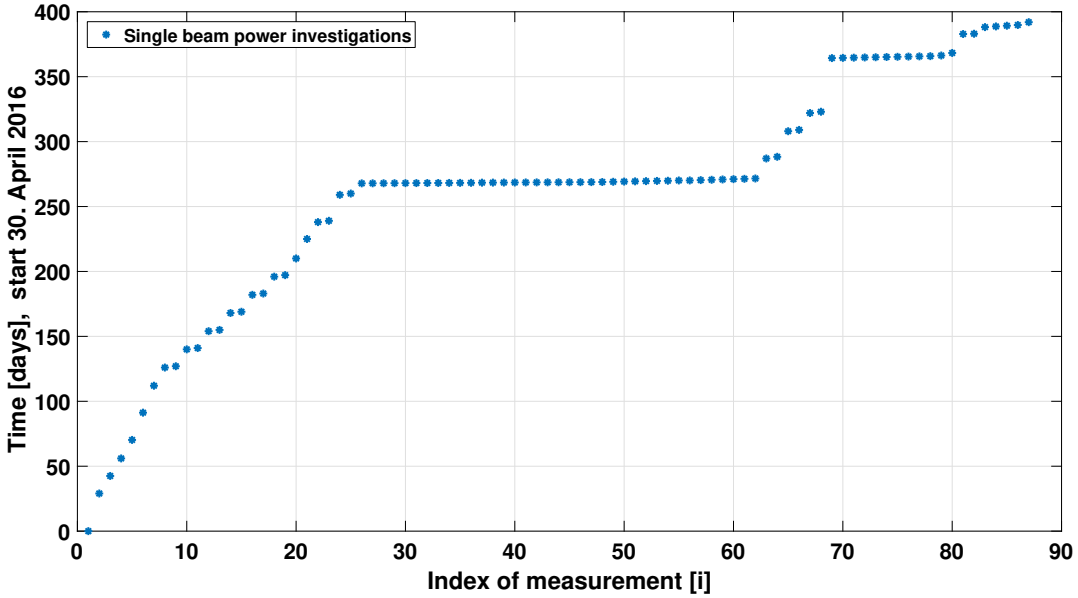

Figure 4.1.: Schedule of all single beam power investigations, performed during flight of LPF. The investigations with index 26 to 62 are taken frequently during the so-called "cool down" phase.

only one interferometer is recorded and downloaded at a time. This led to the measurement procedure, described in Box 4.1.1:

Box 4.1.1: Single beam power measurement:

For one single beam power measurement the following commanding procedure was executed:

1. Change the satellite operating mode to a TM control mode, so that the capacitive TM position read-out is used for drag free control.
2. Turn the fast power CL of beam 1, corresponding to the measurement beam, off.
3. Turn the RF power to the corresponding AOM1 off.
4. Record all power data in the interferometers, sequentially:
   - starting with the TM1 interferometer for one minute,
   - then proceed with the differential TM interferometer for a minute,
   - then the frequency interferometer,
   - and finally the reference interferometer.
5. Turn the RF power to AOM1 back on.
6. Turn the fast power CL of beam 1 back on.
7. Proceed with step 2 to 6 for beam 2, corresponding to the reference beam.

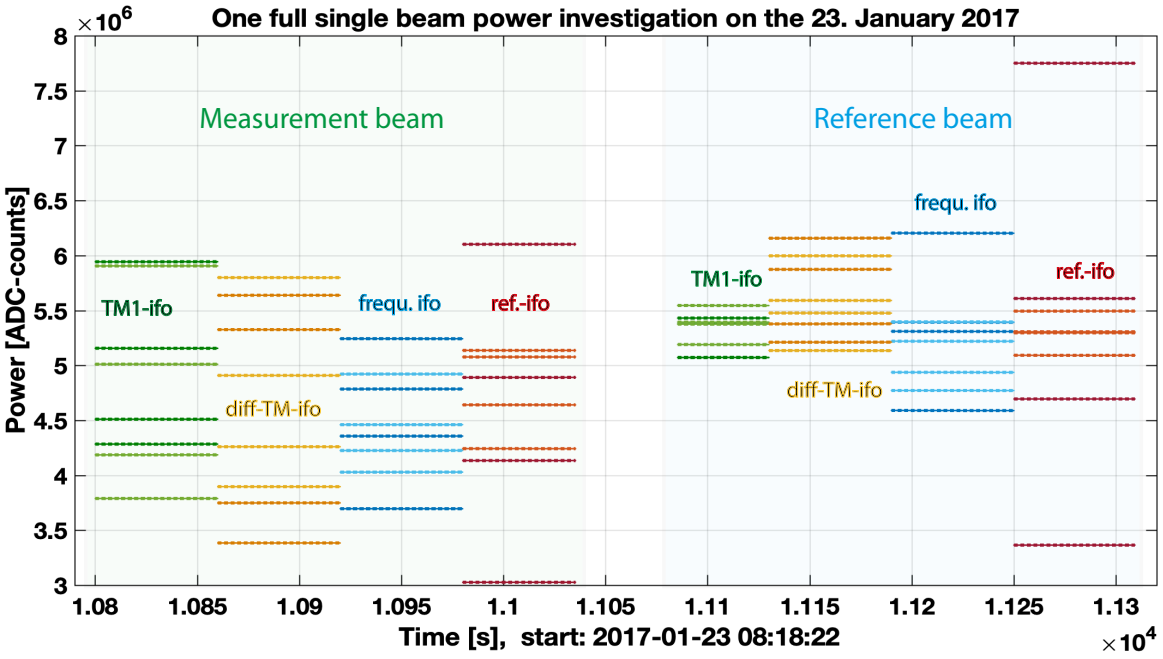

Figure 4.2.: Example time series from the 23rd of January in 2017, of a single beam power investigation. The beams are shut off one after another and the powers of the individual quadrants are measured sequentially for the four interferometers.

An example time series of the raw-data (the DC parameters in ADC-counts without calibration with the corresponding C^{DC}-coefficient) from a typical investigation can be seen in Figure 4.2. The four quadrants of one diode are plotted with the same colour, because they are summed up in the following analysis to the power of the particular beam on the individual diodes. The colour coding of the resulting 8 QPD powers on the OB is shown in Figure 4.3. It is kept through all of this thesis for clarity. The powers are measured in ADC counts without any calibration. As described in the following, the powers were therefore normalised to the overall measured power on the OB, leading to a scaled, unit-less quantity.

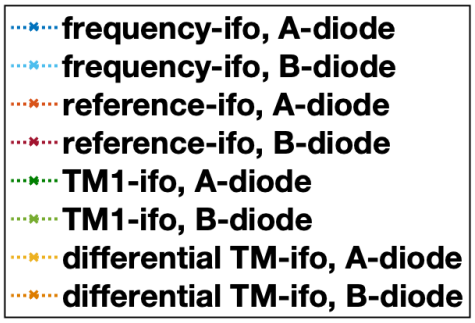

Figure 4.3.: Colour coding of power measurements at OB QPDs.

4.2. Noise sources affecting the single beam power measurements

The TM reflectivity experiment had the advantage of cancelling power noise by design, as described in Chapter 3. However, the minor change of measuring the beam powers subsequently in the different interferometers, degraded that noise suppression. The time series of the different PD powers, used for TM reflectivity retrieval, are not detected at the same time. Therefore, also their power noise does not cancel by division with Equation 3.7, any more. In consequence, the power noise on the time scale of the investigation duration still affects the measurement observable.

The impact of high frequency power noise is reduced by averaging 10 Hz data over a minute. Low frequencies are furthermore reduced by the comparably short investigation duration of about 10 minutes. Hence, only power noise at frequencies in between this upper and lower limit is relevant to the measurement. The RIN on LPF is below 10^{-5} W/W for frequencies above 10 mHz (compare to Figure 6.12). Therefore, the measurement accuracy was not limited by RIN, as derived in the following.

Another relevant noise source is caused by beam pointing from angular TM motion. In consequence, the measurement beam scans over the surface of the TM interferometer PDs. The slits between the quadrants and inhomogeneous responsivity profiles of the PD active surfaces could have led to extra power noise. The capacitive read-out, used for the TM motion control, is less sensitive than the interferometer one. Therefore, the control mode that is used during the single beam power measurements further increases a possible beam pointing effect, due to a higher TM jitter.
The induced noise can be investigated by a closer look at the differential power fluctuations on the particular quadrants of one diode. Therefore, the quadrant powers of the example data set from the 23rd of January 2017 (compare to Figure 4.2) were normalised to their particular average power, depicted in Figure 4.4.

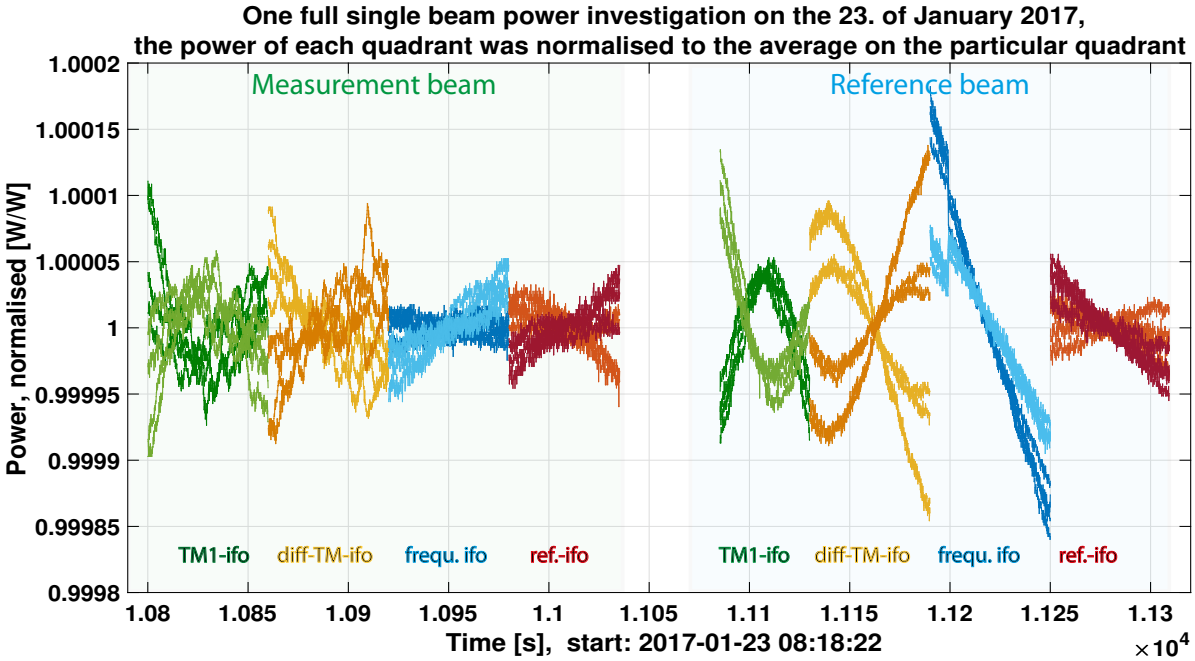

Figure 4.4.: Differential power fluctuations of the eight quadrants from A and B diodes for the example data set (compare to Figure 4.2). Surprisingly, the differential powers of the quadrants from one diode are similar, wherefore the difference in A and B diode is much stronger.

Overall, the normalised differential power fluctuations are in the order of 10^{-4} and therefore very small. The measurement beam on the TM interferometer diodes indeed shows additional fluctuations, but the full range (between highest and lowest detected differential power) within a minute is not greater than for the other diodes. Hence, it seems that another effect is possibly dominating the differential power noise on those diodes.

For the reference beam power on the frequency interferometer diodes clearly an overall trend is visible. An equivalent, but smaller trend, can be observed for the reference diode. Also the measurement beam shows this behaviour in the frequency and reference interferometers. These trends are most likely induced by a slow change of parallel polarised power on the OB. A comparison to the dedicated pattern, as described in Box 7.0.1, agrees.

Furthermore, it is striking that the differential powers in the TM1 and differential TM interferometers, drift inversely for the A and B diodes. For the reference beam this is clearly not a cause of the TM motion, since there are no TMs in the beam path.
Furthermore, the inverse power drifts between A and B diode do not fit with the theory for polarisation-induced power fluctuations. On the one hand, the off-nominal polarised power is filtered out to a high extent for the differential TM interferometer. On the other hand, the induced trend in differential power should be highly correlated between different diodes for the same beam. The power with off-nominal polarisation differs between the different PDs, but the time series of changes in polarisation is unique to the particular beam.

As a consequence, the question is, what else could have led to a differential power noise on these diodes.
One possibility is the sequential recording of the power in the interferometers: After switching the power of one beam off, the temperature of the PDs will decrease, due to the smaller incident power. Consequently, the responsivity will change due to its dependency on temperature. Since the temperature gradient is strongest for the measurements directly after one beam is turned off, the first two minutes could be more effected by resulting noise than the latter ones. However, such an effect should be untouched by the A and B labels, since both diodes experience about the same temperature gradient.

The inverse behaviour of A and B diodes therefore points to a different origin before detection at the PDs: the recombination BSs divide the beam into A and B paths. Thus, they are suspected to cause the observed fluctuations, as described in the following.

A time-dependent jitter in the splitting ratio of a recombination BS would agree with the observations. This jitter might possibly be induced by temperature changes in the coating or a beam pointing over the surface of the BS. However, the analysis of spot positions showed stable beam positions during a measurement [44]. Therefore, only temperature-dependent properties of the coating are left. A rough estimation of the numbers for the thermo-optical and thermal expansion coefficients of common materials for BSs clearly disagrees. Furthermore, already a logic argument rules out such an effect: Each interferometer has 2 more BSs before the recombination BS. A temperature-dependent jitter in the splitting ratio would therefore cause differential power changes between the different interferometers — just by superposition of three of these BSs. Since the average power in the interferometers is constant (except for the polarisation-induced slow drifts), a temperature-dependent BS splitting ratio jitter can be ruled out.

Besides the power splitting of a BS, the interference signal also shows an inverse distribution between the A and B port due to the phase shift of π (which is a consequence of energy conservation, compare to Section 2.3). Combining this assumption with the known presence of ghost beams in the interferometer (as described in Reference [45]) leads to a theory in agreement with the observations: as Gaussian beam, a ghost beam, located close to a PD, might still have non-negligible power at the surface of the PD. If direction and polarisation of

ghost and main beam agree, the beams interfere with each other. Since a ghost beam has the same frequency as its main beam, the resulting interference signal is static. Due to the phase shift of π, a constructive interference on diode A leads to a destructive one on diode B. A slow change in relative phase between ghost and main beam (for example, due to temperature) therefore produces an inverse drift in differential power on the A and B diodes, as observed for the TM interferometers.

The normalised interference signal between a beam with power P_{main} (reference or measurement beam), and a ghost beam (from the main one) of power P_{GB}, can be written as follows (compare with 2.3):

$$P_{\mathrm{norm}} = 1 + 2 \cdot \frac{\sqrt{P_{\mathrm{main}} \cdot P_{\mathrm{GB}} \cdot \eta}}{P_{\mathrm{main}} + P_{\mathrm{GB}}} \cdot \cos(\phi_{\mathrm{GB}}(t) - \phi_{\mathrm{main}}(t) + \arg(\beta)) \,, \tag{4.1}$$

with the interferometric efficiency $\eta = \mathrm{abs(b)}^2$, given by the squared magnitude of the overlap-integral $\mathrm{abs}(\beta)$ of main and ghost beam (details can be found in Reference [46]).

However, the single beam power measurements only last for a minute. In this short duration the phase relation $\Delta(\phi) = \phi_{\mathrm{GB}} - \phi_{\mathrm{main}}$ is not going through a full cycle. For a rough estimation, a signal amplitude of $1.5 \times 10^{-4}\,\mathrm{W/W}$ for the normalised homodyne interference signal is used (compare to the reference beam power in the differential TM interferometer in Figure 4.4):

$$2 \cdot \frac{\sqrt{P_{\mathrm{main}} \cdot P_{\mathrm{GB}} \cdot \eta_{\mathrm{hom}}}}{P_{\mathrm{main}} + P_{\mathrm{GB}}} \approx 1.5 \cdot 10^{-4} \left[\frac{\mathrm{W}}{\mathrm{W}}\right] . \tag{4.2}$$

With $P_{\mathrm{GB}} << P_{\mathrm{main}}$ this gives a ghost beam power of:

$$P_{\mathrm{GB}} \cdot \eta_{\mathrm{hom}} = P_{\mathrm{main}} \cdot \frac{9}{16} \cdot 10^{-8} \left[\frac{\mathrm{W}}{\mathrm{W}}\right] . \tag{4.3}$$

Therefore, a power of $\frac{P_{\mathrm{GB}}(\text{in-mode})}{P_{\mathrm{main}}+P_{\mathrm{GB}}} = \frac{9}{16} \cdot 10^{-8}\,\mathrm{W/W}$ was found to be in mode with the main beam with approximately $\frac{P_{\mathrm{main}}}{P_{\mathrm{main}}+P_{\mathrm{GB}}} \approx 1\,\mathrm{W/W}$.

Possible candidates for ghost beams are inner reflections on the BSs, or transmissions through mirrors. The reflection at BS4 is particularly suspected, because it reflects the reference beam into the beam path of the x12 and the x1 interferometer (compare with Figure 2.5 and 2.6).

To give an overview of the full data set, the standard deviation of the average normalised power on each diode, so the sum of its four quadrants, normalised to its average power, is shown in Figure 4.5 for both beams and all investigations.

The standard deviations of the normalised single beam powers are for all investigations smaller than 10^{-5} with the units of $[\mathrm{W/W} = 1]$.
During mission extension, the data management of the differential TM interferometer diodes changed: the powers are only sampled with 1 Hz and measured during the full 4 minutes of the particular single beam investigation (i.e. as long as the other beam was turned off). The standard deviation of the differential TM interferometer diodes therefore is slightly higher for the last 25 samples.
Furthermore, the standard deviation of the frequency interferometer powers in Figures 4.5 show some spikes. These are likely induced by polarisation drifts, as discussed above and described in Part II.

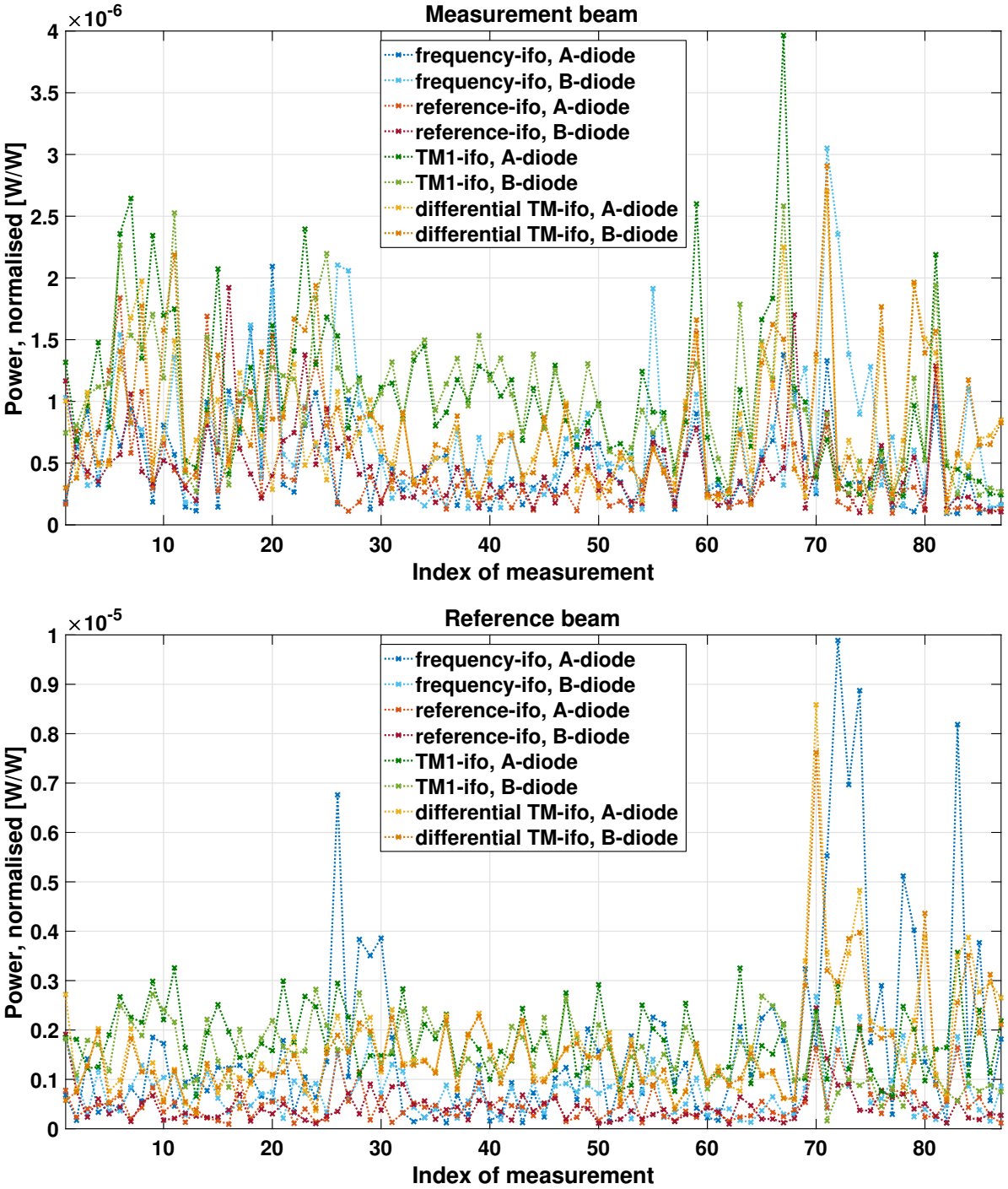

Figure 4.5.: Standard deviation of the normalised, average power on one diode for all single beam power investigations. The upper figure describes the measurement beam and the lower one the reference beam. All standard deviations are below 10^{-5} W/W.
Instead of time, the index of measurement is used (see Figure 4.1).

For the other investigations, the standard deviation is even below $3 \cdot 10^{-6}$ W/W for both beams. Assuming uncorrelated noise (because the data was taken sequentially), the propagated error to R_{TM} is lower than $1 \cdot 10^{-5}$ W/W. Even for the worst case correlation, where all errors of the power measurements add up, the propagated error to the computation of R_{TM} is still below $2 \cdot 10^{-5}$ W/W.

In contrast to the differential power noise, described above, the low frequency polarisation noise is breaking with the measurement requirement — the optical properties of mirrors and BS were assumed to be constant. However, for different polarisation states of the light, as present on LPF, the BS splitting ratio changes. Therefore, the polarisation-induced power fluctuations need to be removed from the data set, before the TM reflectivity can be computed.

Besides the polarisation noise, also offsets of the PDs are capable of breaking with the measurement requirement: the power measurements of reference and measurement beam on one PD are combined in a way that cancels the temperature-dependent PD responsivity. But, since the reference and measurement beam appear to have different powers, an offset of the applied power and the induced photo current has a different relative effect on these two powers. A change in temperature, translating to a change in PD responsivity could therefore lead to errors that do not cancel by the estimation of R_{TM} (compare with Equation 3.6 and 3.7). Furthermore, the offsets themself could also be dependent on the temperature .

As a consequence, a reference measurement is used for estimation of the overall error of the estimated TM reflectivity, as described in the following Section 4.3. The reference measurement shows that the uncertainty of R_{TM} is in the order of 10^{-3} W/W. Therefore, differential power noise is not limiting the measurement accuracy. Systematic errors of the different single beam power measurement samples, like PD offsets, are assumed to be the limiting noise source.

Box 4.2.1 | Summary: Noise affecting the single beam power measurements

The stochastic noise sources affecting one single power measurement are:

- relative intensity noise,
- read-out-noise,
- TM jitter,
- and ghost beam interference.

The worst case propagation of stochastic noise to $\mathrm{R_{TM}}$ is still below $2 \cdot 10^{-5}$W/W

→ **Negligible effect on the TM reflectivity estimation.**

The systematic errors in the single beam power measurements are:

- the polarisation state,
- and offsets in applied power and induced photo current.

Open questions and next steps:

- How to remove and estimate the impact of systematic errors in the single beam powers to the computation of R_{TM}?

4.3. TM reflectivity over mission duration

Figure 4.6 and 4.7 show the full data set of the single beam power investigations. The upper graphs depict the average reference and measurement beam power on all 8 QPDs with the index of investigation, as scheduled in Figure 4.1. The power measurements were scaled to the overall average power on the OB. In other words, the average of all power measurements on all diodes of both beams and all samples was determined and used for normalisation.

As already mentioned in the previous Section 4.2, most of the channels are affected by significant power noise, due to the effect of polarisation. This unexpected noise source became a new investigation topic, as described in Chapter II. For the TM reflectivity analysis however, the power measurements had to be corrected for nominal polarised light, first.
The corrected single beam powers are shown by the lower graphs, in Figure 4.7 and 4.6. The propagated errors of the used fit (see Section 8.3) are for all samples smaller than $2.8{\cdot}10^{-4}$ W/W and thus not visible in the plot.

With the corrected single beam power measurements, the TM reflectivities were computed following Equation 3.8 and 3.10, derived in Chapter 3.
Exemplarily, all PD combinations, forming R_{TM1}, are shown in Figure 4.8. Here, each parameter estimate was normalised by the average of all samples from this parameter to eliminate a systematic error from different losses, L_i, in the different beam paths:

$$R_{\mathrm{TM1}}^{\mathrm{norm.}}(i) = \frac{R_{\mathrm{TM1}}(i)}{\frac{1}{n}\sum_{i=0}^{n} R_{\mathrm{TM1}}(i)} \tag{4.4}$$

The error bars represent the standard deviation from the averaged minute-long power time series (compare to Figure 4.5), propagated as Gaussian error to $R_{\mathrm{TM1}}^{\mathrm{norm.}}(i)$ with Equation 3.8.

Obviously, the errors of the individual investigations are not limiting the accuracy of the derived TM reflectivity, R_{TM1}. Therefore, the impact of other unknown low frequency noise sources and systematic errors were estimated by a reference measurement: All PD combinations, built analogous to Equation 3.8, using only diodes of the frequency and reference interferometer, or a combination of A and B diodes of the same interferometer, should add up to1 W/W (when normalised to the average parameter estimate). This can easily be understood by looking at the experiment design and Equation 3.3.
Hence, these reference combinations eliminate the measurement observable (or do not contain it) and represent a realistic estimate of the remaining overall noise in the measurement.

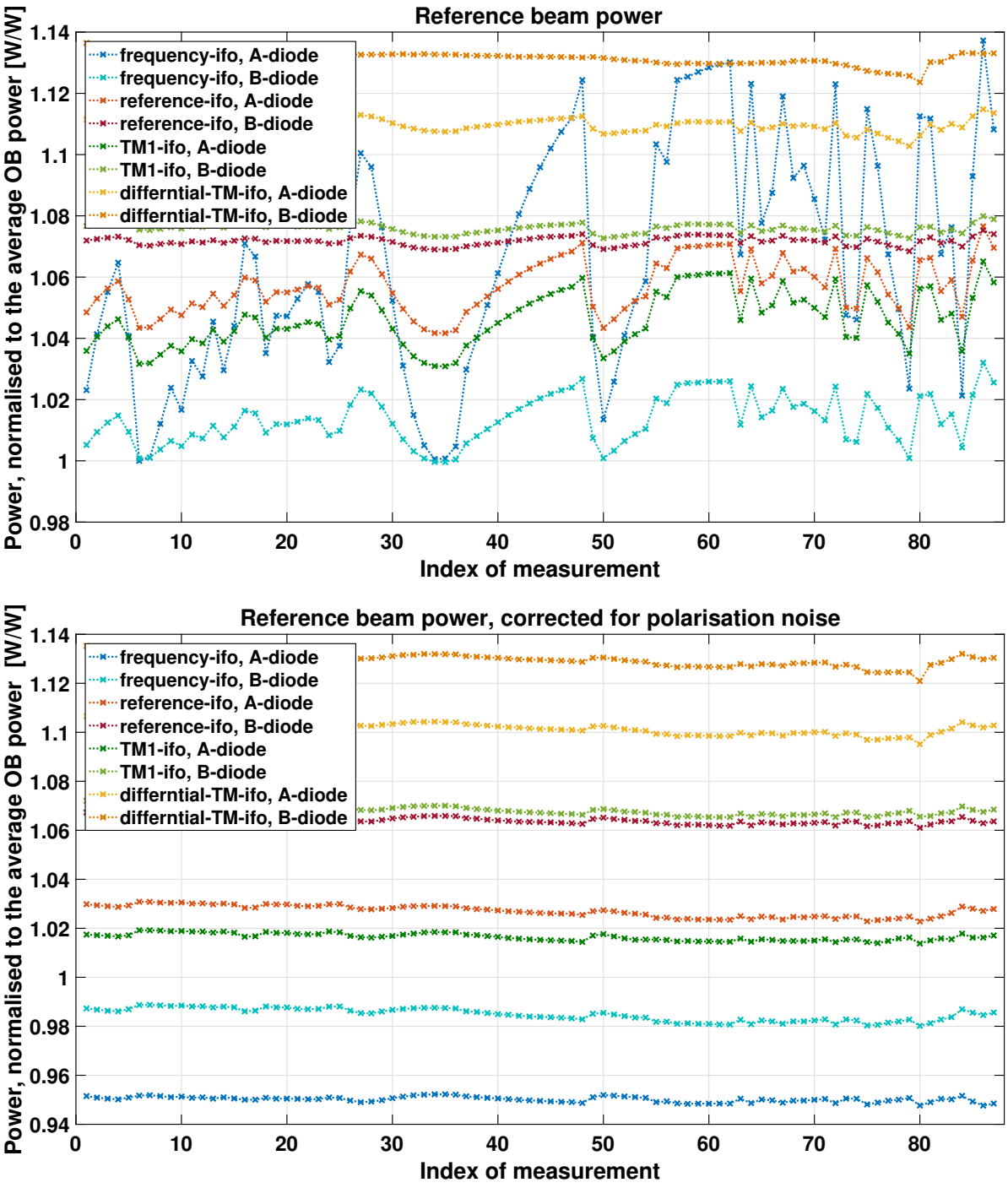

Figure 4.6.: Full data set of **reference beam power** measurements on all QPDs, normalised to the overall OB power.
The lower graph shows the corrected data with removed parallel polarised power.
Instead of time, the index of measurement is used (see Figure 4.1).

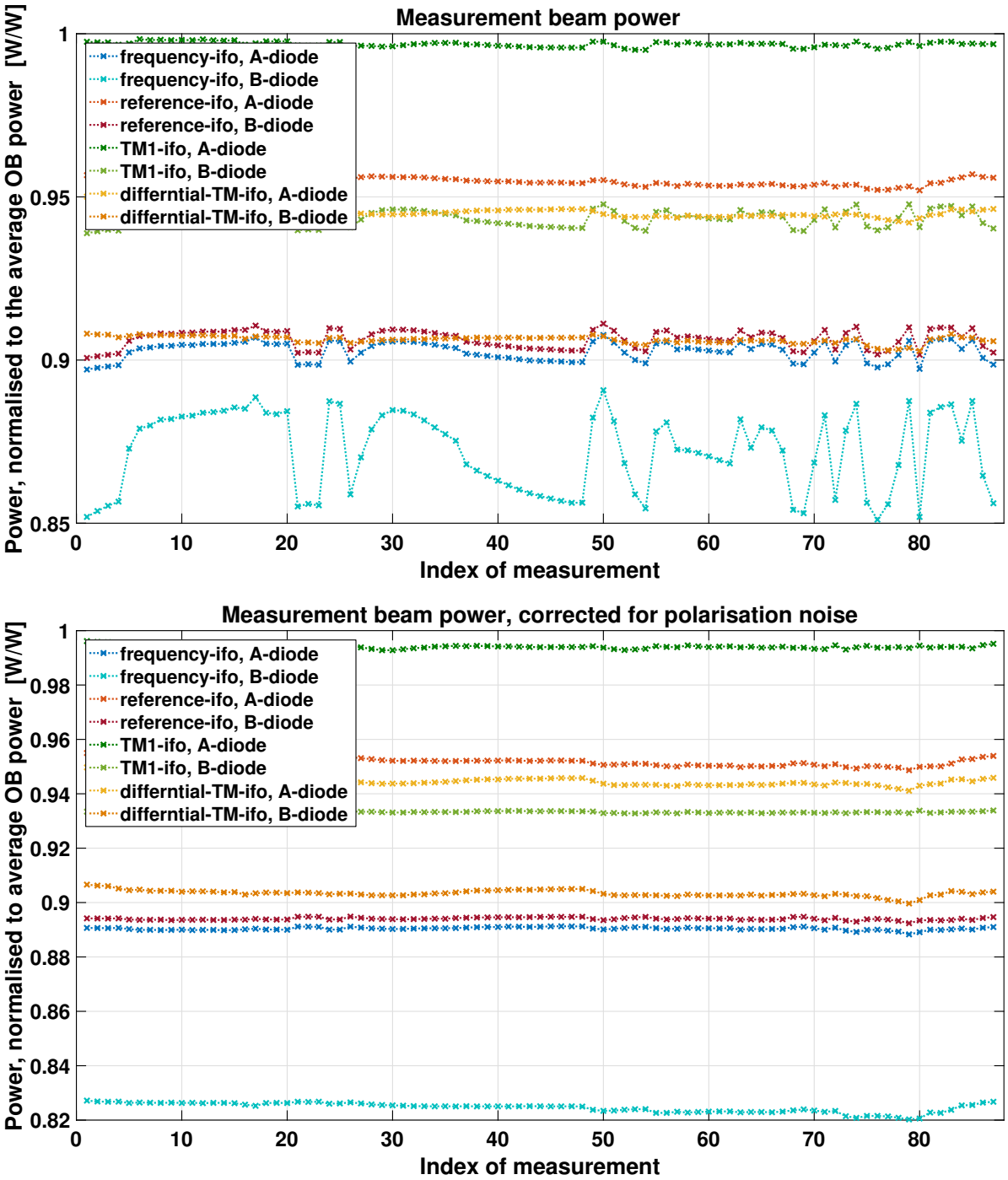

Figure 4.7.: Full data set of **measurement beam power** measurements on all QPDs, normalised to the overall OB power.
The lower graph shows the corrected data with removed parallel polarised power.
Instead of time, the index of measurement is used (see Figure 4.1).

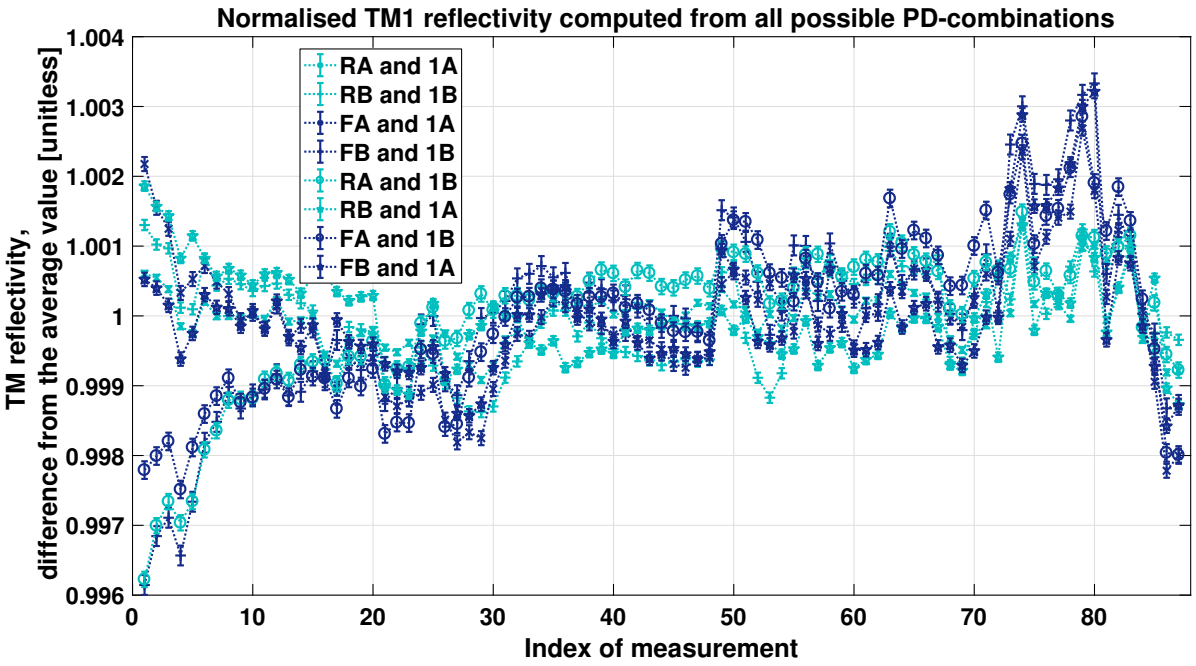

Figure 4.8.: All parameter estimates of the normalised TM1 reflectivity $R_{\mathrm{TM1}}^{\mathrm{norm.}}(i)$ at the beam spot for all single beam power investigations. Each series of parameter estimates is normalised to the average of all investigations. The overall error obviously exceeds the propagated standard deviations of the individual power measurements, represented by the error bars.
Instead of time, the index of measurement is used (see Figure 4.1).

In Figure 4.9 the maximum deviation from 1 W/W of all possible reference combinations is shown by the grey region. Furthermore, the average of all power combinations, leaving R_{TM1} or R_{TM2} (normalised by the corresponding average value), together with their standard deviation, is shown in red and blue.

The estimated error is, with $\pm 4.5 \cdot 10^{-3}$ W/W, greatest for the first investigation and decreases during the next seven samples to about $\pm 1 \cdot 10^{-3}$ W/W. During the investigations with index 73 to 80, the accuracy decreases again with an error up to $\pm 2.5 \cdot 10^{-3}$ W/W.
Nevertheless, the TM reflectivity of both TMs did not change within errors, during the monitoring duration of 392 days.

This leads to the conclusion that the TM reflectivity decreased less than $2 \cdot 10^{-3}$ W/W in a year. A linear extrapolation to a LISA-like mission lifetime of 6 years corresponds to a maximum decrease of 1.2%. From this minor change no significant further losses in light or extra temperature input to the TMs can be expected and, most importantly, a stable transfer of radiation pressure.
Note that a linear extrapolation of the results is only a rough estimation. The longer LISA mission will at least experience a period with high solar activity, of which the effect could not be investigated with LPF (flown during a low solar activity period).

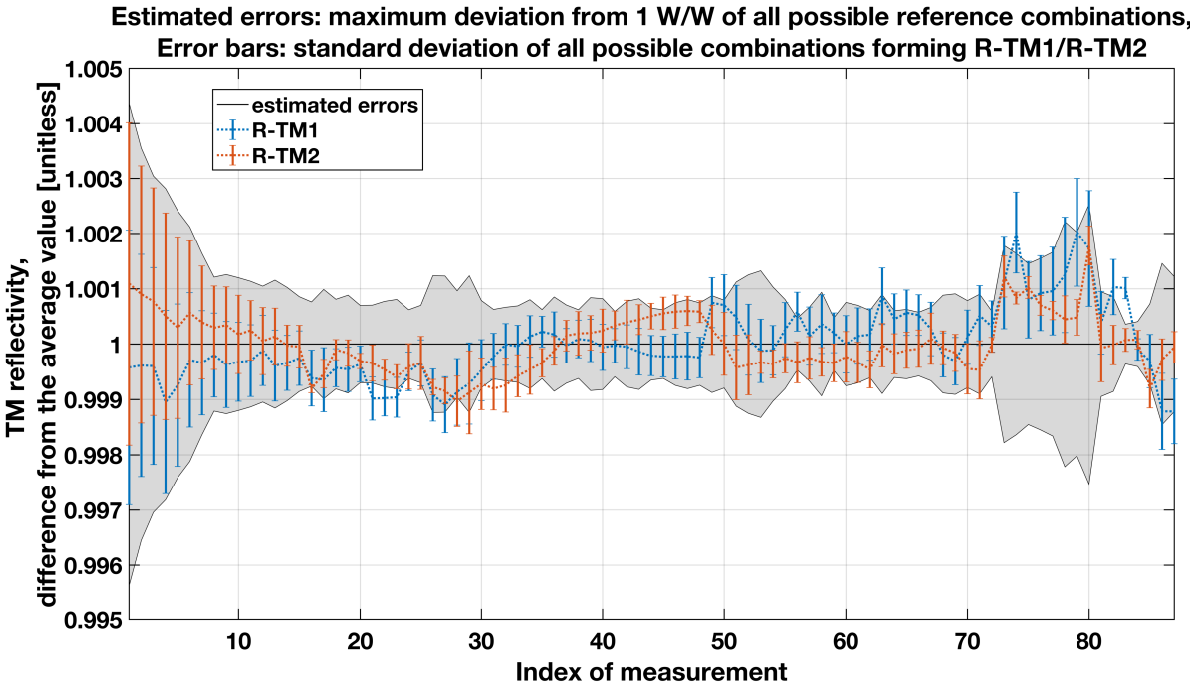

Figure 4.9.: Average of all normalised TM reflectivity estimates for TM1 and TM2 together with the estimated error, visualised by the grey region. The error is estimated by the maximum deviation of all possible reference measurements.
Instead of time the index of measurement is used (see Figure 4.1).

Box 4.3.1 | Summary: TM reflectivity over mission duration

The long-term monitoring on **LPF** shows:

- There is no change of the TM reflectivity within errors of $2 \cdot 10^{-3}$ W/W in more than one year.

A simplified linear extrapolation to a **LISA**-like lifetime shows:

- The degradation of the TM reflectivity is expected to be smaller than 1.2% for a 6-year mission lifetime.

→ Therefore no significant losses and a stable transfer of radiation pressure are expected.

5. Photodiode responsivity monitoring during flight

The responsivities of LPFs PDs were monitored during flight with an experiment that uses the applied radiation pressure to the TMs as a power reference. The design of the exeriment is detailed in described in Sections 3.1 and 3.3.
The following Chapter describes the data set of the executed radiation pressure investigations on LPF and their characterisation in Sections 5.1 and 5.2.
The resulting estimation of the PD responsivity, its stability during flight, and a comparison to pre-flight measurements, are presented in Section 5.3. Furthermore, the corresponding G-coefficients, calibrating the LPF Σ parameters to actual beam power, are listed inSection 5.3.4.

5.1. Radiation pressure modulations during the flight of LPF

The radiation pressure was modulated during flight with a square wave power modulation of the measurement beam power.
Therefore, the CL set-point of the measurement beam power was altered periodically by 0.667 µA photo current at the power monitor diode, corresponding to about 0.1 % of the total measurement beam power, with a modulation frequency of 1.6 mHz and a duration of 10, 000 seconds.
The monitoring procedure was executed as planned (described in Section 3.3), three times during the mission: once at the beginning and end of nominal mission (DOY 152 2016, DOY 021 2017) and a further time during the mission extension (DOY 176 2017). In total a timespan of 389 days could be covered.

The corresponding data is described here using a typical time series segment from DOY021 in 2017, as depicted in Figure 5.1. The red data points (corresponding to the right vertical axis) show the applied power modulation, measured with the diodes of the differential TM displacement interferometer, Σ_{12}. The green data points, corresponding to the left vertical axis, belong to the induced differential displacement of the two TMs measured by that interferometer.

The power modulation changes the radiation pressure and unbalances the electrostatic compensation of the static force to TM2. As a consequence, the TMs move back and forth, as can be seen by the periodic change in their differential displacement in Figure 5.1 (compare to Figure 3.3 in Section 3.3). Of course, the differential TM displacement is partly corrected by suspension control. Therefore, all applied control forces as well as stiffness terms, depending on the TM displacement, need to be accounted for when computing the differential TM acceleration, Δ_g (compare to References [15] and [16]). For the presented segment the differential

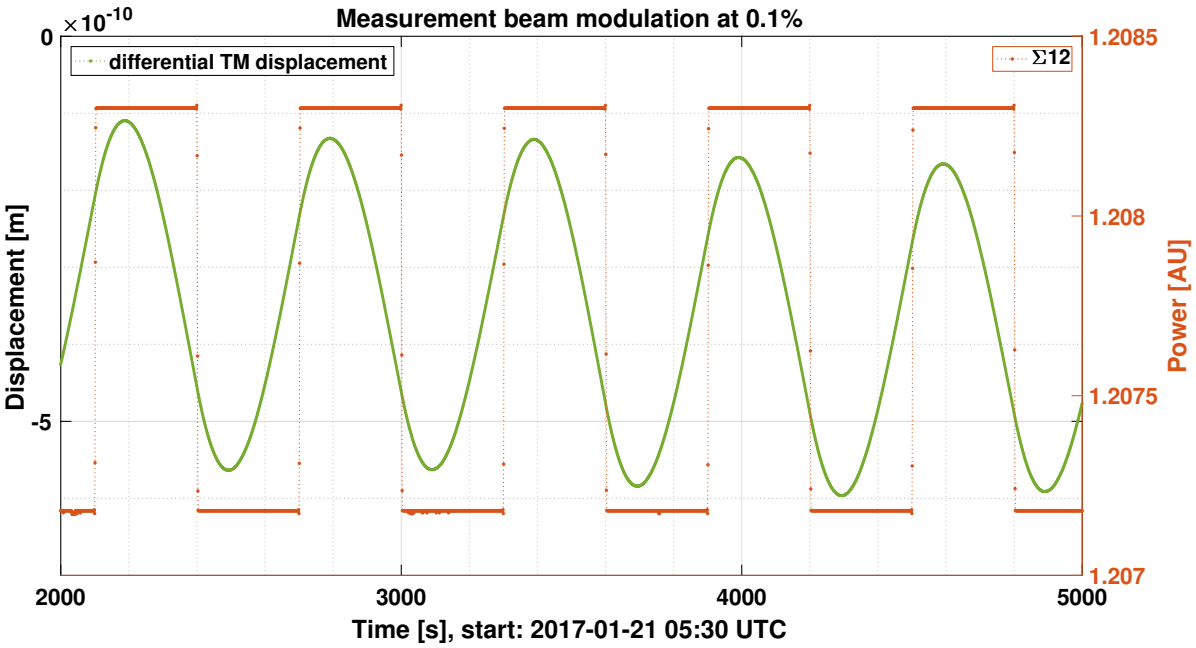

Figure 5.1.: Exemplary segment of the measurement beam power modulation on DOY 21 2017, with an intended modulation depth of 0.1 %. The TM displacement, caused by the power modulation, is shown in green.

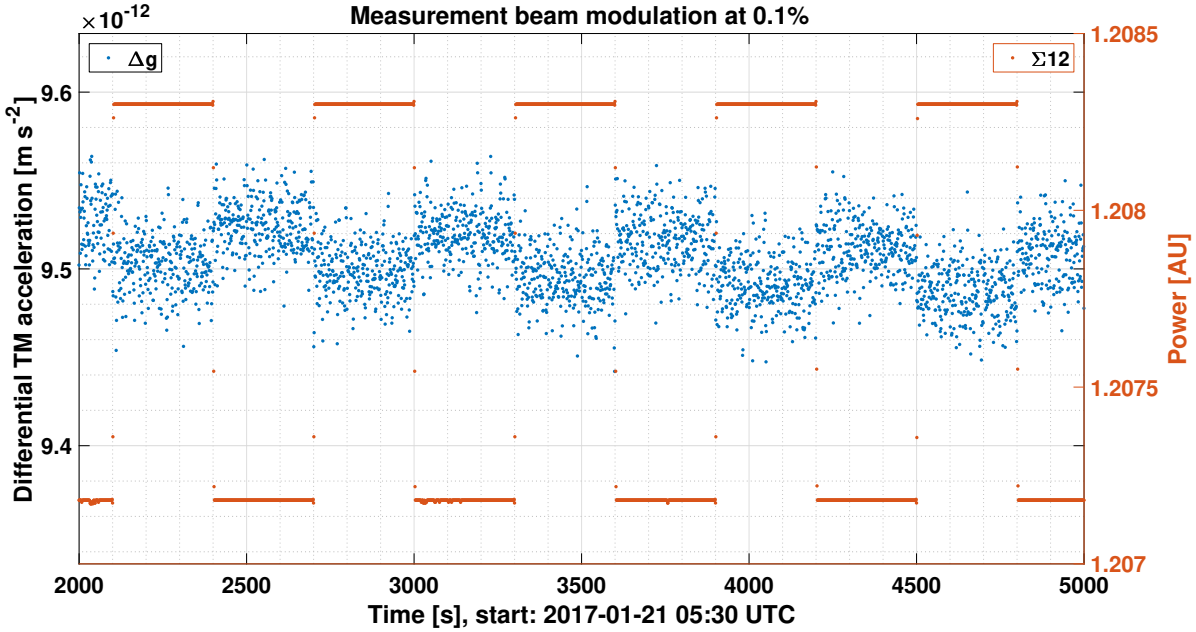

Figure 5.2.: Radiation pressure induced modulation of differential TM acceleration together with the combined beam power, Σ_{12}, in the differential TM interferometer, for the segment as shown above in Figure 5.1.

TM acceleration, Δ_g, is shown in Figure 5.2. The steps in acceleration are distinguishable from the noise even by eye and are in correlation with the power steps.

To derive the applied radiation pressure, the modulated signal powers can be estimated with a discrete Fourier transformation. The results are described in Section 5.3. However, before the results can be used to estimate the PD responsivity, the applied power modulation needs to be characterised, as described in the following.

5.2. Characterisation of the power modulation

The measurement beam power modulation induces a TM displacement that is measurable by the differential TM interferometer. To ensure that only the radiation pressure induced TM displacement is measured without any parasitic coupling of the power modulation to the optical path length difference, three characterisation measurements were executed, as described in the following.

A reference power modulation without an actual signal was applied by modulating the reference beam. Here, the power in the interferometer output was modulated, without a modulation of the power that is hitting the TMs. Any spurious path-length change, leading to an offset in the derived radiation pressure, could therefore be detected in absence of the induced TM displacements.
The linearity between the applied power modulation depth and the induced radiation pressure was checked with another characterisation. The applied modulation depth was increased by about a factor 10 and a factor 20, to intentionally 1 % and 2 % modulation depth of the total measurement beam power.
The third characterisation parameter was the PD temperature. A small part of the incident beam power is usually absorbed by the PD and heats up its active surface until equilibrium state with radiation to the surrounding. The responsivity of a PD in general depends on its temperature [47]. For a power modulation, the average heat input within a modulation cycle does not change against the nominal beam power, since the power is periodically altered. However, at the modulation frequency there is a small temperature gradient induced by the change in power at each step.
To investigate a possible effect of this temperature gradient on the measured path length difference, therefore, a counter modulation was used. It removes the temperature gradient while preserving the desired signal. For the counter modulation the measurement beam is increased when the power of the reference beam is decreased and vice versa. A perfect match in beam power, however, could not be realised at all PDs due to the independent power CLs and differing losses of the individual beam paths. Therefore, the temperature gradient was in fact only suppressed and not fully cancelled.
For completeness, the reference beam and counter modulation were also analysed with increased modulation depth of 1 % and 2 %. Altogether, a set of $3 \cdot 3 = 9$ different modulations were performed on DOY021, including the nominal monitoring measurement procedure.

Figure 5.3 shows the individual beam powers measured with the power monitor diodes, and the combined beam power in the differential TM displacement interferometer, Σ_{12}, during the characterisation measurements. Furthermore, the induced differential TM displacement is plotted in Figure 5.4 for the whole characterisation period.

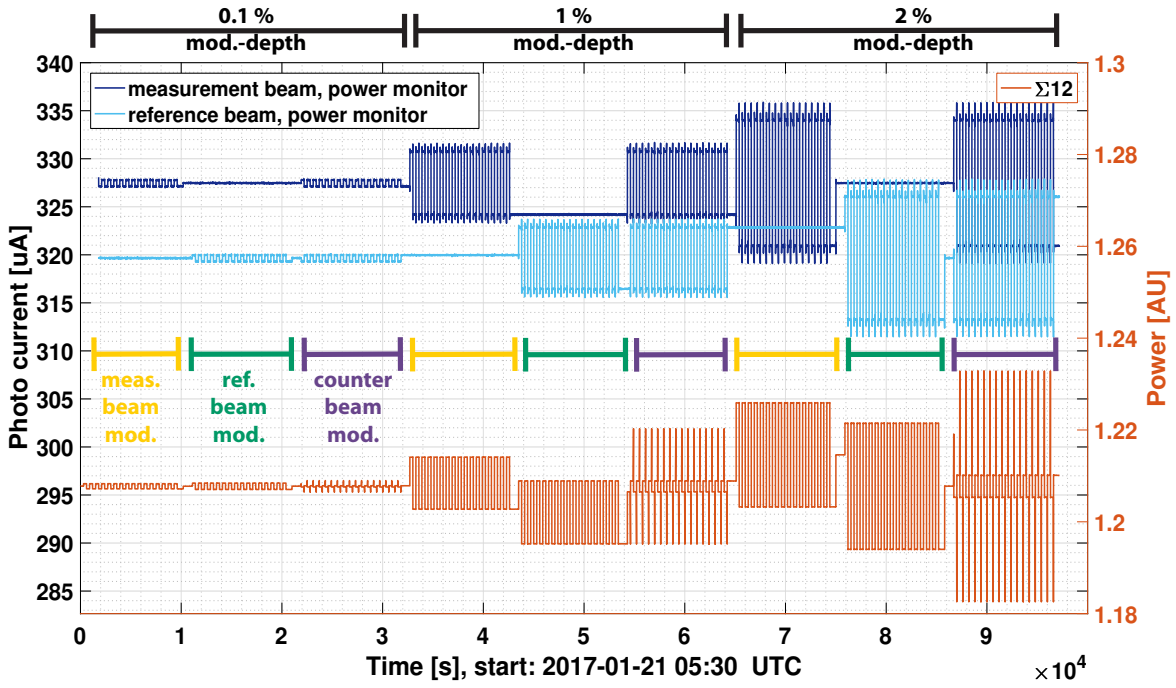

Figure 5.3.: Individual beam powers $P_{\text{pwr-mon, RB}}$ and $P_{\text{pwr-mon, MB}}$, measured at the power monitor diodes, and combined beam power Σ_{12} in the differential TM interferometer, during the 9 power modulation characterisation-sequences

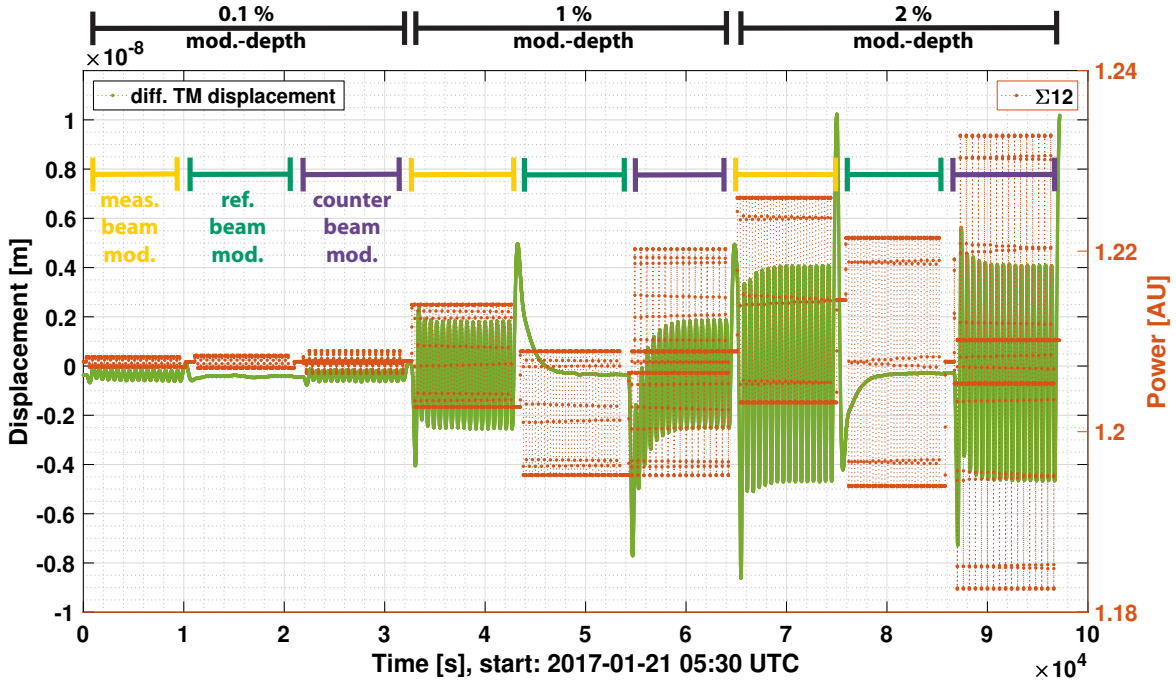

Figure 5.4.: Differential TM displacement measured by the x12 interferometer, together with the combined beam power, Σ_{12}, during the 9 power modulation characterisation sequences.

The schedule starts with the nominal measurement beam modulation at 0.1 % modulation depth (from 0 s to 1×10^4 s). Then the reference beam was modulated individually (from 1.1×10^4 s to 2.1×10^4 s) and afterwards both beams counter-wise (from 2.2×10^4 s to 3.2×10^4 s), both with the nominal 0.1 % modulation depth. The same procedure was then repeated with 1 % modulation depth (from 3.3×10^4 s to 6.4×10^4 s) and again with 2 % (from 6.6×10^4 s to 9.7×10^4 s).

From the Σ_{12} parameter (red line in Figure 5.3) it can easily be seen that the beam powers at the output of the interferometer do not match-up. The measurement beam has less power in Σ_{12} than the reference one, leading to a smaller modulation amplitude and remaining power modulation during the counter modulation sequence.
In contrast, the measurement beam power, measured with the power monitor diode at the front of the OB, is greater than the reference beam one. This inconsistency can be explained by different losses in the two beam paths and unequal responsivities of the power monitor diodes.

The actually applied power modulation depths in Σ_{12} and the power monitor diodes are listed in Table 5.1. They correspond to the peak-to-peak amplitude in power modulation at the modulation frequency, estimated by a Discrete Fourier Transformation (DFT) with a Blackman-Harris window.

	MB-mod.			**RB-mod.**			**counter-mod.**		
	0.1 %	1 %	2 %	0.1 %	1 %	2 %	0.1 %	1 %	2 %
Σ_{12} [%]	0.059	0.59	1.192	0.07	0.722	1.445	0.016	0.146	0.294
P_{RB} [%]	0	0	0.001	0.13	1.269	2.536	0.131	1.269	2.537
P_{MB} [%]	0.127	1.276	2.544	0.001	0	0.001	0.128	1.275	2.545

Table 5.1.: Applied power modulation depth (DFT estimates, peak-to-peak amplitude at ω_{mod}) in combined beam power, Σ_{12}, and individual beam power, $P_{\mathrm{pwr\text{-}mon,\ RB}}$ and $P_{\mathrm{pwr\text{-}mon,\ MB}}$, for all power modulations. The errors are for all parameters below 0.66 % of the estimated value.

Another conspicuous behaviour observable in Figure 5.3, is the presence of prominent spikes in Σ_{12} during the counter beam modulation. They occur at the beginning and end of each power step due to sequential commanding. First, the set-point for the measurement beam is commanded up or down, and directly afterwards the reference beam. During the short period between execution of the two commands, both beams are at the higher or lower power level.

Next to the power mismatch and spikes in Σ_{12}, there were two minor irregularities due to commanding: During the reference beam modulation at 1 %, the power of the measurement beam was kept at the lower level due to a missing command. The opposite is true for the reference beam power during the 2 % measurement beam modulation, where the power stayed at the higher level. These led to different average power levels in Σ_{12}. However, since the DFT method, used to determine the signal power, is only sensitive to a narrow band around the modulation frequency, the commanding mistakes are not relevant for this analysis.

The differential TM displacement in Figure 5.4 is clearly affected by the radiation pressure modulation via the measurement beam. During the reference beam modulations, only the suspension control is visible, pushing the TM back to their set-point of zero displacement. The

overshoots in the beginning of a measurement beam modulation sequence are a consequence of the initial TM displacement and acceleration of zero. Within the modulation sequence, the TMs have a differential displacement and velocity in the opposite direction (here, positive displacement), at the time when the power is stepped to the upper level and the radiation pressure between the TMs is increased (pushing the TMs apart).
The overshoot at the end of the sequence arises from the power set back to nominal power instead of to the higher power level. Therefore, the braking force is smaller and the maximum displacement gets higher before the suspension CL drives the TMs back to the nominal position.

The behaviour of the differential TM acceleration — as the main measurement parameter — is described in the following with more detail for the individual modulations.

5.2.1. The reference beam modulation

Figure 5.5 shows the differential TM acceleration for modulating the reference beam with 0.1 %. In contrast to the measurement beam modulation, no TM acceleration is visible by eye, as expected. The signal amplitude (peak-to-peak) during the reference beam modulation (DFT estimates, with a Blackman-Harris window) is, with $4.86 \pm 2.79 \cdot 10^{-17} \frac{\mathrm{m}}{\mathrm{s}^2}$, negligible in comparison to the radiation pressure induced signal of $1458.02 \pm 9.99 \cdot 10^{-17} \frac{\mathrm{m}}{\mathrm{s}^2}$ for the 0.1 % measurement beam modulation.

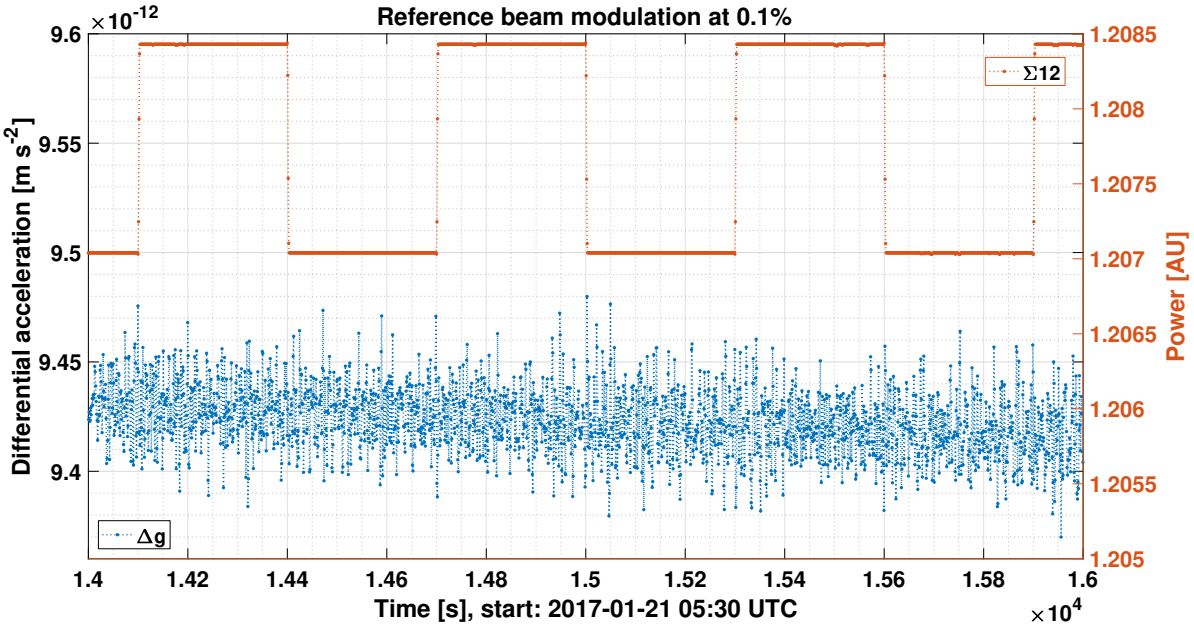

Figure 5.5.: Δ_g for the 0.1 % reference beam power modulation, together with the combined beam power, Σ_{12}. No TM acceleration is detectable.

Therefore, the nominal modulation depth used for the monitoring procedure is within the measurement accuracy unaffected by spurious path length noise.

Also for the 1 % and 2 % modulation depth the signal amplitudes during reference beam modulation are smaller than the error of the corresponding radiation pressure induced signal,

as can be seen in Figure 5.9.
At maximum, a signal-amplitude of $33.67 \pm 2.15 \cdot 10^{-17} \frac{\mathrm{m}}{\mathrm{s}^2}$ for the 2 % reference beam modulation was found.

However, for these higher modulation depths another effect correlated with the modulation can be observed: There are Δ_g spikes in coincidence with the power steps, as can be seen in Figure 5.6.

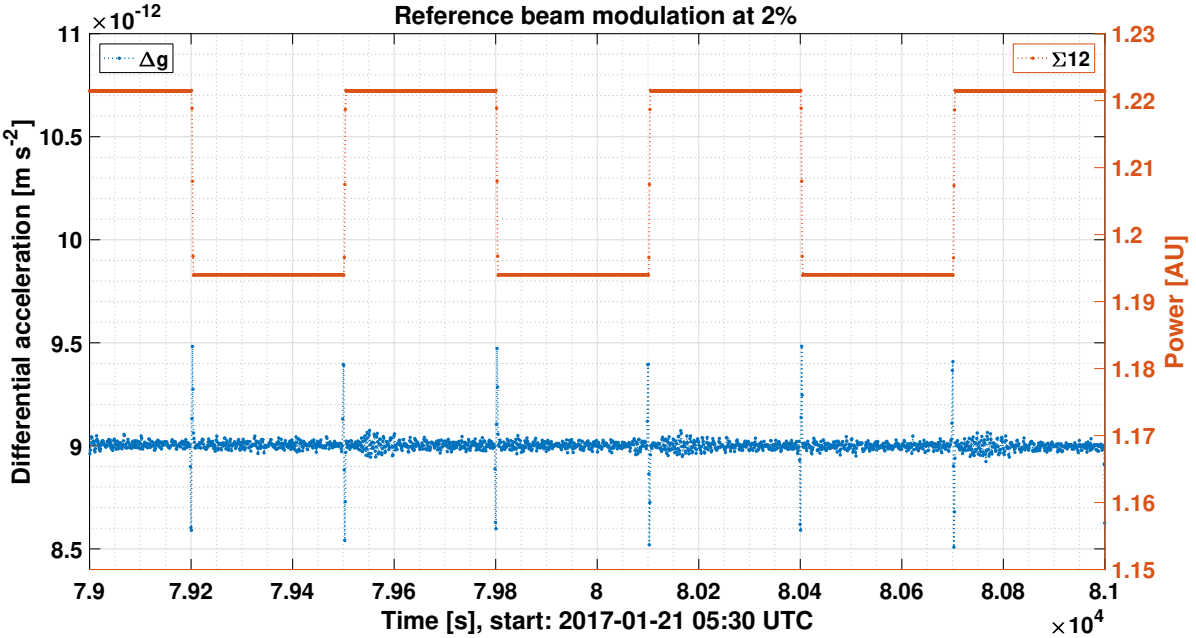

Figure 5.6.: Δ_g for 2 % reference beam power modulation, together with the combined beam power, Σ_{12}. Δ_g spikes are visible in coincidence with the power steps.

5.2.2. The counter beam modulation

In Figure 5.7, Δ_g is shown for the 0.1 % counter beam modulation, again, together with the combined beam power, Σ_{12}.
The power gradient in Σ_{12} is clearly reduced, although the beam powers do not perfectly match-up. The signal amplitude of the counter beam modulation of $1467.25 \pm 8.06 \cdot 10^{-17} \frac{\mathrm{m}}{\mathrm{s}^2}$ agrees within errors with the measurement beam modulation signal amplitude of $1458.02 \pm 9.99 \cdot 10^{-17} \frac{\mathrm{m}}{\mathrm{s}^2}$ (both for 0.1 % modulation depth)). Hence, no detectable coupling of the PD temperature gradient to the measured acceleration at nominal modulation depths could be found.

Figure 5.9 further shows the subtraction of signal amplitudes during the counter and the measurement beam modulation for the 1 % and 2 % modulation. The residuals are all zero within errors.

However, as already found for the reference beam modulation, also the counter modulation shows Δ_g spikes in coincidence with the power steps for the 1 % and 2 % modulation depths (see Figure 5.8).

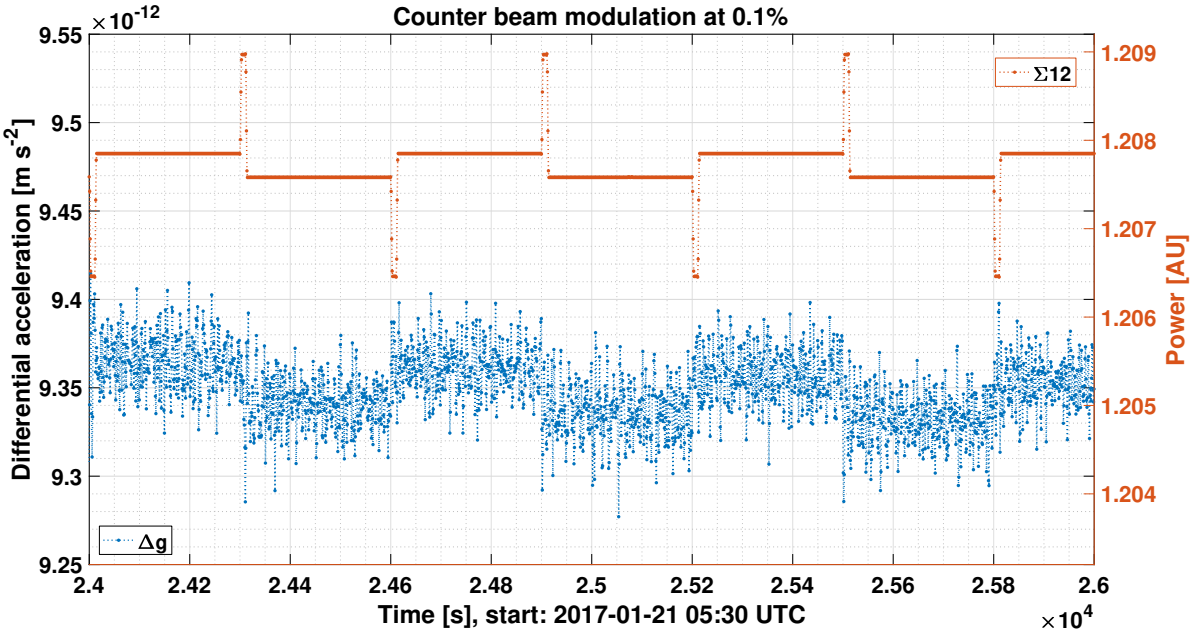

Figure 5.7.: Δ_g while counter modulating the two beams with nominal modulation depth, together with the combined beam power, Σ_{12}. The beam powers do not match-up, but the power gradient in Σ_{12} is clearly reduced.

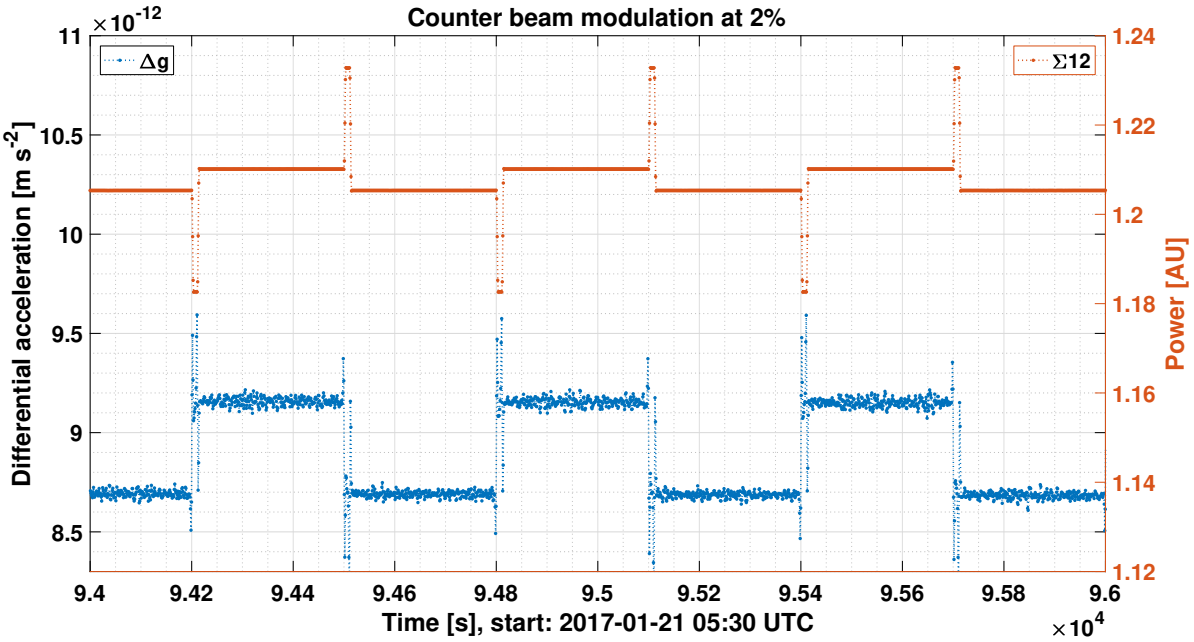

Figure 5.8.: Δ_g while counter modulating the two beams with 2 % modulation depth, together with the combined beam power, Σ_{12}.

5.2.3. Linearity of the induced radiation pressure with the modulated power

For comparison to the measured power signals listed in Table 5.1, also the signal amplitudes of implied radiation pressure were estimated with a DFT at the modulation frequency (again, with a Blackman-Harris window).

Figure 5.9 shows the peak-to-peak amplitudes in Δ_g versus Σ_{12}. The Σ_{12} parameter of the counter modulation is a superposition of reference and measurement beam modulation and therefore does not represent the modulated power at the TMs.
Since the measurement beam is identically modulated during the measurement beam modulation, the DFT estimates of the Σ_{12} parameter are used as horizontal axis for the counter modulation in Figure 5.9 to allow for an adequate comparison.

As already discussed above, the induced Δ_g from the measurement and the counter beam modulation match-up. Their difference is zero within errors, as shown in the lower graph of Figure 5.9. Also the reference beam modulation can be seen in the lower graph of Figure 5.9. For all modulation depths the DFT estimates of the reference beam modulation are smaller than $5 \times 10^{-16}\,\mathrm{m/s^2}$ and furthermore smaller than the the errors within the difference from measurement and counter beam modulation.

For the analysis of the linearity between the measured power modulation and the induced TM acceleration, the signals at higher frequencies are taken into account. Figure 5.10 shows the signal amplitude in Δ_g during the measurement beam modulation for the first, the second, the third and the fifth harmonic of the modulation frequency.
As expected, a negligible signal is detected for the even, second harmonic (the three red data points in Figure 5.10 are approximately zero). However, the third and fifth harmonic provide more data points for a check of the linearity. A linear fit confirms that the acceleration increases linearly with the modulated power, also at higher frequencies.

The characterisation measurements ensured no parasitic effects on the measured differential TM acceleration. Therefore, the estimated radiation pressure can be used to determine a reference power for the calibration of the PDs, as described in Section 5.3.

However, one unexpected effect could be observed for the higher modulation depths: There are spikes in Δ_g — correlated with the power steps. This effect was further analysed, as described in the following.

5.2.4. Observation of longitudinal phase steps

A spike in acceleration can have several reasons because the TM displacement as well as applied forces are used for its estimation. One possibility is a step in the measured displacement, which translates to a spike in acceleration. Therefore, the interferometric longitudinal signal was checked again for coupling of the power steps to the measured phase — corresponding to differential TM displacement.

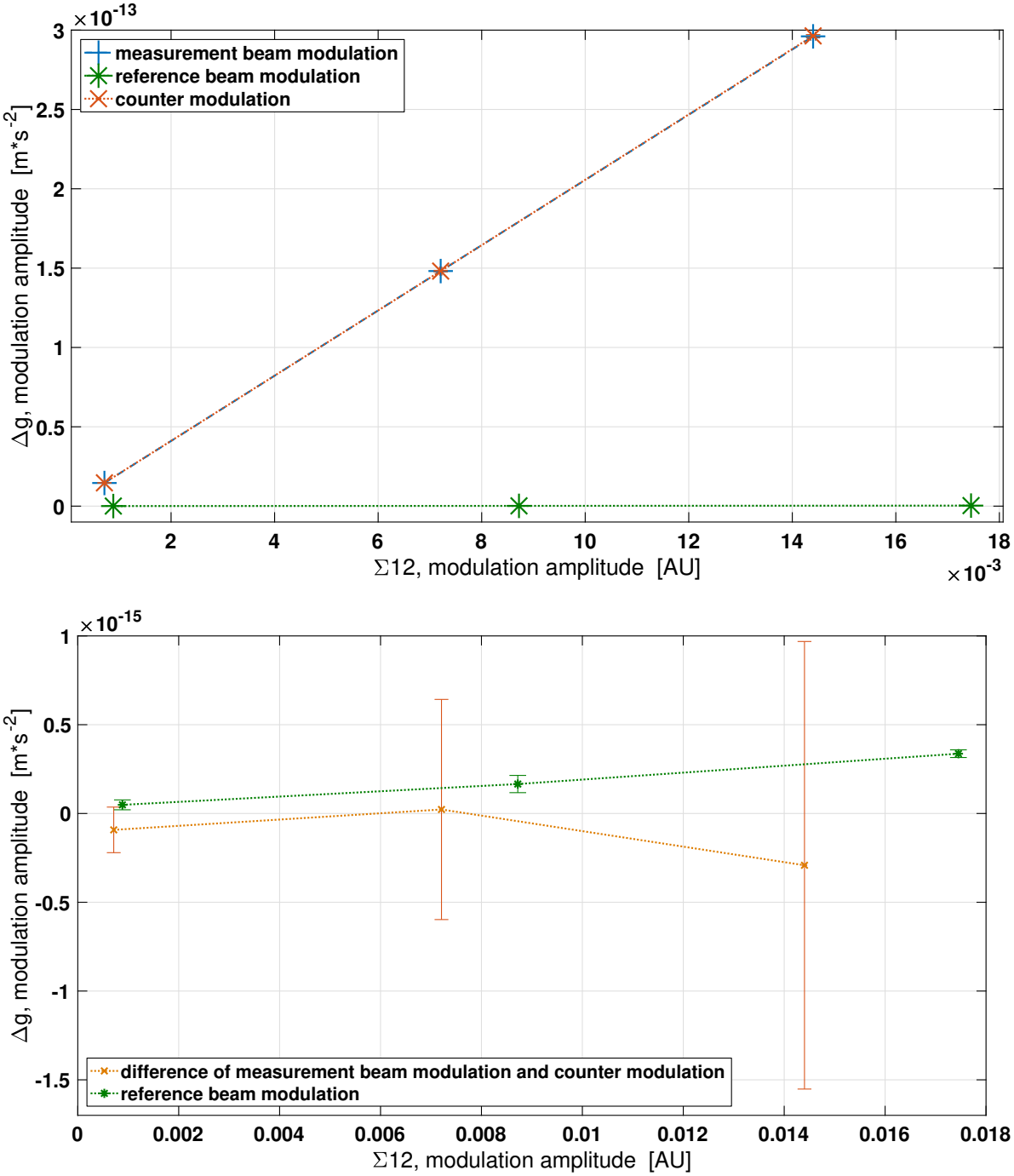

Figure 5.9.: **Upper figure:** Signal amplitude (peak-to-peak, DFT estimates) of differential TM acceleration for all three power modulation types and modulation depths, versus signal amplitude in combined beam power Σ_{12}(also peak-to-peak, DFT estimates).
Lower figure: Difference of signal amplitude in Δ_g of measurement beam and counter modulation together with the signal amplitude during reference beam modulation.

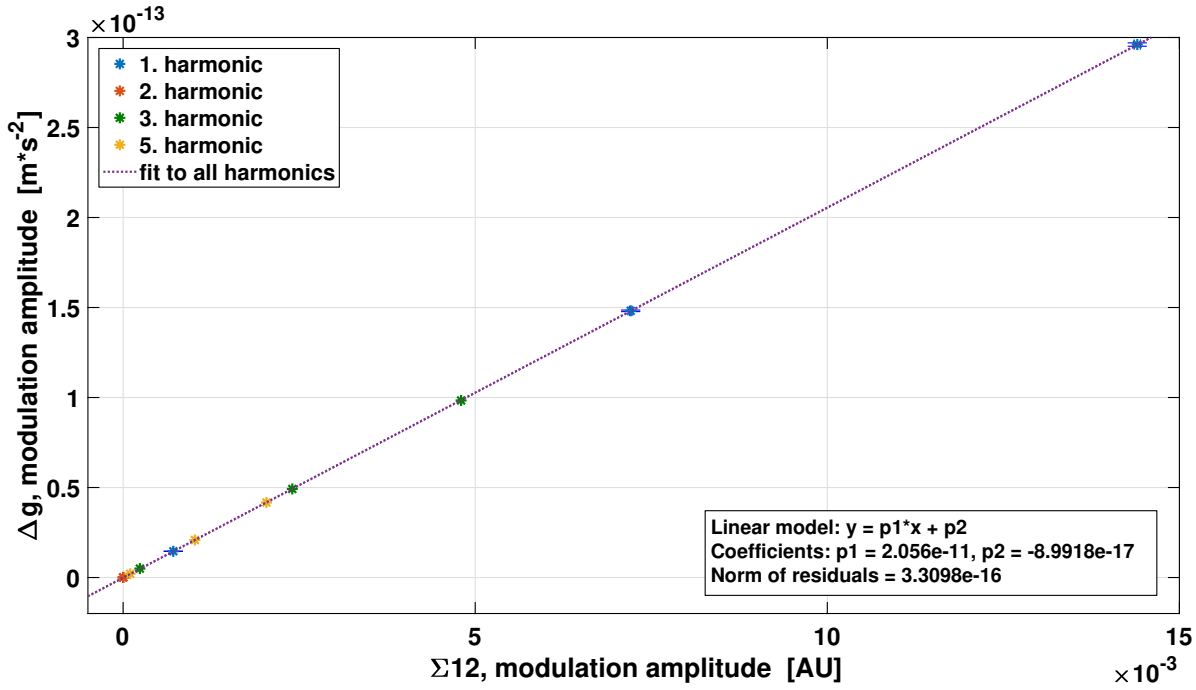

Figure 5.10.: Signal amplitude (peak-to-peak, DFT estimates) in Δ_g versus Σ_{12} for the higher harmonics of the measurement beam modulation.

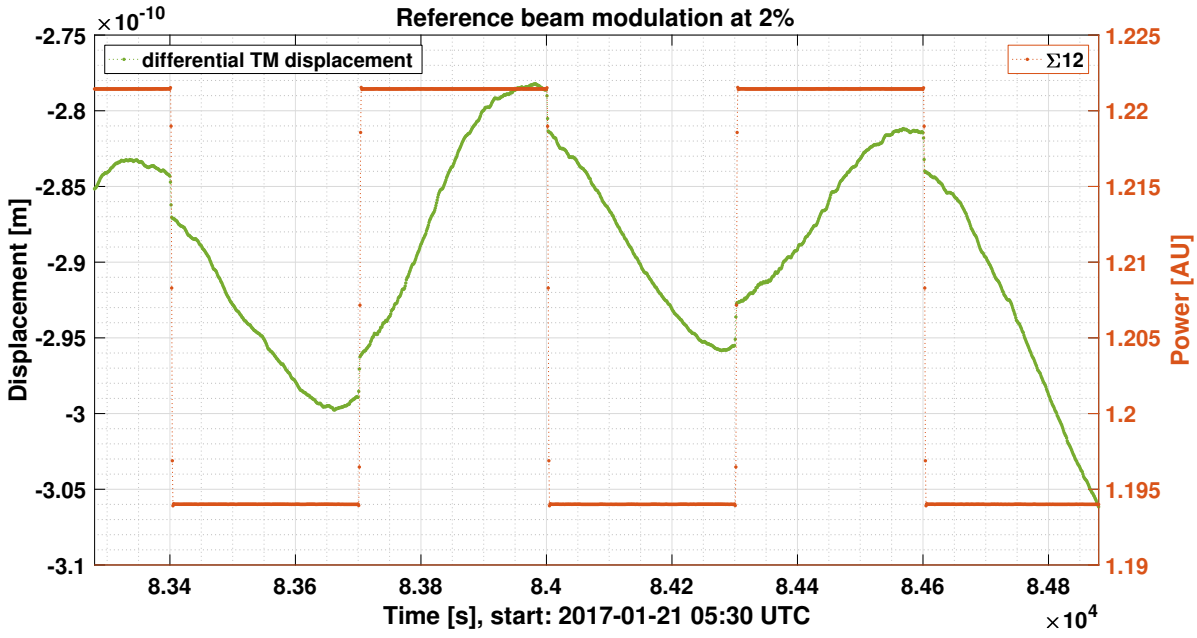

Figure 5.11.: Segment of the differential TM displacement during the 2 % reference beam modulation, together with the combined beam power Σ_{12}.

Figure 5.11 shows the TM displacement during the strongest, the 2 % reference beam power modulation. On the one hand, a slow drift following the power modulation can be observed. It relates to the small signal power detected for the reference beam modulation, as shown in Figure 5.9. Possibly it is induced by the temperature gradient at the photodiodes. This, however, is not provable, due to the bigger error bars of the estimated signal during the counter modulation. But, besides the slow coupling there is also a step in the displacement, correlated with the power modulation: Simultaneously with Σ_{12}, the differential TM displacement appears to step, too. Even the (algebraic) sign of the two steps correspond.

Here it needs to be mentioned that there is a small delay below 1 s between Σ and the phase signals of longitudinal as well as DWS phase. However, this spurious delay results from the data management in the DMU onboard LPF. Since the Σ parameters are available only with a sampling frequency of ≈ 1 Hz a more accurate estimation of this delay is not possible.

The step size is small, but converted to acceleration, even such a small displacement appears as a prominent spike due to its steepness.
In theory there should be no coupling of the measured power to the phase read-out of the interferometric signal. Therefore, the effect was further investigated by the DWS parameters and another LPF experiment, as described in Chapter 6.

Box 5.2.1 | Summary: Characterisation of power modulations

Reference beam modulation without radiation pressure modulation:

- The parasitic acceleration from the nominal power modulation is below $5 \times 10^{-17}\,\mathrm{m/s^2}$ (peak-to-peak amplitude).
- Furthermore, the parasitic acceleration was found to be within the errors of the nominal signal induced by the radiation pressure modulation.

Counter beam modulation with lower temperature gradient:

- No measurable effect on the measured modulation amplitude.

Increase of the modulation depth for the nominal measurement beam modulation:

- The modulated power and the induced acceleration are linearly correlated.

→ **The estimated radiation pressure is therefore usable as a power reference.**

Open questions:

- There are unexpected steps in displacement in correlation to the power steps.
- What is the origin of this power-to-phase coupling?

→ The analysis is described in Chapter 6.

5.3. PD responsivity over mission duration

The characterisation of the power modulation, described in Section 5.2, ensured that the radiation pressure modulation linearly relates to the modulated measurement beam power. Furthermore, for the monitoring modulation depth of 0.1 %, no spurious effects above the errors could be observed.
As a consequence, the measured radiation pressure modulation can be used to determine a reference power for the calibration of the PDs by Equation 3.22, as described in Chapter 3.

The signal amplitudes of the modulations are estimated as before, by a DFT with a Blackman-Harris window (as described with further detail in Reference [48]).

The PD responsivity is then derived by Equation 3.22, as described in Chapter 3. For clarity, the equation is shown here again, with propagation factors of the measurement beam power from the front of the OB to the different Σ parameters, $\lambda^{\perp}_{\Sigma_i,\,\mathrm{MB}}$, and to the TM1 , $\lambda^{\perp}_{\mathrm{TM1,\,MB}}$, and between the two TMs, $\lambda^{\perp}_{\mathrm{TM1\text{-}TM2}}$:

$$\eta_i = \frac{\Sigma_i|_{\omega_\mathrm{m}}}{\Delta_g|_{\omega_\mathrm{m}}} \cdot \frac{\lambda^{\perp}_{\mathrm{TM1,\,MB}}}{\lambda^{\perp}_{\Sigma_i,\,\mathrm{MB}}} \cdot \left(\frac{1+\mathrm{R_{TM1}}}{c \cdot m_{\mathrm{TM1}}} + \lambda^{\perp}_{\mathrm{TM1\text{-}TM2}} \cdot \frac{1+\mathrm{R_{TM2}}}{c \cdot m_{\mathrm{TM2}}} \right) \cdot \frac{\mathrm{U_{ADC}}}{\mathrm{R_{TI}}} \,. \tag{5.1}$$

Figure 5.12 shows the corresponding PD responsivity in all four interferometers (the virtually combined responsivity of the two QPDs in the interferometer A and B port) during the three monitoring measurements. A trans-impedance amplifier resistance of $\mathrm{R_{TI}} = 6600\,\Omega$, an ADC range of $\mathrm{U_{ADC}} = 5\,\mathrm{V}$ and the propagation factors λ, as listed in Appendix B were used.

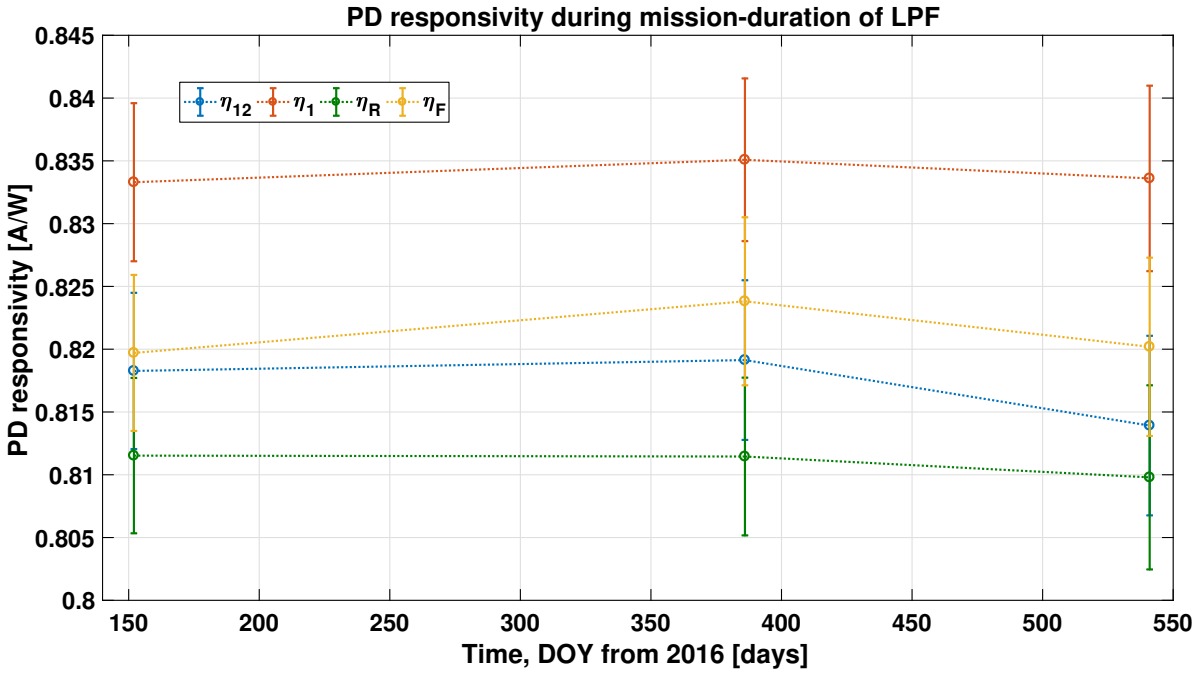

Figure 5.12.: PD responsivities of the virtually combined PDs in the four LPF interferometers, during flight of LPF.

The responsivity of the PDs in all four interferometers changed less than the errors of less than ±1 %. During the whole monitoring duration the change in responsivity of a particular interferometer diode was therefore smaller than 2 %.

The propagation factors, λ_i, are of course affected by systematic errors, since the losses at the individual optical components are only known within errors. For the BS splitting ratios (listed in Table 8.1), a Gaussian error propagation of the maximum errors to Equation 5.1 leads to a systematic error of 1 % for η_{12}, about 1.3 % for η_1 and about 3 % for η_R and η_F. However, systematic errors of the mirror reflectivity, the optical window transmissivity and the TM reflectivity also need to be considered.
Nevertheless, the systematic errors are assumed to be constant during the mission. Therefore, changes during the monitoring duration are measurable with the accuracy of the DFT estimates of power and Δ_g modulation, shown by the error bars in Figure 5.12.

Besides the noise in Δ_g and Σ, there are two other effects that add a different error to the three individual responsivity estimates.
One is the temperature dependency of the PD responsivity. The OB temperature increased within the three investigations by 1.2°C. Using experimentally determined PD temperature coefficients of identically constructed PDs (internal measurements made by Dr. Dr. Germán Fernández Barranco at the AEI), an average decrease of 0.29 % in responsivity can be found for the LPF measurements (maximum and minimum decrease of [0.25 %, 0.34 %]). Hence, the effect of temperature on the PD responsivity is within the measurement accuracy.

The second effect is introduced by off-nominal polarised light in the interferometers. The propagation coefficients λ differ for parallel polarised light. If the amount of power with off-nominal polarisation is different for the three modulation investigations, the corresponding error spuriously appears as a change in PD responsivity.
The frequency interferometer is the most sensitive one to polarisation noise. In contrast, the signal amplitudes of the measurement beam modulation agree within errors for the four Σ parameters of the different interferometers. Therefore, A worst case approximation of the impact of parallel polarisation can be done by assuming that the frequency interferometer Σ parameter changed during the three investigations by its full uncertainty of 1 %, only due to a change in parallel polarised power. As a consequence, the measurement beam power at the front of the OB would have changed approximately by $1\,\% \cdot \left(\frac{T^{\perp}_{BS}}{T^{\parallel}_{BS}}\right)^2 \approx 0.4\,\%$ power, due to parallel polarisation. Further conversion forward to TM1 gives a maximum change in the parallel polarised power of $0.4\,\% \cdot \left(\frac{R^{\parallel}_{BS}}{R^{\perp}_{BS}}\right) \approx 0.16\,\%$ and even less at TM2. The corresponding maximum error to the PD responsivity estimation (Figure 5.12) is therefore smaller than the stochastic errors of the measurement.

In summary, the change in PD responsivity during flight was found to be smaller than 2 % during the full monitoring-duration of 389 days.

5.3.1. Comparison to on-ground measurements

In preparation to the mission, the responsivities were measured for the QPDs in place on the OB, described in Reference [49]. Here, the PD responsivities are the result of a combination

of two measurements.
In the first step the transmitted part of the beam power from the MB to the several interferometer output ports was measured by one single PD. The results are propagation factors of the beam power to the different interferometers. In the second step, the response of the interferometer QPDs was measured for a known input power, measured by a calibrated power meter. The PD responsivity was then derived by a combination of the two measurements. Of course, the measurement accuracy relies on the calibration of the power meter and the alignment of the PD for the estimation of the propagation factors.

The resulting responsivities are shown together with the average in-flight responsivities in Table 5.2.

	Ground		**Flight**
	ref. beam	meas. beam	meas.beam
η_{12}	0.8292	-	0.817 ± 0.005
η_1	0.8652	-	0.834 ± 0.005
η_R	0.8574	0.8823	0.811 ± 0.005
η_F	0.8412	0.8530	0.821 ± 0.005
$\langle \eta^{\text{ground}} \rangle$	0.855 ± 0.019		-
$\langle \eta^{\text{flight}} \rangle$	-		0.821 ± 0.01
$\eta^{\text{spec.}}$	0.85 to 0.86		-

Table 5.2.: PD responsivities before and during flight, with statistical errors. All values are given in [A/W]. There are no statistical errors for the responsivities on ground available. However, the comparison of values derived with different beams deviates by up to 2.9 % percent. Furthermore, in the lower line, the average value of all ground flight measurements with the standard deviation or the propagated errors (for the flight measurements) are given, as well as the manufacturer specification.

The test setup on ground had no dummy TMs in place and therefore only measurement beam power measurements in the rigid interferometers.
The accuracy of the pre-flight measurements is most likely limited by alignment and probably in the order of some percent. The accuracy of the pre-flight measurements can roughly be estimated by the deviation of responsivity estimates from the measurement and reference beam. The estimates deviate at maximum by 2.9 % for the same diode, although the two beams are both well-aligned (also described in Reference [49]).

However, the average responsivity (with standard deviation) of all PDs measured before flight, is with $\langle \eta^{\text{ground}} \rangle = 0.855 \pm 0.019$A/W in good agreement to the manufacturer tests, reporting values of $\eta^{\text{spec.}} = 0.85$ A/W to 0.86 A/W, (internal documents on responsivity tests from *OSI optoelectronics* and [49]).

All responsivities derived with the Flight data set are smaller than the ground measurements. However, with $\langle \eta^{\text{flight}} \rangle = 0.821$ A/W$\pm$0.01 A/W, the average PD responsivity (with propagated statistical error) during flight is less than 4 % smaller than on ground. This is in contrast to the expectations from pre-flight radiation tests, described in Section 2.5. A bombardment with protons indicated that an average degradation of 17.5 % in responsivity is expected. The deviation is therefore significant, even when considering the margin of systematic errors of a few percent.

Because of this disagreement, at first the computed propagation coefficients from Section 5.3 were cross checked, to verify the result. Therefore, the propagation coefficients, λ_{TM1} and λ_{Σ_i}, from Appendix B, were compared with measurements from Reference [49].
Note: In Reference [49], the power that would be transmitted to TM1 was measured before it was blocked. This allows to compute the propagation factors between TM1 and the two rigid interferometer diodes.

The best available estimate for the errors in the ground measurements is given by the maximum deviation in PD responsivity of the two beams on one PD of 2.9 %. A Gaussian error propagation to the ratios, listed in Table 5.3 results in an uncertainty of up to $\approx 6\,\%$. For the in-flight parameters, the maximum error of the BS splitting ratio (listed in Table 8.1) propagates to the ratios in Table 5.3 with a 3 % error margin.

	Ground	**Flight**
$\frac{\lambda_{\Sigma_F}}{\lambda_{\mathrm{TM1}}}$	0.2117	0.2155
$\frac{\lambda_{\Sigma_R}}{\lambda_{\mathrm{TM1}}}$	0.2208	0.2277

Table 5.3.: Propagation coefficients between TM1 or Σ_F and Σ_R. The available best estimates of systematic errors to the "Ground" measurement are at maximum $\approx 6\,\%$ and for the "Flight" parameters, $\approx 3\,\%$.

The measured losses on ground (in Table 5.3) are 2 % and 3 % greater than the computed ones from Appendix B, which is within the systematic errors of the two measurements. Nevertheless, an underestimation of the losses between TM and PDs would even lead to a greater value of the PD responsivity during flight (because the actual losses between TM and PD are 2 % or 3 % higher).
Therefore, the result of a very small degradation of the PDs within the whole mission duration is further supported by this cross check.

Another confirmation of the result can be found by a closer look back to the expected radiation for the different phases of the LPF mission. In Reference [40] (on page 10) it is written that the expected damage was assumed to be dominated by solar particles. The responsivity monitoring during flight however, showed no decrease of the responsivity within errors of a percent for the whole mission (see Figure 5.12). Therefore, the effect of solar protons is likely to be overestimated by the estimations, previous to flight. This is also supported by the observed lack of Solar Energetic Particless (SEPs) at higher energies during flight, as described in Reference [50].

Besides a deviation in the actual amount of particles, the proton energies, used in the test procedure, could have led to an overestimation of the radiation damage as well. Higher proton energies lead to less displacement damage of an InGaAs PD, as described by a lower NIEL (compare to Section 2.5). For a quite solar phase the maximum flux is expected at proton energies that are an order of magnitude higher (compare to Reference [51] page 147) than the ones, used during the radiation tests (maximum proton energy during the tests was 35MeV, Reference [40]). Therefore, the induced damage per particle could have been less during flight. The trapped particle environment already was assumed to have a negligible effect on the degradation of the PDs (compare to the citation Reference [40] above). Hence, only the solar

protons during Low Earth Orbit Phase (LEOP) and transfer phase need to be considered. The shielding and solar activity should at least be comparable for these phases. Therefore, it can be assumed that the impact of solar protons was overestimated also during the LEOP and transfer phase.

In summary it can be concluded that the PD responsivities degraded, with only a few percent, much less than expected for the full mission duration including the launch and transport through the earth radiation belts.

5.3.2. Extrapolation to LISA

To interpret this result in the context of LISA, the worst case scenario of the maximum undetectable change of 2 % responsivity in 389 days is assumed.

Since LPF was monitored on a period greater than a year, a linear extrapolation of the worst case scenario to a LISA lifetime is used here as a rough estimate. The displacement damage on the PDs is assumed to be linear for low particle fluxes. Of course, the total dose of cosmic radiation is in reality not stationary on timescales of years, due to the changes in solar cycles.

For an approximately 6 years total nominal mission duration (nominal 4 years mission duration, 15 months of transport to the final LISA orbits, plus a commissioning phase) therefore, a maximum decrease of 12 % PD responsivity can be expected. With a possible mission extension of 5 years, the total decrease should still be lower than 22 %. Therefore, the Signal-to-Noise Ratio (SNR) of LISA at frequencies where shot noise is the limiting noise contribution, would be reduced by up to 12 % with:

$$\eta_{\text{red.}}^{\text{max.}} = 0.78 \cdot \eta_{\text{start}} \tag{5.2}$$

$$\text{SNR}_{\text{start}} \propto \sqrt{I} = \sqrt{P \cdot \eta_{\text{start}}} \tag{5.3}$$

$$\rightarrow \text{SNR}_{\text{red.}}^{\text{max.}} \propto 0.88 \cdot \text{SNR}_{\text{start}} \,, \tag{5.4}$$

due to a possible degradation of the PDs.

As already mentioned above a linear extrapolation of the LPF results to a LISA-like lifetime is of limited validity, due to the changes in solar activity. The findings, therefore, need to be adapted for a dedicated radiation environment simulation with the final mission design.

5.3.3. Power related parameters during the monitoring experiments

To complete the monitoring experiment, all available power related quantities are compared between the three investigations. The average current to the laser pump diode, as well as the average output power — measured with an internal photodiode, also used for stabilisation — are shown in Figure 5.13 in yellow and purple. In the next step, the power, arriving on the OB, is monitored with the power monitor diodes (blue data-points) and controlled via the power amplification to the RF drivers of the AOM (shown in red). In the end, the power is detected by the QPDs in the interferometers. Therefore, the sum of all QPD powers is shown in green. For comparison, all quantities are normalised by their average value during the three investigations.

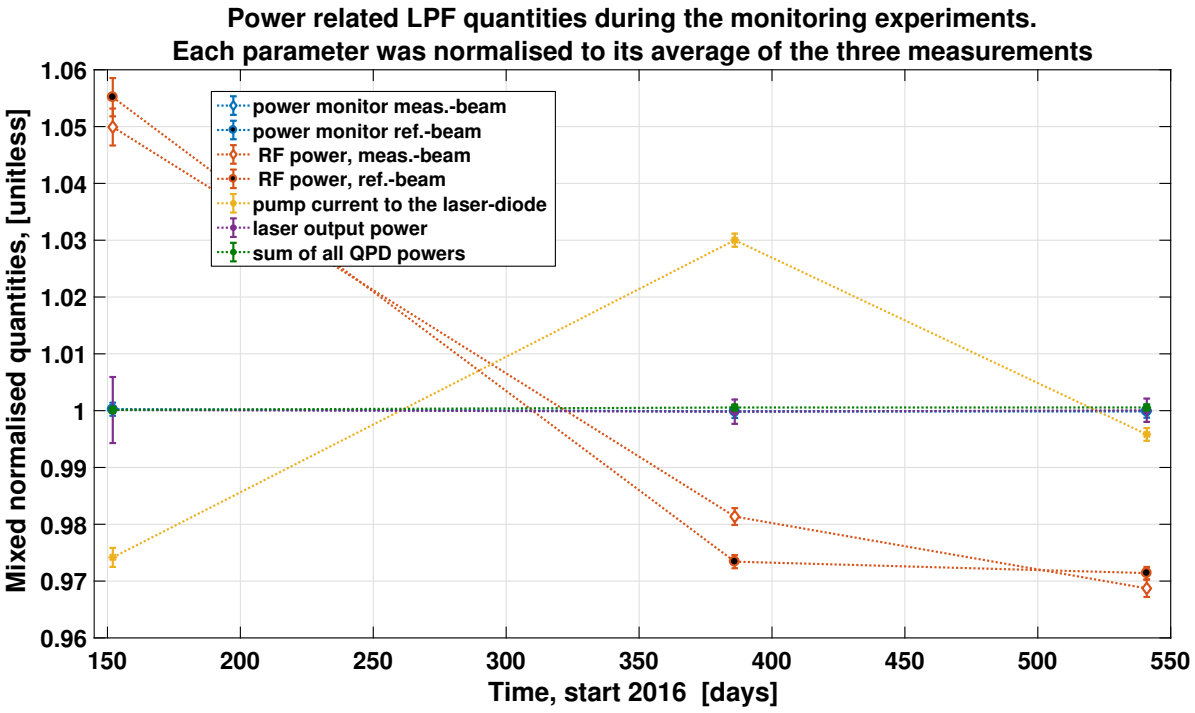

Figure 5.13.: Power related quantities on LPF during the monitoring experiments.

As expected, the power monitor diodes and the laser output power, are — as sensors for power stabilisation — approximately constant. Also the detected power in the interferometers (the sum of all QPD powers) is constant within errors.

In contrast, the laser diode pump current and the RF driver voltage change — as control loop actuators — by several percent during the monitoring experiments. For the laser, the needed pump current leading to the stabilised output power is increasing between the first two monitoring steps, but also decreasing towards the last one. Therefore, no trend, indicating a degradation of the pump diode or the laser crystal, or a degradation of the power monitor diode can be observed.

For the average RF power, the applied voltage to the AOMs for the same power on the OB gets even lower within the three monitoring experiments. However, in the analysis of the LPF polarisation effects in Part II, the RF power is found to fluctuate over the mission duration by about 15 %. Hence, also the RF powers give no evidence for a trend in the transmitted power from the modulation bench to the optical bench.

In summary, neither a degradation of the laser crystal nor a degradation of the fibres, nor of the power monitor diodes can be identified.
However, the uncertainty in transmitted power to the OB is high, because relevant fluctuations in the polarisation were observed (as described in Part II) and the off-nominal polarised power is dumped at the front of the OB. Therefore, an error of some percent needs to be assumed here.

Box 5.3.1 | Summary: PD responsivity over mission duration

- The responsivity of LPF's PDs degraded only by a few percent for the full mission duration including the launch and transport through the earth radiation belts.
- For the in orbit phase, the PDs showed no degradation of their responsivity with a measurement error of $\pm 1\,\%$.
- The transmitted power from the laser to the modulation bench and finally to the optical bench showed no trend.
  → Therefore, the laser, the fibres and the power monitor diodes also show no detectable degradation within errors of some percent.
- A simplified linear extrapolation to a 6 years LISA mission duration expects:
  – A decrease in the PD responsivity of less than $12\,\%$,
  – and an SNR reduction of less than $\approx 6\,\%$ for a shot noise limited antenna.

5.3.4. G-coefficents

The so-called G-coefficients, G_i, are given by the average PD responsivities of the three monitoring experiments:

$$\mathrm{G}_i = \frac{\mathrm{U}_{\mathrm{ADC}}}{\langle \eta_i \rangle \cdot \mathrm{R}_{\mathrm{TI}}} \,. \tag{5.5}$$

These coefficients are more useful in practice than the PD responsivities, since they directly calibrate the available Σ parameter to the beam power in Watts:

$$P_i = \Sigma_i \cdot \mathrm{G}_i \,. \tag{5.6}$$

Therefore, the average conversion factors, G_i, of the average PD responsivity in the three monitoring experiments from Table 5.2 are listed below:

$$\begin{aligned} \mathrm{G}_{12} &= (9.272 \pm 0032) \cdot 10^{-4} \,, \\ \mathrm{G}_1 &= (9.084 \pm 0.01) \cdot 10^{-4} \,, \\ \mathrm{G}_\mathrm{R} &= (9.342 \pm 0.011) \cdot 10^{-4} \,, \\ \mathrm{G}_\mathrm{F} &= (9.225 \pm 0.0259) \cdot 10^{-4} \,, \end{aligned} \tag{5.7}$$

in units of $\left[\frac{\mathrm{W}}{\mathrm{AU}}\right]$, with AU $\equiv$ arbitrary units of Σ.

6. Effect of power-to-phase coupling

The analysis of the power modulation characterisation measurements, described in Section 5.2, unveiled an unexpected coupling between the beam power and the longitudinal phase in the differential TM interferometer. The coupling is very weak and could only be observed due to the extremely low noise in the differential TM interferometer.
The overall great performance of the OMS allowed the further analysis of the power-to-phase coupling in the DWS signals, as described in Section 6.1. Besides the power modulations, another LPF experiment with steps in the beam power, the so-called contrast experiment, was identified. The analysis of the power-to-phase coupling during this experiment is described in Section 6.2.
In Section 6.3 the observations on the spurious coupling are summarised and possible mechanisms for an origin of the effect are discussed.

6.1. Power coupling to the Differential Wavefront Sensing signal

In the power modulation sequences, described in Chapter 5, the single beam powers are modulated with a square wave and modulation depths up to 2 %. The observation of spurious spikes in the differential acceleration led to the identification of tiny steps in the differential TM displacement in correlation with the power steps, as described in Section 5.2.4: In coincidence with a step in the beam power, the differential x12-interferometer shows a step of a few pico-metres, too. The steps are only identifiable for the reference beam modulation, in absence of a radiation pressure induced signal.

For further investigation of the effect, the next obviously interesting parameters are the DWS phase signals. Surprisingly, they show more significant coupling of the power modulation.

Figure 6.1 depicts all four DWS TM angles during the 2 % measurement beam power modulation. Note,that the DWS signals are already converted to TM angles. This includes subtraction of offsets in DWS, measured with the optimal aligned TMs. These offset angles are a result from system-calibration (compare to Reference [36], page 30 to 33).

In coincidence with the power steps, the DWS angles step, too. Afterwards, the control loops slowly rotate the TM back to its set-point. The steps appear to have no delay and the increase in DWS, and hence the duration of the steps, seems to be as fast as the power step itself.
Besides this, the angles appear to have different step sizes. φ_1 shows the strongest coupling, whereby the other three angles experience smaller steps.

A comparison with the reference and counter beam modulation in Figure 6.2 reveals another property of the unknown coupling: The reference beam modulation couples the same.

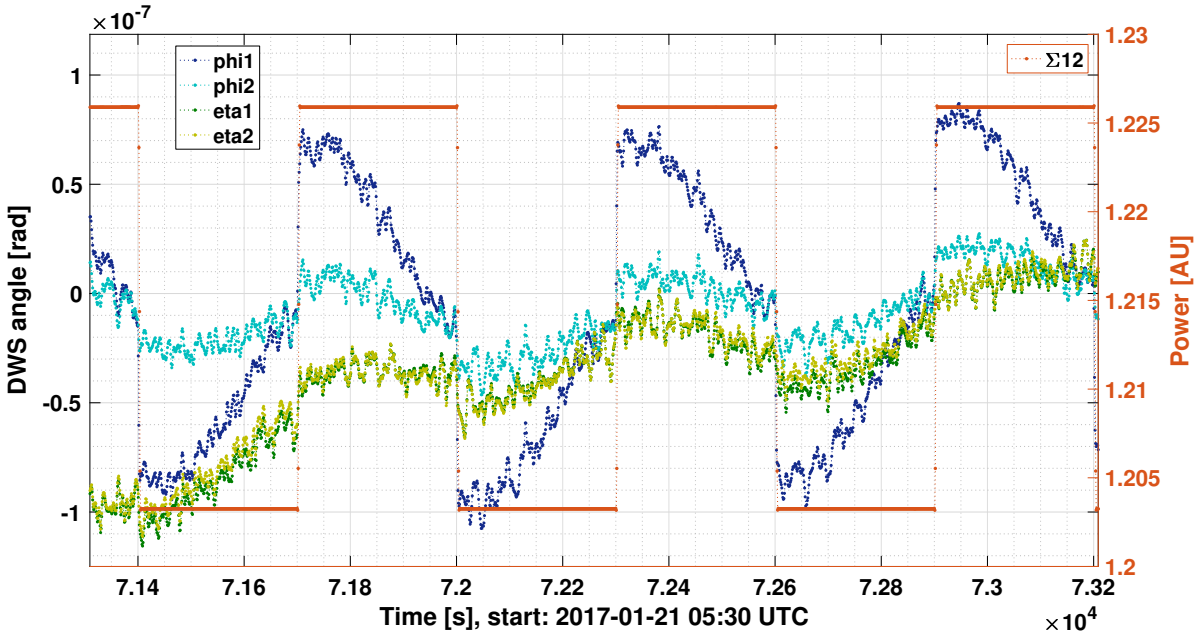

Figure 6.1.: Segment of DWS TM angles during 2 % reference beam power modulation, together with the combined beam power, Σ_{12}.

As a consequence, the observed coupling can obviously not be real TM-motion, because the reference beam does not hit any TM.
A comparison to the DC angles, describing the displacement of the beam spot position on the QPD surface, shows no consistent correlation with the observed properties of the DWS angles (compare to Appendix D.1).

A closer look at the DWS angles during counter modulation (lower panel of Figure 6.2) shows a similar behaviour as the Σ_{12} parameter. When the power is increased by the first beam, the DWS signal increases. Some seconds later, the power of the other beam is decreased to compensate for the power step and so the DWS signal decreases as well.
However, the similar shape of Σ_{12} and DWS could have two reasons:

(i) the coupling mechanism could be related to the combined beam power, Σ_{12},

(ii) or it is induced by superposition of the single beam effects in DWS (like the Σ_{12} parameter is a superposition of the single beam powers).

Therefore, the DWS step sizes implied by a step in reference and measurement beam power were estimated. This was done by subtraction of the last sample before a step and the first one afterwards. The average values of all steps for 1 % and 2 % power modulation depth are shown in Figure 6.3.

The sequential commanding further allowed to separately estimate the contribution from measurement and reference beam during counter modulation (separated by a few seconds).

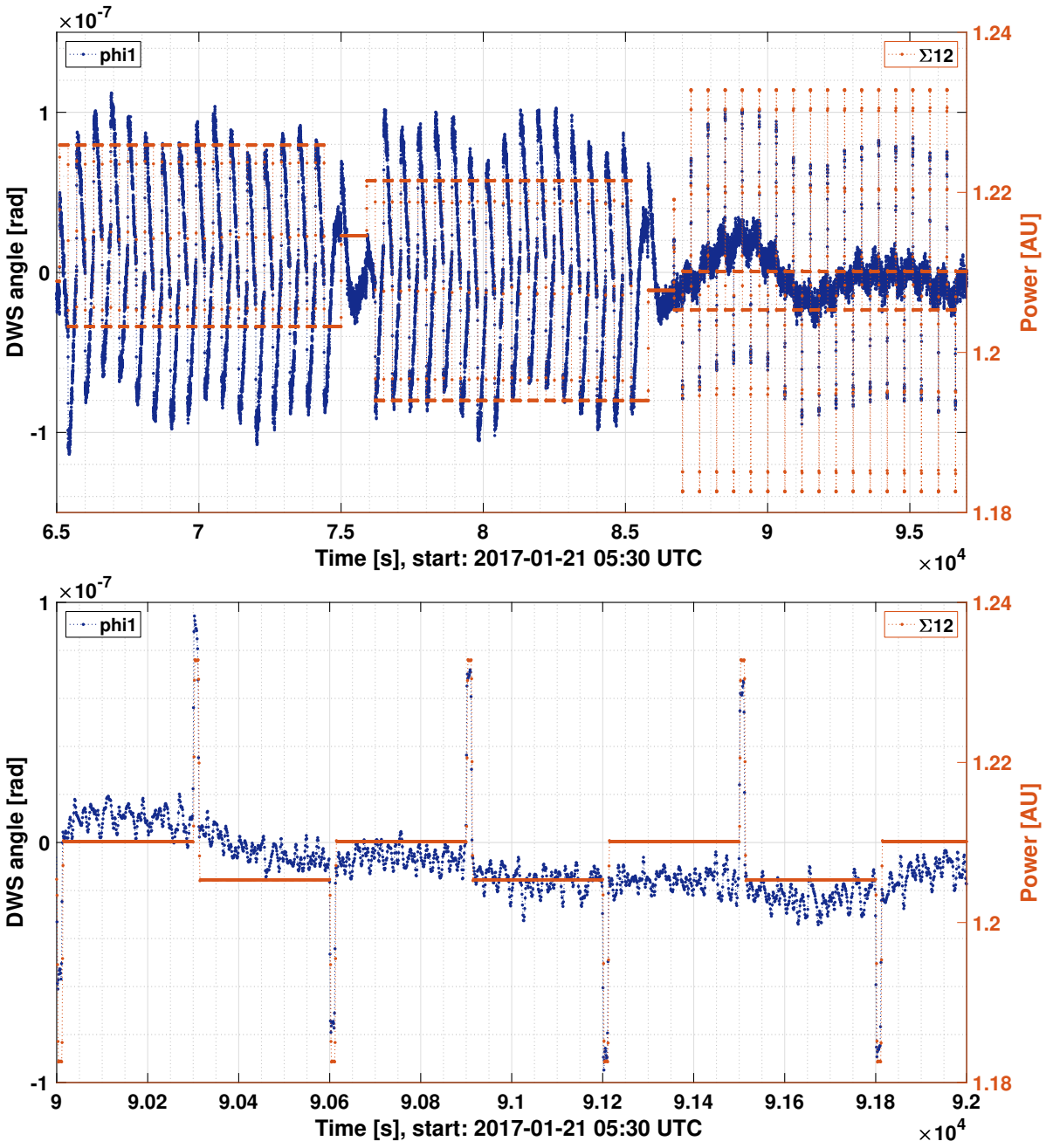

Figure 6.2.: **Upper figure:** DWS φ_1 TM angle during the 2 % beam power modulations. Reference and measurement beam power modulation show significant coupling to phi1. **Lower figure:** Sequence of the counter modulation. The coupling is significantly reduced as is the combined beam power. Correlated to the power spikes at beginning and end of a modulation cycle, the DWS-phase appears to experience a spike, as well.

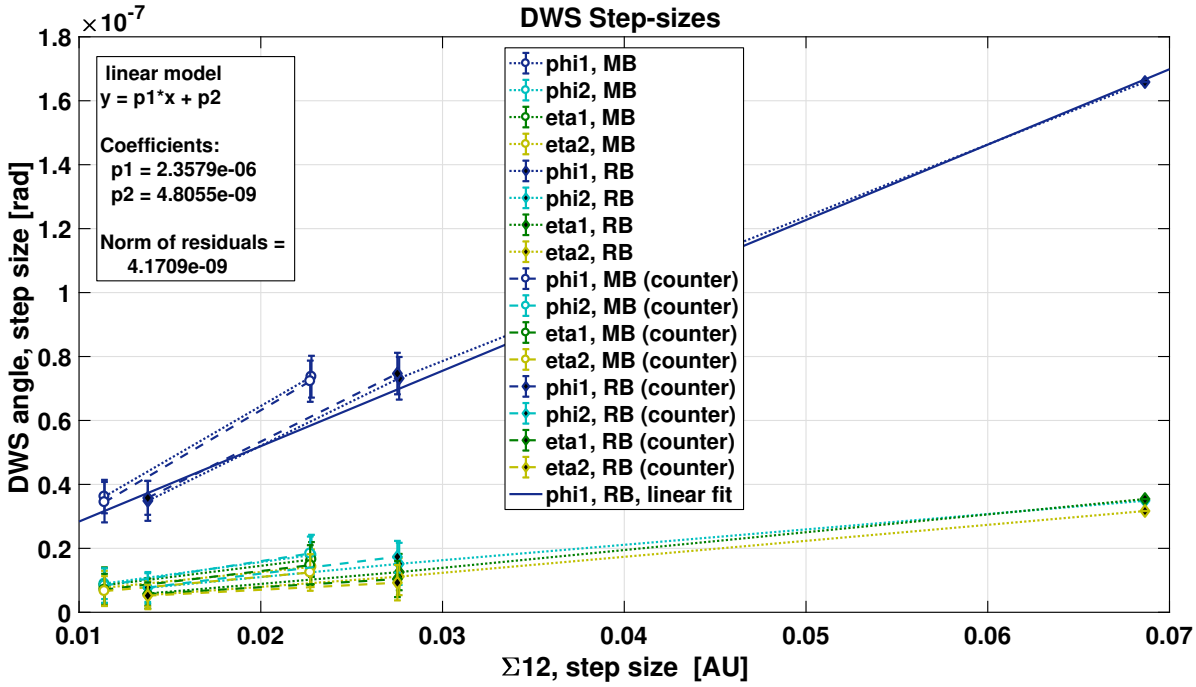

Figure 6.3.: Average DWS step sizes for reference (RB in the legend) and measurement beam modulation (MB in the legend). The counter modulation step sizes (counter in the legend) could be separated in reference and measurement beam step. For the reference beam modulation one further step size is included from the contrast experiment.

In contrast to the power step sizes in combined beam power , the DWS step sizes of reference and measurement beam agree within errors, (compare to Figure 5.1). This can easily be seen in Figure 6.3 by the vertical axis values of the black and white filled points (DWS step sizes correlated with reference and measurement beam modulation). They agree within errors, whereby the values at the horizontal axis are different, corresponding to the power-mismatch of measurement and reference beam at the Σ_{12} diodes.
The step sizes during the counter modulation (shown by the dashed lines) obviously match the step sizes of the single beam modulations, labelled with the dotted lines.
Therefore, the similar shape of the DWS step and Σ_{12} during the counter modulation seems to result from superposition of the single beam power effects.

As a consequence, if the coupling is unique for the individual beams, it could possibly be an optical effect of the beam profile. For example, the modulation induced change in RF power to the AOMs could have led to a wavefront distortion by temperature or stress-induced changes of the refractive index pattern in the active crystal.
However, an optical effect should be correlated between different diodes, since they are all hit by the same beams with comparable good beam overlap. In contrast, φ_1 couples more than 4 times stronger than the other parameters. So, also an optical effect seems to disagree with the observations.

Clearly, at this point of the analysis the most striking question was: What is special about φ_1 so that it couples stronger with power than the other angles?

A check for correlations with related parameters pointed in a new direction: Only one parameter was found that correlates to the coupling strength of the different DWS angles — the DWS offset angles. As mentioned above, these offsets are a result from system calibration and describe the DWS angles, measured for the optimally positioned TMs. They are further set as set-points for the angular control loops. In the data processing they need to be subtracted from the raw data to describe a tilt of the TM towards its nominal position.
Table 6.1 lists the DWS offset angles and the average DWS step sizes during the 2 % reference beam modulation. The step sizes are estimated by simple truncation of the steps. Therefore, the Σ_{12} time series is used to identify the last sample before and the first sample after a power step. Due to the resolution of 1 Hz and the fast operating power control loop, a step only lasts 4 samples. Afterwards, the DWS steps within this step duration were estimated. Of course, the results are affected by DWS noise on that time scale.

DWS angles / TM displacement				Raw phase signals		
	offset phase [μrad]	DWS step [nrad]	c_{trans} [10^{-3}]		offset phase [mrad]	DWS step [μrad]
φ_1	-61.2	73.2 ± 6.66	-1.196 ± 0.109	φ_1^{raw}	302.3	-362.7 ± 33
φ_2	-9.7	15.1 ± 6.59	-1.562 ± 0.679	$\varphi_{12}^{\text{raw}}$	51.3	-80.2 ± 34.8
η_1	-4.9	12.6 ± 5.68	-2.566 ± 1.159	η_1^{raw}	-23.5	60.3 ± 27.2
η_2	-3.3	11.2 ± 5.8	-3.382 ± 1.758	η_{12}^{raw}	17.1	-57.9 ± 30.1
	avg. displ. [pm]	displ. step [pm]	c_{trans} [10^{-3}]		avg. phase [mrad]	phase step [μrad]
x_{12}	-302.886	2.76 ± 0.17	-9.122 ± 0.548	o_{12}^{raw}	-3.58	32.63 ± 1.96

Table 6.1.: Comparison of DWS offset angles with the average DWS step sizes correlated with a step in reference beam power corresponding to $\Delta(\Sigma_{12}^{\text{step}})/\langle\Sigma_{12}\rangle = (2.2868 \pm 0.0004)$ %. Furthermore the actual longitudinal phase in x12 during the step, compared to the correlated average displacement step size are shown for the reference power steps. The error estimates are given by the standard deviation of all 30 full steps. Only for the displacement step sizes, the number of steps had to be reduced to 15 steps, because for the first 15 steps the TMs were moving too much.

From the first two rows of Table 6.1 it can easily be seen that a greater absolute DWS offset angle correlates with a greater step size in DWS. Hereby, the sign of the DWS step is in positive correlation with the power and negatively correlated to the offset angle. A coefficient of linear translation $c_{\text{trans}} = \frac{\text{DWS step size}}{\text{offset angle}}$ is shown in the third column. It increases towards angles with smaller offset phase. A reason for this could be the noise in DWS, which is high in comparison to the small step sizes for all angles except φ_1 (as can be seen by their standard deviations). Nevertheless, also within the errors, c_{trans} increases slightly towards the lower offset angles. Therefore, a non-linear correlation between offset angle and step size is likely, although the amount of available data is too small for a reasonable analysis.

The average step size in longitudinal phase is also listed in Table 6.1. For comparison to the DWS angles, all parameters are converted back to raw phases via the g-coefficients, as described in Section 2.4.
The step size in longitudinal raw phase, as well as the absolute measured longitudinal phase, are smaller than for the DWS angles. Like for the DWS steps and the DWS offset phases, the correlation of absolute displacement and displacement step size is negative. However, the

coupling coefficient $c_{\text{trans}} = \frac{\text{displ. step}}{\text{avg. displ.}}$ is significantly greater, as it is for the DWS angles. Of course, also the processing of the signal is different. For the longitudinal phase, the average phase of the A and B diode in the reference interferometer is subtracted from the x12 interferometer ones. For the DWS signals, the complex amplitude of one side of the A and B diodes is divided by the other one (compare with Section 2.4). Therefore, a comparison of the translation coefficient between DWS and longitudinal phase is not trivial, and due to the low amount of data, also unclear in this context.

Nevertheless, the DWS angles show greater step sizes for greater absolute measurements in DWS phase. No other comparably consistent correlation could be found in the analysis. Therefore, a causation between the two parameters is preliminary assumed for the further investigations. As a consequence: The coupling mechanism is assumed to originate within the phasemeter, since the phase information is interpreted, not before there.

This involves an inconsistency with the previous analysis: The coupling between Σ_{12} and DWS step size is slightly stronger for the measurement beam, although the phasemeter has no knowledge about the particular beam being modulated.
For clarification, two different possible explanations were found: The first one is that the different beam spot positions result in a different coupling of the two beams. The spot position of the beam leads to different powers at the individual quadrants. Therefore, the same power modulation could have led to different results in the processing of the two beams. However, the previously made check for correlations between the DC angles and the DWS angles (see Appendix D.1) showed no consistent effects, therefore this idea seems to be unlikely.

Nevertheless, the average beam power of the two beams is also different. Therefore, the second idea is: The coupling strength could scale with the relative power modulation of one beam instead of the the absolute modulated power on the diode. The modulation depth is intentionally equal in the two beams and hence fits the observation of comparable DWS step sizes (see Figure 6.3). The most obvious relevant parameter is the heterodyne amplitude $P_{\text{het}} = 2\sqrt{\eta_{\text{het}} P_{\text{RB}} P_{\text{MB}}}$ (as described in Section 2.3). Here, a relative modulation of one beam leads to the same modulation depth in heterodyne amplitude, independent of the average beam power.

Therefore, the observed behaviour indicates a coupling mechanism originating in the phasemeter and possibly depending on the modulation depth in heterodyne amplitude.
For further investigation, another LPF experiment with power modulations was searched for. Luckily, there is one: the contrast versus differential beam power experiment. Its analysis is described in the following.

6.2. Power-to-phase coupling: contrast experiment

On DOY167 of 2017 another experiment with major steps in the beam power was performed on LPF to investigate the effect on the interferometric contrast. In this case, the power of the reference beam was decreased in 10 % steps, down to 20 % of the initial beam power. Afterwards, the reference beam power was further reduced to only ≈ 17 % of the nominal power, before TM2 was displaced by $\frac{\lambda}{8} = 133$ nm to increase RIN coupling (compare to Reference [17]). Keeping this new TM position, the power was stepped up again to 100 %.

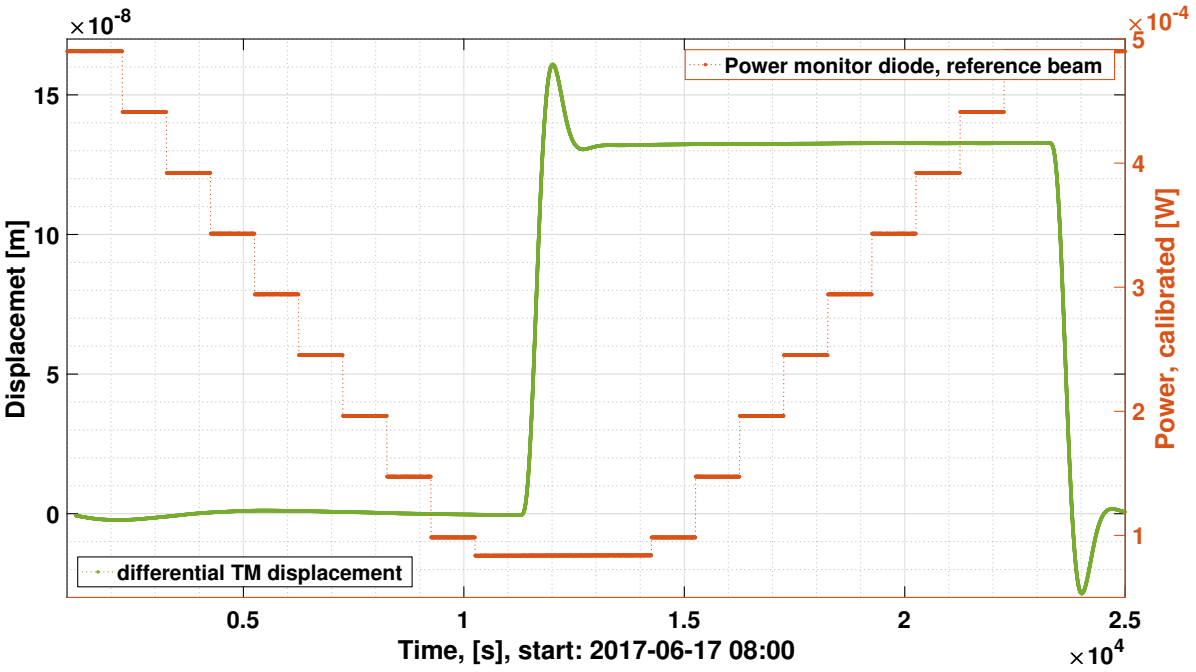

Figure 6.4.: Differential TM displacement and reference beam power during the contrast experiment.

Figure 6.4 shows the reference beam power on the power monitor diode (calibrated to Watts with a PD responsivity of $\eta = 0.76\,\mathrm{A/W}$, measured previous to flight, as described in Reference [49]), together with the differential TM displacement — during the whole contrast experiment.

Figure 6.5 shows the measured DWS signals, calibrated to the TM angles but this time without subtraction of the offset phase, together with the reference beam power.

As expected, the DWS angles show steps in correlation with the power. The steps can be further seen by the high passed time series of the DWS angles in Appendix D.2.

The DWS step sizes correlated to the eight 10 % power steps (between 100 % to 20 %) were determined for the downwards and upwards steps individually, as depicted in Figure 6.6. The step sizes were determined analogously to those for the power modulations — by subtracting the value of the last sample before the step from the first one after. Since there is only one step per power level and step direction, unfortunately no statistical error estimation is available. On the horizontal axis, the average combined beam power, $\langle \Sigma_{12}^{\mathrm{step}} \rangle$ during the step, normalised to the nominal combined beam $\Sigma_{12}^{\mathrm{nominal}}$, is shown.

As found before, the step sizes of φ_1 are much bigger than for the other angles. For the steps at $\langle \Sigma_{12}^{\mathrm{step}} \rangle / \Sigma_{12}^{\mathrm{nom}} = 0.97$ and $\langle \Sigma_{12}^{\mathrm{step}} \rangle / \Sigma_{12}^{\mathrm{nom}} = 0.92$, the step sizes of η_1 and η_2 are slightly higher than φ_2, although their offset phases are a bit smaller (compare to Table 6.1). At first, this looks like a contradiction to the hypothesis of a relation between the two parameters. However, a closer look at the time series in Figure 6.5 clarifies this observation. The angular displacement away from the nominal position in the beginning of the experiment is actually

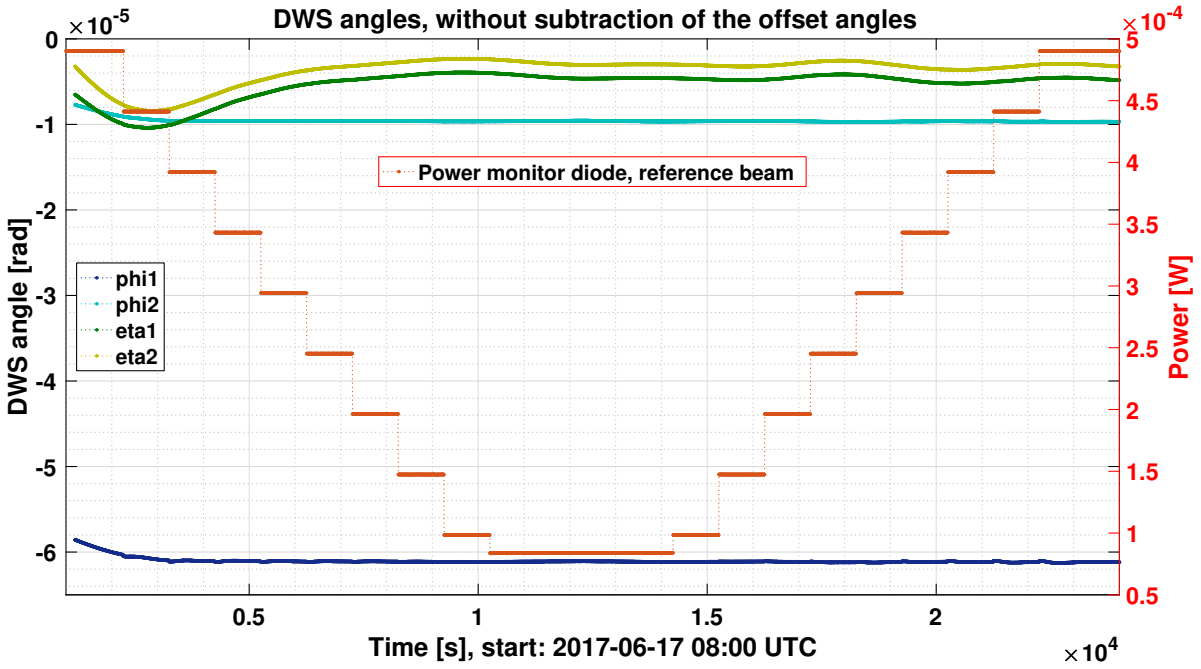

Figure 6.5.: Time series of the DWS angles (without subtraction of offset angles) together with the reference beam power during the contrast experiment.

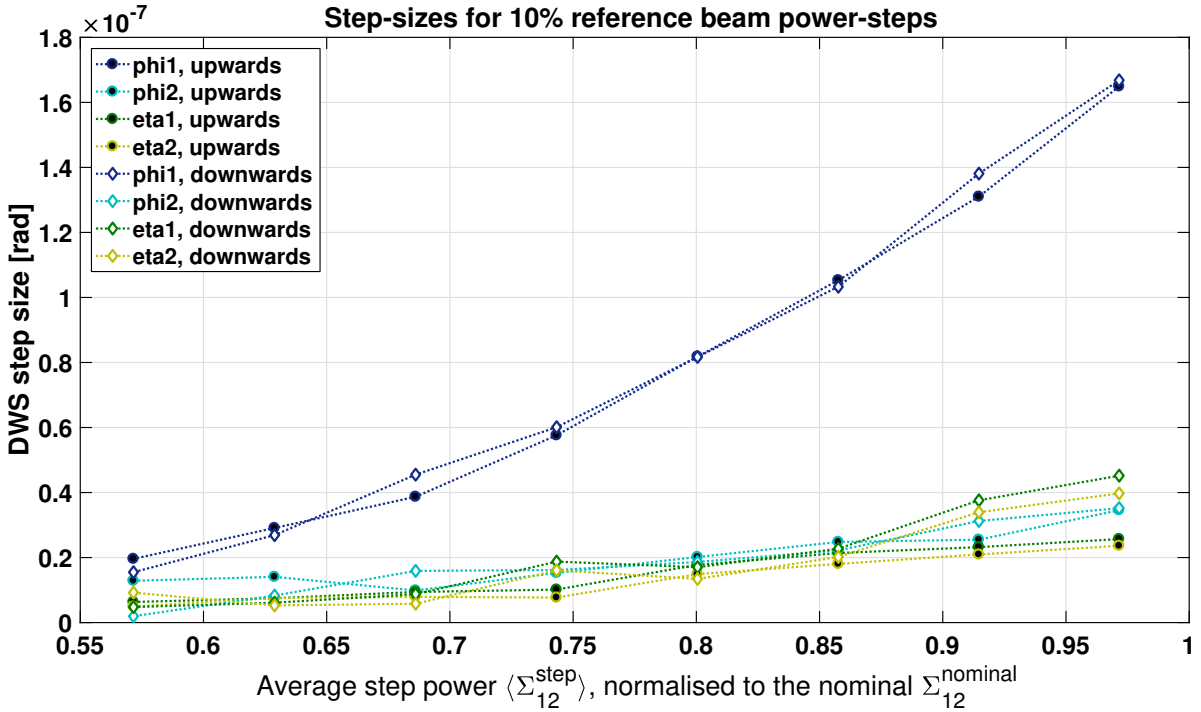

Figure 6.6.: Step sizes in DWS during the contrast experiment with 10 % reference beam power steps versus the normalised combined beam power during one step, $\langle\Sigma_{12}^{\mathrm{step}}\rangle/\Sigma_{12}^{\mathrm{nom}}$. The downwards and upwards steps were estimated separately.

greater for η_1 and η_2 than for φ_2. The bigger DWS step sizes observed during these first two steps, therefore, indeed belong to a higher absolute measured DWS angle.

As a consequence, the theory of a relation between the absolute value in DWS (which only agrees on average with the offset angles) and the corresponding power induced step size could be further supported.

Besides agreement with the previous observations, another surprising property of the effect can be observed: the DWS step size is not only dependent on the modulated power and the offset angle, but also on the average reference beam power. The lower the reference beam power gets, the smaller the DWS steps are — although offset angle and power step size stay the same (as can be seen in Figure 6.6). Relative to the current average reference beam power, the power step size is even increasing, whereas the DWS step size decreases.

In the previous section the comparable value in step sizes between reference and measurement beam modulation gave evidence to suppose that the product of the beam powers is the relevant quantity, which correlates to the coupling. Therefore, the measured step sizes of φ_1 (with the strongest coupling) are shown in Figure 6.7 together with the interferometric contrast $C = \frac{2\cdot\sqrt{P_{\mathrm{RB}}P_{\mathrm{MB}}}}{P_{\mathrm{RB}}+P_{\mathrm{MB}}}$, assuming perfect beam-overlap (heterodyne efficiency of $\eta_{\mathrm{het}} = 1$).

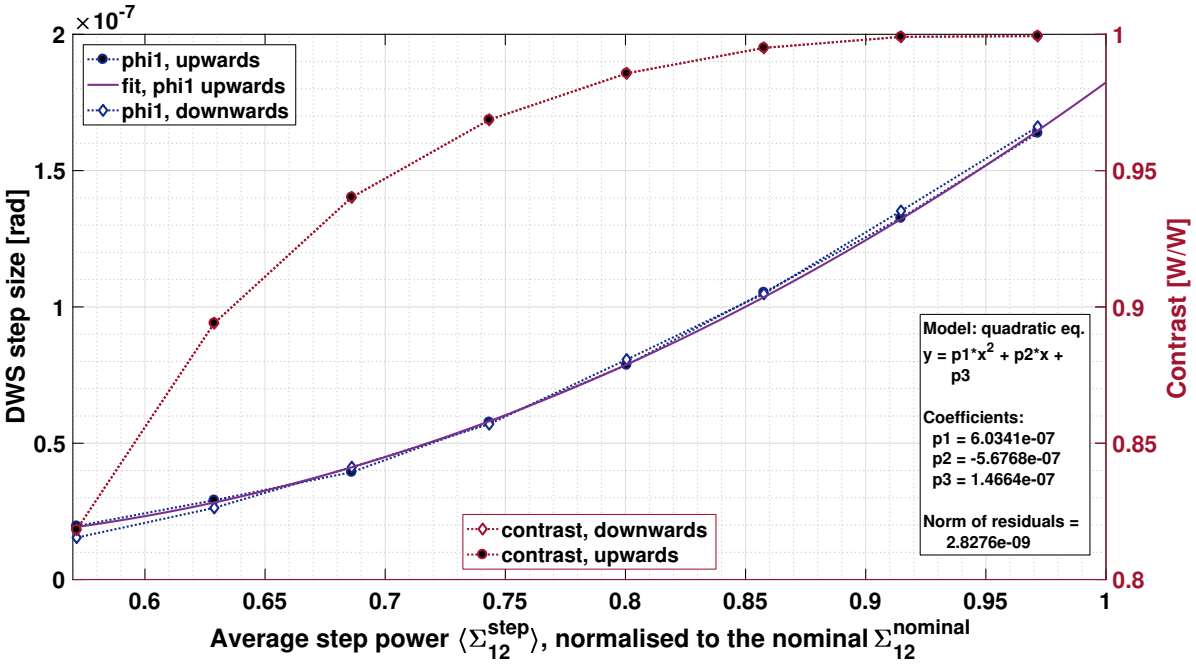

Figure 6.7.: Basic fit of the φ_1 step size during the contrast experiment together with the interferometric contrast C for perfect beam overlap, dependent on the combined average beam power $\langle\Sigma_{12}^{\mathrm{step}}\rangle/\Sigma_{12}^{\mathrm{nom}}$.

The functional shape of the DWS step size versus $\langle\Sigma_{12}^{\mathrm{step}}\rangle/\Sigma_{12}^{\mathrm{nom}}$ fits a simple quadratic form, as can be seen in Figure 6.7. On the contrary, the interferometric contrast is dominated by $\sqrt{P_{\mathrm{RB}}\cdot P_{\mathrm{MB}}}$ and therefore inversely curved. Obviously, a correlation of the step size and the heterodyne amplitude seems unlikely and stays unclear.

How could a possible correlation to power then look like? One idea is a constant error in the phase estimation, somehow related to $P_{\mathrm{RB}} \cdot P_{\mathrm{MB}}$. Changing the power of one beam would then lead to an error (maybe further dependent on the measured phase) which appears as a step in DWS. Since the estimation of the step size basically works as a numerical derivative (difference of two values with the same short temporal distance), the primary relation to the error would need to include $(P_{\mathrm{RB}} \cdot P_{\mathrm{MB}})^3$, to fit with the observed quadratic shape in step size (as can be seen in Figure 6.7).

Besides the DWS signal, the differential TM displacement is also expected to be affected by the coupling (because it was effected by th power modulation, described in the previous Section 5.2.4, too). A closer look at the time series in Figure 6.4 indeed shows that the differential TM displacement reduces immediately when the power is stepped down.

The upper panel of Figure 6.8 shows the time series of φ_1 and differential TM displacement for the step from 50 % to 40 % reference beam power. The lower panel of Figure 6.8 shows the same power step back up from 40 % to 50 % power, with the displaced TM2 (by $\frac{\lambda}{8}$, as described above).

Surprisingly, a glitch in TM displacement appears during the upwards power step. Instead of the logically expected upwards step in TM displacement — lasting 2 seconds — the differential TM displacement signal decreases in the first second and increases during the second one to a higher displacement than before the step.

Therefore, the step sizes for the differential TM displacement were estimated by simple truncation as before, but for the increasing power steps, the glitch was analysed individually, too. Since one step is only two samples long, the drop down in the the first half of the glitch and the rise back up in the second one are truncated individually. The sum of these two half-steps then equals the full step size of the upwards step. Figure 6.9 shows the resulting analysis of the step sizes.
Interestingly, the sum of the two half-steps, corresponding to the full upwards step (with white filling), has a similar size as the downwards step with black filling of the markers, at the nominal TM position.

Hence it seems that the change in TM position has not affected the power-to-phase coupling effect itself, but introduced another effect, producing a glitch in correlation with a power step. In contrast to the previously analysed power-to-phase coupling, the new effect is only present *during* the power step and vanishes afterwards (because the size of the full upwards step approximately agrees with the downwards step at the nominal TM position). Therefore, this behaviour points to the coupling of relative intensity noise, just with the difference in the expression "noise". In this experiment not the changes in power due to power noise are observed, but the change in power by a defined power step. Of course, the coupling mechanism is the same for power fluctuations declared as noise or resulting from a power modulation. As described in Appendix A, the processing of the optical phase by demodulation generally cancels power noise. An exception to this are power fluctuations at the demodulation frequency, which are further suppressed by the so-called balanced detection scheme (compare to Section 2.4). Left is the coupling at twice the heterodyne frequency: $2 \cdot f_{\mathrm{het}}$. Power fluctuations at this frequency couple into the phase read-out and are not suppressed by balanced detection (compare with Reference [17]). Fortunately, the induced spurious phase from intensity fluctuations at $2 \cdot f_{\mathrm{het}}$ also appears in the reference interferometer. Therefore, the subtraction of the TM and reference

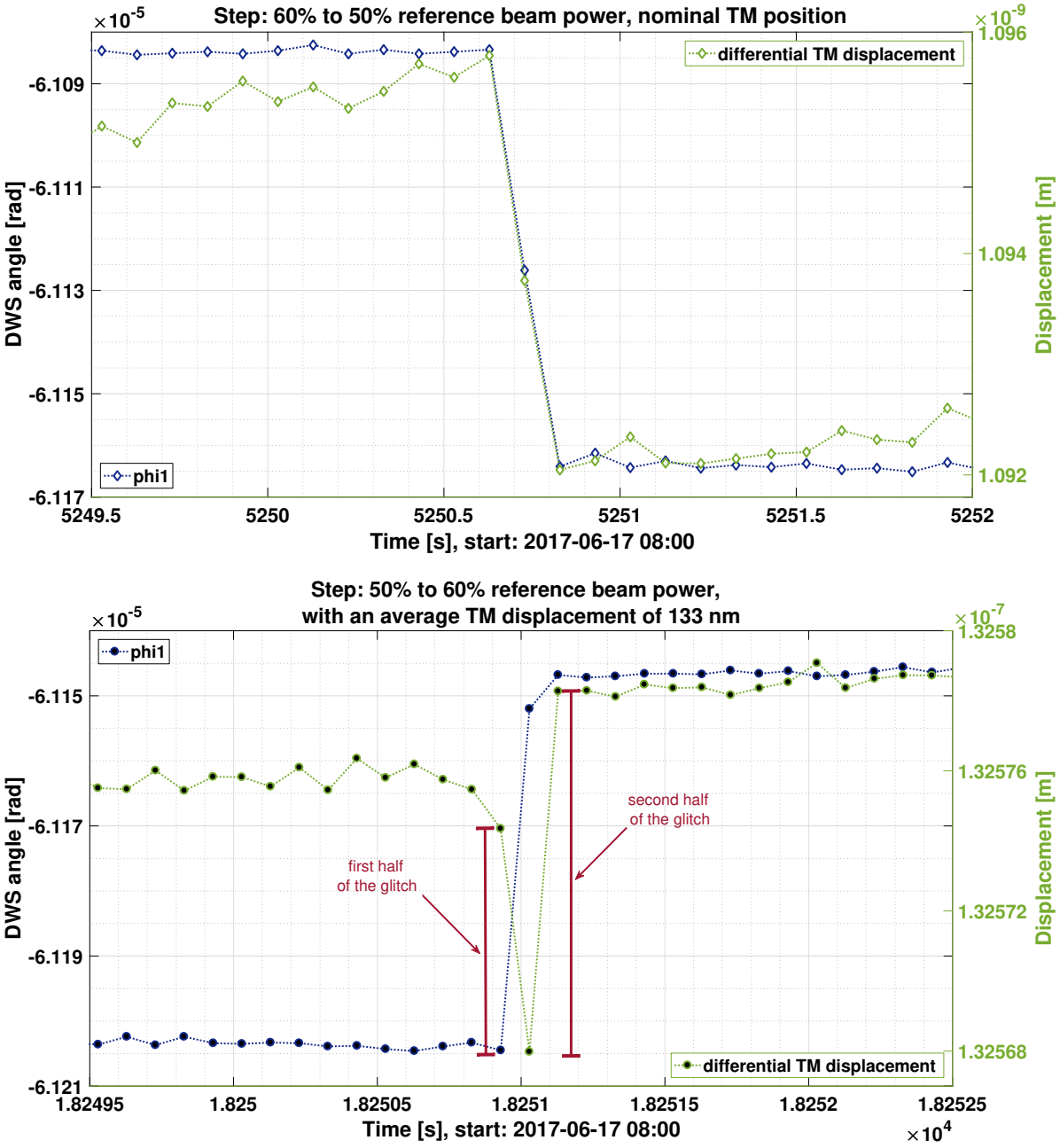

Figure 6.8.: Time series of step in x_{12} and φ_1 from 50 % to 40 % power and vice versa. Before the upwards step, the TM was displaced by $\frac{\lambda}{8}$, leading to a glitch: the x_{12} signal steps down first and then up again.

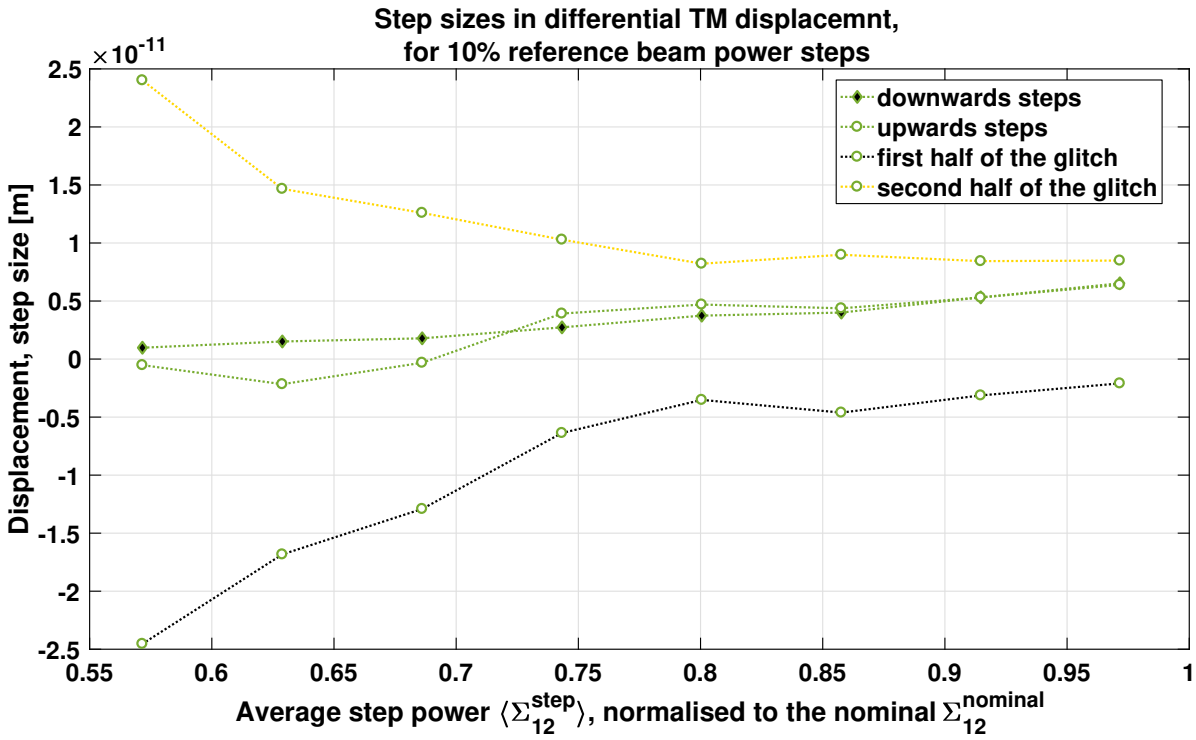

Figure 6.9.: Step sizes in differential TM displacement during the contrast experiment with 10 % reference beam power steps versus the average combined beam power $\langle\Sigma_{12}^{\mathrm{step}}\rangle/\Sigma_{12}^{\mathrm{nom}}$. The upwards steps are affected by a glitch. The step sizes were measured for the first and second half of the glitch, individually, as plotted with the yellow and black dotted lines.

interferometer also cancels the noise at $2 \cdot f_{\mathrm{het}}$. However, with the displaced TM to $\frac{\lambda}{8}$ exactly this cancellation is disabled. This happens, because the effect of the same intensity fluctuation on the heterodyne phasor of reference and TM interferometer is different (the error is dependent on the relative phase between heterodyne phasor and intensity noise induced phasor). As a result, the contribution of the power step at $2 \cdot f_{\mathrm{het}}$ couples to the longitudinal phase for the displaced TM. The DWS phases should be unaffected by the displacement of the TM, since there is no subtraction of the reference interferometer. Furthermore, the coupling of $2 \cdot f_{\mathrm{het}}$ to DWS should be small anyway, because the heterodyne phase of left and right, or up and down segments is close. Hence, the observation of no glitch in DWS fits with the $2 \cdot f_{\mathrm{het}}$ RIN theory. This is also true for the step size of the glitches. Towards the smaller reference beam powers, the relative step size in power, as well as the glitch size increase. This is in particular interesting, because only $2 \cdot f_{\mathrm{het}}$ RIN is independent on the absolute power and only dependent on the relative power changes.

Therefore, with good indication, the origin of the glitch in TM displacement (for the displaced TM) can be identified as coupling of power fluctuations at $2 \cdot f_{\mathrm{het}}$, resulting from the step in reference beam power.

However, the steps are — with only 2 samples — highly under-sampled and — with only one measurement per average power and direction (upwards or downwards) — without statistical evidence. Therefore, the information is too small to do more substantiated investigation.

For comparing this contrast experiment to the characterisation modulations from the last section (Table 6.1), the step sizes of the 10 % steps are summarised similarly in Table 6.2. Since the average reference beam power is an important property, only the most similar steps from 100 % to 90 % power and 90 % to 100 % are listed in Table 6.2. These two steps have an average power of 95 % nominal reference beam power, whereby the modulation experiments modulate around the nominal power.

DWS angles / TM displacement			
	avg. phase [μrad]	step size [nrad]	c_{trans} [10^{-3}]
φ_1	-61.09 ± 0.1	165.9 ± 1.3	-2.715 ± 0.017
φ_2	-9.65 ± 0.01	34.9 ± 0.4	-3.618 ± 0.045
η_1	-4.29 ± 0.42	35.4 ± 13.8	-8.454 ± 4.036
η_2	-2.68 ± 0.42	31.2 ± 11.4	-12.291 ± 6.171
	avg. displ. [nm]	displ. step [pm]	c_{trans} [10^{-3}]
x_{12}	132.7	6.215	0.0568
x_{12}	-0.1	6.8	75.22

Table 6.2.: DWS offset angles and DWS step sizes for the reference beam power step from 100 % to 90 % (and 90 % to 100 %) corresponding to $\Delta(\Sigma_{12}^{\text{step}})/\Sigma_{12}^{\text{nom}} = 5.683 \pm 0.001$ %.

Obviously, the step sizes in the second column of Table 6.2 are greater than the ones during the 2 % reference beam power modulation (Table 6.1). This is easily justifiable by the greater power step of $\Delta(\Sigma_{12}^{\text{step}})/\Sigma_{12}^{\text{nom}}(\text{contrast exp.}) = 5.683 \pm 0.001$ % for the contrast experiment compared to the one for the characterisation measurement with 2 % reference beam power modulation, $\Delta(\Sigma_{12}^{\text{step}})/\Sigma_{12}^{\text{nom}}(\text{char. exp.}) = 2.2868 \pm 0.0004$ %.

The translation coefficients in the third row increase towards lower offset angles, as observed for the steps during the power modulation, listed in Table 6.1. This could again be a hint for a non-linear correlation between absolute measured value and step size.

The two 10 % step sizes from Table 6.2 are also added to the plot in 6.3. With this additional data there are three data points available for the reference beam power steps that agree with a linear fit within errors.

Box 6.2.1 | Summary: Power-to-phase coupling — Observations

Steps appear in longitudinal and DWS phase correlated with the applied power steps.

- Properties of the steps:
  - They are tiny.
    - → The highest observed step was in φ_1 with 0.17 µrad DWS angle for a 10 % step in the reference beam power.
  - They have no detectable delay,
  - the same duration,

  - and the same direction (positive or negative sign).
- The DWS step size is correlated with the DWS offset phase.
- A TM displacement by $\frac{\lambda}{8}$ has no impact on the longitudinal phase step size.
  - However, a glitch during the power step is introduced.
  - → Coupling of intensity fluctuations (induced by the step in power) at twice the heterodyne frequency is assumed to cause the glitch.

The size of the induced phase steps is correlated with power in a more complex way:

- The step size correlates with the relative modulated power of a single beam or with the product of beam powers (indistinguishable with the available data).
  - → The heterodyne amplitude could be a relevant parameter.
- Furthermore, the effect correlates to the average reference beam power, or the average product of beam powers, or the sum of the beam powers, Σ_{12} (again indistinguishable with the available data).
  - → quadratic correlation found between the DWS φ_1 step sizes and Σ_{12} (for constant steps in the reference beam power, constant measurement beam power and approximately constant average phase)
- An increase of the step size in power results in an increased step size in DWS and longitudinal phase (for constant average power, DWS offset and longitudinal phase).
  - → A linear fit agrees with the relation between the step size in power and the one in phase.

Unfortunately, all conclusions drawn on the origin of the power-to-phase coupling are barely constrained by the available information. The weak SNR ratio of all phase steps, except φ_1, the small number of parameters — only 4 different DWS offset angles, whereby three of them are close together — and the lack of statistics for the correlation with power — having only one measurement per step and direction — does not allow for a substantiated analysis. Nevertheless, the following section uses the observations and indications found, to discuss possible coupling mechanisms.

6.3. Coupling mechanism: Phasemeter processing and C-coefficients

The previous section described several properties of a power-to-phase coupling (see Box 6.2.1), observed during the power modulation experiments. The mechanism is preliminarily assumed to originate in the data processing. For clarification, all previously drawn conclusions to a possible origin are summarised in the following Box 6.3.1.

Box 6.3.1: Conclusions on the origin of the power-to-phase coupling:

On LPF the power is modulated with AOMs, which are the actuators of the fast power control loop (described in Section 2.1). The chain of all involved steps from power modulating the beams at the AOMs and processing of the corresponding signal to the heterodyne phase can be summarised in blocks as follows:

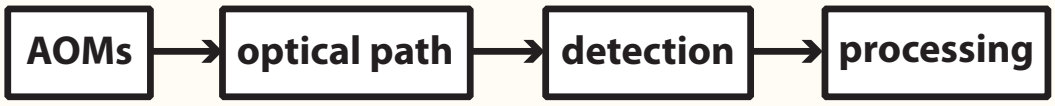

All conclusions drawn on the possibility of the coupling mechanism origin within these blocks are summarised below.

AOM

Beam pointing could have actually tilted the beam on a PD and induced a DWS signal:

- DC angles do not correlate with the effect in DWS.

→ Therefore, this leads to a disagreement with the expected leaver arm induced change in spot position.

A distortion of the beam profile could have changed the average phase on the different quadrants of the PDs.

- φ_1 couples significantly more intensively than the other angles.
- However, a beam distortion should couple alike in different interferometers with comparable beam overlap.

→ The idea is disagrees with the observations.

Optical path

Radiation pressure could have induced electrostatic compensation that coupled into a TM rotation.
Furthermore, the applied **photon impulse** to the TMs could have had a **component off the horizontal axis** and thus induced angular motion.

- However, the reference beam power modulation couples almost as strong as the measurement beam.
- Since the reference beam does not hit the TMs, it can not apply radiation pressure.

→ Obviously, radiation pressure can not be the originator of the power-to-phase coupling

Detection

The power modulation could have induced a **temperature gradient** at the PDs that possibly led to **thermal expansion** of the active detector crystal or a change of **temperature-dependent PD responsivity**.

- However, the observed immediate coupling of the step with "edges" disagrees with a temperature effect that is expected to be delayed to the change in power.
- Furthermore, the power-to-phase coupling scales with the relative modulation depth of a beam instead of the absolute modulated beam power.

→ Of course, this disagrees with a temperature-related effect that should depend on the power that was actually modulated.

Processing

A coupling of the **power modulation at the demodulation frequency.**

- A step in power gives signal at many frequencies and likely also a contribution at the heterodyne signal.

→ It should be the same for all quadrants with similar power modulation, so there should be no steps in DWS.

→ Furthermore the coupling of the power modulation should only be present during the step (as the glitch observed in longitudinal phase for the displaced TM to $\frac{\lambda}{8}$).

Quantisation noise

- The quantisation steps of a non-ideal ADC are not uniformly distributed (for details see Reference [52]).
- The "integral non-linearity" describes the assembled error of several steps (by a discrete integral of the actual deviation of two adjacent steps from the least significant bit).

→ The "integral non-linearity" could have introduced an individual power dependent error for each quadrant.

→ However, several observations disagree with quantisation noise as originator:

  – The uniformities in the steps should be randomly distributed, individually for each ADC.

  – There should be no correlation with the DWS offset phase,

  – and also no correlation with the direction of the step in power.

  – The induced error should be dependent on the absolute modulated power (the certain ADC steps) and not on the relative modulation depth of a beam.

Remaining possible coupling mechanisms:

- **Phasemeter processing:** The demodulation of the optical signal and non-linearities of the digitised signal could be relevant.
- **Pre-processing:** The normalisation of the phasemeter signals with the C-coefficients could be relevant.

All possibly relevant parameters in the path from the power modulation at the AOMs to the detection with the QPD disagree with at least one of the observed properties. Therefore in the next step, possible coupling mechanisms originating in the data processing of the phasemeter are considered.

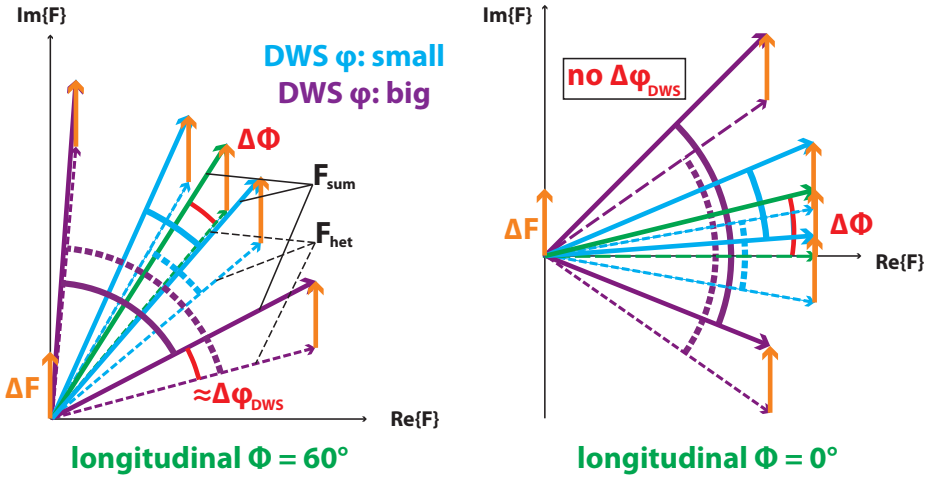

Figure 6.10.: Exemplary phasor diagram for the effect of a constant error, $\Delta\vec{F}$, on the heterodyne phase, ϕ_{het}, and the DWS phase, φ_{DWS}.

In the LPF phasemeter the data processing consists of two major steps — the demodulation of the optical signal and the normalisation in the phasemeter back-end — to retrieve the components of the complex vector $\vec{F}$ (as described in Appendix A). After the pre-processing the signals are further geometrically calibrated to TM-related quantities.

The observed power-to-phase coupling correlates with the relative beam power, such as the heterodyne amplitude.

As a consequence the question is, how a change in the heterodyne amplitude, corresponding to the length of the complex-vector $\vec{F}$, could produce an error in its phase.

Since a step in power also produces a step in phase, it is at first assumed that a constant error — depending on the power — is added in the phase read-out. A change in power should either change the error or the length of the heterodyne phase, so that the relative effect of the error increases. Such a constant error can be described with an additional constant phasor $\Delta\vec{F}$, as illustrated exemplarily by the small orange vector in Figure 6.10. The resulting vector $\vec{F}_{\mathrm{sum}} = \vec{F}_{\mathrm{het}} + \Delta\vec{F}$ is given by the superposition of the heterodyne phasor and the error phasor.

Furthermore, the DWS phase, φ_{DWS}, is illustrated by rotation of the average longitudinal phase vector, to the left and to the right, to represent the phase delays by the tilted wavefront on the sensor. Therefore, it may represent the average phase on the left and the right side of a QPD. Of course, the illustration exaggerates the phase difference between the QPD sides for clarity. It can easily be seen by the left side of Figure 6.10 (for $\phi = 60°$) that the phase error is not subtracted by the DWS signal. So the phase difference between the two rotated vectors results in a DWS phase error, $\Delta\varphi_{\mathrm{DWS}}$. It can further be seen that the resulting DWS error gets bigger for greater DWS angles, as compared by a big DWS angle in purple and a small one in cyan. A change in the relative length of the heterodyne vector or the error would therefore produce a step in the longitudinal phase and the DWS signal, depending on the DWS signal strength. This fits with the observations on DWS offset angles, summarised in Box 6.2.1. However, the resulting error would not only depend on the DWS signal strength, but also on the absolute measured phase. As illustrated to the right of Figure 6.10, with a different longitudinal phase of $\phi = 0°$ the effect on the DWS angle vanishes. This clearly disagrees with the observations for both, the longitudinal phase and the DWS signal, since the induced error is constant for different absolute measured phases and only dependent on the DWS offset angle.

Hence, the next obvious idea would be an error, having a constant phase relation with the heterodyne amplitude, as depicted in Figure 6.11. A change in the length of the error, $\Delta\vec{F}$ or the heterodyne phasor, $\vec{F}_{\mathrm{het}}$, would then lead to a change in the measured phase — independent on the average longitudinal phase. However, for this case, the DWS signal perfectly cancels the error, because of its constant phase relation with the heterodyne phase.

Therefore, no simple model of a phase error meets all observations from Box 6.2.1.

Since the effect is clearly correlated to the relative beam powers, an obvious step in data processing to look at, is the normalisation via the so-called C-coefficients, described in Appendix A.

In this step, the phasemeter output signal is normalised to 1 and a constant offset, relative to the DC power, is removed. During analysis, an abnormality was found for these coefficients: the C-coefficients differ in the fourth decimal place between real- and imaginary-part, although they should, as normalisation factors, be identical.

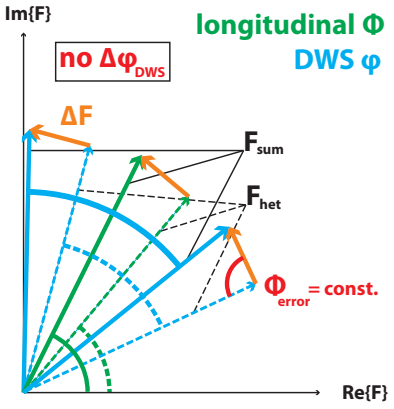

Figure 6.11.: Exemplary phasor diagram for the effect of an error, $\Delta\vec{F}$, with constant phase relation to the heterodyne phasor, $\Delta\vec{F}_{\mathrm{het}}$, on the DWS phase, φ_{DWS}.

The reason for the deviation is the sampling frequency of 50 kHz. One cycle of the heterodyne-signal is digitised with 50 samples. Surprisingly, the sum of all 50 samples in one cycle is different between a sine and a cosine wave, leading to the observed different C-coefficients. The phase difference between sine and cosine is one quarter of a full cycle, so $\frac{\pi}{2}$. Therefore, the cosine would need to be shifted by $\frac{50}{4} = 12.5$ samples to superpose with the samples of the sine wave. Hence, the sine and the cosine are sampled at different phases. Rounding of the samples to the ADC resolution then leads to different numerical errors. Also the subtraction of the DC component in the real and imaginary part is done by different scaling factors (their corresponding C-coefficients).

Therefore, the normalisation process may have introduced an error, related to the power of the heterodyne signal, by unequal scaling of the cosine and sine component or the subtraction of the DC component.

However, the investigation on that processing step could not be finished within the scope of this thesis. First analysis results show that the different scaling factors alone do not produce a significant error in the read-out. Maybe an additional non-linearity in the optical heterodyne signal, introduced by the digitalisation, could be relevant. The impact of such a non-linearity could easily be modelled as a next step. However, the relevance of the numerical errors in the normalisation coefficients remains unclear at this level of analysis.

Another possible originator for a disturbing phasor is the power modulation itself. A possible coupling of low frequency relative intensity noise is still a subject under investigation in the development of the LISA phasemeter. However, there is also a logic argument against a connection to RIN: the change in phase is constant, even after the power is stable again. A coupling of intensity fluctuations should only produce a spurious phase during the modulation. Afterwards, with stable power, the "real" phase should be measured again, which is not true for the effect observed here. Nevertheless, the results of the dedicated analysis in this topic might anyway help to solve the riddle of the power-to-phase coupling.

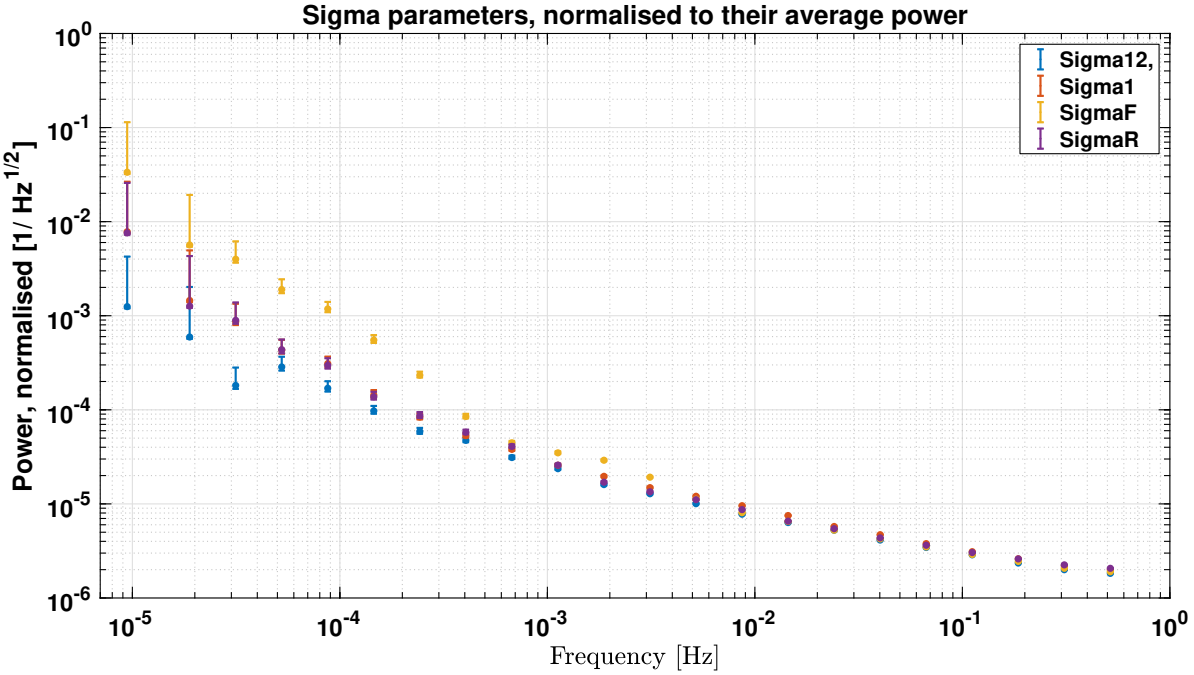

Figure 6.12.: Amplitude Spectral Density (ASD) of the RIN in all four interferometers, as during the longest LPF noise run, starting on the 13th of February in 2017.

Even though the origin of the power-to-phase coupling could only be confined, the impact of the power-to-phase coupling on the OMS performance can be estimated. For this, a simple linear extrapolation of the observed power-to-phase coupling to the RIN at low frequencies is used, since a direct coupling between laser power and phase read-out was observed. The steps from the 2 % reference beam power are used for extrapolation, because of the best available

statistics (see Table 6.1). However, it needs to be noted that the following estimation is only valid for a frequency independent linear coupling between power and phase.

The LPF differential TM acceleration noise was dominated by optical read-out noise at frequencies above 30 mHz [16]. The measured RIN at these frequencies, however, was found to be below $5 \cdot 10^{-6}/\sqrt{\text{Hz}}$, as shown exemplarily for the long February noise run, in Figure 6.12. A step in differential TM displacement was determined to be $\Delta x_{12} = (2.76 \pm 0.17)$ pm for a $\Delta\Sigma_{12} = (2.2868 \pm 0.0004)$ % step, measured in the combined beam power. A linear extrapolation down to the RIN at 30 mHz of $5 \cdot 10^{-6}/\sqrt{\text{Hz}}$ would leave a differential displacement noise below $(0.6 \pm 0.04)\,\text{fm}/\sqrt{\text{Hz}}$. The corresponding maximum step in the DWS angle was determined to be $\Delta\varphi_1 \approx (73.2 \pm 6.66)$ nrad. With the same linear extrapolation the noise can be expected to be below $(16 \pm 1.5)\,\text{prad}/\sqrt{\text{Hz}}$ at 30 mHz.
As a consequence, the power-to-phase coupling gives a negligible contribution to the OMS, when linearly extrapolated to the observed in-flight RIN [19, 53].

Therefore, it is important to mention that the described effect is important for further understanding of the noise in the phasemeter processing, but in no way limiting or relevant for its functionality.

Box 6.3.2 | Summary: Origin of power-to-phase coupling

The available amount of data is insufficient for a substantiated analysis.

→ **Therefore all deductions on a coupling mechanism stay speculative.**

Conclusions:

- The coupling is assumed to originate in the data processing of the phasemeter or phasemeter back-end.
- No simple coupling mechanism could be found that agrees with all observations listed in Box 6.2.1.
- A possible impact of a numerical error in the normalisation process of the phasemeter output could not be concluded on.
  - → Further investigation and modelling is needed.
- A possible direct coupling of low frequency relative intensity noise into the phase read-out is subject under investigation in the LISA phasemeter development.
  - – However, a direct coupling of the power modulation should be present only during the power modulation (during the step).
    - → The induced phase error in contrast is constant and therefore disagrees with the direct coupling of the power modulation.
  - → Nevertheless, the results of this dedicated analysis could possibly help to find the solution of this riddle.

Impact on OMS performance

- The effect gives a negligible contribution to the OMS noise, when linearly extrapolated to the in-flight RIN at frequencies down to 30 mHz.

Part II.

Polarisation effects on LISA Pathfinder

The long-term monitoring of the single beam powers, described in Part I, revealed unexpected low-frequency noise that turned out to be induced by the beam polarisation.
However, there was a long path from the initial observation of the low-frequency noise, to the identification of polarisation, as the relevant parameter. Since the further analysis of its origin and impact on LPF was a process with several side roads, the chronological path is described at first in Chapter 7.
The dependency of the LPF single beam powers on the beam polarisation is described in Chapter 8. The derived model could be used to estimate the power with off-nominal polarisation for the single beam power measurements.
The amount of spurious off-nominal polarisation is compared to single beam power measurements with the LPF OB, before the flight, in Chapter 9.
Furthermore, a flight spare of the relevant optical component — a polarising cube BS, defining the polarisation axis — was experimentally investigated, as described in Chapter 10.
The results implied further experiments with the spare OB at the University of Glasgow, as detailed in Chapter 12. In the last Chapter 14, the impact of the polarisation fluctuations on the LPF science measurements is investigated. Subsequent measurements with vacuum baked flight spare PBSs are detailed in Chapter 13.
An overview of the whole investigation process on polarisation for LPF is depicted in Figure6.13.

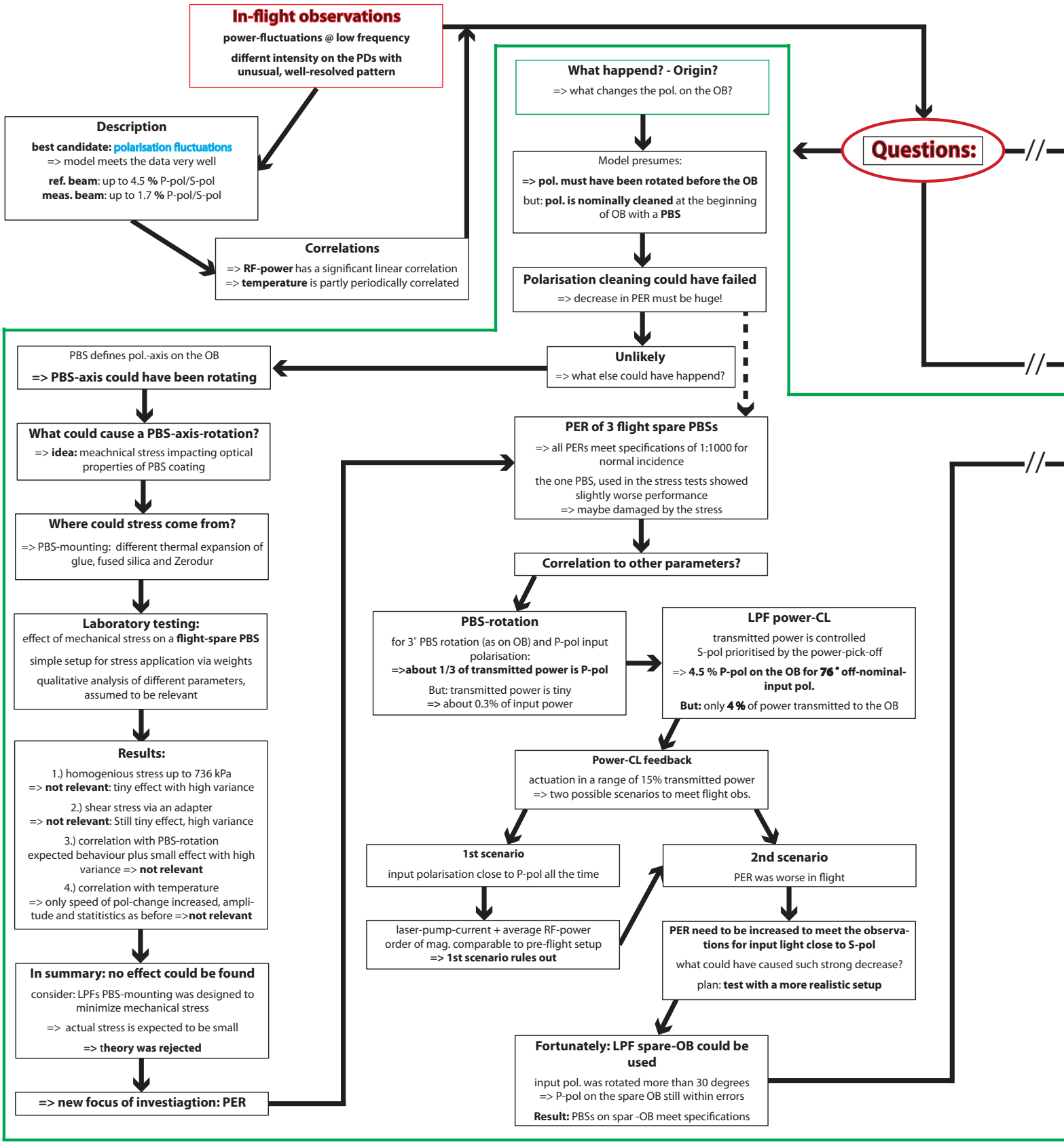

Figure 6.13.: Overview of Part II.

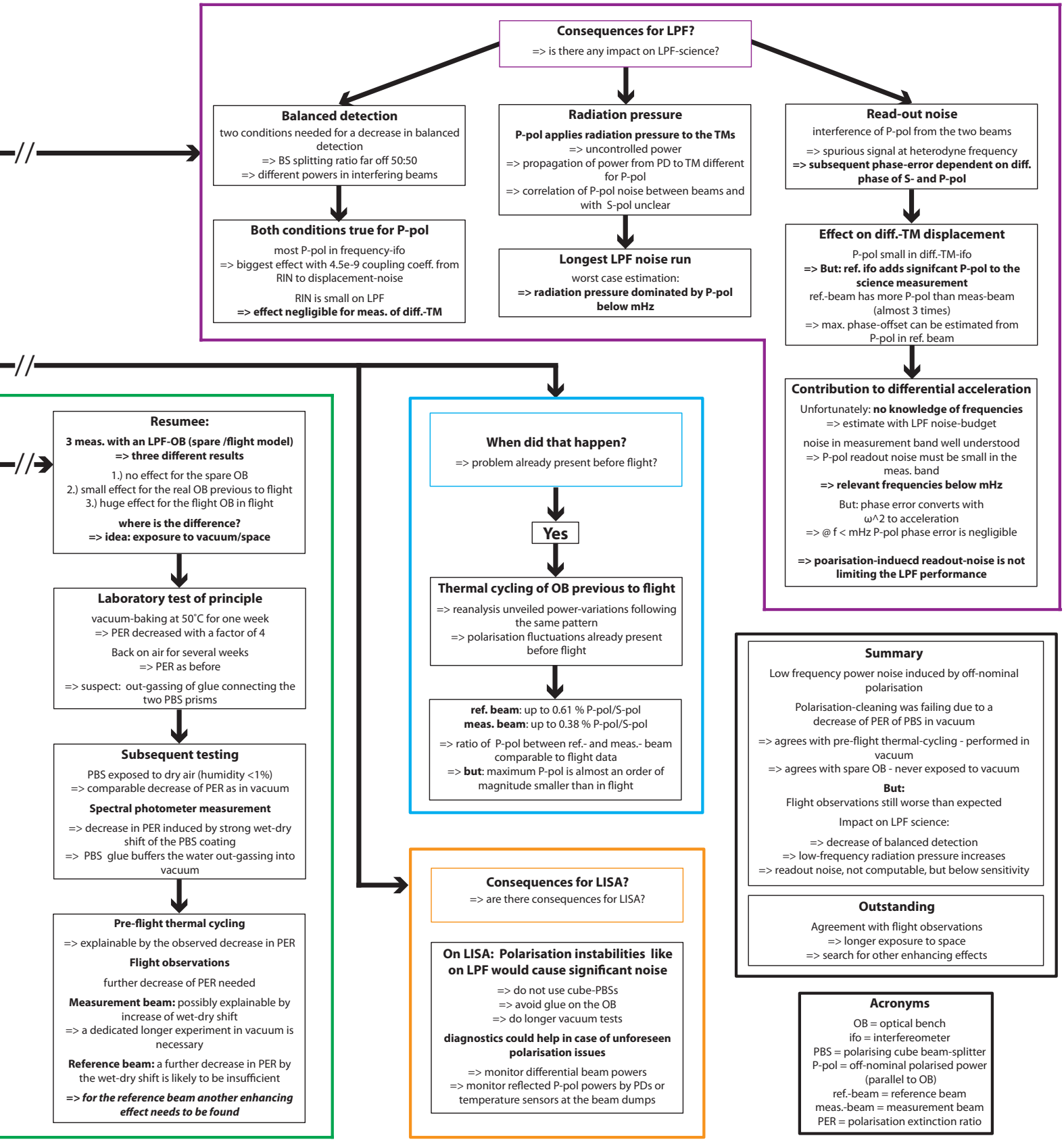
Consequences for LPF?
=> is there any impact on LPF-science?
Balanced detection
two conditions needed for a decrease in balanced detection
=> BS splitting ratio far off 50:50
=> different powers in interfering beams
Both conditions true for P-pol
most P-pol in frequency-ifo
=> biggest effect with 4.5e-9 coupling coeff. from RIN to displacement-noise
RIN is small on LPF
=> effect negligible for meas. of diff.-TM
Radiation pressure
P-pol applies radiation pressure to the TMs
=> uncontrolled power
=> propagation of power from PD to TM different for P-pol
=> correlation of P-pol noise between beams and with S-pol unclear
Longest LPF noise run
worst case estimation:
=> radiation pressure dominated by P-pol below mHz
Read-out noise
interference of P-pol from the two beams
=> spurious signal at heterodyne frequency
=> subsequent phase-error dependent on diff. phase of S- and P-pol
Effect on diff.-TM displacement
P-pol small in diff.-TM-ifo
=> But: ref. ifo adds signifcant P-pol to the science measurement
ref.-beam has more P-pol than meas-beam (almost 3 times)
=> max. phase-offset can be estimated from P-pol in ref. beam
Contribution to differential acceleration
Unfortunately: no knowledge of frequencies
=> estimate with LPF noise-budget
noise in measurement band well understood
=> P-pol readout noise must be small in the meas. band
=> relevant frequencies below mHz
But: phase error converts with ω^2 to acceleration
=> @ f < mHz P-pol phase error is negligible
=> poarisation-induecd readout-noise is not limiting the LPF performance
When did that happen?
=> problem already present before flight?
Yes
Thermal cycling of OB previous to flight
=> reanalysis unveiled power-variations following the same pattern
=> polarisation fluctuations already present before flight
ref. beam: up to 0.61 % P-pol/S-pol
meas. beam: up to 0.38 % P-pol/S-pol
=> ratio of P-pol between ref.- and meas.- beam comparable to flight data
=> but: maximum P-pol is almost an order of magnitude smaller than in flight
Resumee:
3 meas. with an LPF-OB (spare /flight model)
=> three different results
1.) no effect for the spare OB
2.) small effect for the real OB previous to flight
3.) huge effect for the flight OB in flight
where is the difference?
=> idea: exposure to vacuum/space
Laboratory test of principle
vacuum-baking at 50°C for one week
=> PER decreased with a factor of 4
Back on air for several weeks
=> PER as before
=> suspect: out-gassing of glue connecting the two PBS prisms
Subsequent testing
PBS exposed to dry air (humidity <1%)
=> comparable decrease of PER as in vacuum
Spectral photometer measurement
=> decrease in PER induced by strong wet-dry shift of the PBS coating
=> PBS glue buffers the water out-gassing into vacuum
Pre-flight thermal cycling
=> explainable by the observed decrease in PER
Flight observations
further decrease of PER needed
Measurement beam: possibly explainable by increase of wet-dry shift
=> a dedicated longer experiment in vacuum is necessary
Reference beam: a further decrease in PER by the wet-dry shift is likely to be insufficient
=> for the reference beam another enhancing effect needs to be found
Consequences for LISA?
=> are there consequences for LISA?
On LISA: Polarisation instabilities like on LPF would cause significant noise
=> do not use cube-PBSs
=> avoid glue on the OB
=> do longer vacuum tests
diagnostics could help in case of unforeseen polarisation issues
=> monitor differential beam powers
=> monitor reflected P-pol powers by PDs or temperature sensors at the beam dumps
Summary
Low frequency power noise induced by off-nominal polarisation
Polarisation-cleaning was failing due to a decrease of PER of PBS in vacuum
=> agrees with pre-flight thermal-cycling - performed in vacuum
=> agrees with spare OB - never exposed to vacuum
But:
Flight observations still worse than expected
Impact on LPF science:
=> decrease of balanced detection
=> low-frequency radiation pressure increases
=> readout noise, not computable, but below sensitivity
Outstanding
Agreement with flight observations
=> longer exposure to space
=> search for other enhancing effects
Acronyms
OB = optical bench
ifo = interfereometer
PBS = polarising cube beam-splitter
P-pol = off-nominal polarised power (parallel to OB)
ref.-beam = reference beam
meas.-beam = measurement beam
PER = polarisation extinction ratio

7. In-flight observation of low-frequency power noise: Chronological path to the polarisation theory

In the beginning of LPF operations, the investigation of single beam power measurements — already executed a few times — was analysed as planned (described in Chapter 3), to determine the TM reflectivity. Surprisingly, the results appeared to show big fluctuations in TM reflectivity. A cross-check with the redundant data set, given by the power in the frequency interferometer, showed even higher fluctuations. So, obviously the measured changes could not be induced by the TM reflectivity. What first appeared as the measurement parameter, seemed to be a spurious noise with different strengths in the different interferometers, spoiling the measurement of TM reflectivity.

Nevertheless, as more single beam power data measurements were collected in the proceeding mission, a specific pattern became clear: for the reference beam, the A diode of each interferometer measures more noise than the B diode; for the measurement beam the opposite is true. This behaviour clearly points to the recombination BS and therefore led to rejection of several theories concerning a correlation with the photodiodes.
Since it seemed to be important if a beam was reflected at a BS or transmitted through it, the beam polarisation was already suspected as a relevant parameter in the very beginning. However, on LPF the polarisation is cleaned by a polarising cube BS (a PBS) at the front of the OB. This should eliminate almost all incident polarisation impurities. Therefore, the idea was rejected soon and replaced by a more established problem: The known presence of ghost beams that are generated by inner reflections in the BSs. They could have caused extra power noise at the different PDs.

As the mission proceeded, more and more measurements were collected and the pattern got clearer and more complex. Not only did the A and B diodes show a regular behaviour, but also the four interferometers showed a constant intensity distribution. The surprising detail was that the distribution of noise power between the four interferometers was about the same for the two beams, although their noise time series were different and their A and B diodes showed inverted behaviour.

Figure 7.1 shows all measurements taken during flight of LPF. Each data point was normalised to the average of all power measurements at that particular diode. Therefore, the size of the error bars scales with the error of the computed average (propagated to the normalised powers). Clearly, the noise is different between the two beams and splits up into four different levels. The fluctuating power in the reference beam is about three times higher than for the measurement beam. The pattern is described in Box 7.0.1.

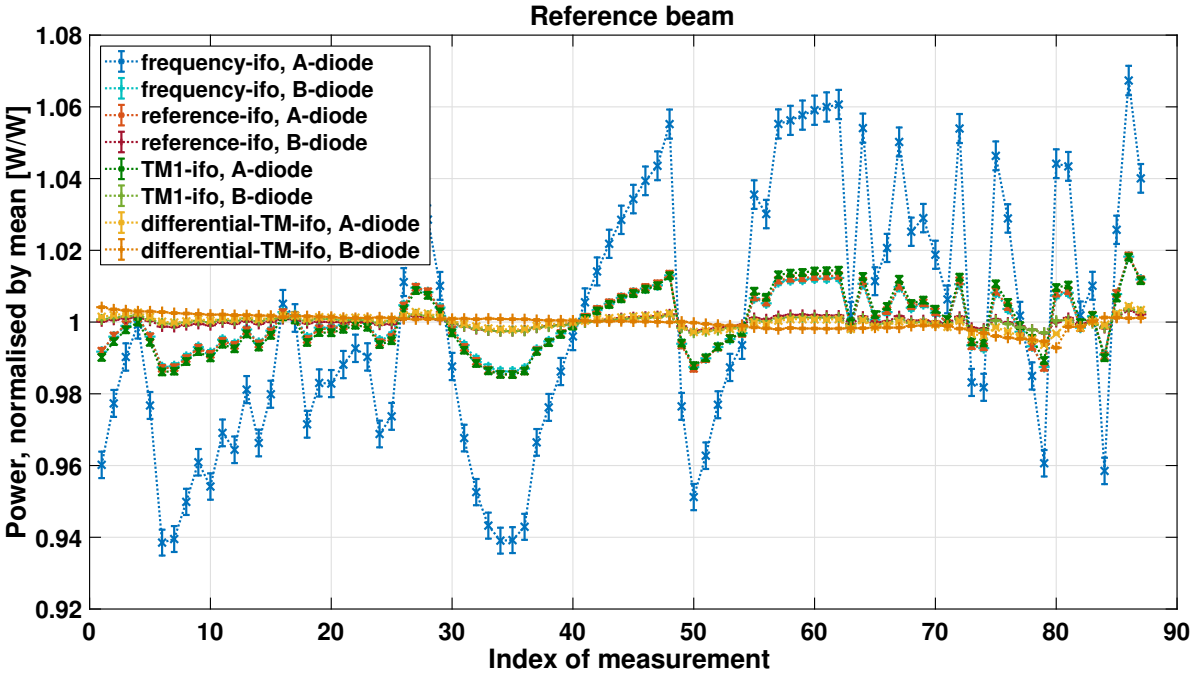

10pt

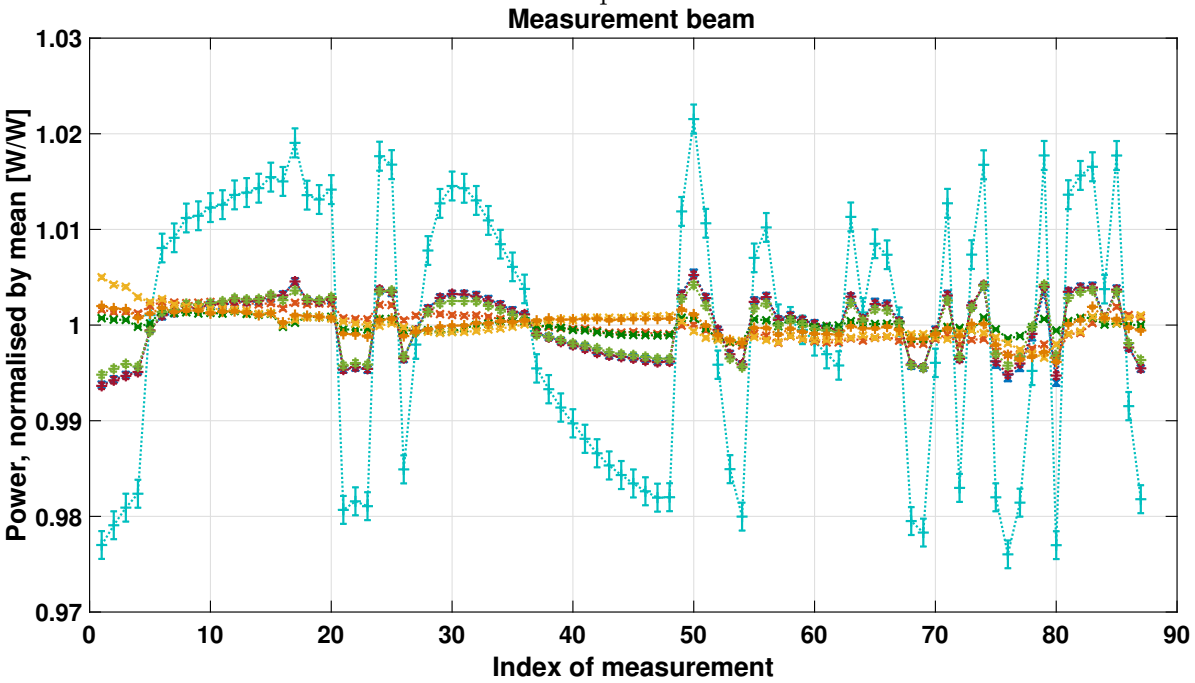

Figure 7.1.: Single beam power measurements (DC parameters), normalised by the average of the particular diode. Instead of time, the index of measurement is used (see Figure 4.1).

Box 7.0.1: Pattern of noise distribution

Reference beam:

- The frequency interferometer A diode has the highest noise power.
- The frequency interferometer B diode, the reference interferometer A diode and the x1 interferometer A diode share the next highest power level.
- The reference interferometer B diode, the x1 interferometer B diode and the x12 interferometer A diode share the second lowest power level.
- The x12 interferometer B diode seems to be unaffected by the noise.

Measurement beam:

- The frequency interferometer B diode has the highest noise power.
- The frequency interferometer A diode, the reference interferometer B diode and the x1 interferometer B diode share the next highest power level.
- The reference interferometer A diode, the x1 interferometer A diode and the x12 interferometer B diode, share the second lowest power level.
- The x12 interferometer A diode seems to be unaffected by the noise.

The unusual, but well-resolved pattern allowed the rejection of most of the theories that came up in between, just by simple logic. A partly periodic correlation to temperature led to an expansion of the ghost beam theory by an interferometric component. The temperature could have induced changes of the optical path-length in a BS, impacting on the interference of a ghost beam with the nominal beam.

Besides, all components and coatings on the OB were checked for a correlation with the power distribution of the noise. Exclusively the number of transmissions through 50:50 BS was found to fit the pattern. Therefore, the interference conditions in such a coating were checked. It turned out that the thermally induced change in optical path-length is smaller than needed for at least one period of interferometric signal in the observed temperature range.

Collecting all findings and presenting them to the Albert Einstein Institut (AEI) research group led to the final hint. A colleague brought up knowledge about a different splitting ratio of the OB BS for parallel polarised light (special thanks go to Soenke Schuster) that could fit the observed pattern. So, the theory of polarisation fluctuations, rejected at the very beginning, came up again. Light with parallel polarisation would be split differently at each BS, leading to a different power distribution in the four interferometers — correlated to the number of BS transmissions. Already some numbers for typical 50:50 BS matched the observations in amplitude very well and the further analysis reinforced the theory at each step.

Therefore, finally the polarisation could be identified as the origin of the low-frequency power noise on LPF. With a model for the polarisation-dependent power, detected at the PDs, the share of parallel polarisation at the beginning of the OB was derived to be 4.5 %, at most. However, this also raised the question, why the polarisation cleaning was failing.

As already mentioned, the polarisation axis is defined by a PBS at the beginning of the OB. But what could have happened to it so that such a great amount of parallel polarised light is detected on the OB? The first idea was parallel polarised light coming out of the fibre being transmitted through the PBS. However, with a typical PBS extinction ratio of 1 to 1000, its degradation must have been unrealistically huge and the input polarisation far off-nominal. In consequence, the theory was rejected and a second one was followed: Temperature dependent mechanical stress at the PBS inducing a tilt of its optical axis. The experimental investigation of this theory is described in Section 10. The results show only a small impact of stress on the parallel polarised transmission, not able to explain the observations during flight.

Hence, the extinction ratio of the PBS came into focus again, as described in the second part of Section 10. Furthermore, the effect of the power control-loop and a rotation of the PBS around its vertical axis on the transmitted parallel polarised power were considered. However, still no effect strong enough to explain the LPF observations could be found.

The analysis of data from pre-flight thermal tests showed that even before flight there was more parallel polarised power transmitted to the OB, than expected. The transmitted off-nominal polarised power is about seven times smaller than in-flight, but also about five times stronger than measured for flight-spare PBSs. However, what could have caused the difference between the experiment on ground and the observations during flight? In the pre-flight tests the OB was moved into a vacuum chamber and then thermally cycled in a range of 50 °C around room temperature. So the thermal and environmental conditions were comparable to the measurements taken during flight. However, the input-polarisation could have been different.

The power CL feedback during LPF flight shows actuation in a range of 15 %. This 15 % power could be a compensation for off-nominal polarised light, being reflected at the PBS. In the pre-flight thermal tests, the detected power is fluctuating by more than 30 %. As for the in-flight setup, there is no measurement of the rejected power at the PBS. So it stays unclear, if the input polarisation is comparable between ground and flight.

The best idea at that time was still that mechanical stress in the PBS induced the high transmission of parallel polarisation. The next step therefore was an improvement of the setup, closer to the actual OB. Ideally, the most similar setup — the spare OB — could be investigated in cooperation with the University of Glasgow.

Surprisingly, in contrast to the expectations, no effect could be observed — the PBSs at the spare OB clean the input polarisation exactly as they should. This finding lead to the rejection of all previous theories based on the way the PBSs are mounted.

However, having a measurement with a third setup allowed to reconsider the question, where the difference between the three setups was — the OB in-flight, the OB during thermal tests and the spare OB in the Glasgow laboratory? Since the two OBs are identically constructed, the only difference between the three measurements is the environment. The spare OB was tested in a dedicated travel container in air, for the thermal tests, the flight OB was placed into vacuum for thermal testing and during flight, it was exposed to the spacecraft environment for several months. Therefore, the measured parallel polarised power in the interferometers corresponds to the duration of exposure to vacuum. So maybe, out-gassing could be responsible for the observed decrease in purity of the PBS output polarisation.

As a consequence, another laboratory test was performed: One PBS was vacuum baked at 50 °C for more than two weeks, while another one was stored in dry air. Both PBSs showed a decrease of their extinction ratio up to a factor of 4.8. Obviously, out-gassing of water is responsible for this decrease. A spectral analysis of the PBS transmission showed a strong wet-dry shift of the optical properties, which further supported the hypothesis.

The measured decrease in Polarisation Extinction Ratios (PERs) for the dried PBS already explained the observed off-nominal polarised power during the thermal tests previous to flight. However, the in-flight fluctuations are still higher by at least an order of magnitude.
Therefore, a possible further decrease needs to be investigated with a longer experiment. Such a long experiment was out of scope for this thesis. So it is still possible that another unidentified effect enhances the off-nominal polarised power on the OB during the flight of LPF.

The observations, experiments and analysis are described with more detail in the following Chapters 8 to 13.

8. Description of the Optical Bench power measurements considering polarisation

LPF has no detectors sensitive to polarisation. However, the optical properties of some OB components are strongly dependent on it. Therefore, in the following a model of the OB is derived, to retrieve information about the in-flight polarisation state.
The splitting ratio of the 50:50 BSs differs a lot for light offset from their designated polarisation. For light, orthogonal polarised to the nominal one, much more power is transmitted with a splitting ratio of about 20:80. This leads to a distribution of power on the OB, strongly dependent on polarisation. Using the OB layout, on the one hand allows to compute the power distribution for a given polarisation. On the other hand, information about the polarisation can also be retrieved from the power measurements. However, the phase relation between orthogonal and parallel polarised light has no impact on the splitting at the BSs. Therefore, it can not be retrieved from the measured powers alone. Accordingly, only the projected power onto the orthogonal and parallel polarisation axes are computable by the measured power, without any information about ellipticity or the degree of polarisation.

To derive the associated equation, the terms orthogonal and parallel polarisation need to be defined globally to avoid coordinate transformations for rotated components (like the PBS, reflecting light out of the plane). For simplicity and comparability, the LPF nomenclature is used: the Power with Orthogonal Polarisation (S-pol) is defined to oscillate orthogonal to the OB surface, the Power with Parallel Polarisation (P-pol) is oscillating parallel to the OB as can be seen in Figure 8.1).

For a beam m, with orthogonal and parallel polarised power $P_m^{\perp}$ and $P_m^{\parallel}$, the detected power $\mathrm{DC}_{ij,m}$ at a QPD with responsivity η_{ij} (with i referring to the interferometer and j to the index A or B diode), on the LPF OB can generally be written as:

$$\mathrm{DC}_{ij,m} \cdot \mathrm{c_{DC}} = (P_m^{\perp} \cdot \lambda_{ij,m}^{\perp} + P_m^{\parallel} \cdot \lambda_{ij,m}^{\parallel}) \cdot \eta_{ij} \,. \tag{8.1}$$

Here, the constant factor $\mathrm{c_{DC}} = \frac{\mathrm{U_{ADC}}}{\mathrm{R_{TI}}}$ converts the ADC scaled voltage back to photocurrent.

The polarisation-dependent variables $\lambda_{ij,m}^{\perp}$ and $\lambda_{ij,m}^{\parallel}$ describe the part of the beam m, being transmitted to QPD ij. Therefore, it accounts for the polarisation-dependent reflectance $R^{\perp}$ and $R^{\parallel}$ and transmissivity $T^{\perp}$ and $T^{\parallel}$ of the OB components and remaining losses L_{ij} in the particular beam path for example at anti-reflection coatings. The LPF OB beam paths consist of BSs, mirrors, TMs and optical windows. The corresponding coefficient can therefore exemplarily be written for parallel polarisation by Equation 8.2:

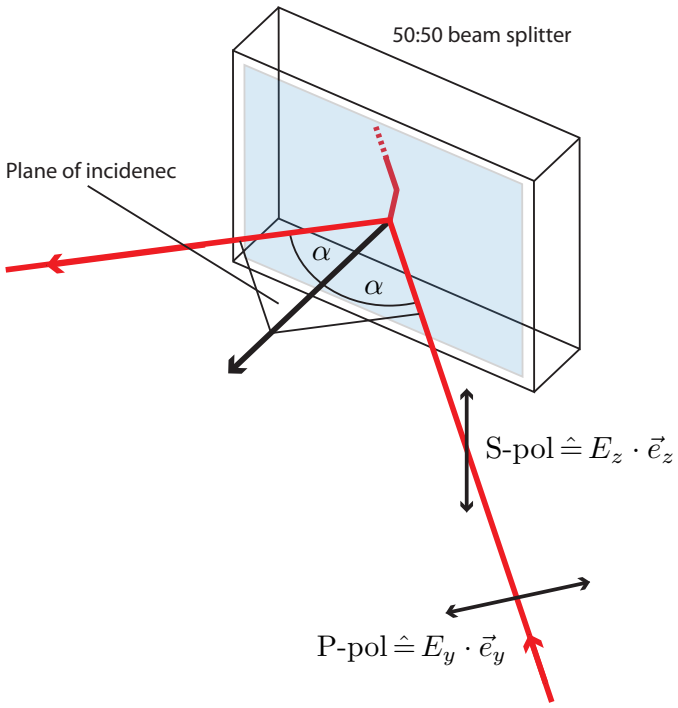

Figure 8.1.: Beam-incidence to a BS on the OB of LPF. The OB plane defines S-pol and P-pol as orthogonal and parallel polarised towards its surface.

$$\begin{aligned}\lambda^{\parallel}_{ij,m} =& R^{\parallel}_{\mathrm{BS}}{}^{\mathrm{N_{BS,R}}} \cdot T^{\parallel}_{\mathrm{BS}}{}^{\mathrm{N_{BS,T}}} \\ & \cdot R^{\parallel}_{\mathrm{M}}{}^{\mathrm{N_M}} \cdot R^{\parallel}_{\mathrm{TM}}{}^{\mathrm{N_{TM}}} \cdot T^{\mathrm{N_{OW}}}_{\mathrm{OW}} \cdot (1 - L_{ij})\,,\end{aligned} \tag{8.2}$$

where the index BS refers to the Beam Splitters, M to the mirrors, TM to the Test Masses and OW to the optical windows. The exponent N_i describes the number of reflections or transmissions at, or through, the type of component in the particular beam path. Some OB components are mounted with an offset angle to the nominal 45°, due to design reasons (for the narrow angle of incidence of 4.5° to the TMs). Since the reflectivity and transmissivity at a surface generally depend on the angle of incident (compare with the Fresnel formulas in Reference [25], page 234 and following), Equation 8.2 needs to be expanded for the angle of the particular component (as described in the following, see Equation 8.12).

In total, there are 8 different PDs with two different beam paths for the two different beams, resulting in 16 equations, corresponding to the 16 power-measurements on LPF. The full set of the propagation factors is listed in Appendix B.

8.1. Deducing a model for the orthogonal and parallel polarised input power

During flight of LPF the full set of single beam powers on all QPDs was measured 87 times (see Chapter 4).

To deduce a model for a fit to this data set from Equation 8.1, some general thoughts need to be included, first.

The desired main result of the fit is the power in parallel and orthogonal polarisation, for each of the 87 single beam power data sets. The polarisation on LPF itself is not actively controlled. Since the measurement dates are temporally separated by at least one hour (compare to Figure 4.1) the fluctuations in polarisation are assumed to be uncorrelated between the individual investigations. This allows the treatment of P-pol and S-pol as individual parameters for each sample in the fit:

- The polarisation on LPF is not actively controlled,
- and there is no correlation of theS-pol and P-pol between the different measurements, but the power control action.

→ **Therefore, the P-pol and S-pol can be fit as an individual variable for each measurement sample.**

Furthermore, the optical properties of the OB components are assumed to be constant in time and global to the fit. For simplicity, deviations from manufacturing are neglected, so that only the average optical property (without tolerance) for a special type of component is fit (for example the average reflectivity of a BS for parallel polarised light). That is:

- The optical properties of the OB components are time-independent,
- and all samples of the same kind have identical optical properties.

→ **Therefore, the properties of the components are global variables to the fit.**

Applying these assumptions to Equation 8.1 leads to the following representation 8.3, with sample index k:

$$\mathrm{DC}_{ij,m}(k) \cdot \mathrm{c}_{\mathrm{DC}} = \left(P_m^{\perp}(k) \cdot \lambda_{ij,m}^{\perp} + P_m^{\parallel}(k) \cdot \lambda_{ij,m}^{\parallel} \right) \cdot \eta_{ij} \,. \tag{8.3}$$

The colours represent the type of parameter in the fit:
Magenta-coloured parameters, carrying the index k, are fit individually for each of the 87 samples. The colour petrol indicates a parameter that is different for each beam and photodiode (index ij, m), but constant for the different samples k. The orange parameter is furthermore constant for the two beams m and only different for the 8 QPDs, ij.
In the following, global parameters are also used and coloured in cyan. These are global to the fit or at most, differ between the two beams with index m.

Obviously, Equation 8.3 cannot be used to fit the data set yet, since the parameters are strongly linearly dependent. Furthermore, there are other variables driving the measured power, which

are not yet accounted for by the model, such as the environmental temperature or the impact of power control.

Therefore, in the following, the raw model from Equation 8.3 is expanded to be more accurate and explicit, so that the S-pol and P-pol are unambiguously defined for each sample.
At first, the impact of temperature on the PD responsivity is included. Next, the impact of the power control loop is modelled adequately. In the end, the polarisation-dependent properties of some OB components and the linear dependency of losses in the beam path and PD responsivity are simplified. Furthermore, the minimum P-pol had to be estimated separately to break the intrinsic linear dependency of PD responsivity and losses in the beam path with the optical power. The full model is written in Equation 8.18.

Afterwards, the results of the fit to the LPF data set are presented and discussed in Section 8.2 and the corresponding errors to the fit are estimated in Section 8.3.

8.1.1. Temperature dependency of PDs

The measurements were taken at different temperatures covering a range of more than 20 °C. Hence, the temperature dependency of the PD responsivity also needs to be taken into account. In the range from 0 °C to 25 °C a linear dependency between temperature and responsivity can be assumed. Equation 8.3 therefore can be expanded with

$$\eta_{ij} \rightarrow \eta_{ij}^{0} - \eta_{ij}^{T} \cdot T_{\mathrm{OB}}(k) \tag{8.4}$$

to:

$$\begin{aligned} \mathrm{DC}_{ij,m}(k) \cdot \mathrm{c}_{\mathrm{DC}} = &\left(P_{m}^{\perp}(k) \cdot \lambda_{ij,m}^{\perp} + P_{m}^{\parallel}(k) \cdot \lambda_{ij,m}^{\parallel} \right) \\ &\cdot \left(\eta_{ij}^{0} - \eta_{ij}^{T} \cdot T_{\mathrm{OB}}(k) \right) , \end{aligned} \tag{8.5}$$

with an average responsivity, η_{ij}^{0}, and a coefficient, η_{ij}^{T}, for the linear dependency on temperature of a particular diode.

The detectors of the power control loops are temperature-dependent PDs as well. Therefore, the factor η_{ij}^{T} describes the difference in temperature-dependence of a particular QPD, to the one of the power control loop monitor diodes:

$$\eta_{ij}^{T} = \frac{\mathrm{d}(\eta_{i})}{\mathrm{d}T} - \frac{\mathrm{d}(\eta_{\text{pwr-CL}})}{\mathrm{d}T} . \tag{8.6}$$

The other OB components are assumed to be stable, due to the negligible impact of temperature on their bulk material (fused silica) and the tiny thickness of their optical layers. A possible linear dependency of temperature on any other OB component would be fit as part of the parameter η_{ij}^{T}.

8.1.2. Integration of power control

The LPF power CL controls the power that is reflected at an uncoated BS (compare to Section 2.1 and 2.2). Using Fresnel Formulas (Reference [25], page 234 and following) allows to compute the reflectivity of the power pick-off. For the bulk material — fused silica — the wavelength of 1064 nm and an angle of incidence of 45°, the reflectivity determines to $R_{\mathrm{fs}}^{\perp} \approx 0.07867$ for orthogonal and $R_{\mathrm{fs}}^{\parallel} \approx 0.00619$ for parallel polarised light. Hence, P-pol is highly discriminated by the pick-off.

The fast power control loop was designed to have significant gain at the heterodyne frequency, 1 kHz, but also has sufficient gain in the LPF measurement band down to 1 mHz to stabilise the DC power around the set-point. This is supported by the fact that during the 87 individual investigations (which span more than a year) the in-loop power monitor diode current varied by less than 0.05 % (each investigation is the average of a five-minute-long time series).

Since the set-point was not changed in between the individual 87 measurements, the effect of the control loop can be written as:

$$\mathrm{C}_m = P_m^{\perp}(k) \cdot R_{\mathrm{fs}}^{\perp} + P_m^{\parallel}(k) \cdot R_{\mathrm{fs}}^{\parallel}\,, \tag{8.7}$$

with a constant control point of C_m for the particular beam.

Rearranging of Equation 8.7 gives the power in S-pol $P_m^{\perp}(k)$, regarding the power CL:

$$P_m^{\perp}(k) = \left(\mathrm{C}_m - P_m^{\parallel}(k) \cdot R_{\mathrm{fs}}^{\parallel}\right) \cdot R_{\mathrm{fs}}^{\perp\,-1}\,. \tag{8.8}$$

With Equation 8.8 the effect of the power control loop can be applied to Equation 8.5:

$$\begin{aligned}\mathrm{DC}_{ij,m}(k) \cdot \mathrm{c}_{\mathrm{DC}} = \Big(\Big(\mathrm{C}_m - P_m^{\parallel}(k) \cdot R_{\mathrm{fs}}^{\parallel}\Big) \cdot R_{\mathrm{fs}}^{\perp\,-1} \cdot \lambda_{ij,m}^{\perp} \\ + P_m^{\parallel}(k) \cdot \lambda_{ij,m}^{\parallel}\Big) \cdot \Big(\eta_{ij}^{0} - \eta_{ij}^{T} \cdot T_{\mathrm{OB}}(k)\Big)\,.\end{aligned} \tag{8.9}$$

8.1.3. Simplifications for the description of losses at the OB components

For simplicity, we neglect the polarisation-dependent reflectivity of the mirrors and the remaining reflection at the coating on the backside of a BS, which intentionally minimises the reflection at that surface. Both are designed to be very small, so that their difference for the two polarisations is even smaller.
Due to the almost normal angle of incidence, the reflection at TMs and the Optical Window (OW) transmission are also assumed to be polarisation independent. For 0° incidence the difference in optical properties for S-pol and P-pol vanishes, since both are parallel to the surface (this can also be seen by the Fresnel formulas, Reference [25], page 234 and following). Furthermore, the 50:50 coating of the BSs is assumed to be lossless, so that: $T_{\mathrm{BS}}^{\perp} + R_{\mathrm{BS}}^{\parallel} = 1$.

Applied to the polarisation-dependent transmission coefficients $\lambda_{ij,m}^{\parallel}$ and $\lambda_{ij,m}^{\perp}$ for the particular beam paths, Equation 8.2 reduces to:

$$\lambda^{\parallel}_{ij,m} \rightarrow \lambda^{\text{red}\ \parallel}_{ij,m} = {T^{\parallel}_{\text{BS}}}^{\text{N}_{\text{BS-T}}} \cdot \left(1 - T^{\parallel}_{\text{BS}}\right)^{\text{N}_{\text{BS-R}}} \cdot (1 - L_{ij,m}) \tag{8.10}$$

$$\lambda^{\perp}_{ij,m} \rightarrow \lambda^{\text{red}\ \perp}_{ij,m} = {T^{\perp}_{\text{BS}}}^{\text{N}_{\text{BS-T}}} \cdot \left(1 - T^{\perp}_{\text{BS}}\right)^{\text{N}_{\text{BS-R}}} \cdot (1 - L_{ij,m})\ , \tag{8.11}$$

with polarisation independent losses $L_{ij,m} = L_M \cdot L_{AR} \cdot L_{TM} \cdot L_{OW}$. As noted in the previous section, the angle of incidence also needs to be included. This enlarges Equation 8.11, exemplarily for P-pol, to:

$$\begin{aligned} \lambda^{\text{red}\ \parallel}_{ij,m} = {T^{\parallel}_{\text{BS}-45^\circ}}^{\text{N}_{\text{BS45, T}}} \cdot \left(1 - T^{\parallel}_{\text{BS}-45^\circ}\right)^{\text{N}_{\text{BS45, R}}} \\ {T^{\parallel}_{\text{BS}-43^\circ}}^{\text{N}_{\text{BS43, T}}} \cdot \left(1 - T^{\parallel}_{\text{BS}-43^\circ}\right)^{\text{N}_{\text{BS43, R}}} \\ {T^{\parallel}_{\text{BS}-47^\circ}}^{\text{N}_{\text{BS47, T}}} \cdot \left(1 - T^{\parallel}_{\text{BS}-47^\circ}\right)^{\text{N}_{\text{BS47, R}}} \\ \cdot (1 - L_{ij,m})\ . \end{aligned} \tag{8.12}$$

Note that the angles in the indices are rounded to degrees for simplicity. The exact angles of incidence are $42.75^\circ \approx 43^\circ$ and $47.25^\circ \approx 47^\circ$.

The reduced losses can be applied to Equation 8.9:

$$\begin{aligned} \text{DC}_{ij,m}(k) \cdot \text{c}_{\text{DC}} = \Big(\Big(\text{C}_m - P^{\parallel}_m(k) \cdot R^{\parallel}_{\text{fs}} \Big) \cdot {R^{\perp}_{\text{fs}}}^{-1} \cdot \lambda^{\text{red}\ \perp}_{ij,m} \\ + P^{\parallel}_m(k) \cdot \lambda^{\text{red}\ \parallel}_{ij,m} \Big) \cdot \left(\eta^0_{ij} - \eta^T_{ij} \cdot T_{\text{OB}}(k) \right)\ . \end{aligned} \tag{8.13}$$

8.1.4. Remove the linear dependency of PD responsivity and losses

The representation of the model in Equation 8.13 obviously still has linear dependencies of power, losses $\lambda_{ij,m}$ and PD responsivity η^0_{ij}. This is physically reasonable, since a decrease in detected power on a photodiode could have been induced by a decrease in input power, an increase of the losses in the beam path or a decrease in responsivity.

At first, the ambiguity of losses and PD responsivity is removed. The simplest solution is to fit the two parameters as one combined parameter:

$$\eta_{ij} \cdot (1 - L_{ij,m}) \rightarrow \eta\lambda_{ij,m} \tag{8.14}$$

$$\left(\eta^0_{ij} - \eta^T_{ij} \cdot T_{\text{OB}}(k) \right) \cdot (1 - L_{ij,m}) \rightarrow (\eta\lambda)^0_{ij,m} - (\eta\lambda)^T_{ij,m} \cdot T_{\text{OB}}(k)\,. \tag{8.15}$$

Next, the linear dependency of the combined parameter $(\eta\lambda)^0_{ij,m}$ with the power needs to be fixed.
The most appropriate solution would be to use the PD responsivities, determined during flight, as described in Chapter 5. However, the responsivities are only known for the virtually combined photodiode $\eta = \eta_{\text{A}} + \eta_{\text{B}}$. Hence, only the sum of A and B diode could be fit with these parameters.
Another option can be found analogously to the one used for the combined losses parameter. The PD responsivities can be fit relative to one channel. The photodiode of this channel then acts as a "reference diode", which all other channels are compared to. To do so, the power and responsivity of the desired reference diode are fit as a combined parameter, so that linear

dependency in the fit is avoided. Since the beam consists of S-pol and P-pol, η_{FA} was chosen as the reference diode for the reference beam and η_{FB} for the measurement beam. Their channels have the highest P-pol for the particular beam, whereby the orthogonal polarised one is comparably high on all diodes. Therefore, the chosen reference diodes give the best restriction in power to both polarisations.

The combined PD responsivity plus losses parameter for the reference beam is therefore given by:

$$(\eta\lambda)^0_{ij,m} \to \frac{(\eta\lambda)^0_{ij,m}}{(\eta\lambda)^0_{\mathrm{FA,\ RB}}} \qquad \text{and} \qquad (\eta\lambda)^T_{ij,m} \to \frac{(\eta\lambda)^T_{i}}{(\eta\lambda)^T_{\mathrm{FA,\ RB}}} \tag{8.16}$$

and for the measurement beam by:

$$(\eta\lambda)^0_{ij,m} \to \frac{(\eta\lambda)^0_{ij,m}}{(\eta\lambda)^0_{\mathrm{FB,\ MB}}} \qquad \text{and} \qquad (\eta\lambda)^T_{ij,m} \to \frac{(\eta\lambda)^T_{ij,m}}{(\eta\lambda)^T_{\mathrm{FB,\ MB}}}\,. \tag{8.17}$$

The last ambiguity to care about is due to offsets of power in parallel polarisation. An offset in P-pol is indistinguishable from spurious losses in the particular beam paths, following the pattern of P-pol distribution on the OB. Hence, only variations in power (distributed like parallel polarised light) are explicitly identifiable in the fit. Fortunately, the difference of A and B diode in one interferometer allows to draw conclusions to the minimum measured power in parallel polarisation. These offsets can therefore be estimated separately to fully restrict the fit. The derivations for the offset powers are described in Appendix C.1.

8.1.5. The full model

Applying all derived modifications from Equation 8.5, 8.9, 8.13, 8.16 and 8.17 to the model 8.3, gives the full model:

$$\begin{aligned}
\mathrm{DC}_{ij,m}(k)\cdot \mathrm{c_{DC}} = \Bigg(& \Big(\mathrm{C}_m - P^{\parallel}_m(k)\cdot R^{\parallel}_{\mathrm{fs}} \Big)\cdot {R^{\perp}_{\mathrm{fs}}}^{-1}\cdot {T^{\perp}_{\mathrm{BS}-45^\circ}}^{\mathrm{N_{BS45,\ T}}}\cdot \Big(1-T^{\perp}_{\mathrm{BS}-45^\circ}\Big)^{\mathrm{N_{BS45,\ R}}} \\
& \cdot {T^{\perp}_{\mathrm{BS}-43^\circ}}^{\mathrm{N_{BS43,\ T}}}\cdot \Big(1-T^{\perp}_{\mathrm{BS}-43^\circ}\Big)^{\mathrm{N_{BS43,\ R}}}\cdot {T^{\perp}_{\mathrm{BS}-47^\circ}}^{\mathrm{N_{BS47,\ T}}}\cdot \Big(1-T^{\perp}_{\mathrm{BS}-47^\circ}\Big)^{\mathrm{N_{BS47,\ R}}} \\
& + P^{\parallel}_m(k)\cdot {T^{\parallel}_{\mathrm{BS}-45^\circ}}^{\mathrm{N_{BS45,\ T}}}\cdot \Big(1-T^{\parallel}_{\mathrm{BS}-45^\circ}\Big)^{\mathrm{N_{BS45,\ R}}} \\
& \cdot {T^{\parallel}_{\mathrm{BS}-43^\circ}}^{\mathrm{N_{BS43,\ T}}}\cdot \Big(1-T^{\parallel}_{\mathrm{BS}-43^\circ}\Big)^{\mathrm{N_{BS43,\ R}}}\cdot {T^{\parallel}_{\mathrm{BS}-47^\circ}}^{\mathrm{N_{BS47,\ T}}}\cdot \Big(1-T^{\parallel}_{\mathrm{BS}-47^\circ}\Big)^{\mathrm{N_{BS47,\ R}}} \Bigg) \\
& \cdot \left(\frac{(\eta\lambda)^0_{ij,m}}{(\eta\lambda)^0_{\mathrm{F}j,m}} - \frac{(\eta\lambda)^T_{i}}{(\eta\lambda)^T_{\mathrm{F}j,m}}\cdot T_{\mathrm{OB}}(k) \right)\,,
\end{aligned} \tag{8.18}$$

with reference diode $\mathrm{F}j = \mathrm{FA}$ for $m = \mathrm{RB}$ and $\mathrm{F}j = \mathrm{FB}$ for $m = \mathrm{MB}$.

The full set of the 16 equations for $i = 8$ photodiodes and $j = 2$ beams can be found in the Appendix C.3, (as implemented in the minimization algorithm).

8.2. Modelling the in-flight low-frequency power measurements

To simplify the fitting process, the measured powers in ADC counts were normalised, so that the samples are close to one. As a normalisation factor, the average overall single beam power on the OB is used, given by the average power of both beams on all PDs for all samples. Furthermore, the temperature data was normalised to be in the range between $(0, 1)$.

As fitter, a least squares optimisation algorithm called "minimizer" was chosen [54]. It uses a combination of two classical algorithms (Nelder-Mead Simplex and Levenberg-Marquardt) with a particle swarm optimization algorithm to effectively find a global minimum. Also, the parameters in the fit were dimensioned close to one but at least in a range between $[-2, 2]$. Details on the used parameters of the fit as well as the range of the fitting variables can be found in the program code, printed in Appendix C.3.

The model was evaluated for $k = 87$ samples. The results are shown together with the data in Figure 8.2 for the reference beam and in Figure 8.3 for the measurement beam.

A good agreement of the evaluated model and its data is obvious, since the fit (represented by the dashed lines) is mostly laying on top of the data (solid line). The residuals — the deviation of the data from its fit — are for both beams and most of the data points smaller than 10^{-3}. Between index 72 to 82 the residuals increase up to $3 \cdot 10^{-3}$. Most likely, the temperature dependency of the PDs is responsible for that.

The OB temperature sensors on the baseplate of the OB have an operational range down to 8 °C. Below that temperature there is no data available. Therefore, the lower temperatures with index 74 to 80 had to be extrapolated with surrounding temperature sensors. Figure8.4 shows the temperature, measured at the OB and at the so-called LTP Core Assembly (LCA) temperature reference point, with an offset of −3.12 °C. It seems like the temperature at the surrounding sensor drops faster than on the OB. However, there are no temperature-sensors closer to the OB available, so that above 8 °C the OB sensors were used and below, the LCA reference point ones (as shown by the blue data points in Figure 8.4). Obviously, the poorly estimated low temperature points degrade the fit results, especially at these samples. Alternatively, the results could possibly be improved by setting the 7 temperature points below 8 °C as variables to the fit. The linear model for the temperature dependency of the PDs could then help to estimate the OB temperature for the seven samples below 8 °C.

The main result of the fit is the power with parallel and orthogonal polarisation, detected in the interferometers.

Figure 8.5 therefore shows the estimated power in parallel polarisation of the two beams on the different diodes.

Similarly, Figure 8.6 shows the S-pol on each PD.

A comparison with Figures 8.2 and 8.3 shows that the huge power fluctuations belong to the P-pol and only the effect of the power control loop leads to the remaining fluctuations of S-pol, negatively correlated to the ones in P-pol

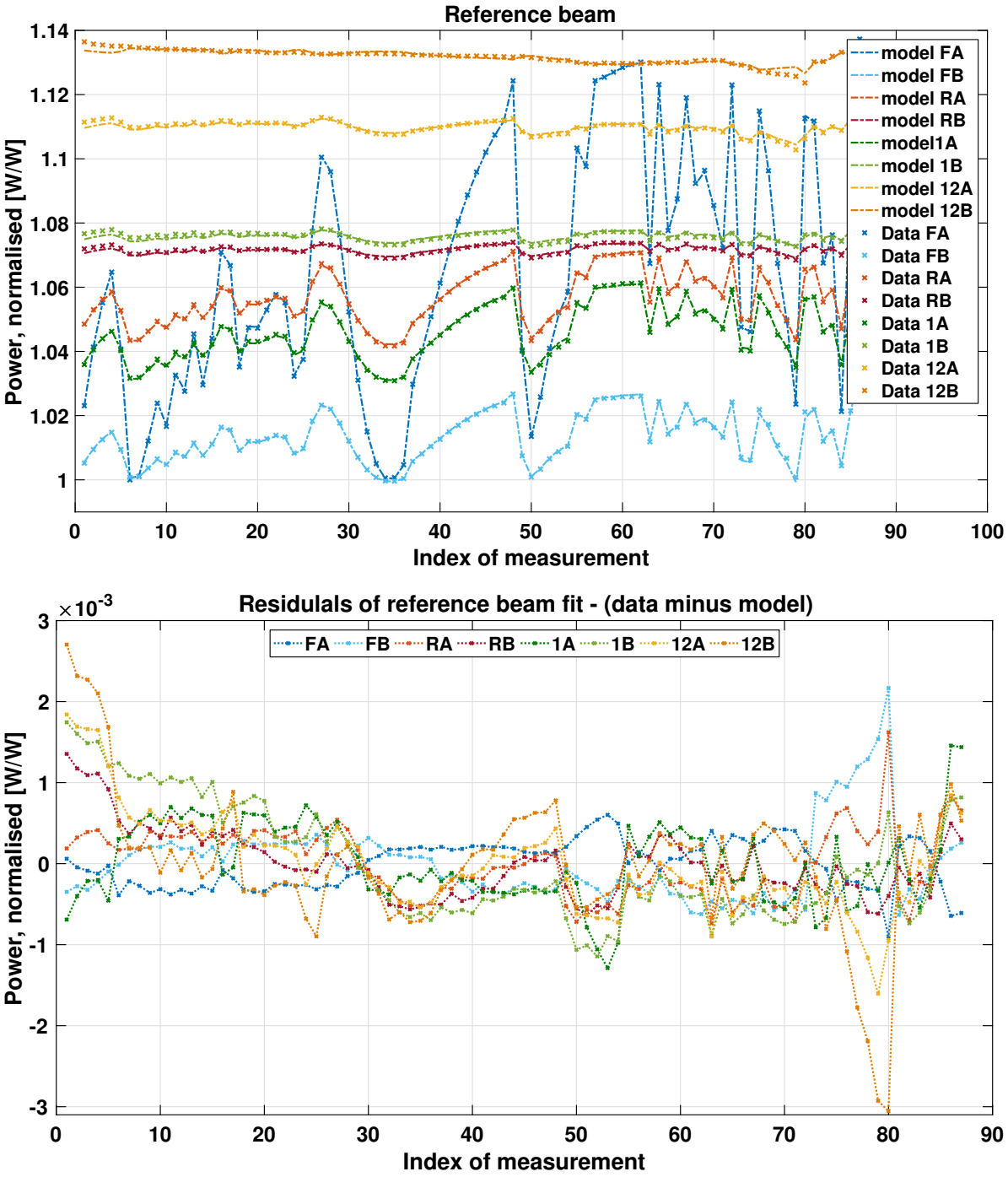

Figure 8.2.: **Upper figure**: Fit of reference beam power measurements on all QPDs together with the data. The measured power was normalised to the average total power on the OB and the measurement dates were replaced by the index of measurement. **Lower figure**: Residuals to the fit.

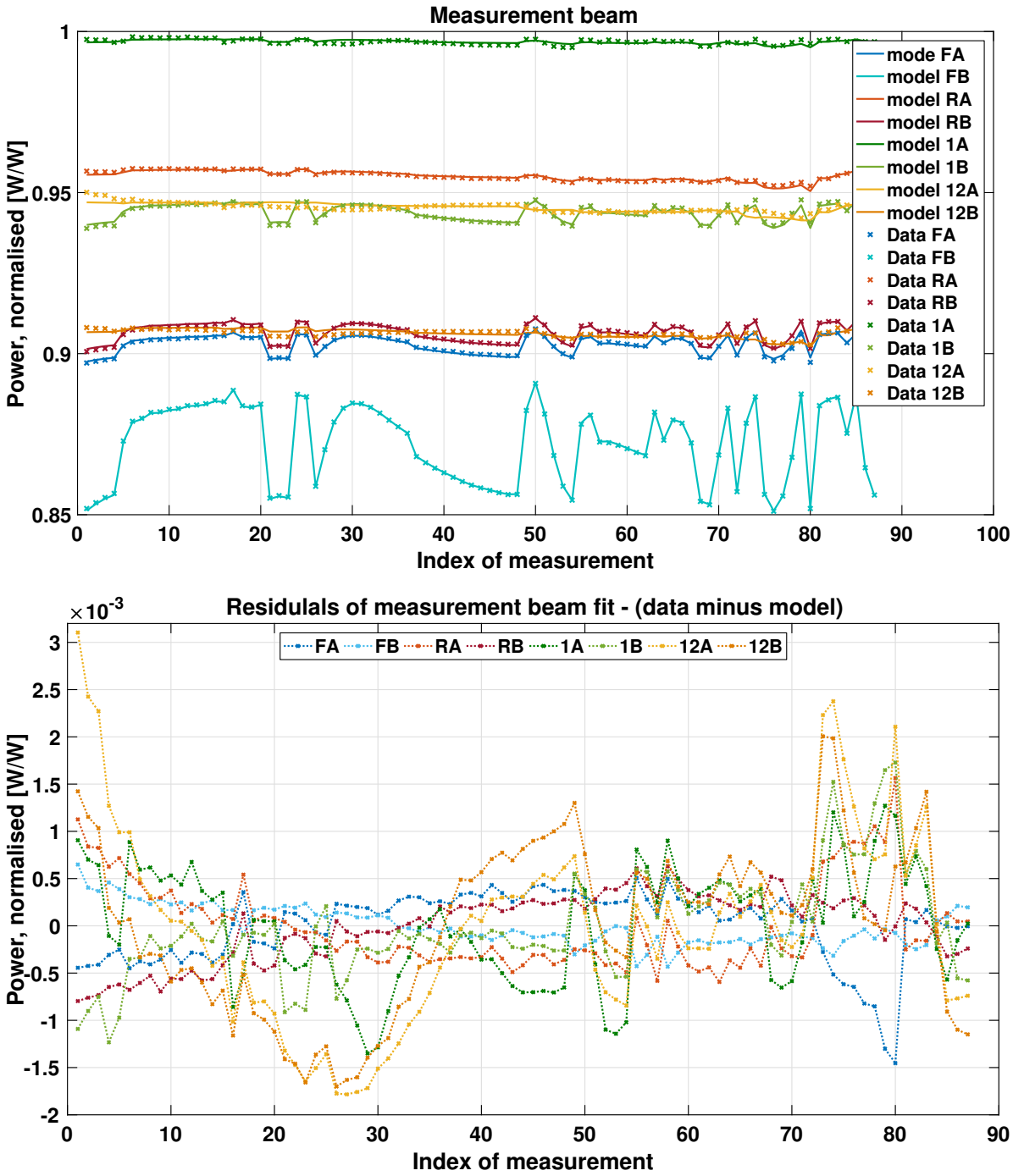

Figure 8.3.: **Upper figure**: Fit of measurement beam power measurements together with the data. The measured power was normalised to the average total power on the OB and the measurement dates were replaced by the index of measurement. **Lower figure**: residuals to the fit.

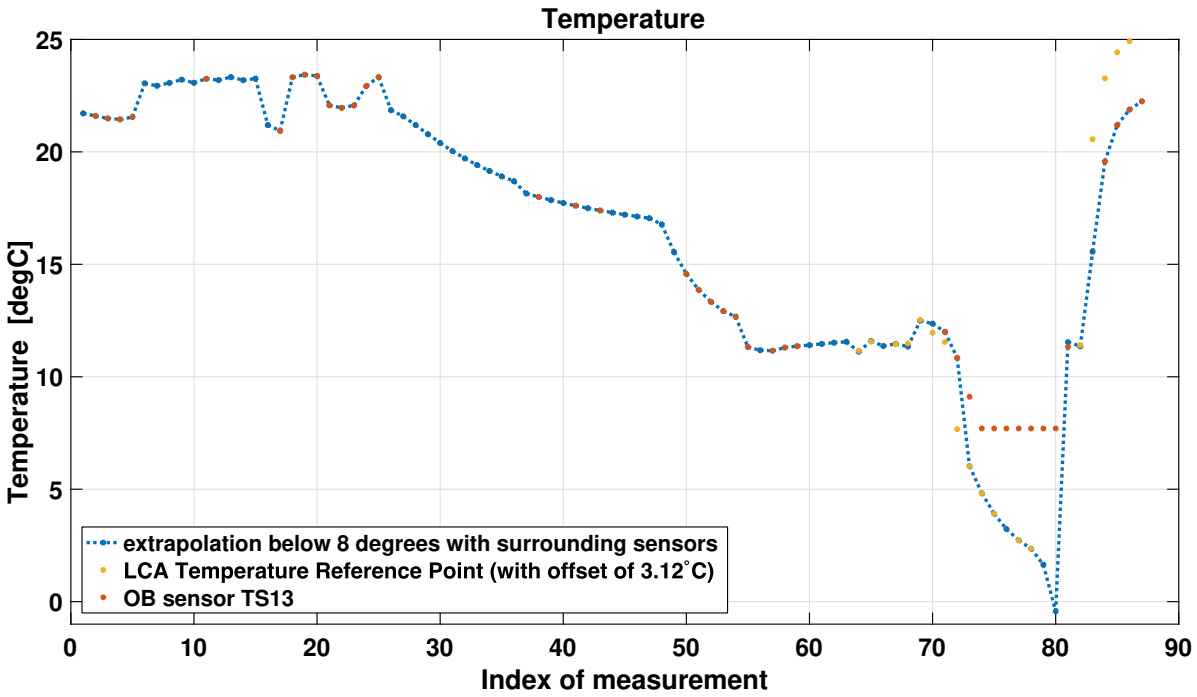

Figure 8.4.: Temperature data of a OB sensor and the LCA temperature reference point (offset by −3.12 °C). The combined data points — as used for the fit — are shown in blue.

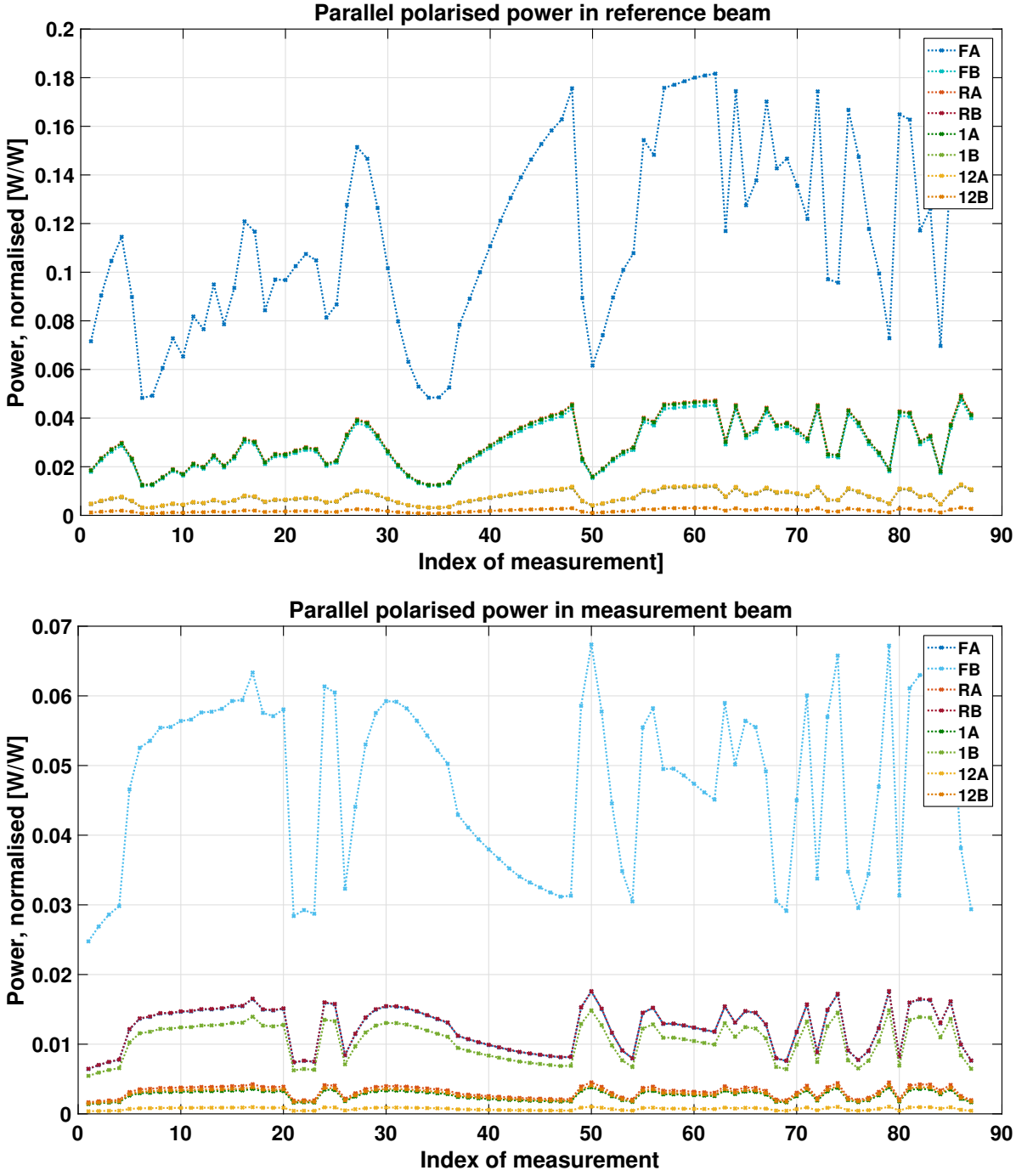

Figure 8.5.: Fit of the P-pol in reference and measurement beam on all OB diodes, normalised to the overall OB power.

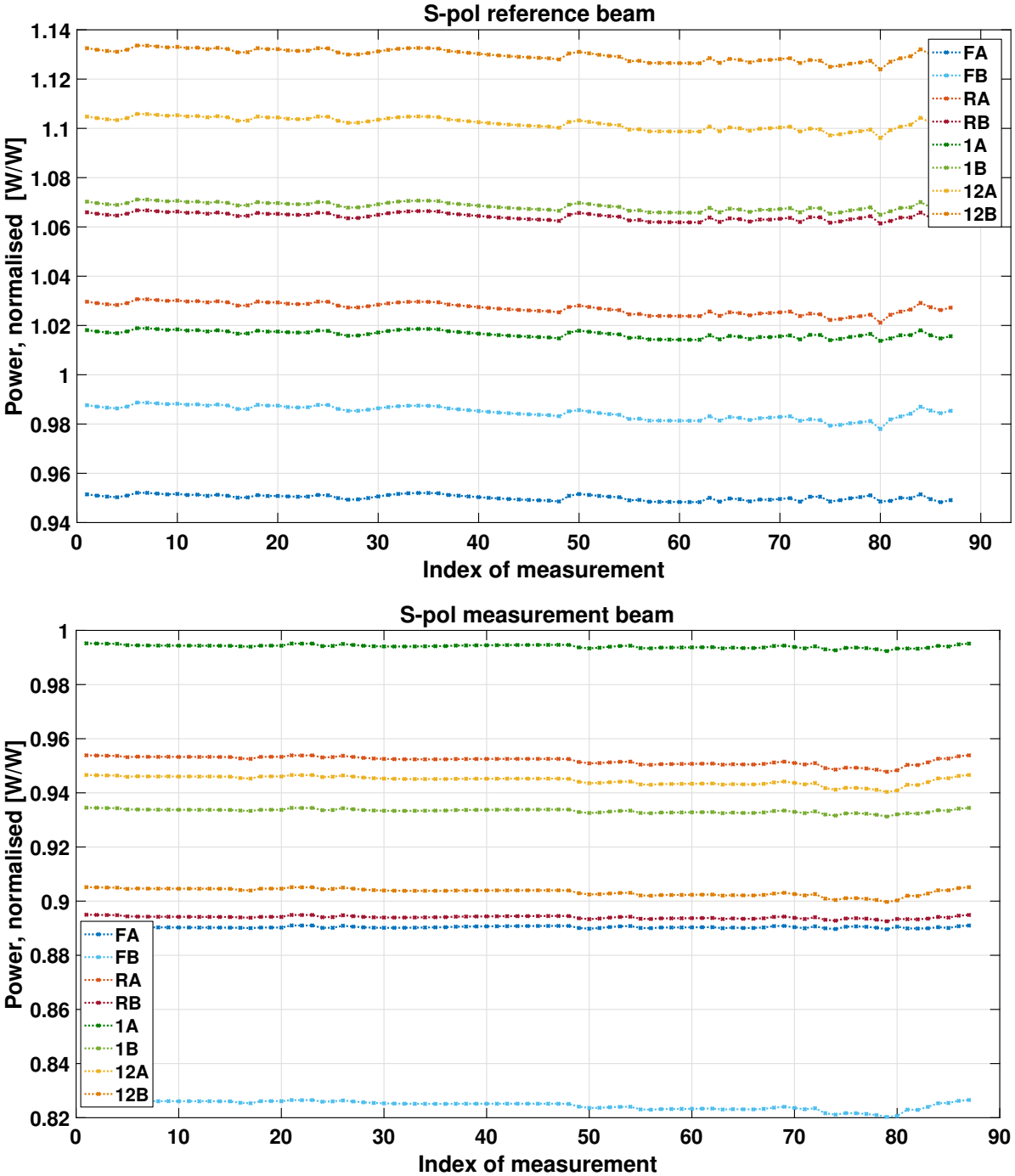

Figure 8.6.: Fit of the S-pol in reference and measurement beam on all OB diodes, normalised to the overall OB power.

8.3. Fit results: Parameter estimates and errors

In Section 8.2 the best fit results for evaluating the full model in Equation 8.18 were presented. The fitting algorithm (the minimizer) provides nominal errors of the fit variables. However, nominal errors are only valid for a Gaussian error distribution. Since the shape of the parameter space for the given variables is unknown, the validity of these errors is unconfirmed.

Therefore, the robustness of the fit and the variance of the results were checked by evaluating the model for 100 sets of randomly distributed starting parameters, normally distributed in their full range. All parameter sets converged at an average quadratic deviation of data and model between $4.889 \cdot 10^{-4}$ and $4.890 \cdot 10^{-4}$.
The corresponding average parameter estimates together with their maximum deviation in the resulting 100 parameter sets are presented in the following.

Figure 8.7 shows the average of all 100 parameter estimates for theP-pol, $P_m^{\parallel}(k)$, at the front of the OB, together with the maximum and minimum parameter estimate, represented by the error bars. With a scatter of less than 2 %(of the estimated parameter) the parameters are determined with sufficient accuracy for further analysis of their origin and derived effects, as described in the following chapters.

As expected, the reference beam has a higher share of P-pol than the measurement beam. It fluctuates between $P_{\mathrm{RB}}^{\parallel}(\min, \max) = [0.012\,,\, 0.047]$ and for the measurement beam only between $P_{\mathrm{MB}}^{\parallel}(\min, \max) = [0.006\,,\, 0.016]$. The dimension is unitless, due to the normalisation with the overall OB power, as described above. Hence, the parameter estimates represent the share of parallel polarisation of one beam that is normalised to the half of the average overall OB power (because the single normalised beams should be close to one). The two beams have a low, significant, negative, linear correlation with a Pearson correlation factor of $c = -0.348$ (compare with Reference [55, 56]). The equivalent P-value of $\mathrm{P} = 9.65 \cdot 10^{-4}$ describes the probability of getting such a correlation coefficient for an uncorrelated set of data, by random chance.

Furthermore, the **constant set-points of the power control loops** were determined to be $\frac{C_{\mathrm{RB}}}{R_{\mathrm{fs}}^{\perp}} = 1.053$ for the reference beam and $\frac{C_{\mathrm{MB}}}{R_{\mathrm{fs}}^{\perp}} = 0.942$ for the measurement beam. Their deviation both come out as $\Delta(\frac{C_{\mathrm{RB}}}{R_{\mathrm{fs}}^{\perp}})/\frac{C_{\mathrm{RB}}}{R_{\mathrm{fs}}^{\perp}} = 6.6\,\%$ and $\Delta(\frac{C_{\mathrm{MB}}}{R_{\mathrm{fs}}^{\perp}})/\frac{C_{\mathrm{MB}}}{R_{\mathrm{fs}}^{\perp}} = 6.6\,\%$. Again, the units refer to the normalisation with the overall OB power, as discussed in Section 4.3.

The relative **reflectivity of the power pick-off** for P-pol fits to $\frac{R_{\mathrm{fs}}^{\parallel}}{R_{\mathrm{fs}}^{\perp}} = 0.119$ with an error of $\Delta\left(\frac{R_{\mathrm{fs}}^{\parallel}}{R_{\mathrm{fs}}^{\perp}}\right)/\frac{R_{\mathrm{fs}}^{\parallel}}{R_{\mathrm{fs}}^{\perp}} = 3.3\,\%$.

The value is higher than expected for an uncoated BS made of fused silica: $\frac{R_{\mathrm{fs}}^{\parallel}}{R_{\mathrm{fs}}^{\perp}}(\text{literature}) = 0.079$. Reason for this deviation could be the reflection at the backside of the BS. Parts of this second reflection could hit the power monitor diode and contribute to the measured power. The backside is coated like the other 50:50 BSs with a reflection-minimizing multi-layer coating. As part of the laboratory analysis of the three flight spare BSs, the reflectivity of these anti-reflection coatings was also studied (Reference [57]). The measured reflectivity for P-pol is, with about R= 0.02, slightly higher than the one for S-pol, with about R=0.017.

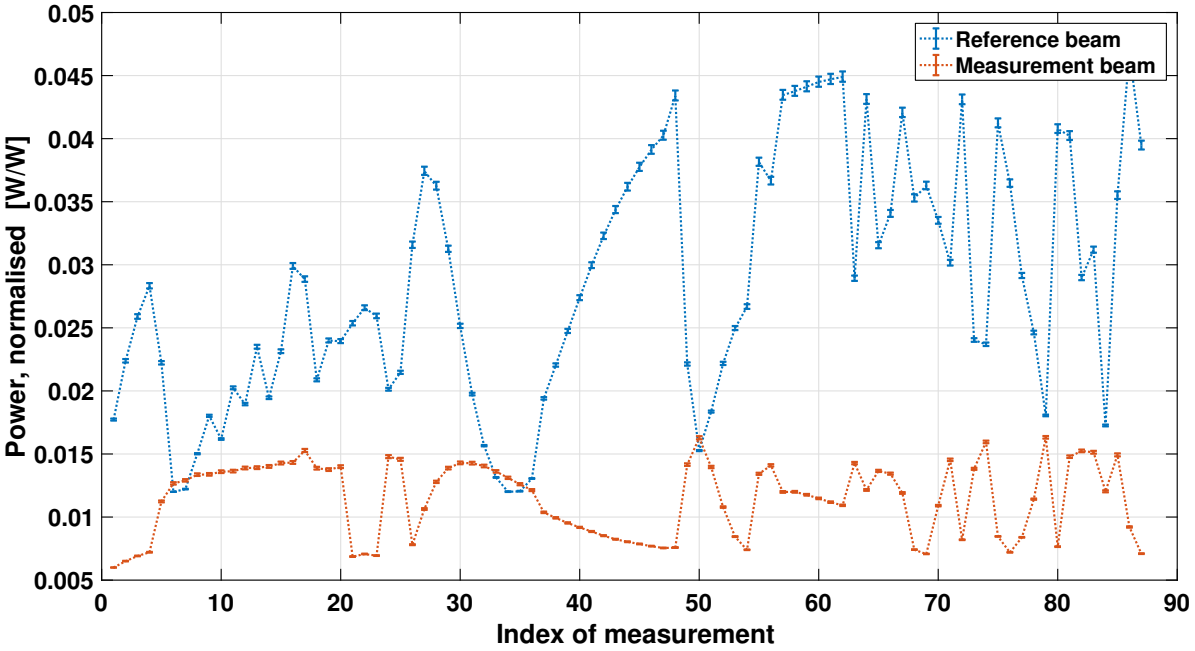

Figure 8.7.: Parameter estimates of P-pol in both beams, together with the full variation of best estimates for a random starting parameter-set.

However, a maximum measurement error of 0.5 % in power, converting to 30 % in anti-reflection coating reflectivity should be considered here. Nevertheless, also for the worst case, the second reflection at the BS would still have a much higher percentage of P-pol than the nominal one. Therefore, smaller parts of the second reflection, hitting the power monitor diode, could also increase the parameter $\frac{R_{\mathrm{fs}}^{\parallel}}{R_{\mathrm{fs}}^{\perp}}$ significantly and explain the deviation of the parameter-estimate from the Fresnel formula result for a single reflection at a fused silica surface.

For comparison to the further analysis, the **ratio of parallel and orthogonal polarisation** is the most convenient parameter. It can be computed with the previously derived fit results by:

$$\frac{P_m^{\parallel}(k)}{P_m^{\perp}(k)} = \frac{P_m^{\parallel}(k)}{\mathrm{C}_m - P_m^{\parallel}(k) \cdot R_{\mathrm{fs}}^{\parallel}} \,. \tag{8.19}$$

The maximum and minimum ratio $\frac{P_m^{\parallel}(k)}{P_m^{\perp}(k)}$ computes to $\frac{P_{\mathrm{RB}}^{\parallel}}{P_{\mathrm{RB}}^{\perp}}(\mathrm{min}) = 1.14\,\%$ and $\frac{P_{\mathrm{RB}}^{\parallel}}{P_{\mathrm{RB}}^{\perp}}(\mathrm{max}) = 4.5\,\%$ for the reference beam and $\frac{P_{\mathrm{MB}}^{\parallel}}{P_{\mathrm{MB}}^{\perp}}(\mathrm{min}) = 0.64\,\%$ and $1.74\,\%$ for the measurement beam, with a propagated maximum relative error of $\Delta\left(\frac{P_{\mathrm{MB}}^{\parallel}}{P_{\mathrm{MB}}^{\perp}}\right) / \frac{P_{\mathrm{MB}}^{\parallel}}{P_{\mathrm{MB}}^{\perp}} = 2\,\%$.

For the combined losses, $\frac{(\eta\lambda)_{ij}^{0}}{(\eta\lambda)_{\mathrm{FA,\ RB/\ FB,\ MB}}^{0}}$, the scatter of the best fit results is higher than for the other parameters, as can be seen in Figure 8.8.

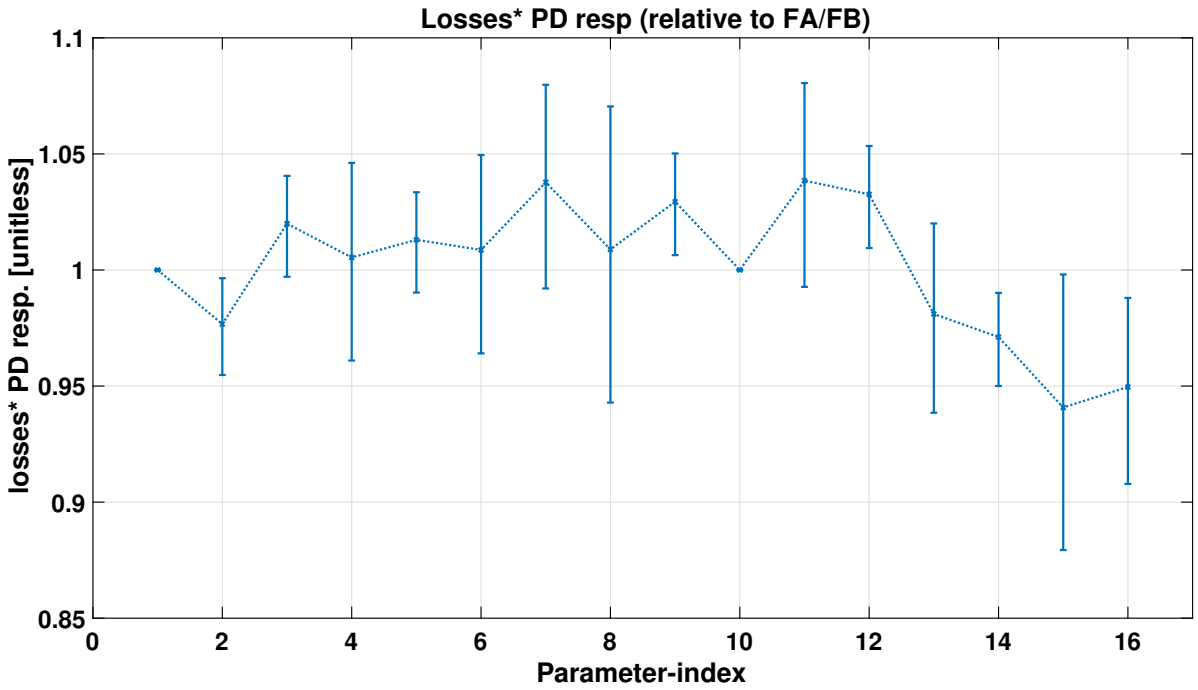

Figure 8.8.: Parameter estimates of combined losses $\frac{(\eta\lambda)^0_{ij}}{(\eta\lambda)^0_{\text{FA, RB/ FB, MB}}}$, together with the full variation of best estimates for a random starting parameter-set.

The reason for this is the previously discussed linear dependence with the beam power, which is only broken by the estimated minimum P-pol and the relative fitting to a reference diode $(\eta\lambda)^0_{\text{FA, RB/ FB, MB}}$. Therefore, it is hard to distinguish between $\frac{(\eta\lambda)^0_{ij}}{(\eta\lambda)^0_{\text{FA, RB/ FB, MB}}}$ and $\frac{C_{\text{RB / MB}}}{R^{\perp}_{\text{fs}}}$, especially for the parameters $i = 7$ and $i = 8$. Here, the P-pol is smallest and therefore the restricting impact of the offset power, too. Although, a reproducibility of $\frac{(\eta\lambda)^0_{\text{12B, RB/ 12A MB}}}{(\eta\lambda)^0_{\text{FA, RB/ FB, MB}}}$ better than 11 % is reached here.

The **splitting ratios of the BSs,** T_{BS} and $R_{\text{BS}} = 1 - T_{\text{BS}}$, were estimated by the fit, as shown in Table 8.1.

	Fit results					Laboratory		
Polarisation	45°	42.75°	47.25°	std. dev.	max. dev.	45°	42.75°	47.25°
S-pol	0.484	0.500	0.466	0.0022	0.0055	0.487	0.504	0.469
P-pol	0.795	0.780	0.810	0.0014	0.0035	0.785	0.770	0.799

Table 8.1.: Fit results: Transmission coefficients T_{BS} of the 50:50 BS, dependent on polarisation. The errors are given by the standard deviation and the maximum deviation in 100 parameter estimates with randomly distributed starting parameters (see 8.3). In the right column, experimentally determined transmission coefficients of three flight spare BSs are shown, for comparison. Their maximum deviation is 1 %.

These splitting ratios were also experimentally determined for three flight spare BSs, as described in Reference [57]. The average splitting ratio is shown to the right in Table 8.1. The

maximum deviation in splitting ratio of the three samples was measured to be 1 %.

The parameter estimates of the splitting ratios for orthogonal polarisation meet the experimentally determined transmission coefficients within errors. For parallel polarisation the parameter estimates are slightly higher than the experimentally determined ones.
Since the fit results are for all angles about one percent greater, the deviation could result from imperfect alignment of the experimental setup (in particular, the mismatch of internal axis of the used polarimeter and the optical bench coordinate system could have led to a systematic error). The transmission of power through the 50:50 BSs is at maximum for parallel input polarisation. If the applied polarisation state in the laboratory setup was not perfectly parallel, the measured splitting ratio would therefore be underestimated, corresponding to the slightly higher fitted splitting ratios.

The average **PD temperature dependencies,** $(\eta^T \cdot \lambda)_{ij}$, are shown together with the minimum and maximum parameter estimate in Figure 8.9.

They describe the differential temperature dependency of a QPD to the PD of the corresponding power control loop.

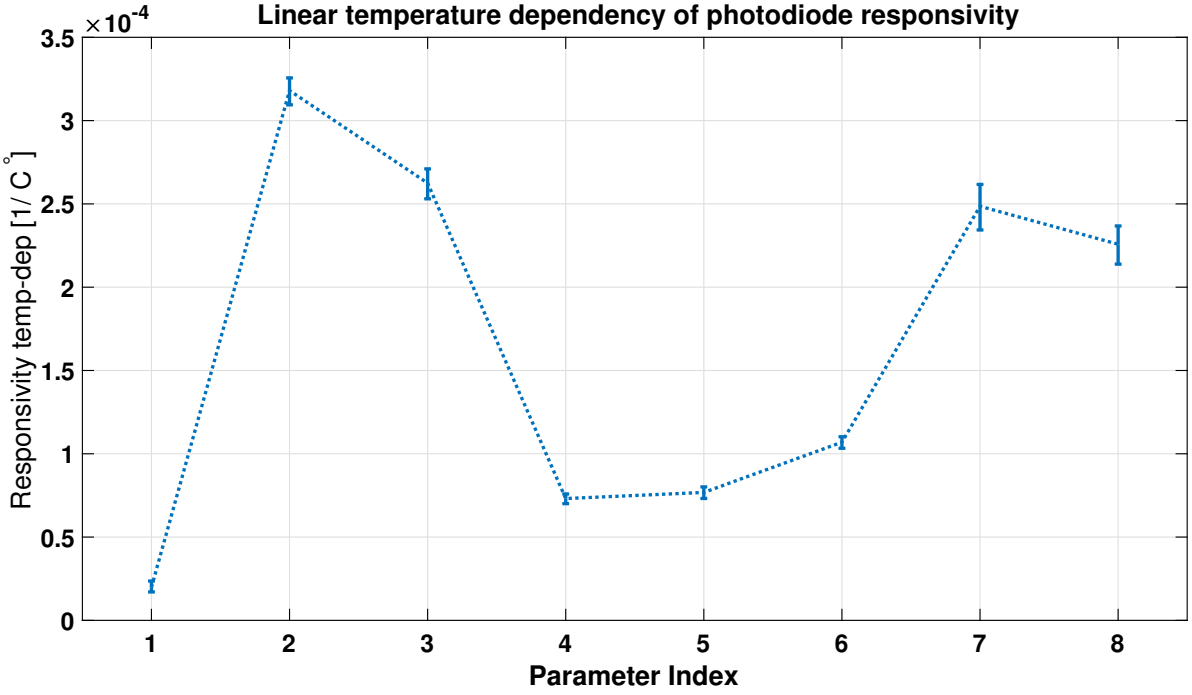

Figure 8.9.: Parameter estimates of PD temperature dependency, together with the full variation of best estimates for a random starting parameter-set.

The parameter estimates are $(\eta^T \cdot \lambda)_{ij} \in \left[1.9 \cdot 10^{-3} \frac{\%}{°\mathrm{C}}, 3.1 \cdot 10^{-2} \frac{\%}{°\mathrm{C}}\right]$. Its maximum scatter is below $3 \cdot 10^{-5} \frac{\text{responsivity}}{\mathrm{C}°}$. They are in good agreement with experimentally determined coefficients of 4 identically constructed photodiodes that showed a maximum variation in responsivity of $\Delta(\eta^T) < 7 \cdot 10^{-2} \frac{\%}{°\mathrm{C}}$ (internal measurements made by Dr. Germán Fernández Barranco at the AEI).

Overall, the results show that the derived model is able to describe the power fluctuations as observed during flight. The agreement between laboratory measurements and fit results of PD temperature dependencies and BS splitting ratios underlines the applicability. As a consequence, the next question to answer is, where such a significant power in parallel polarisation on the OB is coming from. For this, some other interesting LPF parameters are analysed for correlations with the P-pol, to find a hint on the underlying effect.

Box 8.3.1 | Summary: Description of the OB power measurements

Description and fit:

- A model for the measured beam power at the OB PDs was derived, including the polarisation.
  → The LPF data set can be described very well by the model with residuals below $3 \cdot 10^{-3}$.
- The estimated parameters for the BS splitting ratios, as well as the temperature dependency of the PD responsivity, agree with laboratory measurements.

Result:

- There is a varying P-pol in both beams:
  - for the reference beam between 1.14 % and 4.5 % of the total power,
  - for the measurement beam between 0.64 % and 1.74 % of the total power.
- The P-pol of both beams has a significant Pearson correlation factor of $c = -0.348$.

Next step:

- Search for correlations to other LPF data.

8.4. Polarisation noise: Correlation with other variables

In Section 8.2, the observed low-frequency power noise was described by polarisation fluctuations.
In the following, the correlation with two other LPF parameters is described, giving a hint on the origin of the responsible mechanism.

8.4.1. Correlation with the LPF Temperature

Since the temperature is known to change an optical path-length via expansion, a check for its correlation is mandatory. So far, it is clear that the two quantities are not linearly related. Therefore a scatter plot is used at first to visualize the nature of a possible correlation.

Figure 8.10 shows the power in parallel polarisation of both beams, scattered with the temperature. The two quantities seem to have no simple correlation. Parts of the scatter plot

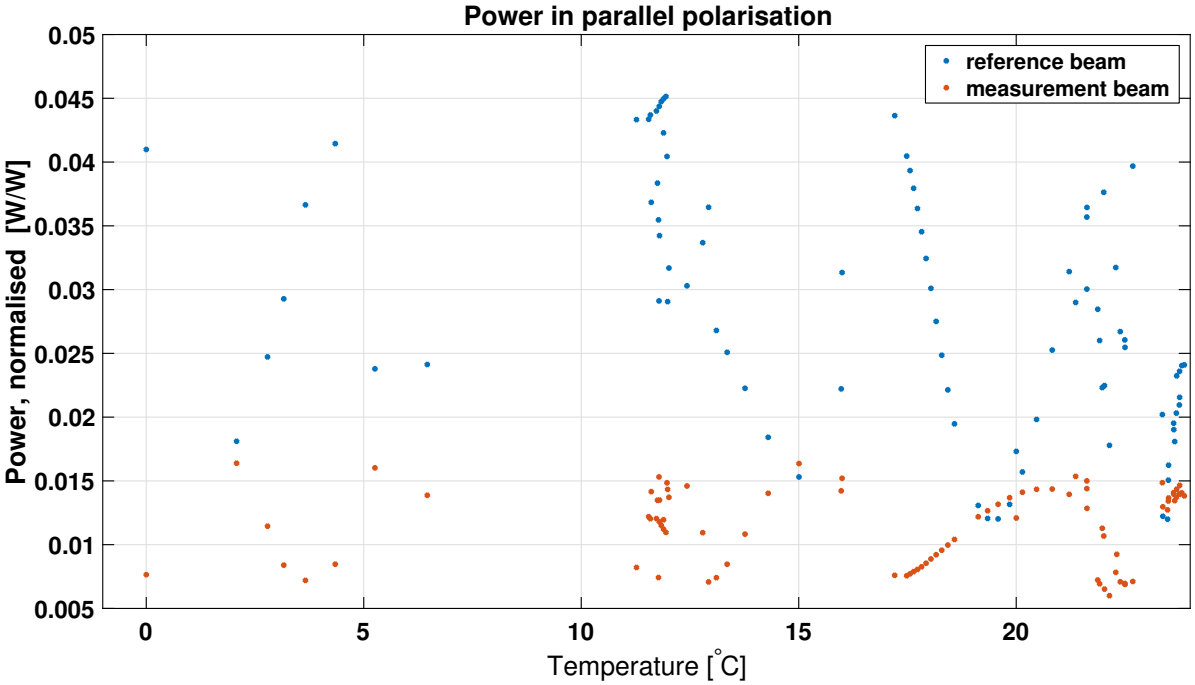

Figure 8.10.: Scatter of power in parallel polarisation and OB temperature during the single beam power measurements.

suggest a periodic correlation, but the sample density is too low to reasonably derive a model with sufficient accuracy.

8.4.2. Comparison to the power control loop

On LPF the individual beam powers entering the OB are controlled with two AOMs, as part of the amplitude CL described in Box 2.1 (see Section 2.1). A decrease of the beam power on the OB, for example induced by reflection of off-nominal polarised light at the PBS in the FIOS (compare to Section 2.2), is therefore compensated by an increase of the RF power in the AOM crystal, leading to more transmitted light through the AOM.

In the operated range, the power amplifier to the RF driving electronics relates approximately linear with the transmitted power through the AOM (see Appendix E).

Hence, the power to the RF driving electronics, which is available as a telemetry parameter (scaled to a 10 V reference voltage), is checked for a possible correlation with the estimated parallel polarisation. In Figure 8.11 the power to the RF driver of the AOM, controlling the reference beam, together with the amount of parallel polarised light in that beam (see Section8.2) is shown. A correlation between the two variables is visible even by eye. The Pearson correlation coefficient derives to $r_{\mathrm{RB}} = 0.482$ with $p_{\mathrm{RB}} = 2.175 \cdot 10^{-6}$, indicating a significant, moderate, positive, linear correlation.

For the measurement beam, the RF power together with the estimated P-pol is shown in Figure8.12. Again, a correlation between RF power and parallel polarisation on the OB is

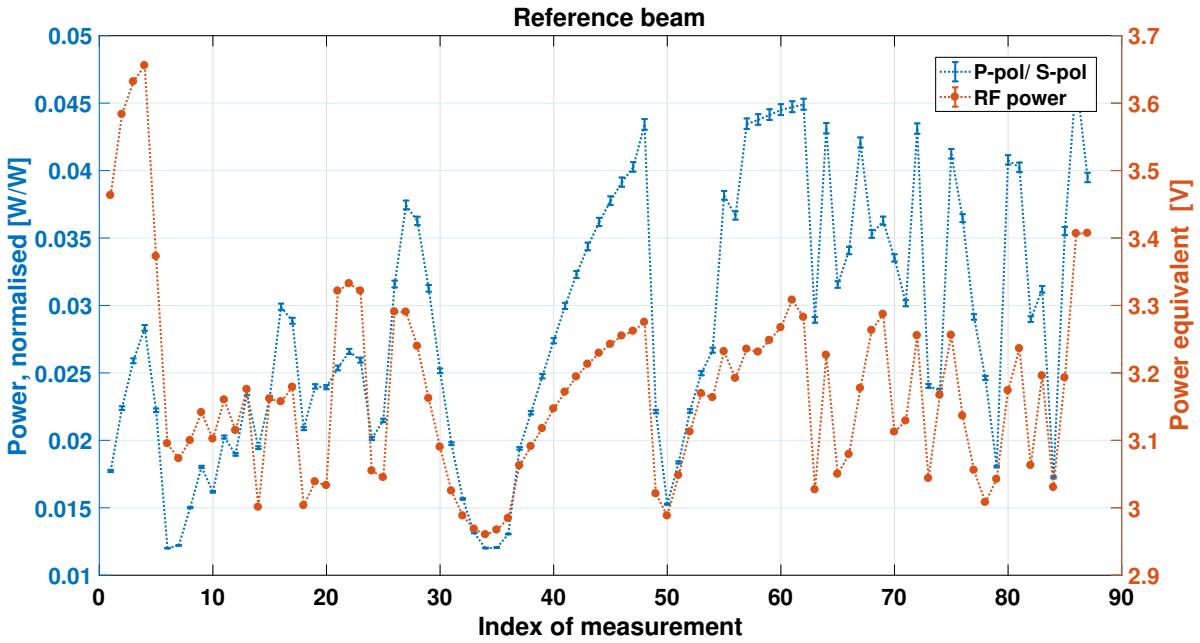

Figure 8.11.: Power of the RF driver of the reference beam AOM (scaled to a 10 V reference voltage) together with the P-pol in the reference beam.

visible. The Pearson correlation coefficient computes to $r_{\mathrm{MB}} = 0.526$ with $p_{\mathrm{MB}} = 1.64 \cdot 10^{-7}$, which indicates again a significant, moderate, positive, linear correlation. However, surprisingly the coupling strength between the two parameters is much weaker than for the reference beam. The same change of RF driving power leads to about 5 times less power in parallel polarisation on the OB than for the reference beam.

Obviously, the subsequent question is, why there is a difference between the two beams leading to more transmission of P-pol through the reference beam PBS onto the OB?

In Section 10, identically constructed PBSs were analysed with more detail in the laboratory. However, before this, the correlation of power control and parallel polarisation is further analysed for a specific part of the data set.

Apparently, the data shown in Figures 8.11 and 8.12 are also affected by other power noise, not correlated to the P-pol on the OB. This is not very surprising, since the different measurement points are distributed over the whole mission duration with many possible noise sources to the beam powers, like: laser output power, losses in the fibres or at the beam path on the modulation bench or the PD responsivities of the power monitor diodes.
Therefore, the next section describes the analysis of a selected part of the mission, the so-called "cool down" phase, where the temperature of the satellite was lowered. During this comparably short period, more frequent measurements were taken that hence should be less affected by slow power drifts, not related to temperature.

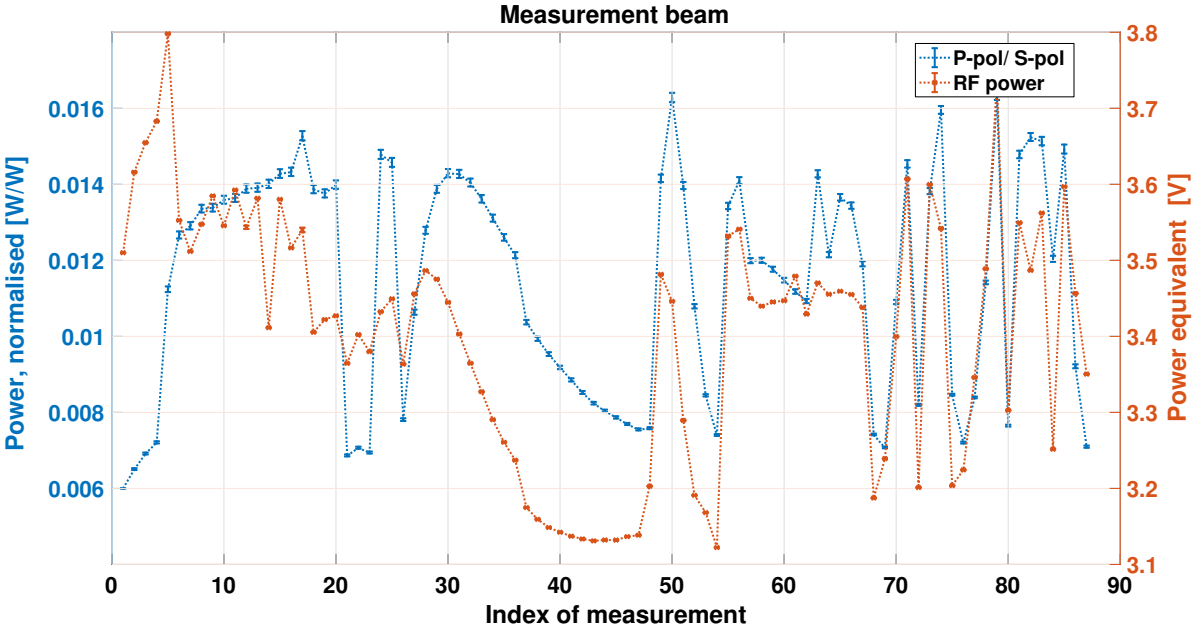

Figure 8.12.: Power of the RF driver of the measurement beam AOM (scaled to a 10 V reference voltage) together with P-pol in the measurement beam.

8.4.3. Correlation with the power control loop during cool down

The LPF mission was very successful — the noise in differential TM acceleration was lower than required and expected (compare with Reference [15] and [16]). Towards lower frequencies the noise is dominated by Brownian noise from the residual gas in the TM tanks. Therefore, the whole satellite was cooled down to reduce Brownian noise and improve the low frequency performance.

During the cool down period also other temperature driven effects, as presumed for the polarisation, could be studied over a wider temperature range. Therefore, the single beam power measurement procedure was executed in intervals of some hours. The resulting low-frequency power fluctuations were analysed with more detail for their correlation with the power control actuation, given by the RF driver power, as described in the following.

The actual measured power at the QPDs is used here, instead of the fit results for P-pol, to avoid an influence of the other data points.

Figure 8.13 shows the reference beam power measurements on $DC_{FA,\,RB}$ and $DC_{12B,\,RB}$, detecting the greatest and lowest P-pol, together with the corresponding RF power (for the measurement beam, $DC_{FB,\,MB}$ and $DC_{12A,\,MB}$ are shown respectively). The powers are normalised to the overall OB power, as described in Chapter 4.

As expected, the RF power is significantly correlated to $DC_{Fj,\,m}$ but only very weakly (and negatively) to $DC_{12j,\,m}$. Surprisingly, there seems to be a delay between the power fluctuations and the RF power. However, there is no reasonable mechanism that could delay the incoming and transmitted power to the OB. Therefore, it is more likely that a superposition with another effect leads to an apparent delay. For example, slow temperature related drifts could

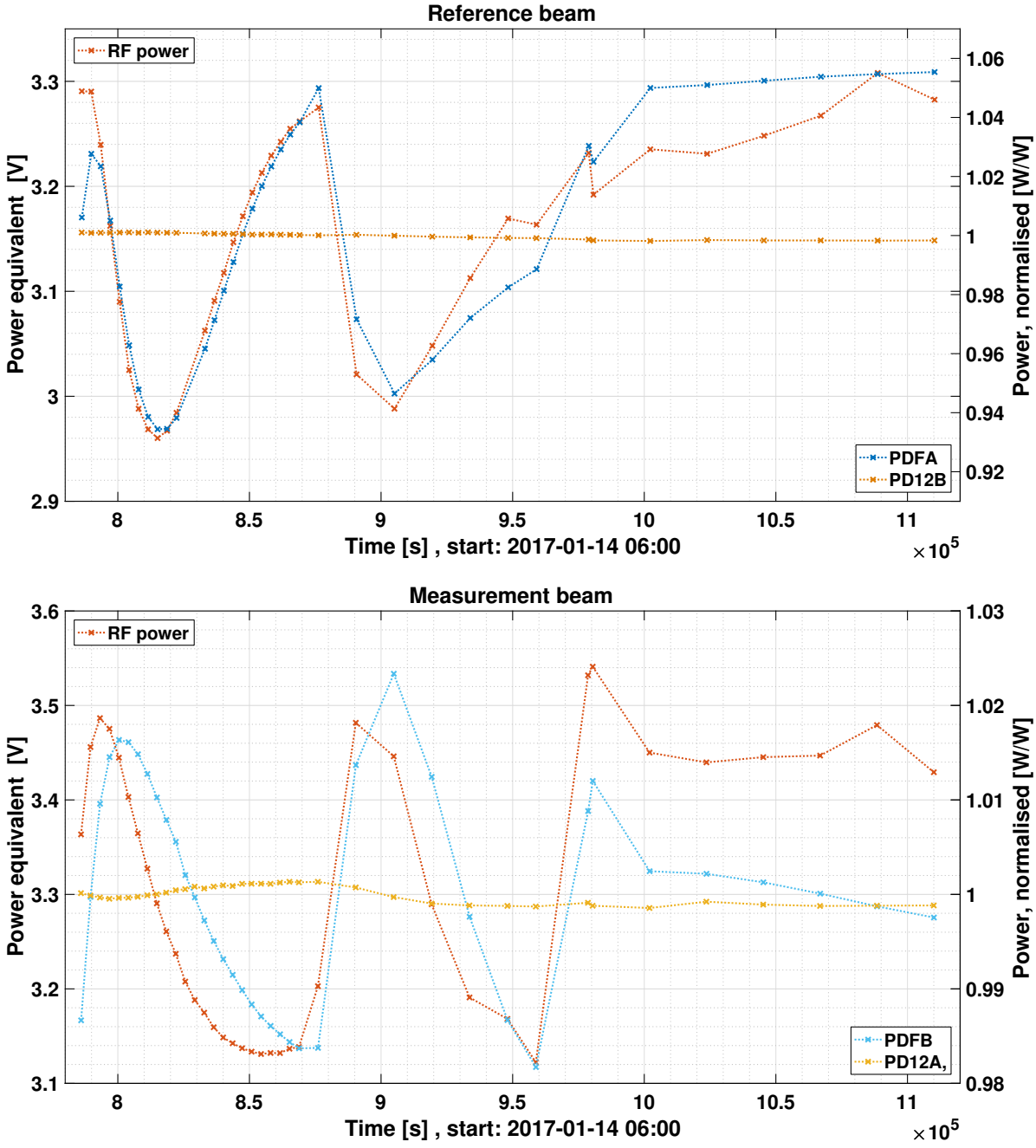

Figure 8.13.: RF driving power of the two beams together with the normalised $DC_{Fj,\,m}$ and $DC_{12j,\,m}$, during the so-called cool down period.

look like a delay of a periodic signal, if only few data points are available. As mentioned above, several other effects besides the polarisation could lead to a decrease in incoming power to the OB that need to be compensated via the control loop. For example, the PD responsivity of the power monitor diodes or temperature induced changes of fibre in-coupling efficiency could have caused further losses.

To visualise the correlation between the power fluctuations on the OB and the RF power, a scatter plot is used, as can be seen in Figure 8.14. Since there is not enough knowledge about remaining temperature-related effects and more importantly, no reliable temperature data on the OB for temperatures below 8 °C, a simple approach of the linear correlated parts is made by a linear fit to the scatter of $\mathrm{DC}_{\mathrm{F}j,\,\mathrm{m}}$ and RF power, as can be seen by the solid line in Figure 8.14.

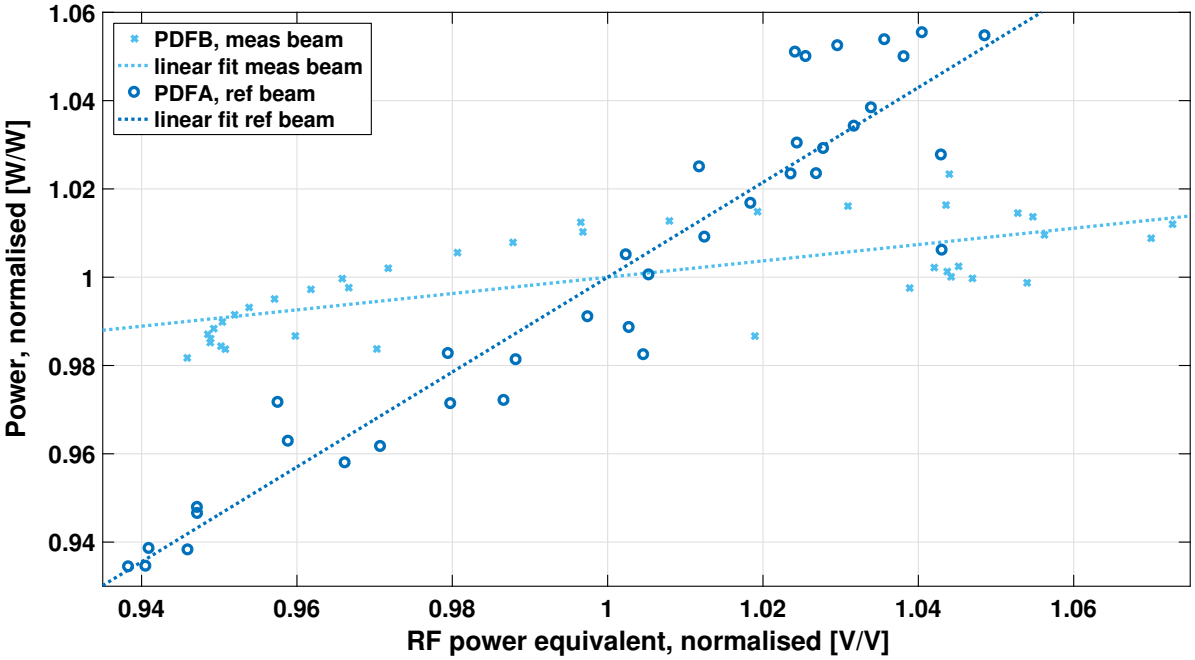

Figure 8.14.: Scatter of the normalised $\mathrm{DC}_{\mathrm{FA},\,\mathrm{R}}$ and $\mathrm{DC}_{\mathrm{FB},\,\mathrm{MB}}$ with the corresponding RF power.

The fit results are given by Equations 8.20 and 8.22 with the norm of residuals (NOR):

$$\langle \mathrm{DC}_{\mathrm{FB},\,\mathrm{MB}} \rangle \left(\langle P_{\mathrm{RF},\,\mathrm{MB}} \rangle \right) = 0.185 \cdot \langle P_{\mathrm{RF},\,\mathrm{MB}} \rangle + 0.815; \ \text{NOR: } [0.050] \tag{8.20}$$

$$\rightarrow \Delta \left(\frac{P^{\parallel}_{\mathrm{MB}}}{P^{\perp}_{\mathrm{MB}}} \right) \left(\Delta \left(\langle P_{\mathrm{RF},\,\mathrm{MB}} \rangle \right) \right) \approx 0.0418 \cdot \Delta \left(\langle P_{\mathrm{RF},\,\mathrm{MB}} \rangle \right); \ \text{NOR.: } [0.0113] \tag{8.21}$$

$$\langle \mathrm{DC}_{\mathrm{FA},\,\mathrm{RB}} \rangle \left(\langle P_{\mathrm{RF},\,\mathrm{RB}} \rangle \right) = 1.074 \cdot \langle P_{\mathrm{RF},\,\mathrm{RB}} \rangle - 0.074; \ \text{NOR: } [0.076] \tag{8.22}$$

$$\rightarrow \Delta \left(\frac{P^{\parallel}_{\mathrm{RB}}}{P^{\perp}_{\mathrm{RB}}} \right) \left(\Delta \left(\langle P_{\mathrm{RF},\,\mathrm{RB}} \rangle \right) \right) \approx 0.242 \cdot \Delta \left(\langle P_{\mathrm{RF},\,\mathrm{RB}} \rangle \right); \ \text{NOR: } [0.0172], \tag{8.23}$$

with dimensionless $\langle \mathrm{DC}_{\mathrm{FA},\,\mathrm{RB}} \rangle$, $\langle \mathrm{DC}_{\mathrm{FB},\,\mathrm{MB}} \rangle$, $\langle P_{\mathrm{RF},\,\mathrm{MB}} \rangle$, $\langle P_{\mathrm{RF},\,\mathrm{RB}} \rangle$, all normalised by its average power.

For the measurement beam especially, the norm of residuals is, with 27 %, high in comparison to the relevant first parameter. For the reference beam this value is, with 7 %, a bit lower, but still the influence of a superposing effect is obvious. Nevertheless, an order of magnitude in coupling between P-pol and RF power can be derived. Therefore, the DC powers were translated to the ratio of parallel to orthogonal polarisation at the beginning of the OB, as can be seen in Equations 8.21 and 8.23. The second fit parameter describes an offset in RF power and beam power at the QPD, which is not transferable to the ratio in parallel and orthogonal polarisation. Therefore, the Δ's are used to describe a change in the power ratio $\Delta\left(\frac{P_m^{\parallel}}{P_m^{\perp}}\right)$ resulting from a change in the RF power $\Delta\left(\langle P_{\mathrm{RF,\,m}}\rangle\right)$.

The resulting parameters clearly show the difference between the two beams: The same actuation in power control is correlated to a 5.8 times higher change in P-pol for the reference beam. This points again to the questions, where the correlation is coming from and why it is so different in the two beams. The most obvious spot, where incoming power and transmitted polarisation could be correlated, is the PBS, reflecting the off-nominal polarised power at the front of the OB.

In principle, two different mechanisms could lead to more reflected power at the PBS: One is a rotation of the PBS optical axis and the other one is more off-nominal polarised light in the incident beam.
Furthermore, there are also two mechanisms that could result in a higher transmission of parallel polarised light through the PBS: Again, one is a rotation of the PBS optical axis and the other one is a degradation of the polarisation extinction ratio.
The plausibility of these mechanisms was further investigated by laboratory experiments, described in Chapters 10 to 13.

However, before the search for the underlying source is described, another imposing question was followed up: How was the polarisation on the OB behaving before flight?

Fortunately, there is corresponding data available: Before flight the OB was thermally cycled while measuring the single beam powers on all QPDs (except the ones with a TM in the beam path, where only the reference beam is detected). These tests were meant for monitoring the beam spot positions with temperature. The analysis of polarisation is described in Chapter9.

Box 8.4.1 | Summary: Correlation of polarisation variations with other parameters

Correlation of P-pol with the OB **temperature**:

- The parameters appear to have a periodic contribution.
- However, the sample density is too low for a dedicated analysis.

Correlation of P-pol to the control signal of the **power CL**:

- The control signal corresponds to the power applied to the AOM RF drivers,
  → **A linear correlation with P-pol is significant.**
- Apparently, the reference beam has a more than 5 times higher translation of RF power and P-pol than the measurement beam.

Open questions:

- What is responsible for the correlation of power control and polarisation on the OB?
- Why is the conversion to $\Delta\left(\frac{P^{\parallel}}{P^{\perp}}\right)$ higher for the reference beam?

9. Pre-flight observations: Single beam powers during thermal cycling of the Optical Bench

In preparation to flight the thermal stability of the OB was tested. Therefore, the OB was moved to an isolated environment. The laser source used for these tests was cleaned in polarisation before it was coupled into the fibres guiding the light to the OB. Then the temperature inside the isolated environment was cycled in a range of 50°C around room-temperature. Thereby, the input light was equally split between the measurement beam, both beams, the reference beam and no beams in a 60 s period. During the cycling process the power of all QPDs was recorded to monitor the beam spot positions, which indicate a possible distortion of the OB. However, since there were no dummy TMs integrated for this test, the beams pointing to the TMs had to be blocked. Hence, the measurement beam was only detected in the reference and frequency interferometers.

Since this experiment measures the single beams over a wide temperature range, it also gives the opportunity for a suitable analysis of the polarisation effects. However, in contrast to the in-flight situation, here the overall power variations are big due to the missing power control. Therefore, the challenge is to dig out a small polarisation effect in much bigger power noise. On the other hand there is also plenty of data in comparison to the 87 "samples" during flight of LPF.

9.1. Reference beam

Figure 9.1 shows the reference beam power together with the temperature of the OB. Common to all channels are power fluctuations up to 40 %. The periodic correlation to temperature strongly points to the fibres as the origin.

Equation 8.1 generally describes the power, measured at one of the LPF diodes. Being a time series, the current data set allows to split the powers with parallel and orthogonal polarisation into a stationary and a non-stationary part $P+P(t)$. The reference beam power measurements at the eight diodes $\mathrm{DC}_{ij,\,\mathrm{RB}}$ can therefore be written as:

$$\mathrm{DC}_{ij,\,\mathrm{RB}} \cdot \mathrm{c}_{\mathrm{DC}} = \left(\lambda^{\perp}_{ij,\,\mathrm{RB}} \cdot (P^{\perp}_{\mathrm{RB}} + P^{\perp}_{\mathrm{RB}}(t)) + \lambda^{\parallel}_{ij,\,\mathrm{RB}} \cdot (P^{\parallel}_{\mathrm{RB}} + P^{\parallel}_{\mathrm{RB}}(t)\right) \cdot \eta_i(T)\,, \tag{9.1}$$

with power $P^{\perp}_{\mathrm{RB}}$ in orthogonal and $P^{\parallel}_{\mathrm{RB}}$ in parallel polarisation and polarisation-dependent transmissivities $\lambda^{\perp}_{ij,\,\mathrm{RB}}$ and $\lambda^{\parallel}_{ij,\,\mathrm{RB}}$ for the reference beam paths. Furthermore, $\eta_i(T)$ describes the temperature-dependent PD responsivity. Note that the index $m = \mathrm{RB}$ for the reference beam is skipped in the remainder of this section, since only the reference beam is described here.

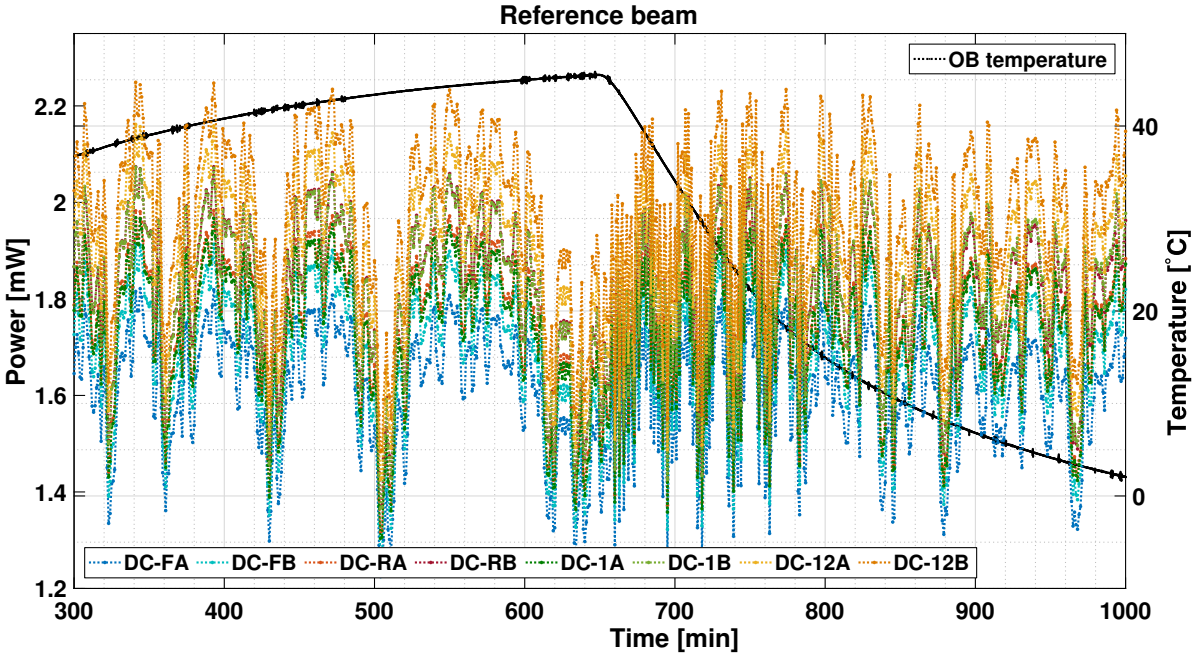

Figure 9.1.: Reference beam power during thermal cycling of the LPF OB, previous to flight, together with the OB temperature.

To compare the data set with the in-flight results, the ratio of parallel to orthogonal polarisation shall be retrieved in the followoing.

The low-frequency power drifts, for example induced by the temperature-dependent PD responsivity, can be removed with a low-pass filter. The polarisation fluctuations are presumed to be periodically related to temperature. Therefore, the corner frequency, f_c, can be chosen such that the polarisation fluctuations at higher frequencies are filtered out and all linearly related temperature effects are kept in:

$$P^{\parallel}(t) \,@\, f > f_c \text{ and } \eta_i(T) \,@\, f < f_c \,. \tag{9.2}$$

The low-pass filtered time series $\mathrm{LP}(P_{ij})_{@f_c}$ can therefore be written as:

$$\mathrm{LP}(\mathrm{DC}_{ij})|_{f_c} = \left(\lambda_{ij}^{\perp} \cdot \left(P^{\perp} + \langle P^{\perp}(t)\rangle\right) + \lambda_{ij}^{\parallel} \cdot P^{\parallel}\right) \cdot \frac{\eta_i(T)}{\mathrm{c_{DC}}} \,, \tag{9.3}$$

with a moving average of $\langle P^{\perp}(t)\rangle$.

The 8 QPD channels can then be normalised with the following equation:

$$\begin{aligned}\frac{\mathrm{DC}_{ij}}{\mathrm{LP}(\mathrm{DC}_{ij})|_{f_c}} &= \frac{\left(\lambda_{ij}^{\perp}\cdot(P^{\perp}+P^{\perp}(t))+\lambda_{ij}^{\parallel}\cdot(P^{\parallel}+P^{\parallel}(t)\right)\cdot\eta_i(T)\cdot\mathrm{c_{DC}}}{\left(\lambda_{ij}^{\perp}\cdot(P^{\perp}+\langle P^{\perp}(t)\rangle)+\lambda_{ij}^{\parallel}\cdot P^{\parallel}\right)\cdot\eta_i(T)\cdot\mathrm{c_{DC}}} \\ &= 1+\frac{P^{\perp}(t)-\langle P^{\perp}(t)\rangle}{P^{\perp}+\langle P^{\perp}(t)\rangle+\frac{\lambda_{ij}^{\parallel}}{\lambda_{ij}^{\perp}}\cdot P^{\parallel}}+\frac{\lambda_{ij}^{\parallel}}{\lambda_{ij}^{\perp}}\cdot\frac{P^{\parallel}(t)}{P^{\perp}+\langle P^{\perp}(t)\rangle+\frac{\lambda_{ij}^{\parallel}}{\lambda_{ij}^{\perp}}\cdot P^{\parallel}} \\ &\approx 1+\frac{P^{\perp}(t)-\langle P^{\perp}(t)\rangle}{P^{\perp}+\langle P^{\perp}(t)\rangle}+\frac{\lambda_{ij}^{\parallel}}{\lambda_{ij}^{\perp}}\cdot\frac{P^{\parallel}(t)}{P^{\perp}+\langle P^{\perp}(t)\rangle}\,. \end{aligned} \tag{9.4}$$

with the approach of much smaller power in parallel polarisation compared to the orthogonal one: $\frac{\lambda_{ij}^{\parallel}}{\lambda_{ij}^{\perp}}\cdot P^{\parallel}\ll P^{\perp}+\langle P^{\perp}(t)\rangle$.

However, Equation 9.4 also removes the constant power in parallel polarisation $P^{\parallel}$, which is therefore not retrievable by the following analysis. Nevertheless, the polarisation fluctuations can still be compared to the in-flight case. The in-flight observations furthermore suggest that the polarisation is mostly non-stationary, so that the smallest measured P-pol can be assumed small compared to the fluctuations in P-pol, even more because of the many samples.

To remove the fluctuating S-pol, the channel with smallest power in parallel polarisation, $\lambda_{12\mathrm{B}}^{\parallel}$, is used for subtraction:

$$\begin{aligned}\frac{\mathrm{DC}_{ij}}{\mathrm{LP}(\mathrm{DC}_{ij})|_{f_c}}-\frac{\mathrm{DC}_{12\mathrm{B}}}{\mathrm{LP}(\mathrm{DC}_{12\mathrm{B}})|_{f_c}} &= \left(\frac{\lambda_{ij}^{\parallel}}{\lambda_{ij}^{\perp}}-\frac{\lambda_{12\mathrm{B}}^{\parallel}}{\lambda_{12\mathrm{B}}^{\perp}}\right)\cdot\frac{P^{\parallel}(t)}{P^{\perp}+\langle P^{\perp}(t)\rangle} \\ &= \left(\lambda_{ij}^{\parallel}-\lambda_{12\mathrm{B}}^{\parallel}\cdot\frac{\lambda_{ij}^{\perp}}{\lambda_{12\mathrm{B}}^{\perp}}\right)\cdot\frac{P^{\parallel}(t)}{\lambda_{ij}^{\perp}\cdot(P^{\perp}+\langle P^{\perp}(t)\rangle)}\,. \end{aligned} \tag{9.5}$$

Since the transmission coefficients for orthogonal polarisation are known to be comparable $\lambda_{12\mathrm{B}}^{\perp}\approx\lambda_{ij}^{\perp}$, and in contrast to that for parallel polarisation the coefficient $\lambda_{12\mathrm{B}}^{\parallel}\ll\lambda_{ij}^{\parallel}\backslash\{\lambda_{12\mathrm{B}}^{\parallel}\}$, Equation 9.5 can be further simplified with $\left(\lambda_{ij}^{\parallel}-\lambda_{12\mathrm{B}}^{\parallel}\cdot\frac{\lambda_{ij}^{\perp}}{\lambda_{12\mathrm{B}}^{\perp}}\right)\approx\left(\lambda_{ij}^{\parallel}-\lambda_{12\mathrm{B}}^{\parallel}\right)$ to:

$$\frac{\mathrm{DC}_{ij}}{\mathrm{LP}(\mathrm{DC}_{ij})|_{f_c}}-\frac{\mathrm{DC}_{12\mathrm{B}}}{\mathrm{LP}(\mathrm{DC}_{12\mathrm{B}})|_{f_c}}\approx\frac{(\lambda_{ij}^{\parallel}-\lambda_{12\mathrm{B}}^{\parallel})\cdot\left(P^{\parallel}(t)\right)}{\lambda_{ij}^{\perp}\cdot(P^{\perp}+\langle P^{\perp}(t)\rangle)}\overset{!}{=}\frac{P^{\parallel}}{P^{\perp}}_{ij}\,. \tag{9.6}$$

The corner frequency was set to $f_c=0.1\,\mathrm{mHz}$. The low-pass filtered power together with the raw data and temperature can be seen in Figure 9.2.

At the edges of the thermal cycles, the temperature gradient decreases and the frequency of the desired polarisation effects moves closer to the corner frequency of the low-pass filter. Therefore, at the flat tops of the temperature cycles, parts of the fluctuating P-pol will be removed accidentally by the normalisation, leading to an underestimation of the P-pol. If there is further interest in the data at the short times around the edges of the temperature cycles, of course a model with linear temperature dependence could be adopted, too.

Nevertheless, in between the edges the corner frequency apparently separates the polarisation fluctuations sufficiently from other linear temperature related effects, since the remaining power

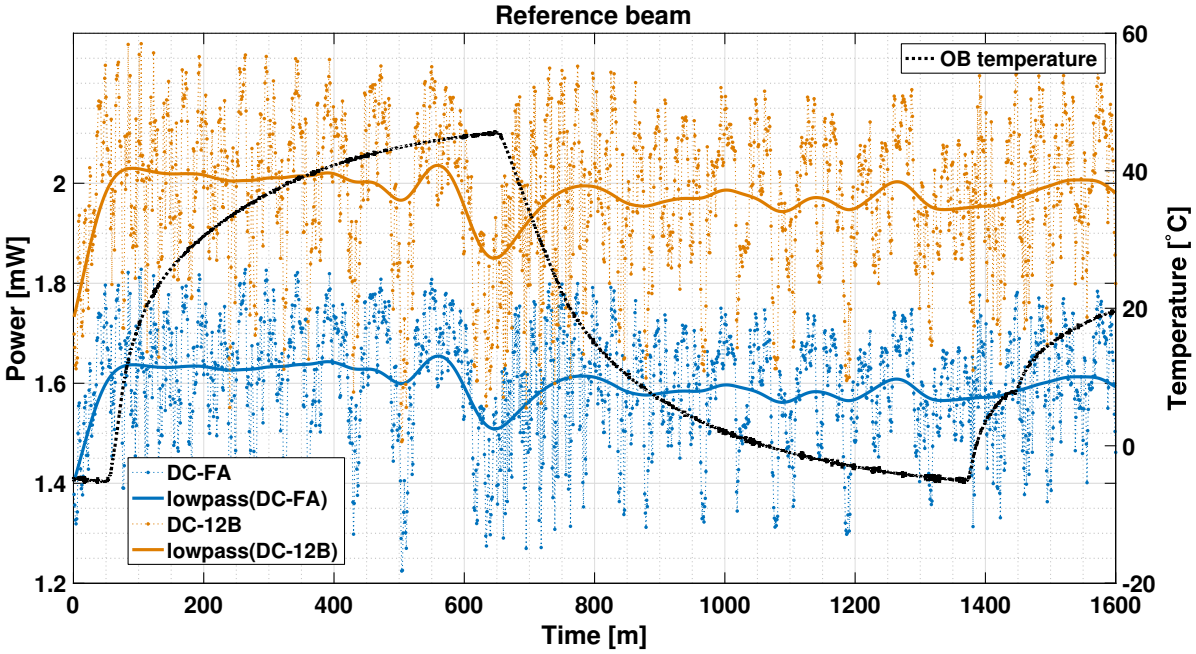

Figure 9.2.: Low-passed reference beam power on PDFA and PDFB (with highest and lowest transmission of P-pol) with corner frequency $f_c = 0.1\,\mathrm{mHz}$, together with the raw data and temperature.

after normalisation fits the typical polarisation model (see Box 7.0.1), as described in the following.

Applying the normalisation in Equation 9.6 to all PD channels (of course, except $\mathrm{DC}_{12\mathrm{B}}$) uncovers the typical power distribution pattern of parallel polarised light (see Box 7.0.1), as can be seen in Figure 9.3. $\mathrm{DC}_{\mathrm{FA}}$ has the highest amplitude of the remaining power fluctuations. The three parameters $\frac{P^{\parallel}}{P^{\perp}}_{\mathrm{FB}}$, $\frac{P^{\parallel}}{P^{\perp}}_{\mathrm{RA}}$ and $\frac{P^{\parallel}}{P^{\perp}}_{1\mathrm{A}}$ have the same but lower amplitude.

The three channels sharing the lowest level of parallel polarisation — $\frac{P^{\parallel}}{P^{\perp}}_{\mathrm{RB}}$, $\frac{P^{\parallel}}{P^{\perp}}_{1\mathrm{B}}$, $\frac{P^{\parallel}}{P^{\perp}}_{12\mathrm{A}}$ — indeed have the lowest remaining power after normalisation. The time series for $\frac{P^{\parallel}}{P^{\perp}}_{\mathrm{RB}}$ and $\frac{P^{\parallel}}{P^{\perp}}_{12\mathrm{A}}$ share the same power. For $\frac{P^{\parallel}}{P^{\perp}}_{1\mathrm{B}}$ the detected power is lower than for $\frac{P^{\parallel}}{P^{\perp}}_{\mathrm{RB}}$ and $\frac{P^{\parallel}}{P^{\perp}}_{12\mathrm{A}}$. Possibly, the remaining noise is too high for resolving these powers in the order of 10^{-3}.

Assuming reasonable numbers of $\pm 0.15\,\%$ for an offset in power between the three channels leads to an uncertainty in $\frac{P^{\parallel}}{P^{\perp}}$, as shown in Figure 9.4 by the error bars. Within these reasonable offsets, $\frac{P^{\parallel}}{P^{\perp}}_{1\mathrm{B}}$ also agrees with the pattern, described in Box 7.0.1.

A further verification of the model can be done by checking the ratio of the different amplitudes of the derived fluctuations in P-pol $\frac{P^{\parallel}}{P^{\perp}}$.

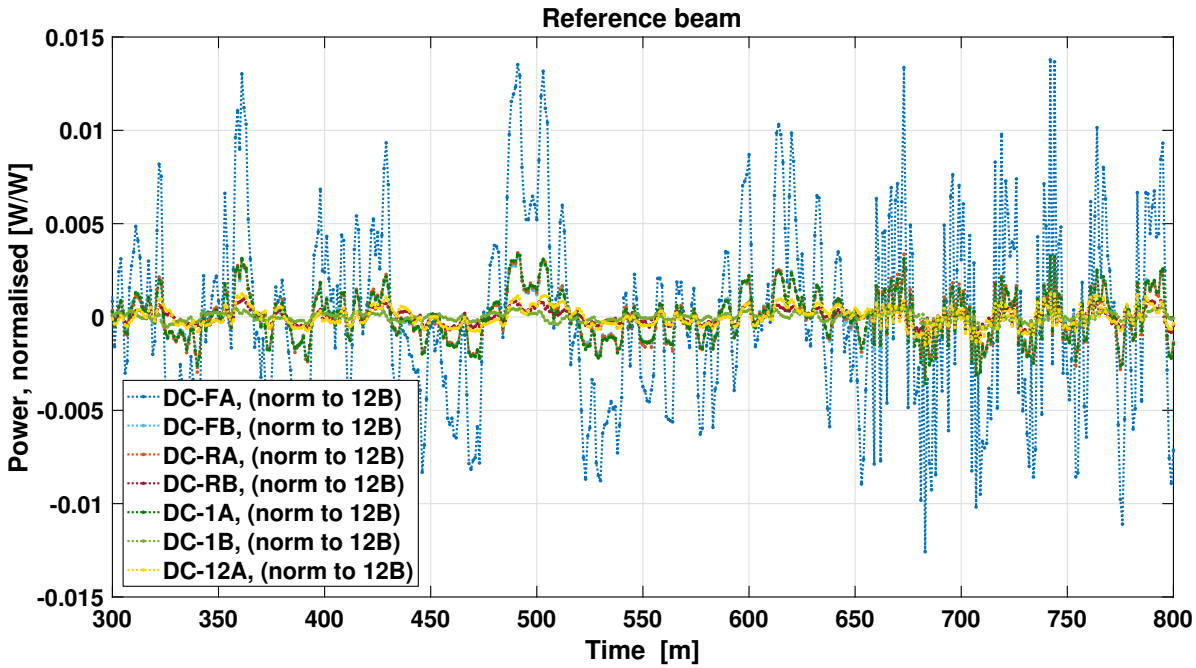

Figure 9.3.: Reference beam power, normalised with Equation 9.6. Polarisation effects following the typical pattern become visible (described in Box 7.0.1).

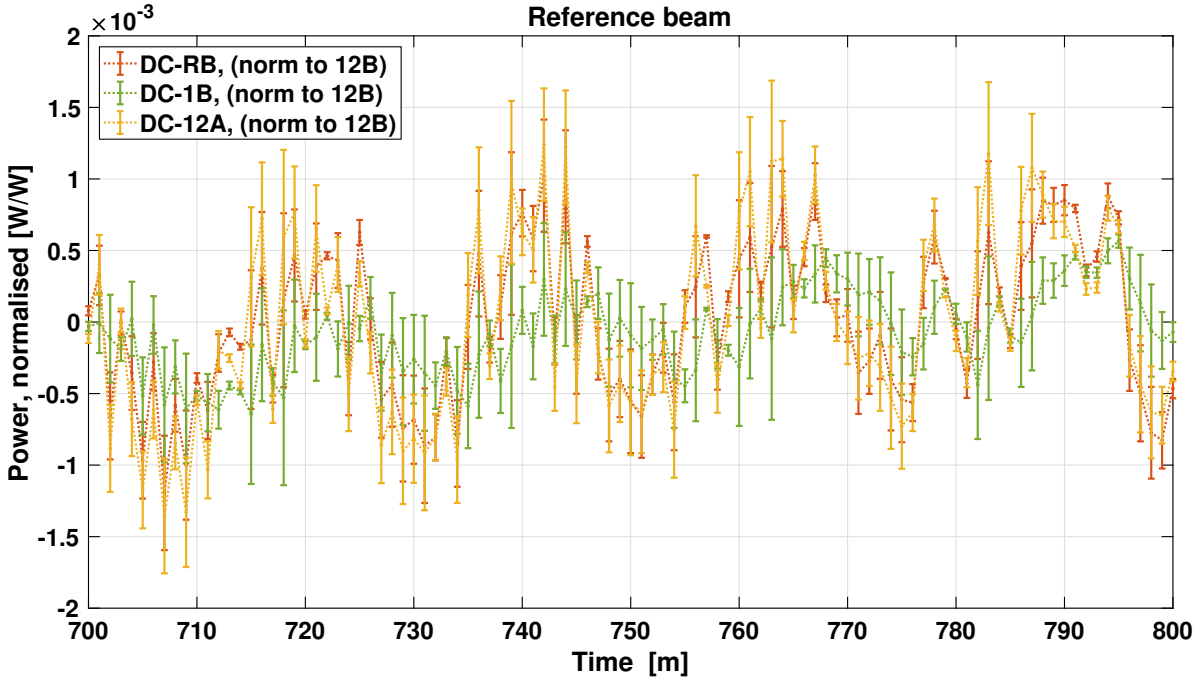

Figure 9.4.: Impact of a PD offset of ±0.15 % on the derived normalised power with Equation 9.6, for the three channels with lowest transmission of P-pol.

The model predicts a ratio of:

$$\frac{P^{\parallel}}{P^{\perp}}_{\mathrm{FA}} \cdot \left(\frac{P^{\parallel}}{P^{\perp}}_{\mathrm{ij}}\right)^{-1} \approx \frac{\lambda^{\parallel}_{\mathrm{FA}} - \lambda^{\parallel}_{\mathrm{12B}}}{\lambda^{\parallel}_{ij} - \lambda^{\parallel}_{\mathrm{12B}}} \tag{9.7}$$

$$\approx 4.1 \text{ , for } ij = \text{ FB, RA, 1A} \tag{9.8}$$

$$\approx 20 \text{ , for } ij = \text{ RB, 1B, 12A .} \tag{9.9}$$

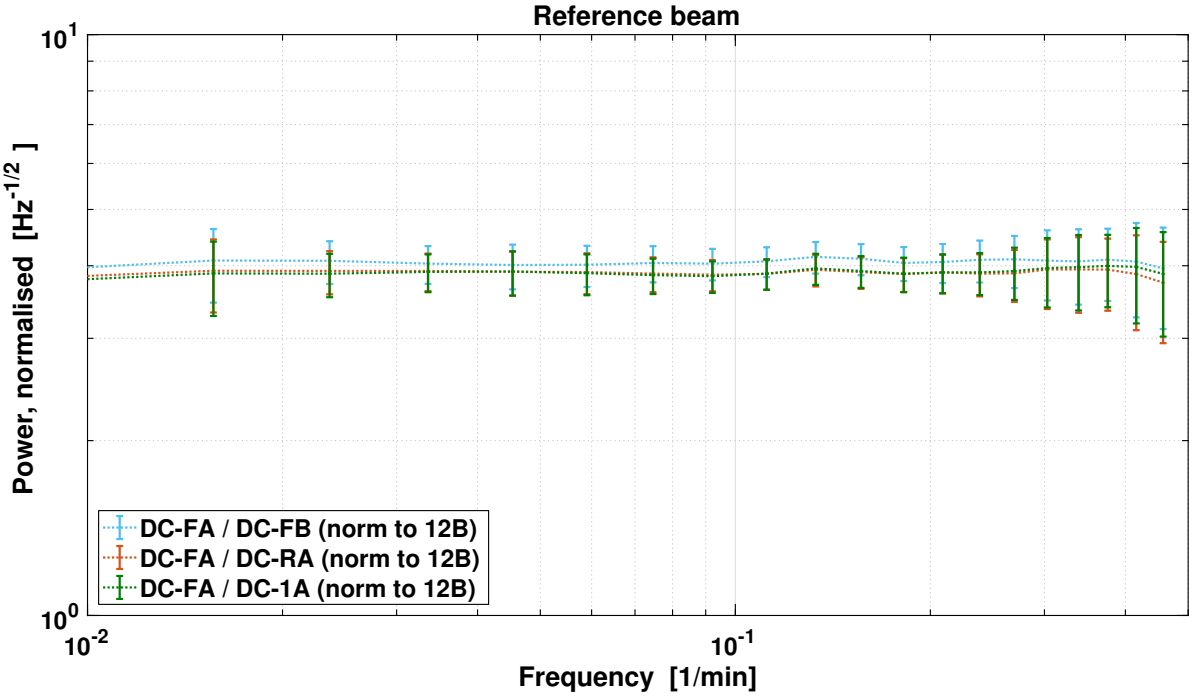

Figure 9.5.: Ratio of ASD in $\frac{P^{\parallel}}{P^{\perp}}_{\mathrm{FA}}$ to the one in $\frac{P^{\parallel}}{P^{\perp}}_{\mathrm{FB}}$, $\frac{P^{\parallel}}{P^{\perp}}_{\mathrm{RA}}$ and $\frac{P^{\parallel}}{P^{\perp}}_{\mathrm{1A}}$. The ratio agrees within errors with Equation 9.9, calculated by the propagation factors of parallel polarised light at the OB.

Figure 9.5 therefore shows the ratio of the amplitude spectral density on a logarithmic frequency scale, following Equation 9.7 for $ij =$ FB, RA, 1A . Their ratios agree within errors with the model prediction from Equation 9.8. The error bars represent the error of the so called LPSD-method [58] with a Blackman-Harris window.

The ratio between the channel with the highest and the lowest P-pol power (Equation 9.9) is dominated by the noise of the low P-pol power channels. Therefore, an estimation of the coupling factor is not reasonable. Nevertheless, within the determined huge uncertainty band of 3 to 26 (ratio of the amplitude spectral density), resulting from possible offsets, the data agrees with the prediction from Equation 9.9 .

Besides the limited validity of the channels with smallest P-pol, all tested parameters fit the model predictions. Therefore, the remaining power after normalisation with Equation 9.6 can be assumed to be parallel polarised and the corresponding quantity for a comparison to flight — the ratio of P-pol and S-pol at the beginning of the OB — can be computed via the following Equation 9.10:

$$\frac{P^{\parallel}(t)}{P^{\perp} + \langle P^{\perp}(t) \rangle} = \frac{\lambda^{\perp}_{\mathrm{FA}}}{\lambda^{\parallel}_{\mathrm{FA}} - \lambda^{\parallel}_{\mathrm{12B}}} \cdot \left(\frac{\mathrm{DC_{FA}}}{\mathrm{LP(DC_{FA})}|_{f_c}} - \frac{\mathrm{DC_{12B}}}{\mathrm{LP(DC_{12B})}|_{f_c}} \right) . \tag{9.10}$$

For this purpose, of course $\frac{P^{\parallel}}{P^{\perp}}_{\mathrm{FA}}$ is used, because it is most sensitive to parallel polarised light and therefore has the lowest impact of remaining noise.

The computed power in parallel polarisation is plotted together with the one for the measurement beam at the end of this Chapter in Figure 9.9.

9.2. Measurement beam

As previously mentioned, the measurement beam could only be detected by the rigid interferometers. Therefore, Figure 9.6 shows the power of the measurement beam on all available diodes, the ones from the reference and frequency interferometers, together with the OB temperature.

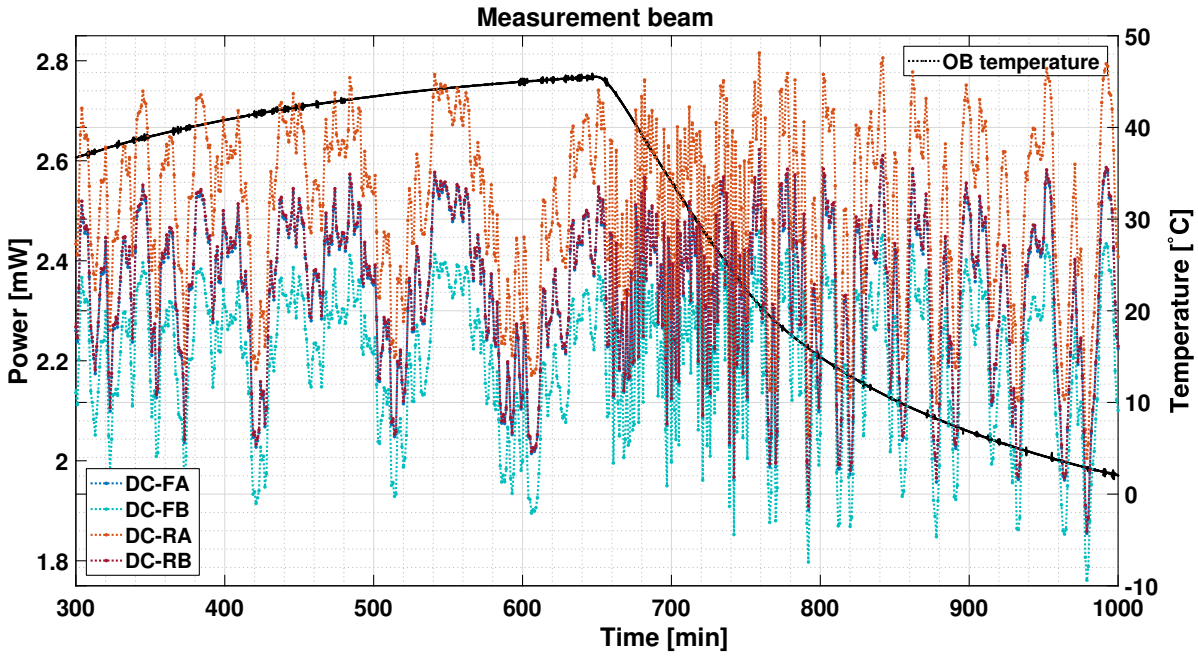

Figure 9.6.: Measurement beam power during thermal cycling of the LPF OB prior to flight, together with OB temperature.

For normalisation, following Equation 9.6, the channel $\mathrm{DC_{RA}}$ is used, because the one with lowest P-pol — the $\mathrm{DC_{12A}}$ channel — is not available. $\mathrm{DC_{RA}}$ has one BS transmission more than $\mathrm{DC_{12A}}$, so that not only all common mode fluctuations in S-pol cancel, but also $\frac{\lambda^{\parallel}_{\mathrm{RA,\,MB}}}{\lambda^{\perp}_{\mathrm{RA,\,MB}}} \approx 27\,\%$ (compare to Equation 8.1) of the parallel polarised light. Figure 9.7 shows the measurement beam power normalised by $\mathrm{DC_{RA}}$.

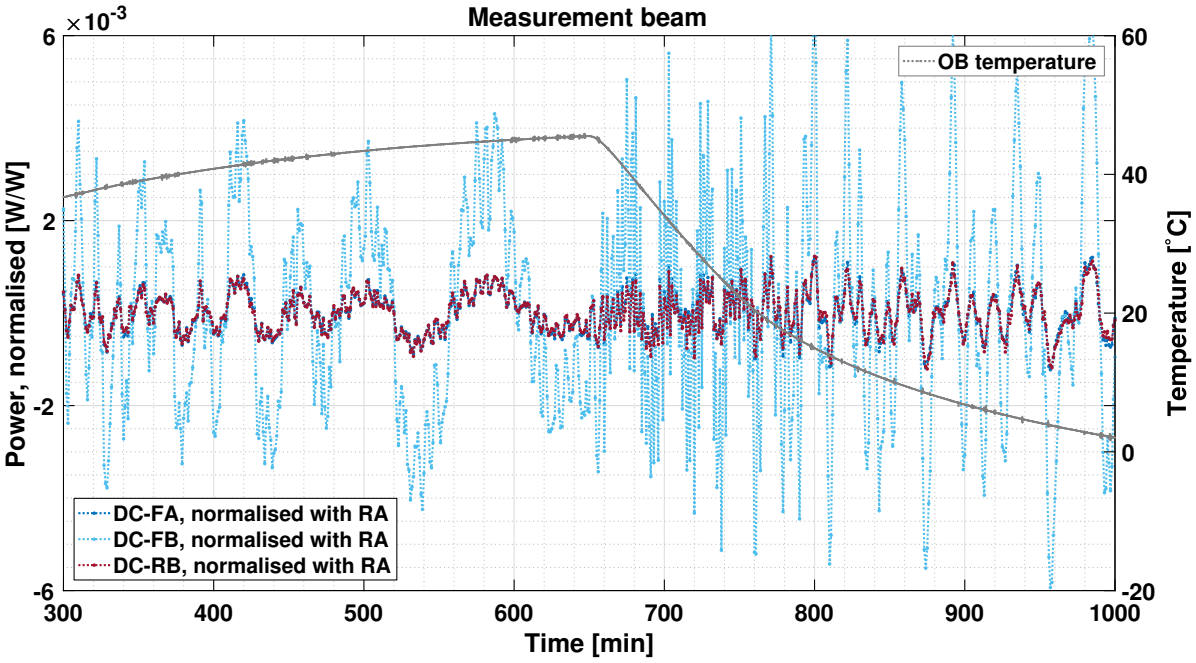

Figure 9.7.: Measurement beam power, normalised by Equation 9.6 (with DC_{RA} instead of DC_{12B}). Again, the remaining power follows the typical polarisation pattern (described in Box 7.0.1)

Again, the typical pattern of power distribution for parallel polarised light becomes visible. As for the reference beam, the model can be verified by the ratio in amplitude between $\frac{P^{\parallel}}{P^{\perp}}_{\mathrm{FB}}$ (most sensitive to P-pol for the measurement beam) and $\frac{P^{\parallel}}{P^{\perp}}_{\mathrm{FA}}$ and $\frac{P^{\parallel}}{P^{\perp}}_{\mathrm{RB}}$.

For comparison between the two beams, the reference beam is renormalised with Equation9.6 to DC_{RB} — the neighbouring diode to the one used for the measurement beam, having the same transmissivity of reference beam power for P-pol like DC_{RA} for the measurement beam.

As a result, Figure 9.8 shows the ratio of P-pol between the channel with highest P-pol and the two channels with the lower P-pol (having one BS reflection) in both beams presented as an ASD with logarithmic frequency scale.

The predicted ratio in amplitude by Equation 9.7 for the different normalisation with DC_{RA} for the measurement beam and DC_{RB} for the reference beam computes to:

$$\begin{aligned} &\frac{\lambda^{\parallel}_{\mathrm{FA,\,RB}} - \lambda^{\parallel}_{\mathrm{RB,\,RB}}}{\lambda^{\parallel}_{ij,\,\mathrm{RB}} - \lambda^{\parallel}_{\mathrm{RB,\,RB}}} \approx 4.9 \text{ , for the reference beam and } i = \mathrm{FB/RA} \\ \approx &\frac{\lambda^{\parallel}_{\mathrm{FB,MB}} - \lambda^{\parallel}_{\mathrm{RA,\,MB}}}{\lambda^{\parallel}_{ij,\mathrm{MB}} - \lambda^{\parallel}_{\mathrm{RA,\,MB}}} \text{ , for the measurement beam and } i = \mathrm{FA/RB}\,. \end{aligned} \tag{9.11}$$

Figure 9.8 shows a good agreement with the prediction from Equation 9.11 within errors, for both beams. Hence, the ratio of P-pol and S-pol can be estimated for the measurement beam by $\frac{P^{\parallel}}{P^{\perp}}_{\mathrm{FB}}$ and Equation 9.10 (adapted to the different normalisation with DC_{RA}), as well.

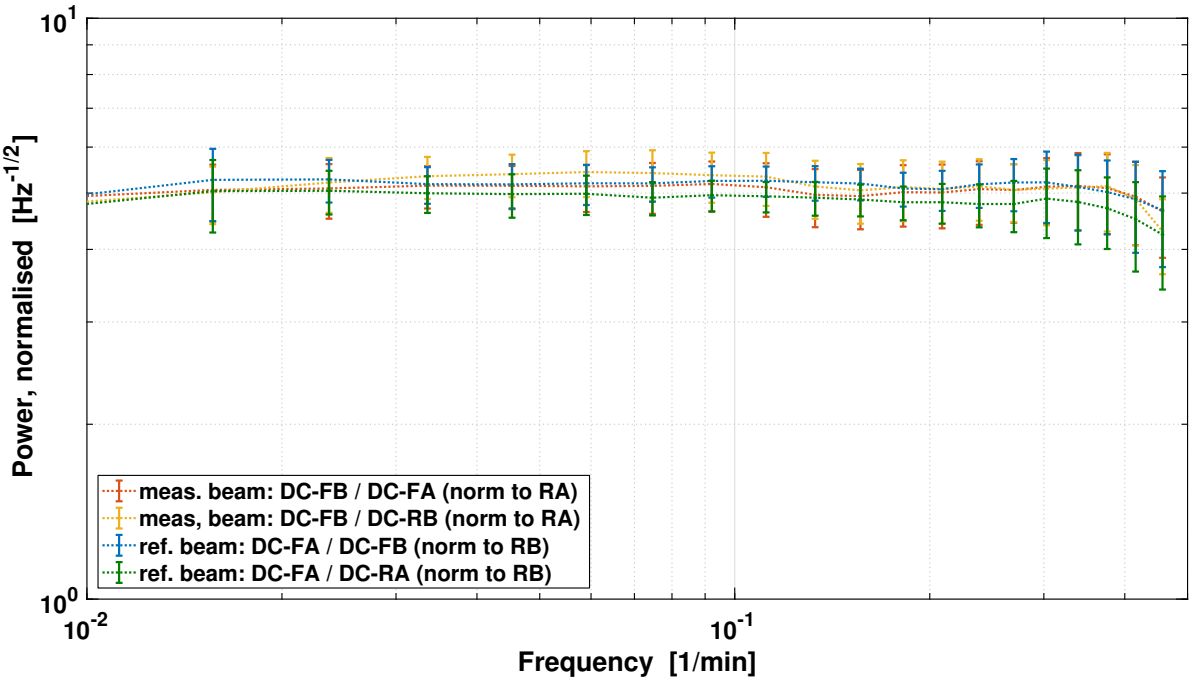

Figure 9.8.: Ratio of the ASD in $\frac{P^{\parallel}}{P^{\perp}}_{\mathrm{FB}}$ to the one in $\frac{P^{\parallel}}{P^{\perp}}_{\mathrm{FA}}$ and $\frac{P^{\parallel}}{P^{\perp}}_{\mathrm{RB}}$.The ratios agree within errors with the prediction in Equation 9.11, determined for the distribution of parallel polarised light.

Therefore, Figure 9.9 shows the main result of fluctuations in P-pol during the pre-flight thermal tests, for both beams.
Surprisingly, the amount of parallel polarised light on the OB is bigger for the reference beam than for the measurement beam, as found with the flight data. This is again a hint to the PBSs as being the responsible component for the observed effects. There could possibly be an unknown effect that influences the transmission of parallel polarised light through the PBS and this effect seems to be stronger for the particular component in the reference beam. However, besides this, the overall power in parallel polarisation is almost an order of magnitude weaker than in-flight.

The error bars in Figure 9.9 represent the propagated, systematic error of possible PD offsets, of $\pm 0.15\,\%$. However, also a systematic error from the maximum deviation in the fit of the BS splitting ratio, propagated to the propagation factors in Equation 9.10, needs to be considered. It determines to be lower than $5\,\%$.

For a comparison to the in-flight observations, the span between the maximum and minimum measured ratio of P-pol to S-pol is derived. It determines to be $(6.1 \pm 0.4) \cdot 10^{-3}$ for the reference beam and $(3.8 \pm 0.3) \cdot 10^{-3}$ for the measurement beam, considering the systematic errors from the propagation factors and the PD offsets.

The correlation to temperature, shown in Figure 9.10, seems to have a periodic nature, as already suspected for the flight data set. However, as can be seen by comparing the heating and cooling period, the related effect seems to be slow. During the high temperature gradient phase at low temperatures for the heating period (and high temperatures for the cooling

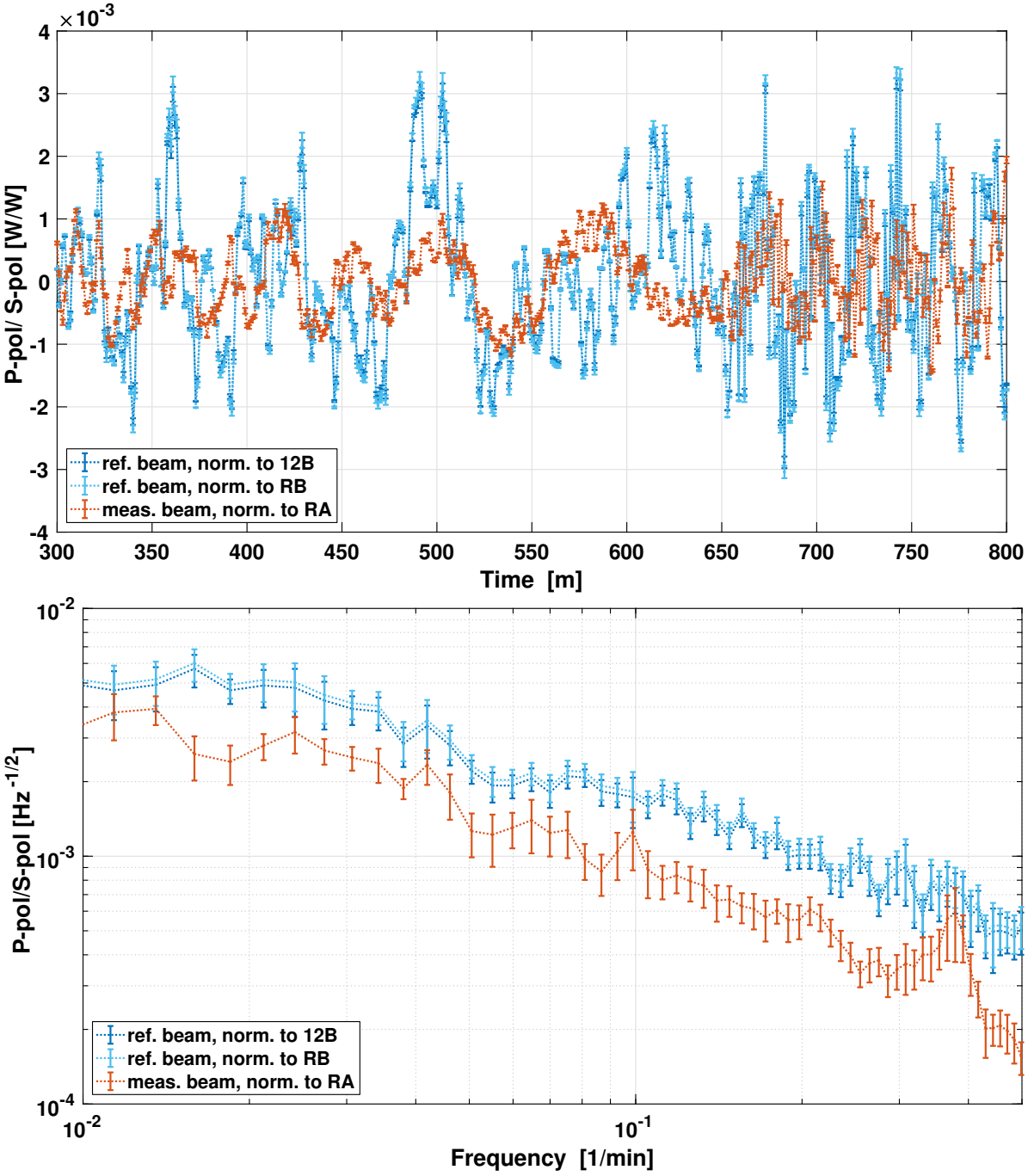

Figure 9.9.: Fluctuations in parallel polarisation of both beams, normalised to the power in orthogonal polarisation. For the reference beam two time series are shown, estimated with two different normalisation diodes.

period), the changes in $\frac{P^{\parallel}}{P^{\perp}}$ per 1 °C are smaller than during the low temperature gradient periods. Such a behaviour would be expected for the output polarisation of the fibres due to temperature induced stress. However, the output polarisation should be cleaned by the PBSs on the OB.

The next step for understanding the observations is a closer look at the PBSs in the FIOSs. Therefore, three identically constructed flight spare PBSs (kindly provided by the University of Glasgow) were analysed experimentally, as described in the following Chapter 10.

Box 9.2.1 | Summary: Pre-flight single beam powers during thermal cycling of the OB

- The OB was exposed to thermal cycles within a vacuum chamber with a range of 50 °C around room-temperature.
- The single beam powers were measured with 0.016 Hz.
  - There is plenty of data available for the analysis.
- There was no control of the power on the OB.
  - → Consequently, high power fluctuations with a range of up to 40 % are affecting the analysis.
  - → Nevertheless, the polarisation-induced noise could be isolated.

Analysis results:

- **The reference beam has higher fluctuations** in P-pol than the measurement beam.
  - → This corresponds to the in-flight observations.
- **However**: the measured P-pol is in **both beams weaker than in-flight** by almost an order of magnitude.

Open Questions:

- Why was the effect weaker on ground?
- Why was more P-pol detected in the reference beam, on ground **and** during flight?

→ **Next step** focuses on the PBSs in the FIOS.

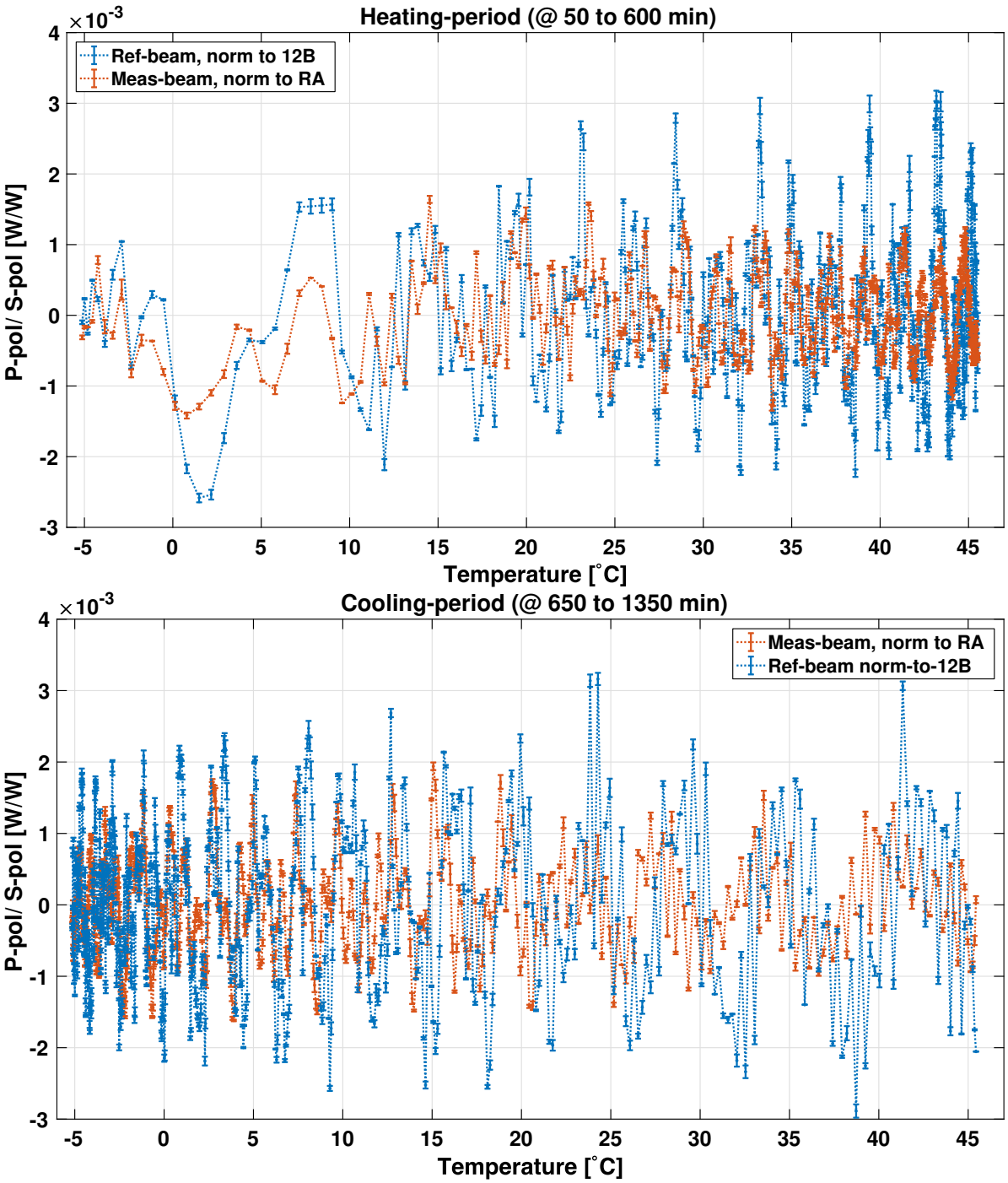

Figure 9.10.: Parallel polarisation of both beams, scattered with the OB temperature. A periodic correlation between temperature and P-pol is apparent. The greater period length at low temperatures during the heating period and higher temperatures during the cooling period furthermore appear to be the effect of a delay, when compared to the temperature gradient (compare to Figure 9.2).

10. Origin of off-nominal polarisation on the OB: Discussion of possible mechanism

In Chapter 8, polarisation fluctuations of the two beams on the LPF OB were identified to cause the in-flight low-frequency power noise (see Figure 7.1). This is surprising, because the light, transmitted to the OB, was cleaned in polarisation by a PBS (as described in Section 2.2). In the following, therefore, possible mechanism are discussed that could have led to the increased off-nominal polarisation out of the PBS.

The PBS was mounted with a rotation of $\approx 3°$ against the incident beam, to avoid back reflections into the beam path. However, this rotation has an effect on the transmitted polarisation through the PBS, due to geometry. This effect is described in Box 10.0.1 for a simplified "perfect PBS".

Box 10.0.1: PBS rotation — Impact on P-pol transmission

A rotation of the PBS around its (vertical) z-axis changes the angle of incidence to the active coating inside the cube, as depicted in Figure 10.1.
The angle of incidence to an optical multilayer coating generally has an impact on the optical properties of the coating.
For correct modelling, the structure of the multilayer system needs to be known. Since this information is not accessible, only the simplified effect of rotating a "perfect PBS" is computed. The terminus "perfect PBS" here implies that it is able to transmit all light, being parallel polarised to its optical axis and reflect all light, being orthogonal polarised to it ([25], page 238). Note that parallel polarised light to the optical axis of LPFs PBS is called S-pol, following the nomenclature described in Chapter 8.

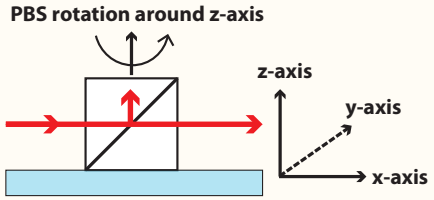

Figure 10.1.: Sketch of a PBS rotation around its vertical axis.

The beam, $\vec{k}$, hitting the PBS is w.l.o.g. defined to point in x-direction with components of the electric field $\vec{E}_y$ and $\vec{E}_z$

$$\vec{k} = k \cdot \hat{e}_x = k \cdot \begin{pmatrix} 1 \\ 0 \\ 0 \end{pmatrix}, \qquad \vec{E}_y = E_y \cdot \hat{e}_y = E_y \cdot \begin{pmatrix} 0 \\ 1 \\ 0 \end{pmatrix}, \qquad \vec{E}_z = E_z \cdot \hat{e}_z = E_z \cdot \begin{pmatrix} 0 \\ 0 \\ 1 \end{pmatrix}. \tag{10.1}$$

The incident S-pol and P-pol on LPF are defined with respect to the OB. Therefore $|\vec{E}_y|^2 = {E_y}^2$ gives the P-pol and $|\vec{E}_z|^2 = {E_z}^2$ the power in S-pol.

The PBS splits incoming light into two beams with polarisations orthogonal to one another. The polarisations of these two individual beams are defined by the direction of the incoming beam and the PBS's active surface with normal, $\hat{n}_{\mathrm{PBS}}$.
The plane of incidence that contains the incoming, the reflected and the transmitted beam, is given by its normal:

$$\hat{n}_{\mathrm{Inc}} = \frac{\hat{n}_{\mathrm{PBS}} \times \vec{k}}{\left|\hat{n}_{\mathrm{PBS}} \times \vec{k}\right|} \,. \tag{10.2}$$

The part of the beam that is oscillating orthogonal to the plane of incidence and parallel to the PBS active surface, is reflected. The electric field vector of the **reflected beam**, therefore, points in the same direction as the normal of the plane of incidence:

$$\hat{e}_{\mathrm{refl.}} = \hat{n}_{\mathrm{Inc}} \,. \tag{10.3}$$

The corresponding amplitude of the reflected beam is given by scalar projection of the incoming field vector onto the reflected one: $E_{\mathrm{refl.}} = \left(\vec{E}_y + \vec{E}_z\right) \cdot \hat{e}_{\mathrm{refl.}}$.

The components of the electrical field, oscillating in the plane of incidence are transmitted through the PBS. The electric field vector of the **transmitted beam** therefore has a direction of:

$$\hat{e}_{\mathrm{transm.}} = \frac{\vec{k} \times \hat{n}_{\mathrm{Inc}}}{\left|\vec{k} \times \hat{n}_{\mathrm{Inc}}\right|} = \frac{\vec{k} \times \left(\hat{n}_{\mathrm{PBS}} \times \vec{k}\right)}{\left|\vec{k} \times \left(\hat{n}_{\mathrm{PBS}} \times \vec{k}\right)\right|} \,, \tag{10.4}$$

with the corresponding amplitude, given by scalar projection of the incoming field vector onto the transmitted one: $E_{\mathrm{transm.}} = \left(\vec{E}_y + \vec{E}_z\right) \cdot \hat{e}_{\mathrm{transm.}}$.

The PBS active surface (as built on LPF) is given by the normal:

$$\hat{n}_{\mathrm{PBS}} = \frac{1}{\sqrt{2}} \cdot \begin{pmatrix} -1 \\ 0 \\ 1 \end{pmatrix} \,. \tag{10.5}$$

A rotation of the PBS by an angle φ around the z-axis, $\hat{e_z}$, gives a rotated normal in the OB coordinate system of:

$$\hat{n}^{\mathrm{rot}}_{\mathrm{PBS}} = D(\varphi)^z \cdot \hat{n}_{\mathrm{PBS}} = \begin{pmatrix} \cos(\varphi) & -\sin(\varphi) & 0 \\ \sin(\varphi) & \cos(\varphi) & 0 \\ 0 & 0 & 1 \end{pmatrix} \cdot \hat{n}_{\mathrm{PBS}} = \frac{1}{\sqrt{2}} \cdot \begin{pmatrix} -\cos(\varphi) \\ -\sin(\varphi) \\ 1 \end{pmatrix} \,. \tag{10.6}$$

Note that in a right-handed coordinate system the active rotation (positive rotation angle) is counter-clockwise.
The front surface of the PBS cube also needs to be considered.
For any PBS rotation angle, φ_{PBS} (different from 0°), the transmitted beam is refracted into the cube made of fused silica. The angle of incidence, φ_{Inc}, between beam and active surface is therefore given by:

$$\sin(\varphi_{\mathrm{Inc}}) = \frac{1}{n_{\mathrm{fs}}} \sin(\varphi_{\mathrm{PBS}}) \,. \tag{10.7}$$

The direction of the electric field vector transmitted through the rotated PBS is then

given by:

$$\hat{e}^{\text{rot}}_{\text{transm.}} = \frac{\vec{k} \times \left(\hat{n}^{\text{rot}}_{\text{PBS}} \times \vec{k}\right)}{\left|\vec{k} \times \left(\hat{n}^{\text{rot}}_{\text{PBS}} \times \vec{k}\right)\right|} = \frac{1}{\sqrt{1 + (\frac{1}{n_{\text{fs}}} \sin(\varphi_{\text{PBS}}))^2}} \cdot \begin{pmatrix} 0 \\ \frac{1}{n_{\text{fs}}} \sin(\varphi_{\text{PBS}}) \\ 1 \end{pmatrix} . \tag{10.8}$$

The electric field vector of the reflected beam has the direction:

$$\hat{e}^{\text{rot}}_{\text{refl.}} = \frac{\hat{n}^{\text{rot}}_{\text{PBS}} \times \vec{k}}{\left|\hat{n}^{\text{rot}}_{\text{PBS}} \times \vec{k}\right|} = \frac{1}{\sqrt{1 + (\frac{1}{n_{\text{fs}}} \sin(\varphi_{\text{PBS}}))^2}} \cdot \begin{pmatrix} 0 \\ 1 \\ \frac{1}{n_{\text{fs}}} \sin(\varphi_{\text{PBS}}) \end{pmatrix} . \tag{10.9}$$

The **share of P-pol in the transmitted light** can furthermore be derived by scalar projection of the normalised transmitted electric field vector onto $\hat{e}_y$, which is parallel to the OB:

$$\left|\hat{e}^{\text{rot}}_{\text{transm.}} \cdot \hat{e}_{\text{y}}\right|^2 = \frac{(\frac{1}{n_{\text{fs}}} \sin(\varphi_{\text{PBS}}))^2}{1 + (\frac{1}{n_{\text{fs}}} \sin(\varphi_{\text{PBS}}))^2} \overset{\text{taylor-exp.}}{\approx} \left(\frac{\varphi_{\text{PBS}}}{n_{\text{fs}}}\right)^2 . \tag{10.10}$$

Note that this share of parallel polarisation in the transmitted beam is the relevant quantity for a comparison to the P-pol on the OB of LPF (since the reflected beam is dumped and only the transmitted beam is detected).

For small PBS rotation angles and an input beam with power P_{in} and orthogonal polarisation, $E_y = 0$ and $E_z = \sqrt{P_{\text{in}}}$, almost all power is transmitted through the PBS:

$$\begin{aligned} \left|\vec{E}_{\text{transm.}}\right|^2 &= \left|\sqrt{P_{\text{in}}} \cdot \hat{e}_z \cdot \hat{e}_{\text{transm.}}\right|^2 \\ &= \left|\frac{\sqrt{P_{\text{in}}}}{\sqrt{1 + (\frac{1}{n_{\text{fs}}} \sin(\varphi_{\text{PBS}}))^2}}\right|^2 \overset{\text{taylor-exp.}}{\approx} P_{\text{in}} . \end{aligned} \tag{10.11}$$

The reflected power for the same input beam (power P_{in} with orthogonal polarisation) and small PBS rotation angles is given by:

$$\left|\vec{E}_{\text{refl.}}\right|^2 = \left|\sqrt{P_{\text{in}}} \cdot \hat{e}_z \cdot \hat{e}_{\text{refl.}}\right|^2 \overset{\text{taylor-exp.}}{\approx} P_{\text{in}} \cdot \left(\frac{\varphi_{\text{PBS}}}{n_{\text{fs}}}\right)^2 . \tag{10.12}$$

Therefore, the ratio of reflected to input power is equivalent to the ratio of P-pol to transmitted power for an orthogonal polarised input beam.

As already mentioned above, the active surface is a multilayer coating, designed to have the desired properties for a specific angle of incidence. Next to the geometrical change of orthogonal and parallel polarised light towards the active surface, the coating performance is also a function of the PBS rotation angle. This effect is not generally computable due to different designs of the coatings. Therefore, in the following, the output polarisation is experimentally determined for a flight spare PBS rotation around the z-axis.

By Equation 10.10 in Box 10.0.1 it can be seen that the 3° PBS rotation on LPF leads to a tiny and constant amount of 0.13 % P-pol on the OB, but not to any fluctuations in the order of percent, as derived from the flight data set.

A real PBS of course is not able to transmit a perfectly clean polarisation state. The polari-

sation cleaning efficiency is defined by the so-called Polarisation Extinction Ratio (PER). It describes the part of the incoming light that should be reflected, but is transmitted instead [59, 60]. Typical values for extinction ratios of standard cube PBSs are better than 1:1000 (for example [61]). The incident light to the PBS should have been polarised close to S-pol, because the laser has a nominal orthogonal output polarisation and the fibres, guiding the light to the OB, are polarisation maintaining.
Therefore, the transmitted part of P-pol through the PBS should have been much smaller than observed with the QPDs at the interferometer outputs on LPF. Possibly, the polarisation was affected between the FIOS and the QPDs.
However, there are arguments ruling out a rotation of a clean S-pol polarisation state on the OB, behind the PBS. On the one hand side, the model, derived in Section 8.2, is consistent with a constant amount of P-pol coming out of the PBS and being split up into the different interferometers. On the other hand, the observed correlation with the power control signal (see Section 8.4) indicates an origin of the P-pol before or at the PBS.
Therefore, all evidence points to the PBSs as the origin of the P-pol on the OB.

As a consequence the question is, what could have happened to the PBS, so that a share of up to 4.5 % of parallel polarised light is being transmitted to the OB.
In principle, there are **two mechanisms** that could have led to an increase of the transmitted P-pol through the PBSs.

The first one is a **degradation of the PER**. An increase in incident off-nominal polarised power would lead to more reflection at the PBS and also to more P-pol on the OB.
However, the degradation of the PER would have needed to be unrealistically high in order to explain the observed effects. Therefore, a degradation of the PER was rejected as the responsible mechanism at that time.

The second mechanism is a **rotation of the PBS optical axis**, as described for a rotation around the z-axis in Box 10.0.1. The incident light would be projected onto the rotated PBS optical axis and split into parallel and orthogonal polarised beams relative to this rotated axis. The reflected beam, as well as the transmitted beam would then be a superposition of S-pol and P-pol in the coordinate system of the OB. As a consequence, more P-pol would be detected on the OB, depending on the rotation angle of the PBS axis . For an orthogonal input polarisation, the reflected power at the PBS would also be increased, leading to a correlated power control signal.

Geometrically, the share of P-pol in transmitted power through a rotated PBS is equivalent to the ratio of reflected and incident power for orthogonal input polarisation (compare to Box 10.0.1). The correlation between the amplitude control signal (the RF power) and the transmitted P-pol to the OB (see Section 8.4) has a translation coefficient lower than one and is furthermore different for the two beams. For an input polarisation state, different from S-pol, a rotation of the PBS optical axis (away from the nominal one) could also have led to less reflected power at the PBS (and therefore more transmitted power to the OB). In consequence, the correlation between power control signal and transmitted P-pol would have been negative. Since this disagrees with the observations, a direct correlation between the PBS axis rotation and the control signal was assumed to be unlikely. The observed correlation could of course have been a result of a correlation to another variable, not yet known, that influences both — the PBS axis and the incident power or polarisation at the PBS.

Subsequently, the next question is, what could have caused such an effect. The most obvious parameter is the influence of temperature.

A change in temperature could have led to a different refractive index and an expansion or tightening of the materials in the PBS. This could have changed the optical path lengths in the PBS or the multiple layers and thus its optical properties. A presumed periodic correlation of the effect with temperature would have at least 3 periods in 20 °C (see correlation with temperature in Section 8.4). The optical path length for 1 cm of fused silica would decrease by half a wavelength in one period ($n = 1.45$ and $\mathrm{d}n/\mathrm{d}T \approx -7.5 \times 10^{-6}/\mathrm{K}$, [62] for $\lambda = 1064\,\mathrm{nm}$). However, the rotation of the PBS around its vertical axis is avoiding back reflections into the beam path, which might have caused an interference signal. Therefore, a coupling of the optical path through the PBS is not relevant. On the other hand, the thickness of the layers in the optical coating is only about half a wavelength small. Therefore, there is no effect on the optical properties expected in a range of 20 °C.

So, the next idea was: a change of the PBS optical properties by mechanical stress. Mechanical stress can change the refractive index of materials and according to the spatial distribution also lead to birefringence ([25] page 241). The PBS made of fused silica is glued to the FIOS base plate, also made of fused silica. However, the base plate itself is bonded with a sidelong mount to the OB, made of Zerodur (compare to Section 2.2). This mount was already designed to reduce temperature induced mechanical stress.

Therefore, a change in temperature could have introduced mechanical stress by the different expansion coefficients of fused silica, Zerodur and glue. This stress-induced birefringence could have changed the phase relation of the interfering beams, reflected at the multiple layers of the PBS active surface. As a consequence, the optical properties of the whole coating could have been changed, in dependence on the temperature.

Hence, the current best theory was found: Temperature changes on the OB could have induced mechanical stress at the PBS that changed its optical properties.

The following Chapter 11, therefore, describes the search for a corresponding effect, somewhere in the parameter space of mechanical stress, temperature, PBS rotation and input polarisation.

Box 10.0.2 | Summary: Origin of low-frequency power noise

The previous analysis shows:

- There is off-nominal polarised power transmitted to the OB, with fluctuating intensity.
- However: **the PBS should have cleaned the polarisation state entering the interferometers**.

  → What could have caused this disagreement?

Possible reasons for the increase of P-pol on the OB:

- Polarisation cleaning could have failed — incident P-pol could have been transmitted to the OB.

→ However, a huge increase of PER would be needed to agree with the observations.

- The PBS optical axis could have been unstable.
  → A rotation of the axis could have changed the output polarisation of the PBS.

Resulting best theory at that time:

- The PBS axis could have been tilted by mechanical stress, induced by different temperature expansion coefficients of the FIOS.

Next questions:

- How does the PBS behave when applied to mechanical stress?
- How much stress is expected for the particular PBS mounting on LPF?

11. Laboratory analysis of flight spare hardware: Properties of the PBS and sensitivity to mechanical stress

The current best theory before starting the laboratory analysis was a mechanical stress-induced change of the PBS optical properties, as discussed in Chapter 10.

Modelling the induced stress at beam height could be affected by large errors, due to possible shear stress in the crystal. Therefore, it was decided to first experimentally investigate possible effects in the multiple parameter space of mechanical stress, PBS rotation and temperature, as described in the following.

11.1. Setup for the analysis of the PBS optical properties

The experimental investigations of stress-induced effects on the PBS optical properties were performed together with Laura Mueller as part of her Bachelor thesis. A detailed description for some of the experiments can be found in her thesis [57].

The most important part in the laboratory setup obviously was the PBS itself. Fortunately, three LPF flight spare PBSs were provided by the University of Glasgow (where the LPF OB was built), for the experimental analysis. Furthermore, an appropriate mount, allowing the application of homogeneous pressure and an optical read-out setup, sensitive to polarisation, were built. Conveniently, a laser beam could be adopted from the LPF engineering model [63, 64]. For polarisation sensitive detection of the light, a polarimeter was used. To probe the desired parameter space, the PBS mount had to fulfil the conditions, listed below:

1. It should allow for the application of homogeneous mechanical stress by setting the PBS under pressure.
2. This implies that
   - the pressure is linearly distributed onto the surface of the PBS,
   - the pressure is stable in time,
   - and well-defined in magnitude.
3. The mount should also be extendible to shear stress application by inhomogeneous distribution of the pressure.

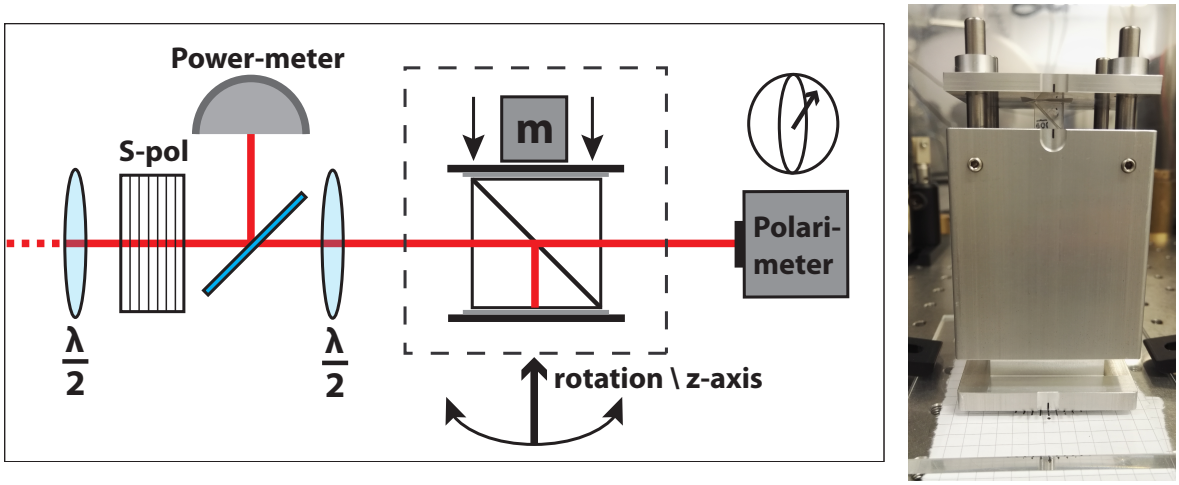

Figure 11.1.: Sketch of the laboratory set up for analysis of stress effects on an LPF flight spare PBS, **To the right**: Photography of the dedicated mount.

4. The PBS needs to be rotatable around the axis normal to the surface of stress application, to allow for a variation of the angle of incidence.

    - The applied pressure should be independent on the PBS rotation.

A very simple and stable possibility for stress application is the use of gravity, via weights. To qualitatively probe the parameter space no vacuum was needed in the first place. This allowed to change the size of a weight, without evacuating a chamber each time. Therefore, a convenient system was found that is easy to calibrate and also easily adaptable to modifications.

The PBS mount designed to meet the requirements listed above is shown to the right of Figure11.1. It provides an inset (1 mm larger than the PBS footprint) to reproduce the alignment when replacing the sample. Four posts at the outer edges of the mount guide a plate down onto the sample, avoiding shear stress by a tilted plate. The weights can be placed directly onto that plate. The whole mount (together with the weight on top) is continuously rotatable around its z-axis with a degree resolution for the angular read-out.

The full set-up is shown in the left of Figure 11.1. The incoming laser beam has a wavelength of 1064 nm and is nominally orthogonal polarised to the optical bench. It is reduced to a few milliwatts by the internal power stabilisation of the laser itself. For fine adjustment of the power, a combination of a $\frac{\lambda}{2}$-plate and a polarisation filter is used. The applied power can be monitored behind the filter by a pick-off (a glass plate) and a power-meter. Furthermore, the polarisation can be linearly rotated by another $\frac{\lambda}{2}$-plate. Then, the beam is guided to the PBS in its dedicated mount. The transmitted beam is analysed by a polarimeter (a PAX 1000 from Thorlabs [65]), while the reflected beam is blocked in the mount itself by diffuse scattering at an abrasive blasted surface. Remaining back-reflection would be reflected again at the PBS', active surface, or transmitted to the upper surface of the mount. However, both of these ghost-beams are offset the main beam and point in a different direction, since the PBS's active surface is tilted by rotation of the PBS. Therefore, a disturbance of the measurement of transmitted power by the PBS reflection is negligible.

11.2. Transmission of orthogonal polarised light through the PBS

For the first experiment series, described in the following, the flight spare PBS — labelled as PBS1 — was used. The transmission of a linear nominally polarised beam through PBS1 was analysed with the setup described in 11.1 for the variation of different parameters.

11.2.1. Influence of a PBS rotation against the incident beam

At first, the relation between a PBS rotation around its vertical axis and the transmission of parallel polarised light was investigated to be compared to the prediction for a simplified PBS, as described in Box 10.0.1.

Therefore, PBS1 was rotated with its mount between −20 and 20 degrees towards the incoming beam. The input light was orthogonal polarised and of comparable power to the in-flight LPF environment. The transmitted light was analysed in polarisation with the polarimeter and cross-checked also with polarisation filters and power meters. The average P-pol transmission of twelve measurements is shown in Figure 11.3 by the red data points together with the theoretical prediction for a simplified PBS from Equation 10.10.

For larger rotations $> 5°$ the measured P-pol transmission is slightly higher than the predicted value (up to $3 \cdot 10^{-3}$). This could be a consequence of the coating efficiency, which is a function of the PBS rotation, as well.

Furthermore, the ellipticity of the transmitted light was measured. The analysis showed, that in contrast to the S-pol and P-pol, their phase relation (defining the ellipticity) was not reproducible within the measurements. A reason for that could be a change of the beam spot on the active surface inside the cube, between several measurements. The glue between the two prisms, forming the cube, could result in a dependency of the phase-relation on the beam spot position.

Nevertheless, during flight the only retrievable quantities are the powers in S-pol and P-pol, without information about their relation in phase. Therefore, the following analysis is also restricted to the measured power with orthogonal and parallel polarisation, disregarding their phase relation.

11.2.2. Influence of mechanical stress in combination with rotation

The next parameter to check was mechanical stress combined with a rotation of PBS1. Therefore, the PBS was put under stress via different weights of up to 7.5 kg. This corresponds to a homogeneous pressure of 736 kPa. The input light was still orthogonal polarised. The stressed PBS was then rotated with its mount towards the incoming beam. Unfortunately, the impact of the stress on the transmitted power in parallel polarisation was very small. Nevertheless, the observed small effect indeed seems to increase with the applied weight.

Searching for an enhancing effect, the applied stress was changed from linearly distributed over the PBS surface to shear stress application by dedicated adapters.

The adapter was positioned in different places between the sample and the upper plate (carrying the weight) to apply the stress at a defined point and as a consequence induce shear stress in the crystal. However, even with the adapters, no major enhancement of P-pol transmission could be found. The orientation of the PBS towards the beam was also inverted without a detectable impact on the transmitted P-pol.

11.2.3. Influence of temperature in combination with mechanical stress and rotation

Another promising parameter for the investigation was the temperature. To limit the parameter range of expected effects, as a first step a very basic device for heat application was chosen: a hot air gun, nominally used for electronic manufacturing. It could be set to 50 °C, unfortunately without accessible temperature control. However, for the proof of principle there was no need for a certain temperature stability. The P-pol transmission through PBS1 was monitored during heat-application, so that the range of effects between room temperature and about 50 °C could be studied. Furthermore, the heated PBS was rotated around its z-axis, to investigate a possible coupling of the two parameters.

Surprisingly, again there was no detectable impact of temperature on the transmitted power in parallel polarisation, although the PBS was constantly stressed throughout the heating process. This was also true for the combination with a PBS rotation.
However, while increasing the applied stress, another effect became visible: although the weak effect on transmitted P-pol was not increasing, the speed of the weak increase in power did.

This effect is shown in more detail with a time series in Figure 11.2: It starts with the PBS (without rotation against the incident beam, so at 0°) at room temperature. At 0 s a weight of 5.6 kg was applied to the PBS. It can be seen that the parallel polarised transmission slowly increases by a small amount. At about 700 s the weight was removed again and the P-pol is decreasing slowly. At 1800 s the heat application with the hot air gun started for about 300 s. The weight was applied again at 2300 s and an instantaneous rise of the transmitted power can be observed. At 2700 s the weight was removed again and the P-pol reduces abruptly. This was repeated at 2950 s and 3100 s. For comparison, also a time series from application of a smaller weight with 3 kg to a cold PBS is shown in the plot (11.2). The stress also increases slowly but the final amount of P-pol is much lower.

The described observations hint that a fluid with temperature-dependent properties of flow contributes to the transmitted P-pol. The only part of the PBS, reasonably fitting such properties, is the already mentioned glue combining the two prisms in the cube.

Resumee

All tested parameters in the first experimental series showed weak effects on the transmitted P-pol, but unfortunately the intensity of them was, despite careful work and efforts in controlling the environmental circumstances, not reproducible. In particular, between several days and re-adjustment, the intensity of the effect differed. Nevertheless, after stress application, the transmitted P-pol increases to a stable power, until the weight is removed. However, in

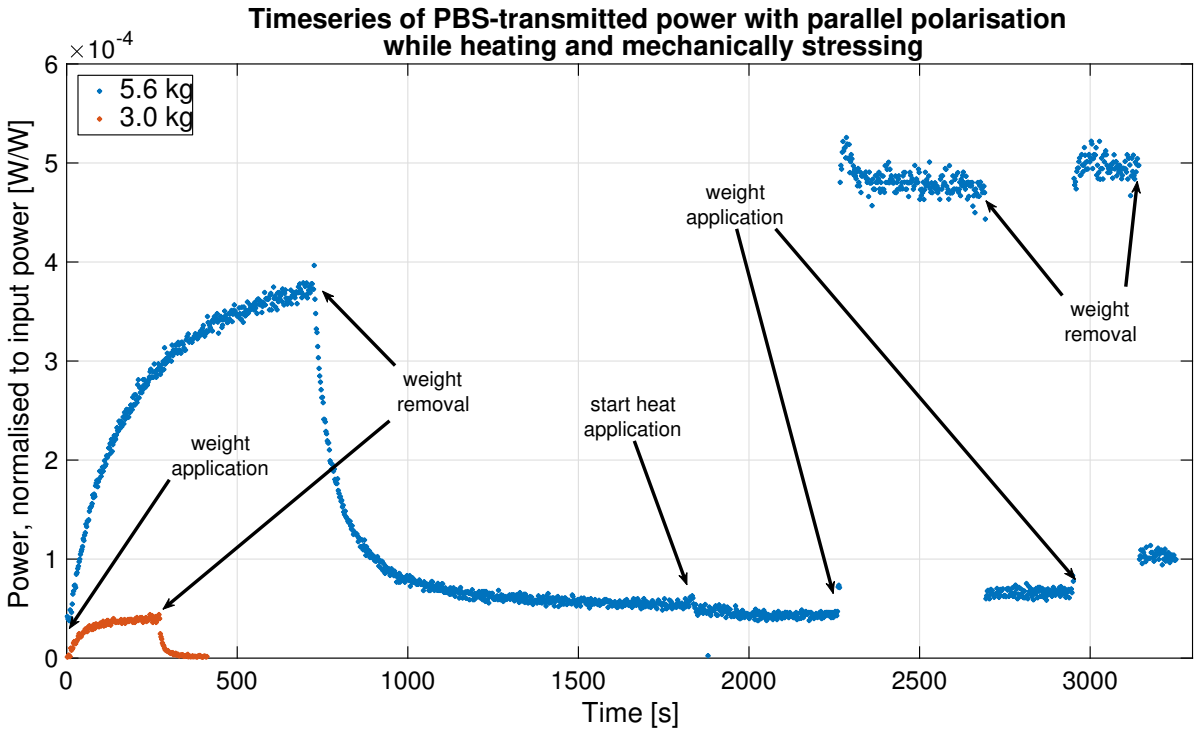

Figure 11.2.: Time series of P-pol transmission through PBS1 (normal incidence) after applying a weight of 3 kg and 5.6 kg (at 0 s) and removing it (at 280 s and 700 s). At 1850 s heat was applied to the PBS with a hot air gun (appointed to 50 °C). Afterwards the weight was reapplied two times (2250 s and 2950 s), clearly the effect on P-pol power has increased in speed for the heated PBS.

between several measurements the achieved power levels differ.
As a possible reason for the different power levels, a strong dependency on the beam spot position at the active surface of the PBS is assumed.

Figure 11.3 shows the variation of all measurements, with the stressed PBS1, including linear stress, shear stress and measurements combined with heat.

On each measurement day a reference measurement without stress was also taken. Their average and variation is also shown in the plot by the red data points.
The average transmitted P-pol is slightly higher for the stressed PBS. However, the unstressed measurements without stress-application show values within the errors of the stressed PBS. Therefore, the chance of having higher P-pol transmission with stress at the PBS rises, but it is also possible that no effect is measured.

In summary the PBS stress-tests show no effect on the P-pol transmission, comparable to the flight observations.

There is more than an order of magnitude between the flight observations and the maximum observed effect during the laboratory experiments. This could imply that the applied stress was still weaker than on the LPF OB, or that the PBS alone cannot be the origin of the P-pol levels measured in flight. Since the FIOS mount was designed to reduce stress at the

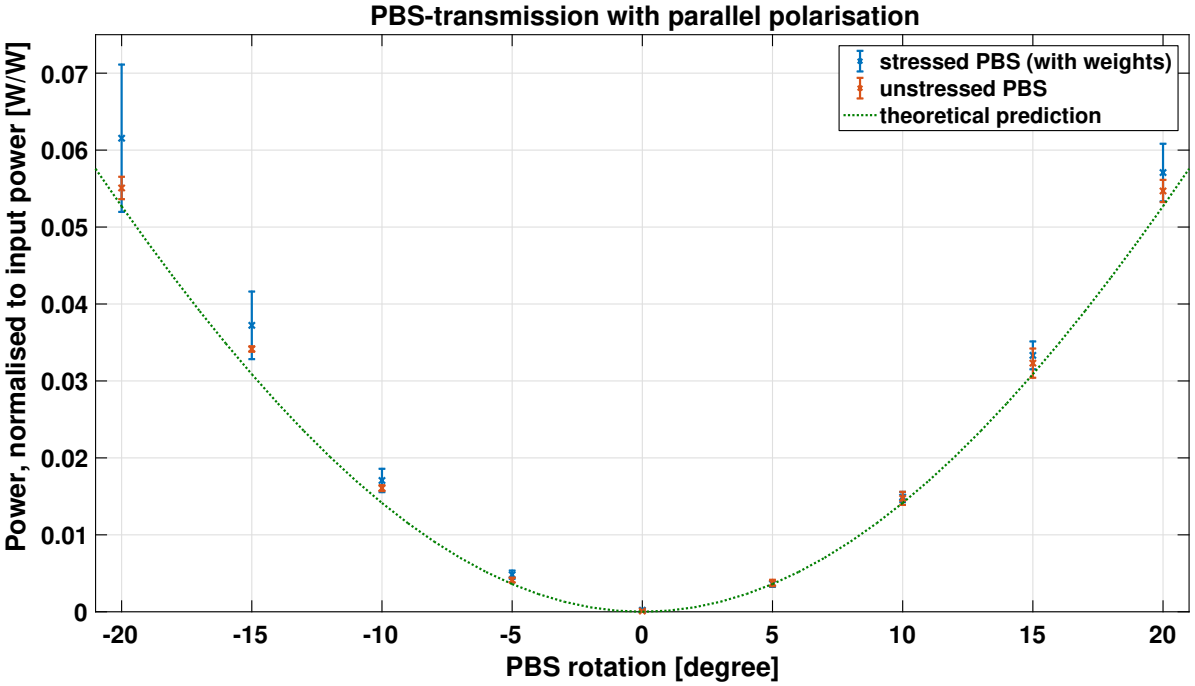

Figure 11.3.: P-pol transmission through PBS1 for a rotation around its vertical axis. The red dots represent the average of twelve measurements (on different days). The blue data points show the average of twelve measurements with stress (linear and shear stress) to the PBS, for some measurements also with heat. The green line is the theoretical prediction for a simplified "perfect PBS", as derived in Box 10.0.1 by Equation 10.10.

optical components, it is more likely that another parameter is contributing to the observed high P-pol levels.

In Box 11.2.1, the results of the measurements are summarised.

Box 11.2.1 | Summary: Influence of mechanical stress on transmission of parallel polarisation through PBS

Mechanical stress was applied by weights to a flight spare PBS (labelled PBS1).
Several parameters were tested:

- homogenous and constant pressure to the PBS, up to 736 kPa,
- punctual application of pressure to the PBS introducing shear stress,
- heat application to the PBS with temperature up to about 50 °C,
- change of PBS orientation: Glue is passed through before or behind the active layer.

Results of the tests:

- Homogeneous and punctual pressure led to a weak increase in transmitted P-pol with fluctuating strength:
  - There is a higher variance of transmitted P-pol between measurements with a stressed PBS, when compared to the ones without stress.
  - **However**: the measurements without stress still agree within errors.

  → Most likely the alignment is dominating the measured coupling strength.
- A **temperature** of $\approx 50\,°C$ increases the speed of changes in transmission, but not their intensity.
- Even the highest measured increase in P-pol transmission is still much smaller than observed during flight.

→ **Mechanical stress to the PBS could not be identified as the only origin of the P-pol on the LPF OB.**

Open questions:

- Could mechanical stress have a significant influence on the PBS extinction ratio?
- Is their another mechanism for increasing the P-pol transmission?

As assumed before, a major degradation of the polarisation extinction could also lead to an increase of P-pol transmission through the PBS, correlated to the incident P-pol.
Therefore, in the second experimental series, the impact of stress on the PBS extinction ratio was investigated, as described in the following.

11.3. PBS extinction ratio versus rotation

The first experimental series showed that a rotation of the PBS axis by mechanical stress is not a major source of P-pol on the LPF OB.
Therefore, as a next step, the extinction ratio of the PBS was investigated.

As already described, a typical PBS has an extinction ratio of about 1:1000. This means that only 0.1 % of the incident off-nominal polarised light is let through. Hence, for fully parallel polarised incident light, the transmitted P-pol would be less than a percent of the incident beam. Of course, in that case, no nominal polarisation would be transmitted any more.

Therefore, not only the extinction ratio needs to be characterized, but also effects need to be found that decrease the cleaning efficiency. Some possible candidates are, again, a PBS rotation, mechanical stress or temperature.

At first, the influence of the PBS rotation on the extinction of P-pol input light was investigated. Figure 11.4 shows the transmission of parallel and orthogonal polarisation through

PBS1 for parallel and orthogonal input polarisation, normalised to the input power. For this, the PBS was rotated between −10° and 10°.

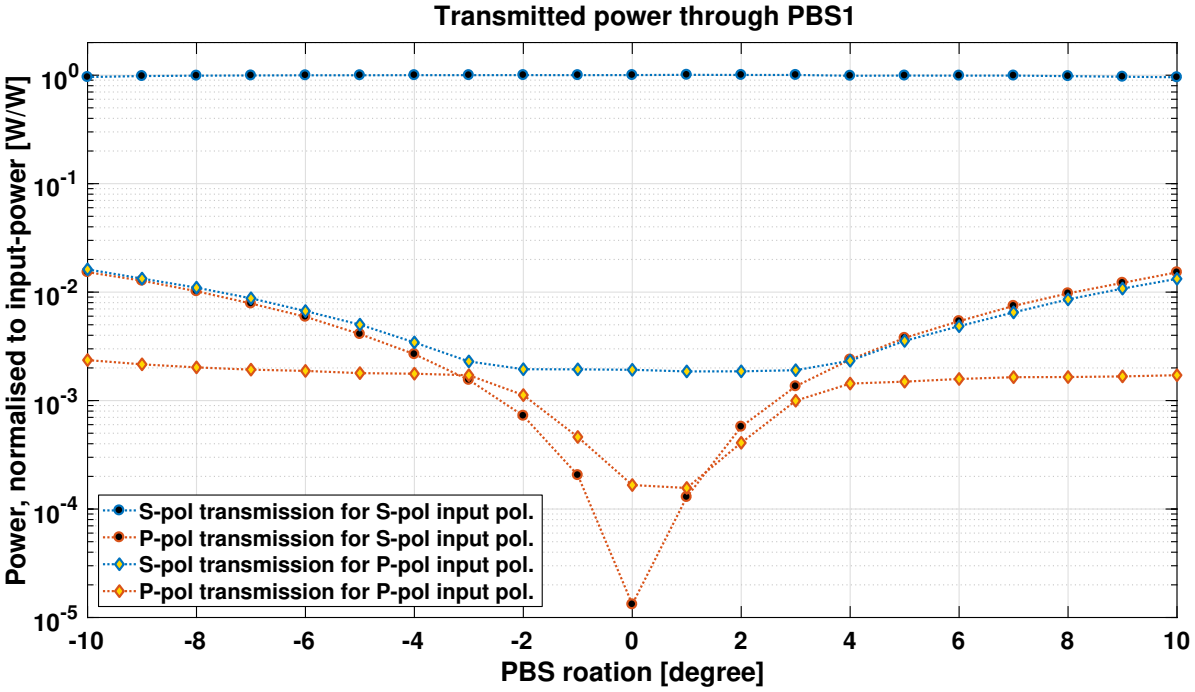

Figure 11.4.: Influence of input polarisation together with PBS rotation: transmission of P-pol/S-pol through PBS1 for S-pol/P-pol input polarisation, dependent on PBS rotation.

Obviously, the data series with parallel input polarisation has an offset on the measured PBS rotation of about 0.5°. This systematic error was most likely the result of placing the PBS in its mount: In the measurement routine the beam was first adjusted in input polarisation with the polarimeter (compare with the setup in Figure 11.1, without PBS in place). Then, the transmitted S-pol and P-pol were measured for different PBS rotation angels with a resolution of a degree (with a lever arm of 20 cm for angular adjustment). For changing the input polarisation the PBS needed to be removed and replaced in its mount with the guidance of the front edge of the inset. This replacement of the PBS, with only 1 cm width, probably caused the offset of half a degree.

Despite the small offset, several aspects could be found with this measurement:

1. For small rotation angles $< 3°$ the extinction ratio meets the requirements:

   → The P-pol transmission for both input polarisations is smaller than 10^{-3}.

2. The minimum P-pol transmission for parallel input polarisation is most likely between the two data points at 0° and 1° and possibly as small as the minimum of P-pol transmission for orthogonal input polarisation.

3. For a rotation $> 3°$ the P-pol transmission for orthogonal polarised input light (red coloured line with black markers) has the same power as the S-pol transmission for parallel polarised input light (blue coloured line with yellow markers).

- The predictions for a simplified PBS (compare to Box 10.0.1 and 11.4.1) , with optical axis rotation, φ (against the nominal one), and an input power, P_{in}, are given by:

$$\vec{P}_{\text{in}}^{\perp} = P_{\text{in}} \cdot \hat{e}^{\perp} \quad \rightarrow \quad P_{\text{out}}^{\parallel} = P_{\text{in}} \cdot \cos(\varphi_{\text{PBS}}) \cdot \cos(90° - \varphi_{\text{PBS}}) \tag{11.1}$$

$$\vec{P}_{\text{in}}^{\parallel} = P_{\text{in}} \cdot \hat{e}^{\parallel} \quad \rightarrow \quad P_{\text{out}}^{\perp} = P_{\text{in}} \cdot \cos(90° - \varphi_{\text{PBS}}) \cdot \cos(\varphi_{\text{PBS}}) \tag{11.2}$$

→ Therefore, the measurement fits the projected input powers for a perfect PBS.

4. The P-pol transmission for parallel polarised input light (red coloured line with yellow markers) is, also for rotations $> 3°$ below $2 \cdot 10^{-3}$.

   → This corresponds to the overall small transmitted power that leads to an even smaller projection onto the P-pol axis.

   - However, the ratio of P-pol to S-pol transmission is still bigger for parallel input polarisation, than for an orthogonal one (although the transmitted P-pol is that small).

   → Therefore, the transmitted P-pol seems to be limited by the efficiency of the coating at that angle (which seems to be worse than the normal PER).

5. The transmission of S-pol for parallel polarised input light (blue line with yellow filling) is conspicuous for angles $< 3°$.

   - It seems to be restricted alike the P-pol transmission for parallel input polarisation, at angles $> 3°$, to $2 \cdot 10^{-3}$.

→ **As a consequence, the transmission of S-pol and P-pol gets closest for parallel input polarisation and a PBS** rotation of 3°.

In summary, it was found that overall the cleaning efficiency of PBS1 is good. For parallel input polarisation the transmitted P-pol is dominated by the efficiency of the coating, whereas the S-pol transmission is restricted by this only for PBS rotations below $< 3°$. For greater rotations, the S-pol transmission corresponds with the prediction of vector projection onto the active surface, described in Box 10.0.1.

Therefore, the measurements of polarisation extinction versus PBS rotation pointed to another mechanism that enhances the P-pol on the OB: **A change of the input polarisation has a higher impact on the transmitted S-pol than on the one in P-pol**.

This effect gets highest for an angle of 3°. At this angle, the ratio of S-pol and P-pol in transmission is for orthogonal input polarisation at about $\frac{P_{\text{out}}^{\parallel}}{P_{\text{out}}^{\perp}}(\varphi_{\text{PBS}} = 3°) = \frac{1.5 \cdot 10^{-3}}{1} = 1.5 \cdot 10^{-3}$. However, for parallel input polarisation the ratio increases to a value between $\frac{P_{\text{out}}^{\parallel}}{P_{\text{out}}^{\perp}}(\varphi_{\text{PBS}} = 3°) = \frac{1 \cdot 10^{-3}}{2 \cdot 10^{-3}} = 0.5$ and $\frac{P_{\text{out}}^{\parallel}}{P_{\text{out}}^{\perp}}(\varphi_{\text{PBS}} = -3°) = \frac{1.5 \cdot 10^{-3}}{2.5 \cdot 10^{-3}} = 0.6$.

Since the power control loop on LPF mainly detects orthogonal polarisation (as described in Chapter 8), the parallel polarised parts in transmission are further enhanced, as described in Box 11.3.1.

Box 11.3.1: Normalisation, similar to the LPF power control loop

On LPF, the PBS reflected beam is blocked and only the transmitted light is sent to the OB. This transmitted power should be kept stable by the fast amplitude control loop, as described in Box 2.1.1. By design, the CL is not controlling the transmitted power, but the reflection at an uncoated BS made of fused silica, the CL pick-off (beam incidence of 45°). Since the reflectivity at that interface is higher for S-pol than for P-pol, with $R_{\mathrm{fs}}^{\perp} \approx 0.079$ and $R_{\mathrm{fs}}^{\parallel} \approx 0.006$ respectively, the loop mainly controls the orthogonal polarised part of the PBS transmission (compare to the Fresnel formulas in Reference [25], pages 234 and following).
To estimate the P-pol that is transmitted into the interferometers, the effect of the control loop is derived in the following with the simplification of perfect control.
The incident power to the OB can be described with:

$$P_{\mathrm{in}} = \left(P_{\mathrm{PBS\text{-}out}}^{\perp} + P_{\mathrm{PBS\text{-}out}}^{\parallel}\right) \cdot C_{\mathrm{CL}} \,. \tag{11.3}$$

The factor C_{CL} describes the control action of the amplitude CL.
The reflected power at the pick-off can be written as:

$$P_{\mathrm{in}} \cdot \mathrm{R}_{\text{pick-off}} = \left(P_{\mathrm{PBS\text{-}out}}^{\parallel} \cdot R_{\mathrm{fs}}^{\parallel} + P_{\mathrm{PBS\text{-}out}}^{\perp} \cdot R_{\mathrm{fs}}^{\perp}\right) \cdot C_{\mathrm{CL}} \stackrel{!}{=} \text{const.} \tag{11.4}$$

The transmitted power into the interferometers is further given by:

$$\begin{aligned} P_{\mathrm{in}} \cdot \mathrm{T}_{\text{pick-off}} &= P_{\mathrm{in}} \cdot (1 - \mathrm{R}_{\text{pick-off}}) \\ &= C_{\mathrm{CL}} \cdot \left(P_{\mathrm{PBS\text{-}out}}^{\parallel} - R_{\mathrm{fs}}^{\parallel} \cdot P_{\mathrm{PBS\text{-}out}}^{\parallel} + P_{\mathrm{PBS\text{-}out}}^{\perp} - R_{\mathrm{fs}}^{\perp} \cdot P_{\mathrm{PBS\text{-}out}}^{\perp}\right) . \end{aligned} \tag{11.5}$$

The constant parameter from Equation 11.4 corresponds to the loop parameters. It is proportional to the set-point of the CL and the responsivity of the power monitor diode. For comparison with the powers that were normalised to the input power, the parameter is chosen as the ratio of power between reflected and transmitted beam for orthogonal polarisation:

$$\text{const.} \stackrel{!}{=} \frac{R_{\mathrm{fs}}^{\perp}}{1 - R_{\mathrm{fs}}^{\perp}} \,. \tag{11.6}$$

The control coefficient, C_{CL}, then derives to:

$$\rightarrow C_{\mathrm{CL}} = \frac{R_{\mathrm{fs}}^{\perp}}{1 - R_{\mathrm{fs}}^{\perp}} \cdot \frac{1}{P_{\mathrm{PBS\text{-}out}}^{\parallel} \cdot R_{\mathrm{fs}}^{\parallel} + P_{\mathrm{PBS\text{-}out}}^{\perp} \cdot R_{\mathrm{fs}}^{\perp}} \,. \tag{11.7}$$

Therefore, the share of parallel and orthogonal polarisation in the interferometers, normalised equivalently to the LPF amplitude CL, derive to:

$$P_{\text{ifo-in}}^{\parallel} = C_{\mathrm{CL}} \cdot \left(P_{\mathrm{PBS\text{-}out}}^{\parallel} - R_{\mathrm{fs}}^{\parallel} \cdot P_{\mathrm{PBS\text{-}out}}^{\parallel}\right) , \tag{11.8}$$

$$P_{\text{ifo-in}}^{\perp} = C_{\mathrm{CL}} \cdot \left(P_{\mathrm{PBS\text{-}out}}^{\perp} - R_{\mathrm{fs}}^{\perp} \cdot P_{\mathrm{PBS\text{-}out}}^{\perp}\right) . \tag{11.9}$$

The nominal rotation of the PBS around the z-axis on LPF is just 3°. Therefore, for pure P-pol input polarisation, more than a third of the power on the OB would be parallel polarised. However, due to the huge amount of reflected power at the PBS, also an increase in laser power by more than two orders of magnitude would be needed to control the power on the OB. Obviously, this is not true for LPF, as known from the RF powers, providing knowledge of the applied control.

As a consequence, the next step is to further investigate with a constantly rotated PBS by 3°. Its transmission for continuous rotation of linear input polarisation is measured and possible P-pol transmission enhancing effects are tested in combination with rotation of linear input polarisation.

11.4. Continuous variation of input polarisation

Based on the results of the previous section, the next investigations involved a continuous rotation of input polarisation for a constantly rotated PBS by 3°. The input polarisation was rotated with a half wave plate, as depicted in Figure 11.1.

The challenge of this measurement is the simultaneous detection of the applied input polarisation: If a power pick-off is used, on the one hand a second polarimeter is needed or some combination of polarisation filters and power-meters. On the other hand, the pick-off will be dependent on polarisation, as well. Hence, a second characterisation measurement for the power pick-off would be needed. Furthermore, the transmitted beam to the PBS is then also affected in polarisation by the power pick-off itself.

Therefore, a different and more simple option was chosen: From the previous measurements it is known that the PBS itself is already a good polarisation sensitive component. With the transmitted power in orthogonal polarisation and the input power, the fraction of S-pol and P-pol of the input polarisation can be retrieved with appropriate errors by simple algebra, as can be seen in Box 11.4.1.

To verify the validity of Equation 11.14, a calibration measurement was done. The input polarisation was rotated to defined values with the polarimeter without the PBS in place. Afterwards the PBS was integrated in the beam path with the nominal offset of 3° and the transmitted power in orthogonal polarisation was measured. Figure 11.6 shows the resulting measurements together with the theoretical prediction by Equation 11.14 and the deviation between the two.

The correspondence is better than 1.4 %, which is good, when including possible alignment errors during the characterisation measurement procedure: The PBS needed to be removed and reintegrated between each measurement point to rotate and measure the input polarisation state.
Accordingly, the measured orthogonal transmission was used to retrieve the input polarisation without adding new components to the beam path and thus without additionally affecting the input polarisation state.

Box 11.4.1: PBS: retrieval of input polarisation

A PBS splits the incoming light into an orthogonal and a parallel polarised beam towards its optical axis (when neglecting the PER and big rotation angles of the PBS). By knowing the orientation of the optical axis and the applied and transmitted power, it is therefore possible to retrieve information about the input polarisation. Since the phase relation between S-pol and P-pol in the input beam has no impact on the projection

onto the PBS optical axis, this information is also not retrievable from the transmitted powers. However, the amount of P-pol and S-pol in input polarisation can easily be retrieved.

For the laboratory setup, a linear polarised beam with power P_{in} is applied to the PBS. Its polarisation is linearly rotated by an angle, φ_{pol}, against the nominal polarisation.

The transmitted power, $P_{\text{trans}}^{\text{PBS}}$, through a simplified "perfect PBS" (compare to Box 10.0.1), can then be derived by projection of the input electric field vectors (which are defined here by the rotation angle of the linear polarisation) onto the PBS optical axis.

For a PBS without rotation (with a perpendicular front surface towards the beam) the transmitted power is given by:

$$P_{\text{out}} = P_{\text{in}} \cdot \cos^2(\varphi_{\text{pol}})\,. \tag{11.10}$$

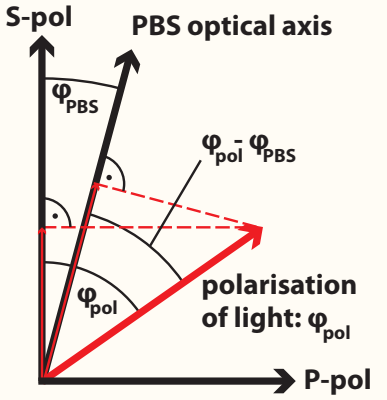

Figure 11.5.: Projection of linear input polarisation onto the PBS optical axis.

For a rotated PBS, the angle of incidence to the surface changes by φ_{PBS}:

$$P_{\text{out}} = P_{\text{in}} \cdot \cos^2(\varphi_{\text{pol}} - \varphi_{\text{PBS}})\,. \tag{11.11}$$

However, for a rotation of the PBS optical axis, the transmitted light is not orthogonal polarised any more.

The resulting transmitted power can be further split into orthogonal and parallel polarised parts:

$$P_{\text{out}}^{\perp} = P_{\text{in}} \cdot \cos^2(\varphi_{\text{pol}} - \varphi_{\text{PBS}}) \cdot \cos^2(\varphi_{\text{PBS}})\,, \tag{11.12}$$

$$P_{\text{out}}^{\parallel} = P_{\text{in}} \cdot \cos^2(\varphi_{\text{pol}} - \varphi_{\text{PBS}}) \cdot \sin^2(\varphi_{\text{PBS}})\,. \tag{11.13}$$

In the laboratory, the P-pol and S-pol in the transmitted light is detected. For a small rotation of the PBS, the transmitted P-pol is small for all input polarisation angles φ_{pol}, whereas the transmitted S-pol is varying by almost the full range between input power and almost zero power. Therefore, the transmitted orthogonal polarisation is used to retrieve the linear input polarisation.

The polarisation angle φ_{pol} of the input light can be retrieved as follows, by using Equation 11.12 and measuring the power $P_{\text{out}}^{\perp}$:

$$\varphi_{\text{pol}} = \arccos\left(\sqrt{\frac{P_{\text{out}}^{\perp}}{P_{\text{in}} \cdot \cos^2(\varphi_{\text{PBS}})}}\right) + \varphi_{\text{PBS}}\,. \tag{11.14}$$

For the laboratory setup, the direction of the input polarisation rotation (clockwise or anti-clockwise) is known to be constant. Furthermore, approximately fully linear polarised input light can be assumed.

Therefore, the following assumptions were made for the analysis of the laboratory data:

1. In the following, the input polarisation can be fully described by the simplified

angle, φ_{pol}, giving the off-nominal rotation of the linear input polarisation.

2. The measured transmitted S-pol needs to be preprocessed in preparation for a retrieval of φ_{pol} as follows:
   - The measured S-pol transmission time series is normalised by the maximum and minimum transmitted power. At these samples, the corresponding input polarisation is assumed to be fully orthogonal and parallel polarised towards the PBS optical axis.

   → Note: The normalisation removes small differences in the losses of the particular beam paths and corresponds to the knowledge of having purely linear polarised light applied.

3. The argument of the square root in Equation 11.14 is positive at all times. Therefore the arccos gives only values between 0 and $\frac{\pi}{2}$.

   → A phase unwrap of the derived angle φ_{pol} needs to be applied to cover the full range between 0° and 180°.
   - Note that this corresponds to the knowledge of having a constant rotation direction of the input polarisation angle.

4. The input power is approximated with the maximum transmitted power to reduce the impact of different losses in the beam paths for different PBSs or readjustment during the experimental procedure. Theses differences likely exceed the small difference between input power and maximum transmitted power of 0.13 % for a lossless PBS.

Note: As mentioned above, there is no knowledge about the phase relation between S-pol and P-pol in the input light. Therefore, for an arbitrary input polarisation state (like on LPF), the ellipticity, as well as the Degree Of Polarisation (DOP), could not be retrieved from the transmitted S-pol.
For example, fully unpolarised input light has equal average projected power onto the S-pol and P-pol axis, as it is true for linear input polarisation with a $\varphi_{\text{pol}} = 45°$ rotation or a circular polarisation state.

Figure 11.7 shows the transmitted powers through PBS1 against linear rotation of the input polarisation. A phase unwrap was applied to show the full range of 0° to 180° degree rotation.

The transmitted S-pol is shown in red and the parallel polarised one in blue. The minimum in parallel transmission is reached at an input polarisation of $\varphi_{\text{pol}} = 90° + \varphi_{\text{PBS}}$. For pure S-pol input polarisation about $1.5 \cdot 10^{-3}$ parts of the input power are transmitted, as expected. At maximum, the P-pol transmission reaches a share of $2 \cdot 10^{-3}$ relative to the input power.

However, as supposed before, the amount of parallel polarised transmission gets higher for rotating the input polarisation off the nominal orthogonal one. For input light being completely parallel polarised to the PBS optical axis, almost all light is reflected by the PBS. Therefore, the transmission of parallel polarised light dips down to almost zero.

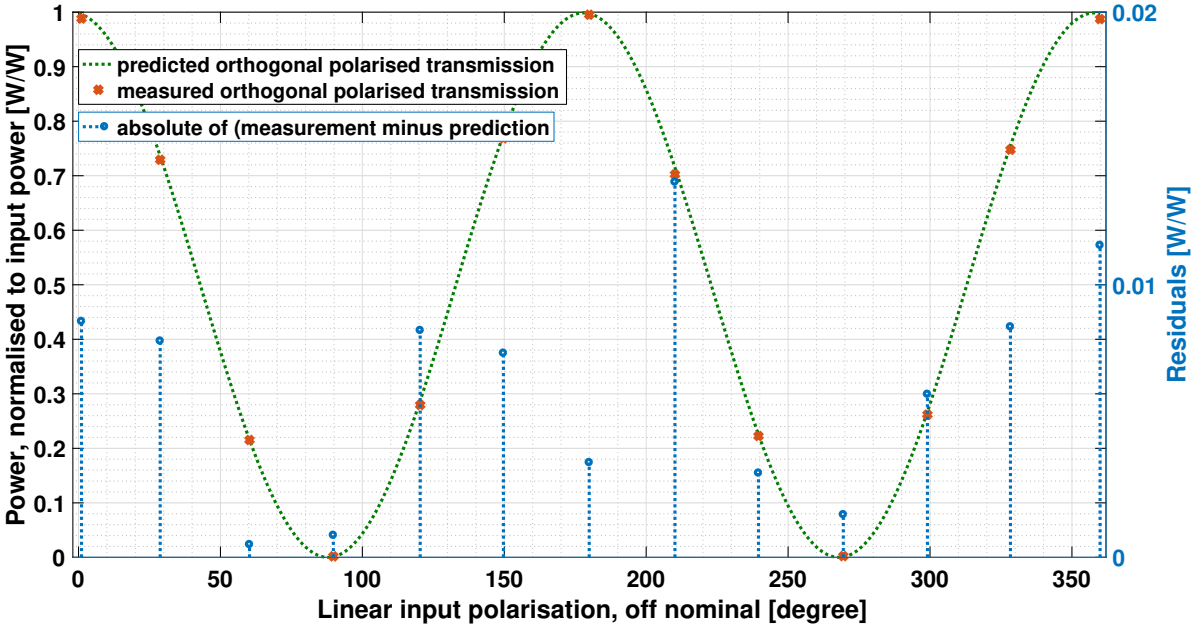

Figure 11.6.: Transmission of orthogonal polarisation through a 3° rotated PBS, for rotation of linear input polarisation. The expected power is shown in green and the measured polarisation states are shown by the red dots. Their deviation is shown in blue.

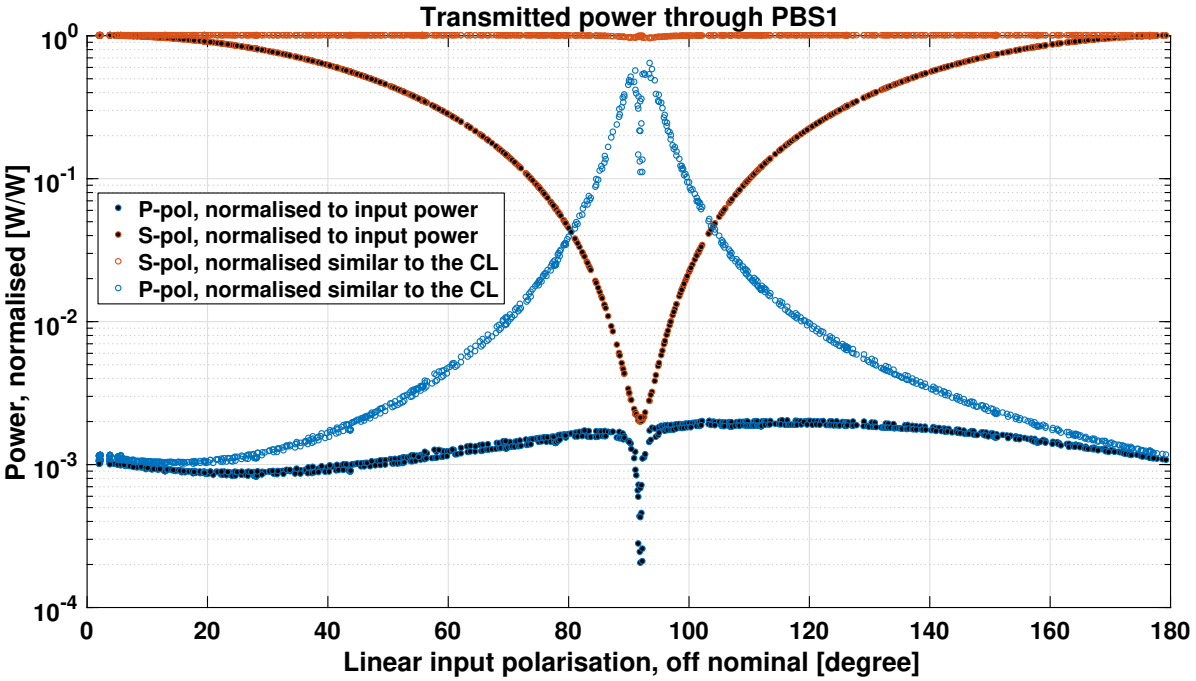

Figure 11.7.: Transmission of P-pol and S-pol through PBS1 for continuous variation of linear input polarisation. Two different normalisations are shown: normalisation to input power (black filling of markers) and a normalisation analogue to the LPF power control (white filling of markers), as described in Box 11.4.1.

If the transmitted P-pol is normalised similarly to the LPF power CL (see Box 11.3.1, assuming perfect control and infinite laser power), it reaches powers as high as observed during flight of LPF.

At 120° input polarisation (60° degree off-nominal) already one percent of P-pol is reached in transmission and at 103° (76° degree off-nominal) with 4.6 %, even more P-pol is measured than observed at maximum during flight.

However, the ratio of transmitted to input power disagrees with the flight observations: At $\varphi_{\mathrm{pol}} = 120°$, only 22 % of the power are transmitted through the PBS and, at $\varphi_{\mathrm{pol}} = 103°$ with 4.1 %, even less. The applied voltage to the actuators of the power CL, the AOMs (see Section8.4.2), shows only a variation of up to 15 % in power. The average RF power was compared to the expectations for the design of the fast power control prior to flight, as described in Reference [21]. It turned out that the average voltage applied to the AOMs is higher than the desired value of 2.4 V, but still in the same order of magnitude. The laser output power and the detected power on the OB (at the power monitor diodes) agree with the design from Reference [21]. Therefore, the losses in the beam paths to the OB during flight seem to be higher than expected, but not in an order of magnitude that agrees with the off-nominal input polarisations, derived above ($\varphi_{\mathrm{pol}} = 120°$ or $\varphi_{\mathrm{pol}} = 103°$). Furthermore, it is unclear if the beam polarisation is the origin of the higher losses in the beam paths or another effect causes it. So, the average input polarisation in-flight is not as far off nominal, as needed to reach the 4.5 % P-pol transmission through PBS1 (compare to Figure 11.7).

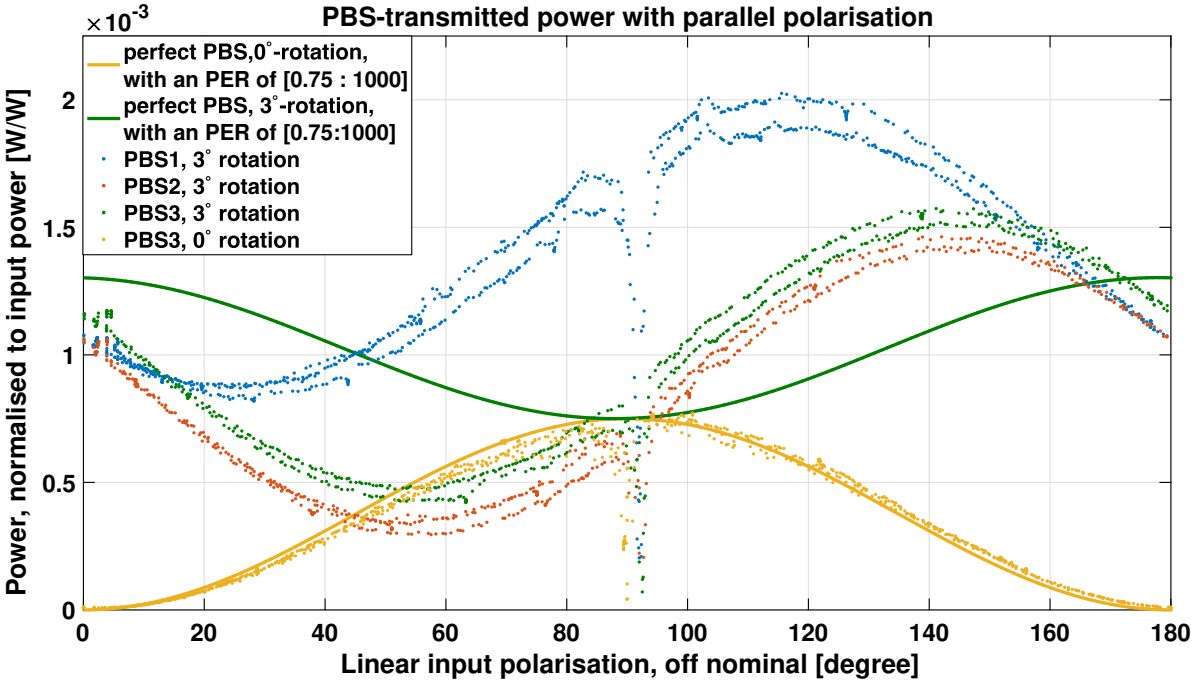

Figure 11.8.: Transmission of P-pol through 3 flight spare PBSs, rotated by 3°, normalised to the input power. For PBS3 the transmission for normal incidence, so 0° PBS rotation, is also shown. The dotted lines describe the theoretical P-pol transmission through a PBS with an extinction ratio of [0.75:1000].

Since the extinction ratio is known to have a specific range between different individual components (due to manufacturing), two other LPF spare PBSs — PBS2 and PBS3 — were analysed in transmission, for rotation of linear input polarisation, as for the first PBS1.
Figure 11.8 shows the transmitted P-pol through all three spare PBSs, normalised to the input power.

The first striking observation is the higher transmission of parallel polarisation through PBS1. A reason for this could be an individual poorer extinction ratio of the particular sample on the one hand. On the other hand it could also be a cause of the stress experiments, carried out on PBS1. Possibly some permanent damage occurred due to some of the tests. PBS2 and PBS3, in contrast, show a comparable transmission.

PBS3 is used as a reference sample in further investigations. Therefore, the transmission of P-pol through PBS3 without rotation was also measured, since these components are designed for normal incidence. A simple model (yellow solid line in Figure 11.8) of P-pol transmission through a perfect PBS with a PER of [0.75:1000] fits the measured transmission very well (with the exception of the dip for parallel input polarisation, where almost all parallel polarised light is reflected at the PBS). For the rotated PBS, the same extinction ratio, together with the model from Box 11.4.1, differs a lot from the corresponding measurement (green solid line in Figure 11.8). Surprisingly, the transmission of parallel polarisation is asymmetric around the PBS rotation angle, where the input polarisation and the transmitted polarisation vector are aligned. A further rotation (in the same direction as the PBS is rotated) leads to less transmission of P-pol than theoretically determined (between $0° + \varphi_{\mathrm{PBS}}$ and $90° + \varphi_{\mathrm{PBS}}$) and a rotation towards the other direction (between $90° + \varphi_{\mathrm{PBS}}$ to $0° + \varphi_{\mathrm{PBS}}$) leads to more P-pol in the transmitted light than expected.

This shows that the P-pol transmission through a rotated PBS is generally not easily computable (without dedicated knowledge of the active layer structure) and therefore, needs to be measured.

As expected in advance, the estimated share of P-pol in input polarisation on LPF is not able to explain the in-flight observations. The cleaning of the PBS should be better than observed. Therefore, the relevant parameter or mechanism that enhances the P-pol transmission through the PBS, is still not identified.
Nevertheless, it can be concluded that the control mechanism enhances the transmission of parallel polarised light on the OB for incident off-nominal polarised light.

Therefore, as a next step — an effect decreasing the extinction of parallel polarisation — is searched for.

11.5. Combination of all parameters

The previously tested parameters — mechanical stress and temperature — showed effects on the transmission of parallel polarised light. However, for orthogonal input polarisation none of them was strong enough to correspond to the big power fluctuations observed during flight. Therefore, the derived relevant parameters were further investigated in accordance to the schedule described in Box 11.5:

Box 11.5: Experimental schedule for parameter correlation:

1. Rotate input polarisation to S-pol,
2. insert PBS1 into its mount,
3. rotate PBS by 3 degrees,
4. start heat application (constantly applied until the end of the experiment),
5. apply mechanical stress:
   - First apply 1.3 kg
   - remove weight
   - then, apply 6.2 kg
   - add 1.3 kg, so 7.5 kg in total
   - remove all weights.
6. Repeat step 5, four times.

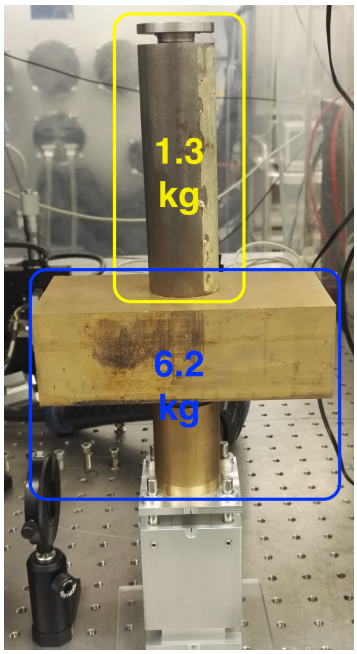

7. Combine rotation of linear input polarisation with mechanical stress.
   - Rotate the input polarisation without mechanical stress,
   - apply 6.2 kg → rotate input polarisation,
   - add 1.3 kg, (7.5 kg in total) → rotate input polarisation,
   - remove the weights.
8. Repeat combination of stress and rotation of input polarisation, 2 iterations.
9. Repeat step 1 to 9 for another sample, labelled PBS2.

Figure 11.9 shows the transmitted P-pol while execution of step 1 to 5 from Schedule 11.5.

In correspondence with the previous findings, the time series clearly shows an effect of the applied weight on the transmitted P-pol. Surprisingly, the application of the lightest weight (1.3 kg) leads to a decrease in P-pol transmission. Possibly this decrease is caused by alignment, since the PBS is pressed into its mount. The two heavier weights clearly show an immediate increase in P-pol transmission, as expected by the constant application of hot air. Qualitatively comparable effects can be observed for the second PBS2, with the exception of the average P-pol transmission when no weight is applied. Again, this deviation might be induced by a systematic error in the alignment (some fraction of a degree, compare to Figure 11.3), when the PBSs are rotated by nominally 3°.
In summary, the five repetitions of applying three different weights clearly fit to the high variation of the resulting effect, as can be seen in Figure 11.3.

This situation is similar for the coupling of stress with rotation of input polarisation, as can

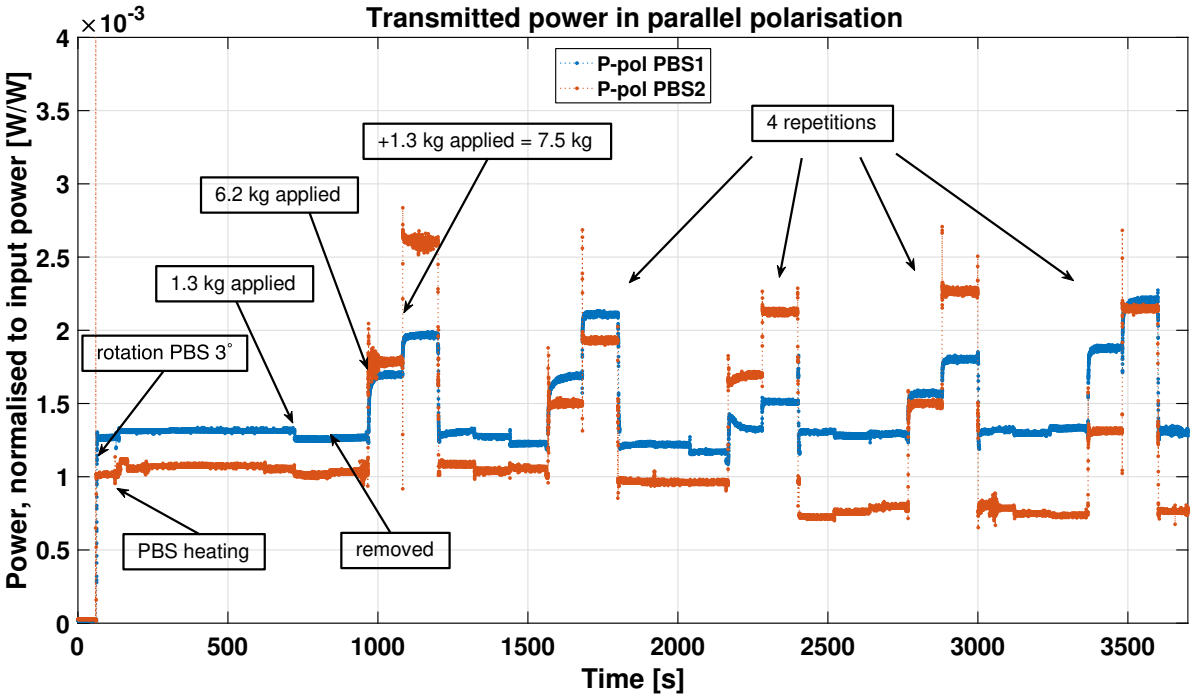

Figure 11.9.: Time series of P-pol transmission through two flight spare PBSs, for parameter correlation testing with rotation, heat and stress, following schedule 11.5, step 1 to 6.

be seen in Figure 11.10.
The blue coloured points give a reference measurement with the unstressed PBS (compare with Figure 11.7). Then 6.2 kg and 7.5 kg were applied to the two PBSs and for both a correlated effect with the input polarisation becomes visible. However, the two repetitions show that the variation between the three samples is as big as the difference between the two weights.
Nevertheless, the effect of stress on P-pol transmission is, despite their statistical variation, qualitatively interesting, because the asymmetry around φ_{PBS} is increased.

However, no conclusion on the cause of this asymmetry could be found, yet. Probably the cement between the two prisms is a relevant parameter or the imposed birefringence. The viscous fluid and the geometry of two prisms may lead to shear stress: the upper prism could possibly 'float' down the lower one. On the other hand, the lower edge of the upper prism could already touch the mount, whereby the compression could be greater at the upper edge (due to the leaver arm).
However, since an unstressed rotated PBS already shows an asymmetry for the direction of input polarisation rotation, the effect might also result from the layer-design.

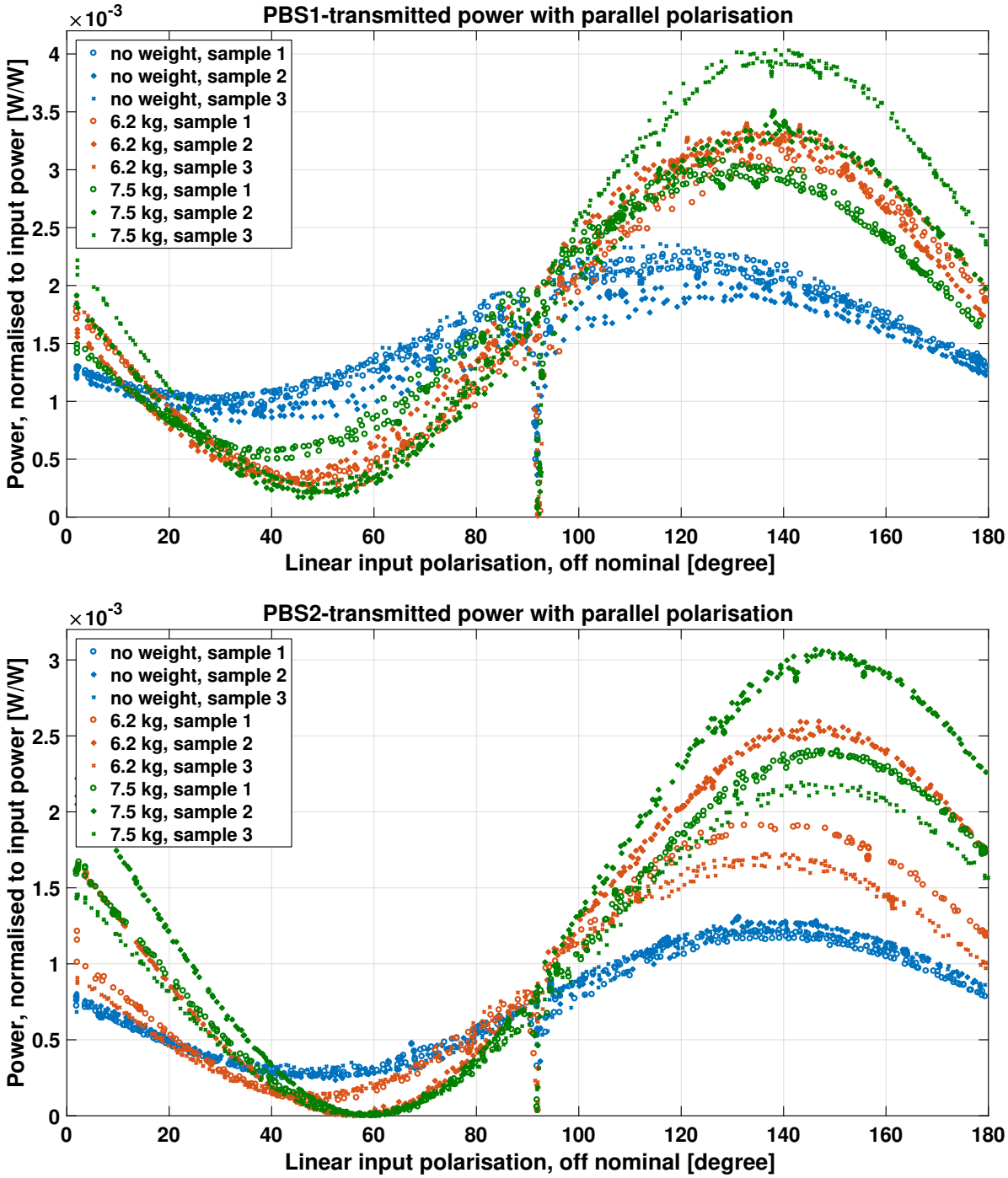

Figure 11.10.: Transmission of parallel polarisation through two PBSs applied to two different stress levels, in dependency of linear input polarisation, following schedule 11.5, step 7 to 9.

Box 11.5.1 | Summary: PBS extinction ratio

The flight spare PBS was analysed in transmission **for a variable input polarisation**, combined with previously used parameters.

The performed measurements have the following results:

- The PBS transmission for **parallel input polarisation** and **variable rotation of the PBS** shows:
  - The nominal transmitted power is at all observable angles small and close to zero for normal incidence.
  - For angles $\varphi_{\mathrm{PBS}} > 3°$ the P-pol transmission is restricted by the efficiency of the coating.
  - For angles $\varphi_{\mathrm{PBS}} < 3°$ the S-pol transmission is also restricted by the efficiency of the coating.
    → Apparently, $\varphi_{\mathrm{PBS}} = 3°$ has a special property: the S-pol and P-pol transmission are only apart by a factor of 2.
  - On LPF, the power CL mainly stabilises the nominal polarised power.
    → Therefore, the transmitted parallel polarisation is significantly enhanced by the power CL for incident P-pol to the PBS.
- The PBS transmission for all three flight spare PBSs with **continuous variation of linear input polarisation** at $\varphi_{\mathrm{PBS}} = 3°$ PBS rotation shows:
  - The measured P-pol transmission disagrees with a simple model of a PBS.
  - PBS1 shows slightly more P-pol in transmission than the other two.
  - The transmitted power has a significant share of P-pol, when normalised similar to the LPF power CL:
    * A rotation of the input polarisation by $\varphi_{\mathrm{pol}} = 76°$ (off-nominal) produces 4.6 % P-pol in transmission, corresponding to the in-flight observations.
    * **However**, the applied range of power actuation during flight (about 15 %) disagrees with the corresponding small amount of transmitted power of 4.1 %.
- A combination of all parameters — **continuous variation of linear input polarisation**, combined with **application of mechanical stress** and **heat** at a PBS-rotation of $\varphi_{\mathrm{PBS}} = 3°$ shows:
  - Mechanical stress leads to an increase in an asymmetric P-pol transmission around orthogonal input polarisation (to the PBS optical axis).

  → However, there was no explanation found, yet.

Open questions:

- The observed effects correlated to mechanical stress are assumed to be dependent on the mount:

→ What is the influence of the dedicated PBS mounting on LPF?

→ Are there other parameters degrading the polarisation extinction?

The laboratory experiments with the flight spare PBSs showed that it is possible to reach the observed levels of parallel polarisation in transmission of the PBS. The important role of the PBS rotation and the power control loop became clear. However, still a part of the findings disagrees with the observations: The incident polarisation to the PBSs on LPF is expected to be much better than needed in the laboratory, to reproduce the P-pol transmission.
Therefore the next step was an investigation with a PBS in a laboratory setup closer to the real mounting on LPF. Very luckily, these experiments could be performed with the most realistic setup — the flight spare OB at the University of Glasgow, as described in the following.

12. Measurements with the flight spare optical bench

Several experiments were performed with flight spare PBSs, analysing the influence of mechanical stress, PBS rotation, temperature and input polarisation, as described in the previous Chapter 11.

Since the measured impact of mechanical stress was very weak and furthermore, not reproducible with the mount used for stress application, the measurements needed to be continued with a more realistic setup. To mimic the LPF mounting in the FIOS, the PBS would need to be glued to a fused silica plate which is sidelong stiff connected to another bulk material with different expansion coefficient (like bonding to a Zerodur plate). Also, the glue would need to possess comparable properties to the one used for the real FIOSs. Since such an experiment would cause significant effort and the used PBS could not be removed from the plate (because it is glued to it), it was decided to directly move to the most realistic setup: **the flight spare OB**.

The spare OB is housed in a dedicated travel container which is stored in a laboratory at the University of Glasgow. The travel container gives access to all fibres and cables of the OB, so that only a read-out system and a suitable laser source were needed. There is also a measurement kit that was already built for OB testing in preparation to flight. For the scope of polarisation analysis, the multi-channel DC beam-position read-out kit (short RoB, Manual [66]) was transferred to Glasgow.
The measurements described in the following were planned and executed in collaboration with our colleagues at the University of Glasgow.

12.1. Parallel polarisation on the spare OB

With the RoB the DC powers of the single beams could be detected on all QPDs of the OB. Due to the missing test masses, the measurement beam could only be detected by the diodes of the rigid interferometers.

The measured powers are normalised analogous to the pre-flight thermal cycling experiments described in Section 9.
Therefore, each channel is normalised by its average power to account for different power levels. Due to the comparably stable temperature, the average of each individual time series accounts for the different power levels, as well as the different PD responsivities. In contrast to Section9, therefore no moving average is needed, here.

Analogously to Section 9, in the next step, the normalised reference beam power is divided by $DC_{12B,\,RB}$ to remove all power fluctuations, except for the ones induced by parallel polarisation.

For the measurement beam $DC_{RA,\,MB}$ had to be used instead, because $DC_{12A,\,MB}$ detects no power due to the missing TMs.

The processed data indeed shows the typical polarisation pattern (described in Chapter 7), but with very small powers.
The resulting time series of parallel polarised beam powers $\frac{P^{\parallel}(t)}{P^{\perp}+\langle P^{\perp}(t)\rangle}$, computed in analogy to Equation 9.10, is shown in Figure 12.1.

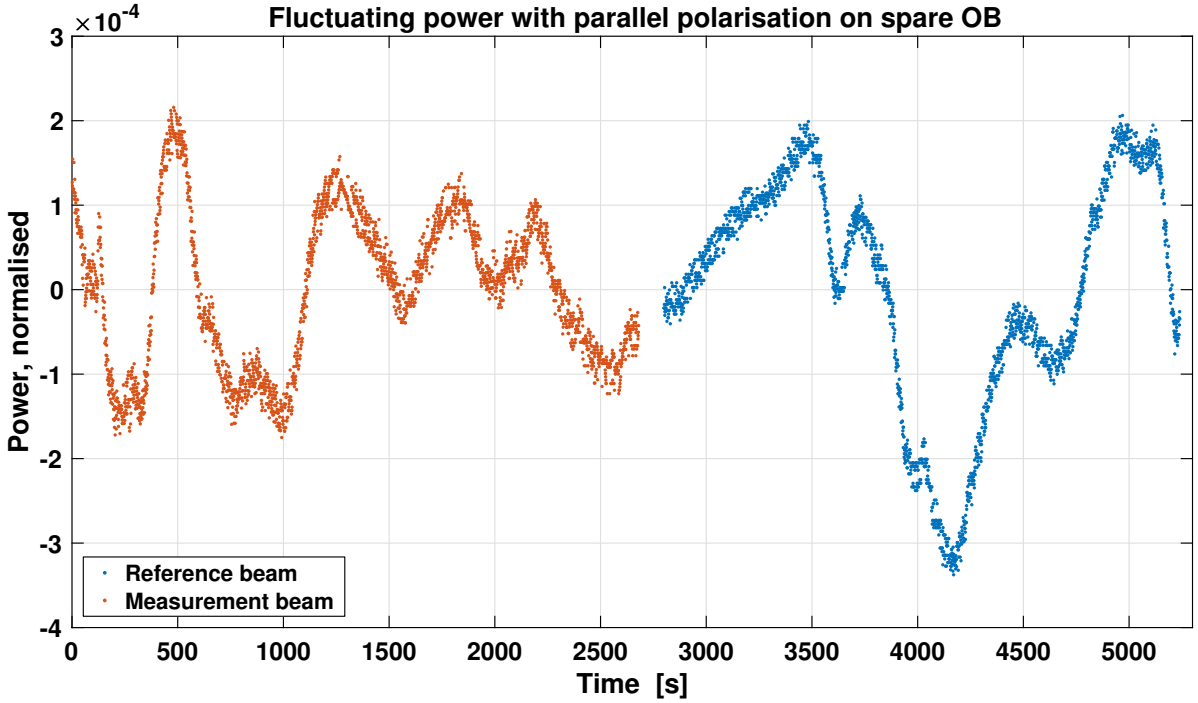

Figure 12.1.: Time series of P-pol on the spare OB, with mechanically stressed fibres.

In comparison with the derived power during ground-testing (as can be seen in Figure 9.9) the fluctuations in parallel polarisation $P^{\parallel}(t)$ on the spare OB are much smaller, although the fibres were mechanically stressed during the measurement. With a variation in P-pol transmission below 10^{-3}, the values are well within specifications for the PBSs.

This result was very surprising, since already the pre-flight observations showed a significantly smaller effect than in-flight. And now, the spare OB shows an even weaker effect than in the ground tests. Stressing a fibre is known to change its output polarisation. Furthermore, the PBS reflected light was randomly checked and, as expected, the rejected power was strongly affected. Nevertheless, the actual input polarisation state is — as for the ground tests — unknown.

Therefore, it was decided to rotate the polarisation directly on the spare OB so that the resulting ratio of P-pol and S-pol, derived by Equation 9.10, following the model from Section8.1, can be tested.

12.2. Rotation of the linear polarisation state on the OB

In contrast to the restricted interactions during flight, the laboratory setup gives the opportunity to rotate the polarisation on the OB and measure its impact. For simplicity, a polarisation filter was used. With its small dimensions it fits in the small gaps between the optics and the output polarisation state is clean and stable. The filter can be applied to the spare OB, with a dedicated mount, as can be seen in Figure 12.2. Before the filter was applied to the OB, its output polarisation state was adjusted and measured in a separate setup, with a polarimeter. Afterwards, the filter was adopted at different points in the beam paths on the OB, as described in the following.

12.2.1. Polarisation filter after the PBS

As a first step, the opportunity was used to verify the derived model in Chapter 8.

Therefore, the filter was placed directly after one of the two FIOSs, as can be seen in picture 12.2. The input laser power was then readjusted to constant power at the particular power monitor diode. This corresponds to the power control on LPF and keeps the power on the OB, and therefore intentionally also on the PDs, constant.

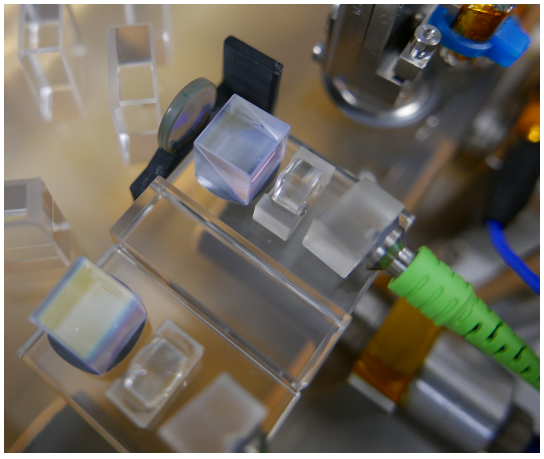

Figure 12.2.: Polarisation filter on the spare OB, **after** the PBS.

For each rotation state, φ, of the filter, the DC beam power, $\mathrm{DC}_{ij,m}(\varphi)$, of the particular beam, m, was measured on all available diodes, ij. To compare the measurements and reveal polarisation effects, the average power per filter state was normalised by the corresponding power at the power monitor diode, $\mathrm{DC}_m(\varphi)$, and a reference measurement without filter, $\mathrm{DC}_{ij,m}(\mathrm{off})$, as described with Equation12.1.

$$\mathrm{norm}(\mathrm{DC}_{ij,m}(\varphi)) = \frac{\mathrm{DC}_{ij,m}(\varphi)}{\mathrm{DC}_m(\varphi)} \cdot \frac{\mathrm{DC}_m(\mathrm{off})}{\mathrm{DC}_{ij,m}(\mathrm{off})} \,. \tag{12.1}$$

Figure 12.3 shows $\mathrm{norm}(\mathrm{DC}_{ij,m}(\varphi))$, for the two beams. The powers clearly split up for increasing rotation of the polarisation state, φ, following the polarisation pattern, described in Chapter 7.

Using the model, derived in Chapter 8, the power in parallel polarisation was retrieved from the measured powers by:

$$P_m^{\parallel}(\varphi) = \left(\frac{\mathrm{DC}_{ij,m}(\varphi)}{\mathrm{DC}_m(\varphi)} - \frac{\mathrm{DC}_{ij,m}(\mathrm{off})}{\mathrm{DC}_m(\mathrm{off})} \right) \cdot \frac{1}{\lambda_{ij,m}^{\parallel}} \,, \tag{12.2}$$

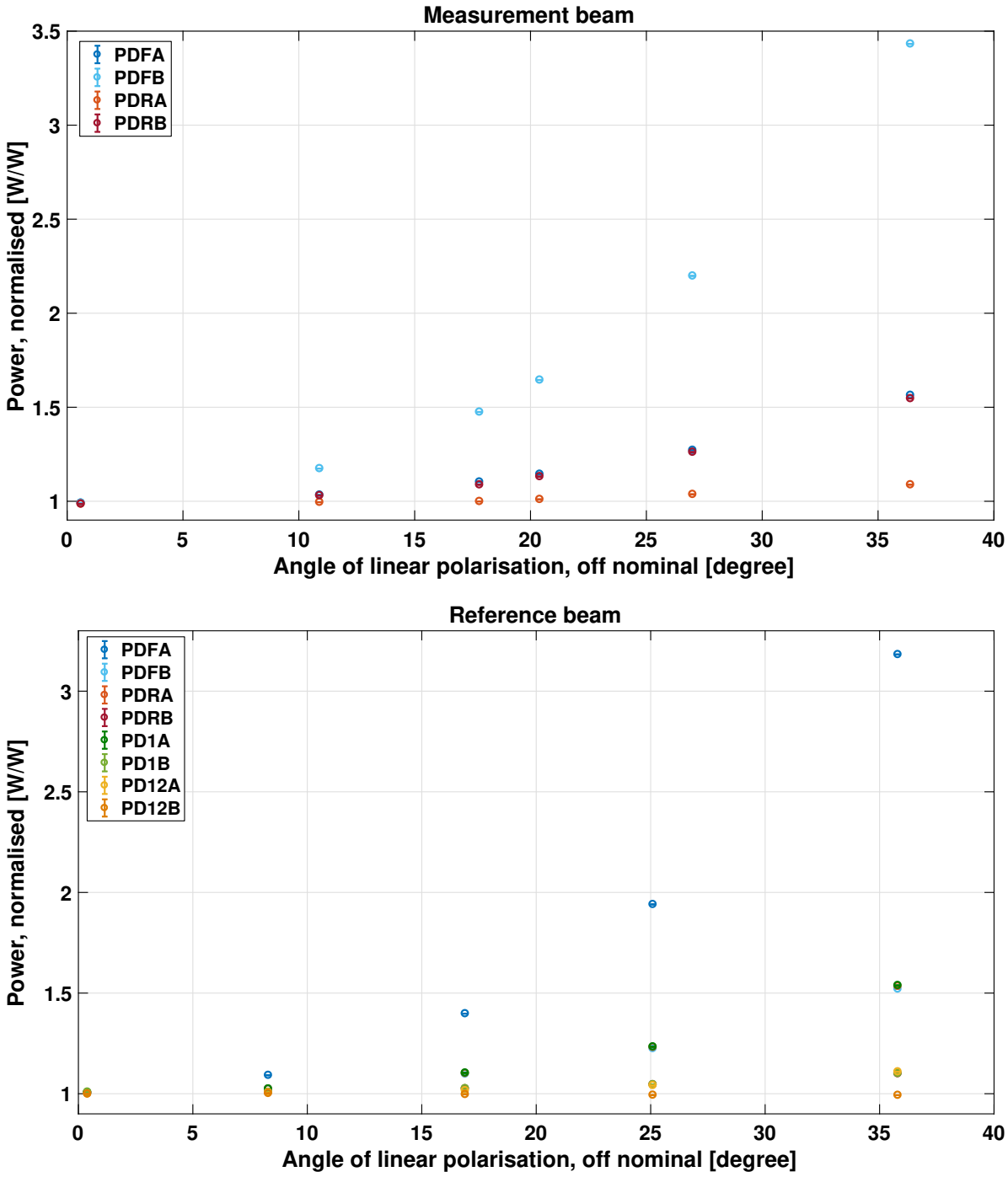

Figure 12.3.: Normalised powers, norm($DC_{ij,m}(\varphi)$), (see Equation 12.1) of the measurement and reference beam on all available diodes for different rotations of linear polarisation state of light **on** the OB (by a filter **after** the PBS).

where $\lambda^{\parallel}_{ij,m}$ refers to the transmission coefficient of the particular beam path, as derived in Chapter 8. The P-pol needs to be compared to the orthogonal polarised share (by this, all polarisation independent losses cancel). For the reference beam, the S-pol was estimated by $\mathrm{DC}_{\mathrm{12B,\,RB}}$, which has negligible power in parallel polarisation.

For the measurement beam, the corresponding $\mathrm{DC}_{\mathrm{12A,\,MB}}$ channel is not available due to the missing TMs. Therefore, the measured powers without filter were used, since there is very little parallel polarisation in the interferometers, as was seen during the first measurement in Figure 12.1. The average in S-pol of the four available diodes without filter was used for the computation of $P^{\perp}_{\mathrm{MB}}$.

$$P^{\perp}_{\mathrm{RB}}(\varphi) = \frac{\mathrm{DC}_{\mathrm{12B,\,RB}}(\varphi)}{\mathrm{DC}_{\mathrm{RB}}(\varphi)} \cdot \frac{1}{\lambda^{\perp}_{12B,m}}\,, \tag{12.3}$$

$$P^{\perp}_{\mathrm{MB}}(\mathrm{off}) = \sum_{n=1}^{4} \frac{\mathrm{DC}_{I_n,\,\mathrm{MB}}(\mathrm{off})}{\mathrm{DC}_{\mathrm{MB}}(\mathrm{off})} \cdot \frac{1}{\lambda^{\perp}_{I_n,m}}\,, \tag{12.4}$$

with $I_n =$ FA, FB, RA, RB .

The resulting ratios $\frac{P^{\parallel}}{P^{\perp}}$ for the different polarisation filter states are shown in Figure 12.4 and 12.5, in dependency of the polarimeter measured angles in the laboratory.

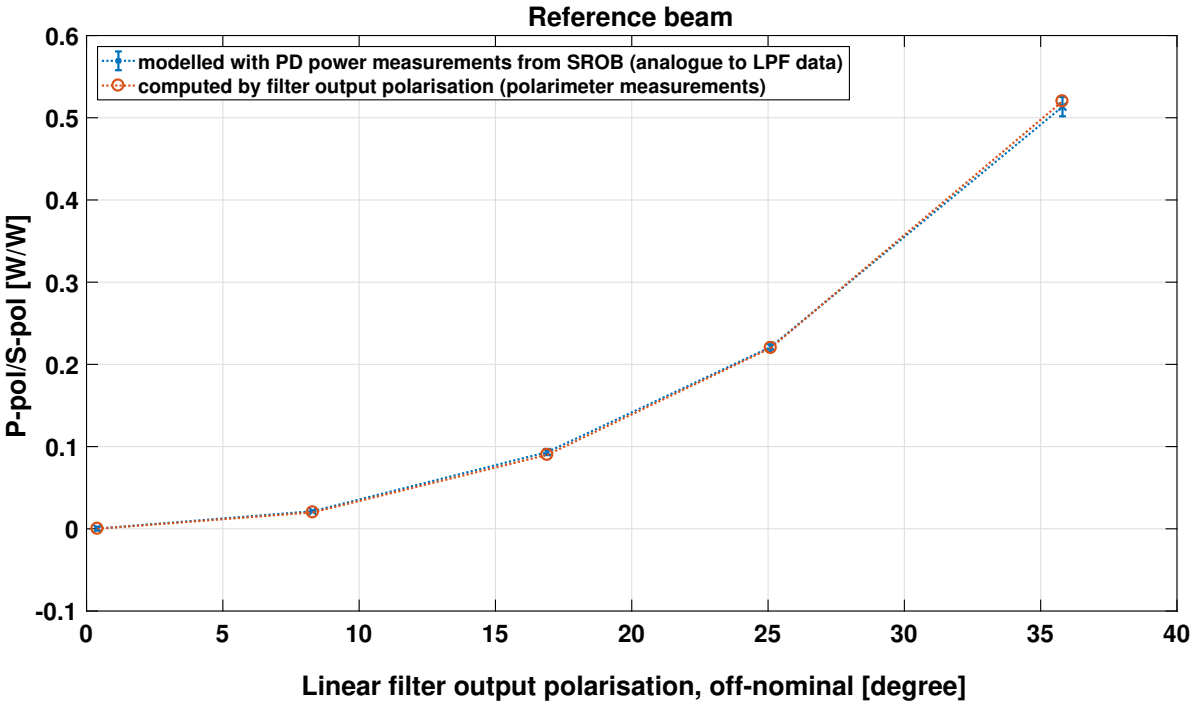

Figure 12.4.: Ratio of $\frac{P^{\parallel}}{P^{\perp}}$ for the reference beam on the OB, once measured with a polarimeter and once computed from the power measurements, analogue to the model derived in Chapter8. The two parameters agree within errors.

Within errors, the retrieved share of parallel polarisation is consistent with the polarimeter measurements for all angles. Therefore, the model is verified to agree with the measured polarisation states, even for very large off-nominal polarisation angles.

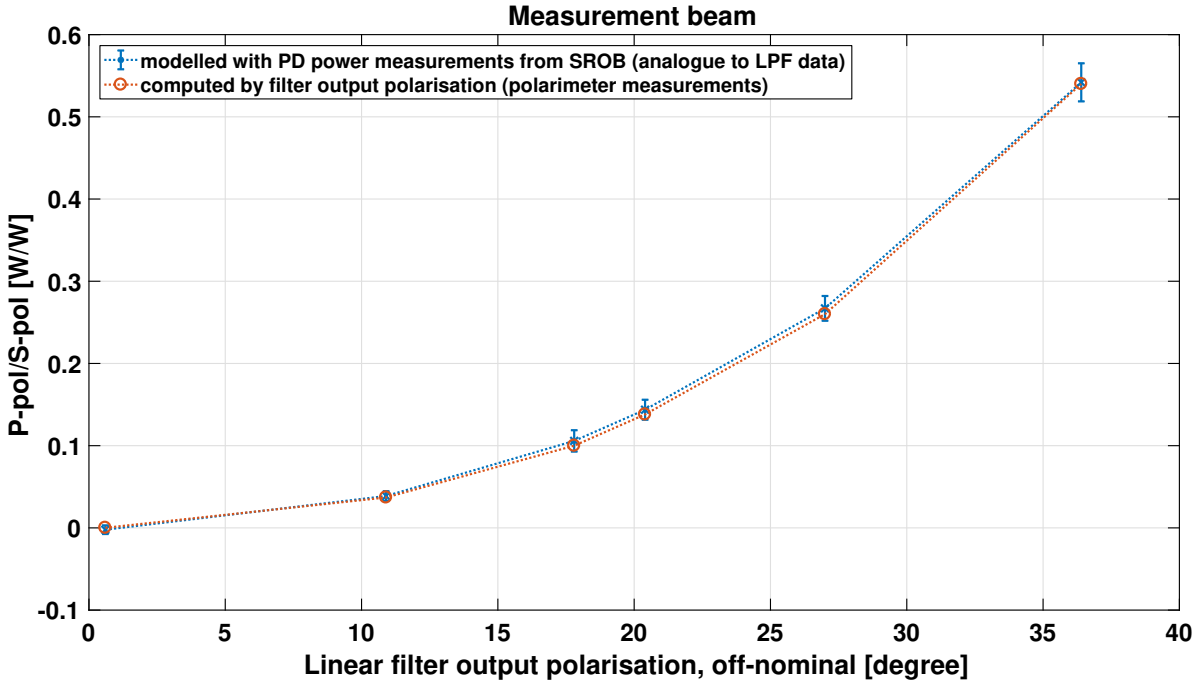

Figure 12.5.: Ratio of $\frac{P^{\parallel}}{P^{\perp}}$ for the measurement beam on the OB, once measured with a polarimeter and once computed from the power measurements, analogue to the model derived in Chapter 8. The two parameters agree within errors.

12.2.2. Polarisation filter before the PBS

As a second step, the impact of polarisation rotation before the OB was investigated. Therefore, the polarisation filter was moved in front of the PBS, into the small gap between lens and PBS (on the FIOS). A new adapter was built, fitting in the tiny gap, as can be seen in Figure 12.6.

Figure 12.6.: Polarisation filter on the spare OB filter **before** PBS.

For the measurement beam, the power was, as before, readjusted for each filter state so that the power on the monitor diode was kept constant.

The data was processed similar to the previous filter positions, as described by Equation 12.1.

Figure 12.7 shows norm($DC_{ij,MB}(\varphi)$) (normalisation by equation 12.1) in dependence of the filter rotation. The measured powers all agree within 2 %. This variation could result from the modified alignment, due to the filter. Furthermore, the variation in normalised power for different filter angles is not greater on $DC_{FB,\,MB}$ (most sensitive to parallel polarised light) than on the other diodes. Therefore, no polarisation-induced changes in power could be observed.

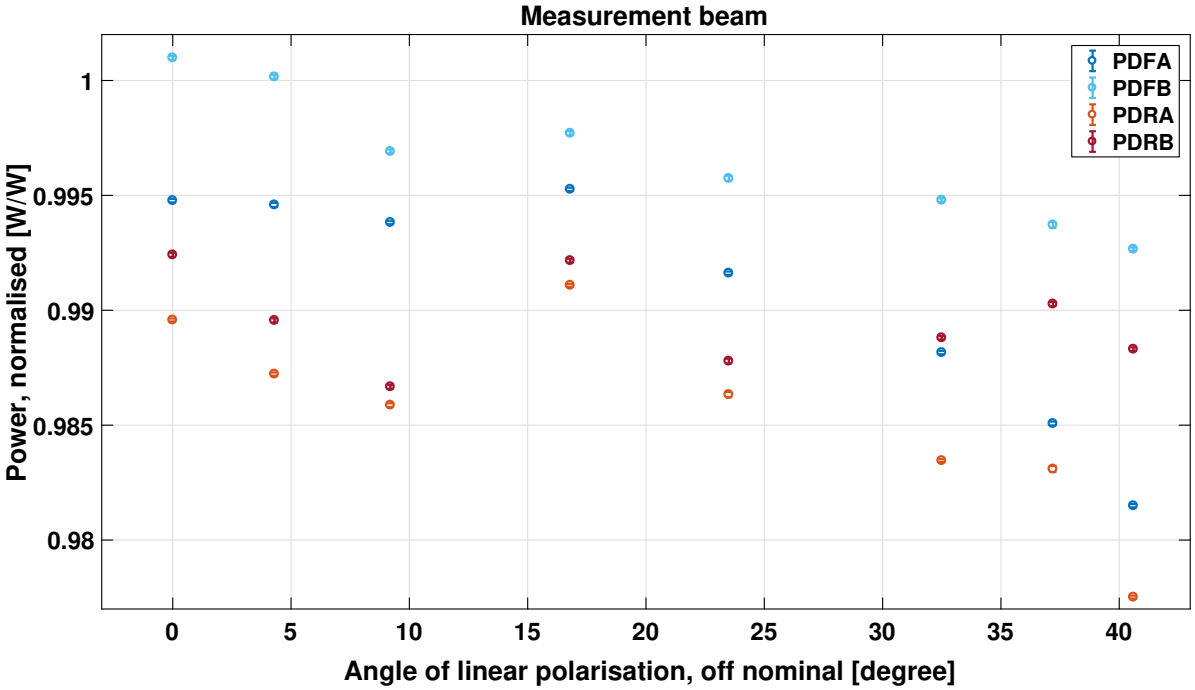

Figure 12.7.: Normalised powers, norm($DC_{ij,MB}(\varphi)$) (see Equation 12.1), of the measurement beam on all available spare OB diodes for different polarisation rotations of light **before** the PBS (by using a filter between the lens and the PBS). The input laser power was readjusted to a constant current at the power monitor diode for each filter rotation.

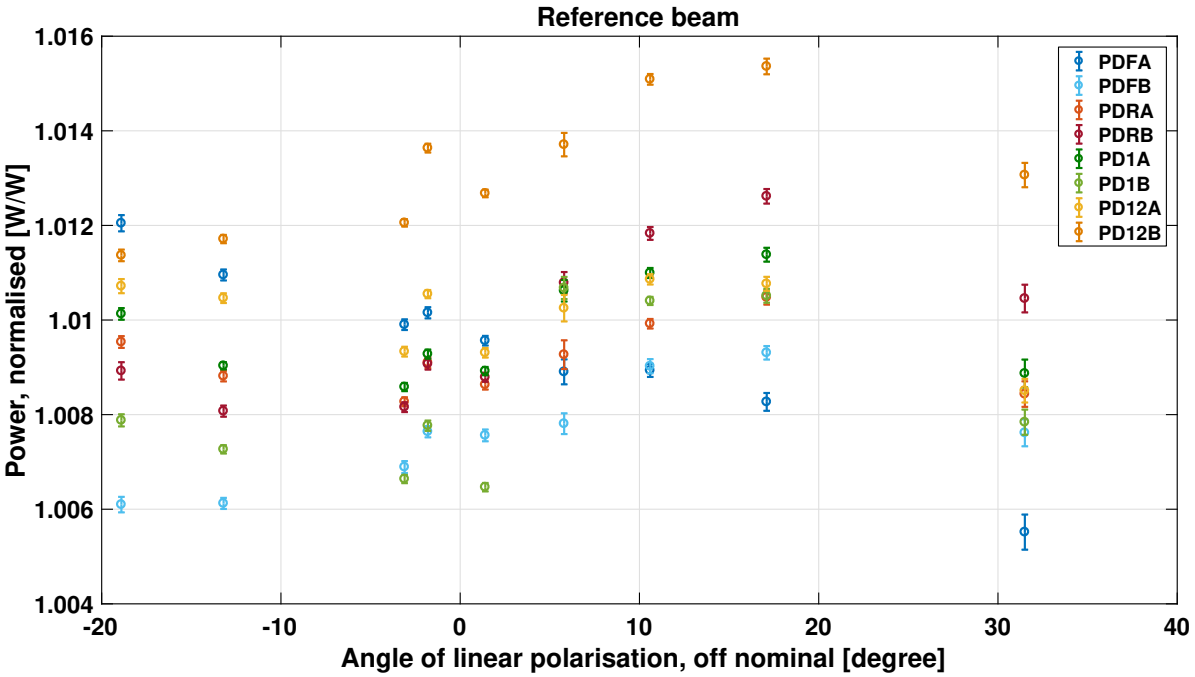

Figure 12.8.: Normalised powers, norm($DC_{ij,RB}(\varphi)$) (see Equation 12.1), of the reference beam on all spare OB diodes for different rotations of linear polarisation of the light **before** the PBS (by using a filter between the lens and the PBS). The input laser-power was kept constant for all measurements.

The experiment was repeated for the reference beam, but due to the slightly thinner gap between lens and PBS, a thinner polarisation filter had to be used.

Again, the filter rotation was measured before applying it to the OB, but for this measurement series (with the reference beam) the power was kept stable during the whole investigation with different filter angles (and not readjusted to a constant power at the power monitor diode). Therefore, the transmitted power through the PBS gets lower for higher filter rotations. This could possibly enhance an impact of photodiode offsets to the analysis.

Nevertheless, the normalisation removes the different power level from the measurement observable $\mathrm{norm}(\mathrm{DC}_{ij,\mathrm{MB}}(\varphi))$, as shown in Figure 12.8.

Again, no power distribution corresponding to the pattern, described in Chapter 7, can be observed. The normalised powers all agree within 1 % and the frequency interferometer, labelled PDFA, which is most sensitive to parallel polarised light, has no significantly higher variation than the other diodes.

Box 12.2.1 | Summary: Measurements with the spare OB

Measured **fluctuations in P-pol on the spare OB** due to a **mechanically stressed fibre** show:

- The transmitted P-pol to the OB is about two orders of magnitude smaller than in-flight.
- It is comparable between the two beams.

→ It further agrees with the specifications of PBS PER.

Rotation of polarisation *on* the spare OB, with a polarisation filter **after** the PBS:

- The estimated P-pol from the power measurements agrees with the measured output polarisation of the filter.

→ The derived model in Chapter 8 was therefore verified.

Rotation of polarisation *before* the PBS, with a polarisation filter between lens and PBS:

- No impact of the polarisation state on the OB above the errors observable.

→ The polarisation cleaning works exemplarily.

Open questions:

- Why was the power in parallel polarisation so much greater during flight?
- ... and about one order of magnitude smaller during pre-flight thermal cycling ?
- ... and on the spare OB again about an order of magnitude smaller and well within specifications?

→ **What is the critical difference between the three measurements?**

13. Subsequent laboratory analysis of the flight spare PBSs: The effect of vacuum baking

All measurements with the spare OB, described in Chapter 12, disagree with theories, related to the way in which the PBS is mounted. Hence, a new idea for an effect, enhancing the P-pol transmission, must be found.

Since the spare OB and the flight OB are identically constructed, the mechanism cannot be related to the OB design. Also, the data processing is comparable. However, the environment of the experiment changed: The flight spare OB is stored in air. For the thermal cycling prior to flight, the OB was moved into vacuum and during flight, the OB was already exposed to satellite atmosphere for several months.
So, the next idea was that the vacuum could have a long-term effect on the PBSs. A possible reason for such an effect could be a degradation of the glue, combining the two prisms of the cubical PBS. Possibly, dissolved molecules in the glue were out-gassing in the vacuum and causing a change of the optical properties of the material. The tiny interaction surface of glue and space could have led to a slow degradation that was not reaching its maximum during the comparably short pre-flight tests.

Therefore, two of the flight spare PBSs were vacuum baked at 50 °C, as described in the following.

13.1. Vacuum baking of a PBS

To qualitatively investigate a possible effect of a vacuum on the PBS, two of the three flight spare PBSs were put into a vacuum chamber for about one week. The whole tank was heated up to 50 °C to speed up any possible out-gassing.
The temperature of 50 °C was chosen because the thermal cycling and the mechanical stress tests already used this temperature without any observable damaging effect to the PBSs.

One PBS — labelled as PBS3 — was kept in air, as a reference component.

At the end of the week, the temperature was reduced to room temperature. After re-thermalisation, the vacuum chamber was opened and the two PBSs were immediately moved to the previously used measurement setup (see Figure 11.1). The transmission of parallel polarisation for rotation of input polarisation was measured for all three PBSs. The data was then processed like the previous measurements of the PER, as described in Section 11.4.

Figure 13.1 shows the results for the pre-vacuum (labelled "air") and vacuum baked PBSs, all with a rotation of 3° around their z-axes.

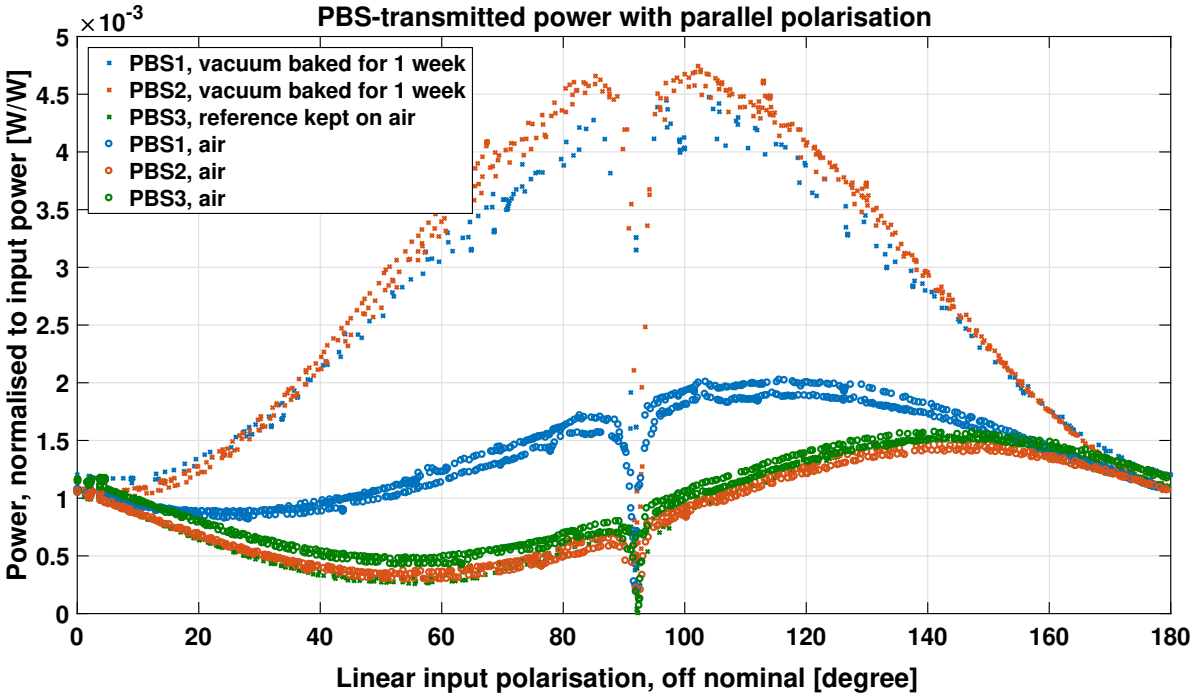

Figure 13.1.: Transmission of P-pol, dependent on input polarisation, for all three PBSs before and after vacuum baking. The data sets were resampled to a 1-degree grid.

Since PBS3 was not exposed to the vacuum, the good matching to the pre-vacuum measurement, labelled " PBS3, air" (see Figure 13.1), gives confidence on the stability of the setup, in between the two measurements.

During the pre-vacuum test, PBS2 had a comparable P-pol transmission with PBS3. However, after vacuum baking its transmission of P-pol increased significantly for any input polarisation offset the nominal orthogonal polarisation.

PBS1 had a higher transmission of parallel polarisation compared to PBS2 and PBS3 already observed before vacuum baking. As mentioned before, this could be a consequence of possible damage by the several mechanical stress testing applied to PBS1 in advance. Nevertheless, after vacuum baking also for PBS1 the transmission of parallel polarisation further increased for an input polarisation offset the nominal polarisation.

13.1.1. Combination of vacuum baking and stress

Figure 13.2 shows the P-pol transmission through the two vacuum baking flight spare PBSs (together with the reference PBS3), again rotated by $\varphi_{\mathrm{PBS}} = 3°$, for linear rotation of input polarisation. But at this time, the PBSs were constantly set to mechanical stress with a weight of 6.2 kg.

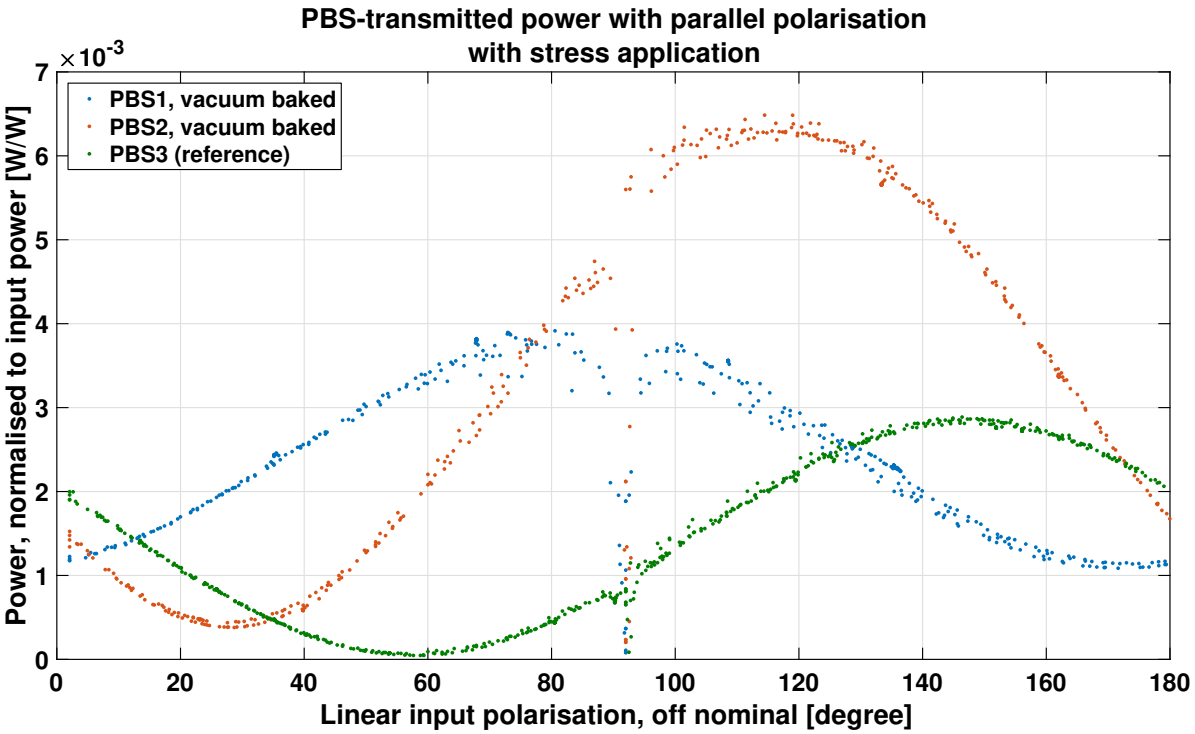

Figure 13.2.: Transmission of P-pol through a constantly stressed PBS. The PBSs are rotated by 3 degree offset and the constant stress is applied by a weight of 6.2 kg. PBS 1 and 2 were exposed to vacuum for about one week, PBS 3 gives a reference, kept on air all time.

The transmission of P-pol through PBS2 is more asymmetric around the input polarisation parallel or orthogonal to the PBS optical axis. This effect was already observed for the PBSs in air, before vacuum baking (compare with Figure 11.10). The asymmetry leads to higher transmissions of P-pol for input polarisations between $\varphi_{\mathrm{pol}} = 90° + \varphi_{\mathrm{PBS}}$ and $\varphi_{\mathrm{pol}} = 180° + \varphi_{\mathrm{PBS}}$. Surprisingly for PBS1, there is no effect of the stress application visible. This could be caused by the statistical variation of the stress effect (described in Section 11.5) or actually different behaviour, like the previously observed higher P-pol transmission through PBS1 on air. The measurement would need to be repeated to clarify the anomalous behaviour of PBS1.

Another difference of the stressed vacuum baked PBSs is the transmitted P-pol power at orthogonal input polarisation. Here, the stressed reference PBS3 transmits more P-pol than the stressed vacuum baked ones. This increase seems to be induced by the asymmetry, described in Section 11.5, together with the PBS-rotation of $\varphi_{\mathrm{PBS}} = 3°$, wherefore the S-pol input polarisation is not parallel to the optical axis on the PBS. For the vacuum baked PBS2, the change in symmetry due to mechanical stress appears to be slightly different: the maximum and minimum transmissions of parallel input polarisation move closer to the orthogonal and parallel polarisation state. At S-pol and P-pol input polarisation (now in the normal coordinate system with respect to the OB), the transmission is therefore closer to the unstressed case.

However, the observed effects are described by only two vacuum baked samples, with one of them showing anomalous behaviour previous to being vacuum baked.

Therefore, the observations can only give evidence on the actual effect leading to the LPF polarisation variations with limited validity, of course.

13.1.2. Acclimatisation back in air

Since in the previous section clearly an effect of vacuum baking on the PBS PER could be observed, the next question is, if the effect is permanent. Therefore, the P-pol transmission for linear rotation of input polarisation through all three PBSs (rotated by $\varphi_{\mathrm{PBS}} = 3°$) was measured after storage of the PBSs for several weeks in a "stay-fresh" box with silica gel pads. The results are presented in Figure 13.3.

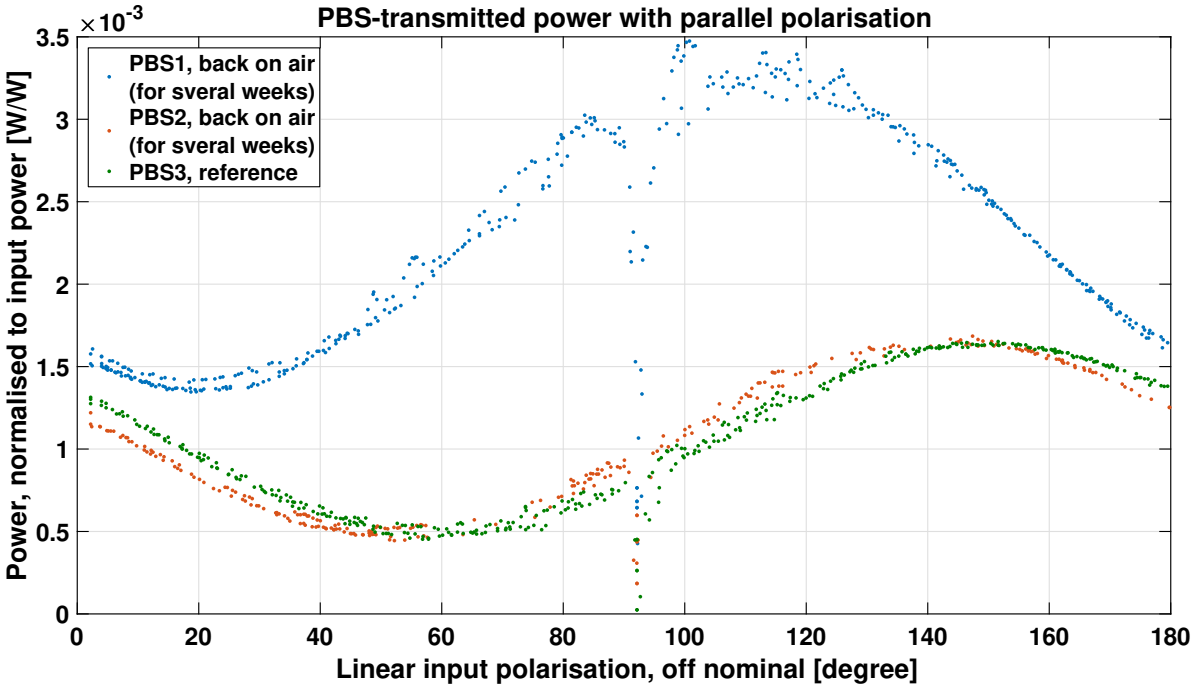

Figure 13.3.: Transmission of P-pol through all three PBSs after acclimatisation back on air (in a box with silica-gel) for several weeks. PBS 3 gives a reference, kept on air all time. The PBSs are rotated around the z-axis by 3 degree.

The transmission of P-pol through PBS2 totally recovered back to the pre-vacuum state, as can be seen by the comparison to the reference PBS3. Surprisingly, the P-pol transmission through PBS1 for off-nominal input polarisation decreased only slightly and is still higher than before the vacuum baking (compare to Figure 11.8). The differing behaviour of PBS1 could again have many reasons: maybe the recovering time was too short, or the reduced humidity inside the box by the silica gel pads led to an incomplete recovery of PBS1. On the other hand, PBS1 could also just have differing properties, possibly caused by permanent damage, due to the stress tests or simply due to differences in manufacturing.

13.1.3. Storage in ultra-dry air vs vacuum baking

The observed total and incomplete recovering of PBS2 and PBS1 in a box with air and reduced humidity, led to a subsequent test: PBS1 was stored in a sealed glass with phosphorus pentoxide P_2O_5 for about three weeks, as can be seen in Picture 13.4. The phosphorus pentoxide reduces the humidity to below 1 %.

In the meanwhile, PBS2 was again vacuum baked for 2 weeks at 50°. In the third week, the temperature was reduced to room temperature and PBS2 was simply kept in vacuum.

As before, PBS2 and PBS1 were analysed in transmission for linear rotation of input polarisation (with a PBS rotation by $\varphi_{\mathrm{PBS}} = 3°$), directly after taking them out of their specific environment. The resulting P-pol transmission is shown in Figure 13.5 together with the corresponding measurement through the reference PBS3.

Both PBSs show a comparable decrease in extinction of parallel input polarisation. In comparison to the one week vacuum baking (Figure 13.1), the maximum ratio of $P^{\parallel}/P_{\mathrm{in}}$ in transmission is about $1 \cdot 10^{-3}$ and therefore roughly 20 % stronger after 3 weeks.

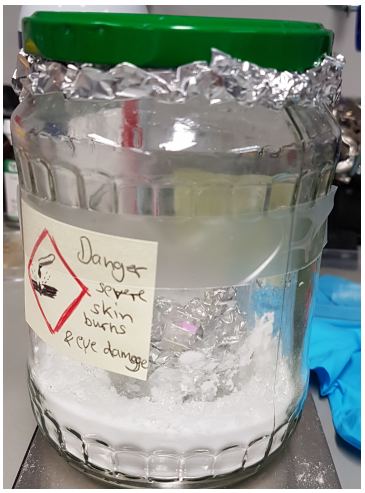

Figure 13.4.: PBS1 stored with phosphorus pentoxide, P_2O_5.

Obviously, the corresponding assumption is that water out-gassing is the driving force of the PER decrease.

To verify this theory, the dried PBSs were analysed in transmission with a spectral photometer. Figure 13.6 shows the transmission of parallel and orthogonal polarisation through all three PBSs in dependency of the input wavelength.

Due to the mounting inside the photometer, the PBSs could not be rotated around their z-axis. Therefore, the measurement was taken for normal incidence (with an undetermined adjustment error). Another difference to the measurements in the laser laboratory are the photodetectors. Corresponding to the wavelength, different detectors are used in the photometer detecting all transmitted power. Therefore, only the total transmitted light, without a splitting into parallel and orthogonal transmitted parts is measurable.

Nevertheless, the qualitative spectral behaviour of the transmitted power gives evidence for the originating effect: **The spectra of the dried and vacuum baked PBSs shift towards shorter wavelengths.**

This behaviour is commonly referred to as wet-dry shift [67, 68, 69, 70], generated in multi-layer-coatings with loose packing of the atoms building the layers. Here, water can depose in the gaps, lengthening the optical path through the layer. As a result, the spectral properties of the multi-layer system shift towards longer wavelengths, as observed for the reference PBS3, kept on wet air (at normal humidity and room temperature). When the water is removed, by out-gassing, the spectrum shifts again towards smaller wavelengths, as observable for the dried PBS1 and vacuum baked PBS2 in Figure 13.6.

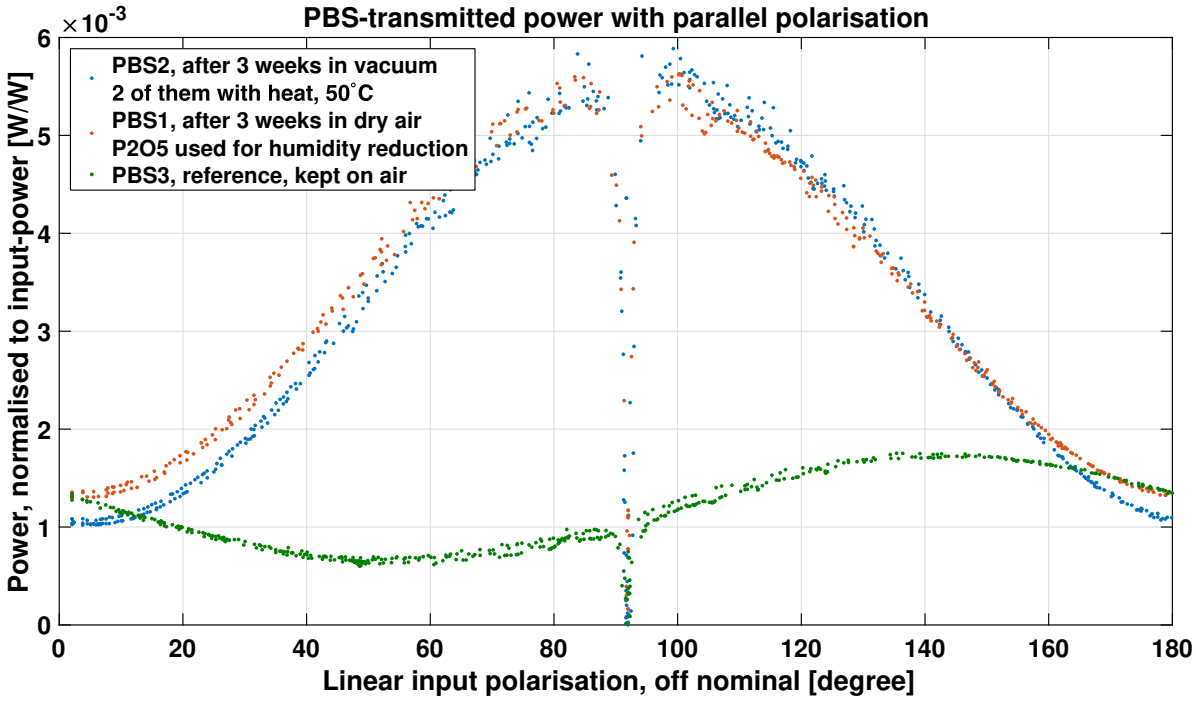

Figure 13.5.: Second vacuum test: PBS2 was in vacuum for three weeks and PBS1 in phosphorus pentoxide. PBS3 was again kept as reference.

At this point, the glue — heavily suspected to be related to the observed effects — comes to mind: The glue seals the coating and hence avoids the water from out-gassing in the environment. However, since the glue is still a fluid with a tiny interaction surface to the surrounding (the edges of the cube), it is only buffering the out-gassing of water. The dissolved water in the glue needs to be out-gassed first, so that the water, enclosed in the coating, can diffuse into the glue and pass through to the environment.

However, a spectral shift of the coating properties is only relevant if the used frequency is close to an edge in the spectral band with the desired properties. In the case of a PBS, these are the extinction of parallel polarisation and the transmission of orthogonal polarised light.

A zoom into the spectral transmission of parallel polarised input light around the LPF laser wavelength of 1064 nm (see Figure 13.7) convincingly shows that the wet-dry shift shifts the spectrum across the used laser frequency to the edge of the desired band with appropriate properties.

At this point, it shall be mentioned again that the transmitted light in Figure 13.7 is the sum of orthogonal and parallel polarised transmission (compare to Figure 11.4). The values are therefore not easily comparable to the transmission with parallel polarisation measured at the laser frequency (shown in Figure 13.5). Furthermore, the angular adjustment in the spectral photometer is of lower accuracy than with the dedicated mount in the laser laboratory. Therefore, smaller aberrations between the polarisation axis and the PBS axis are possible, leading to a shift in the narrow dip around perfect parallel polarised input light.

Because of the tiny interaction surface of the glue with its surrounding space, given by the

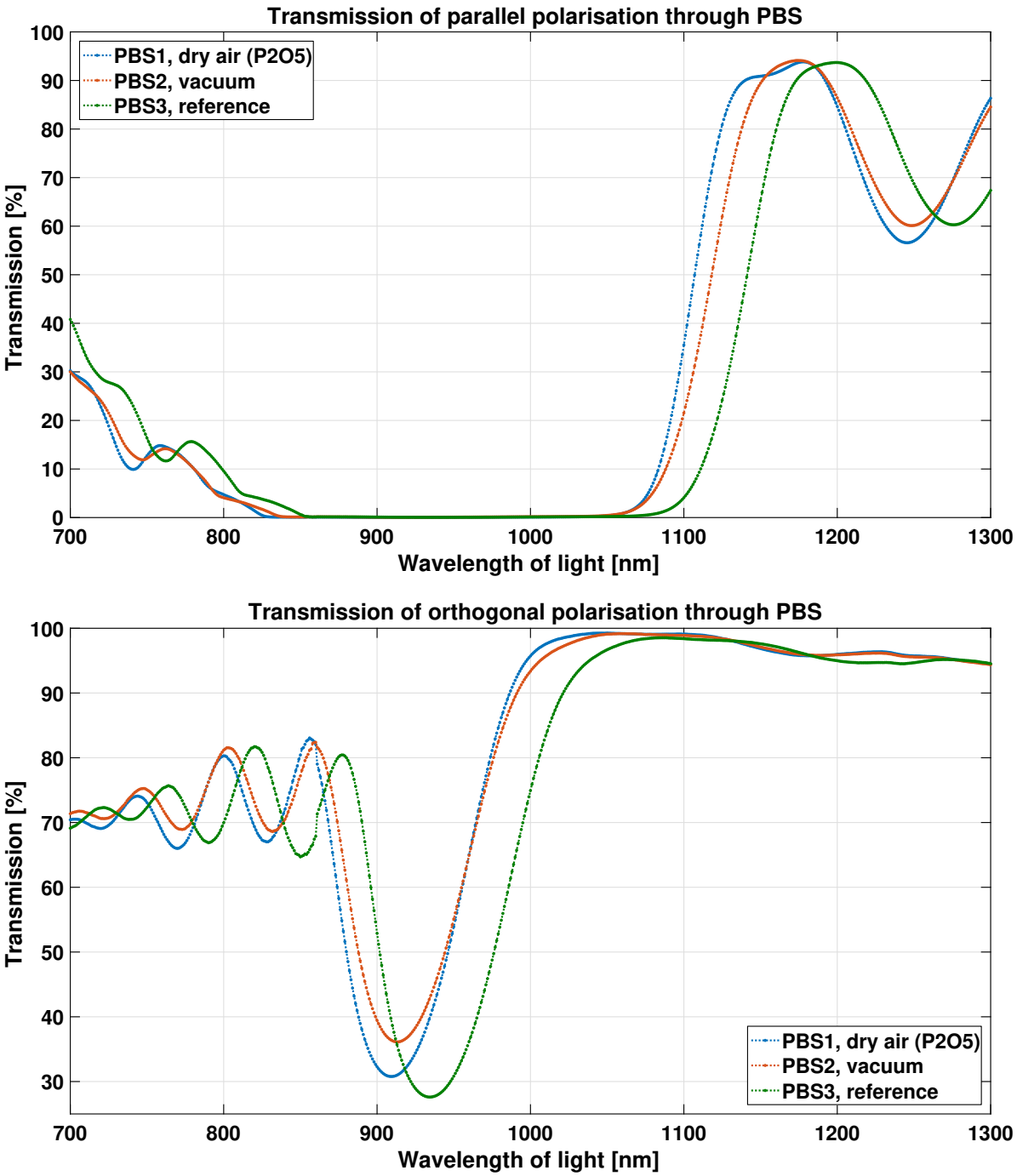

Figure 13.6.: Spectral transmission of orthogonal and parallel polarised light through all three PBSs, measured with a spectral photometer, one week after the second vacuum test. For the last week PBS1 and PBS2 were stored in phosphorus pentoxide. The PBSs could not be rotated in the photometer. Therefore, the incident angle is approximately normal to the PBS surface.

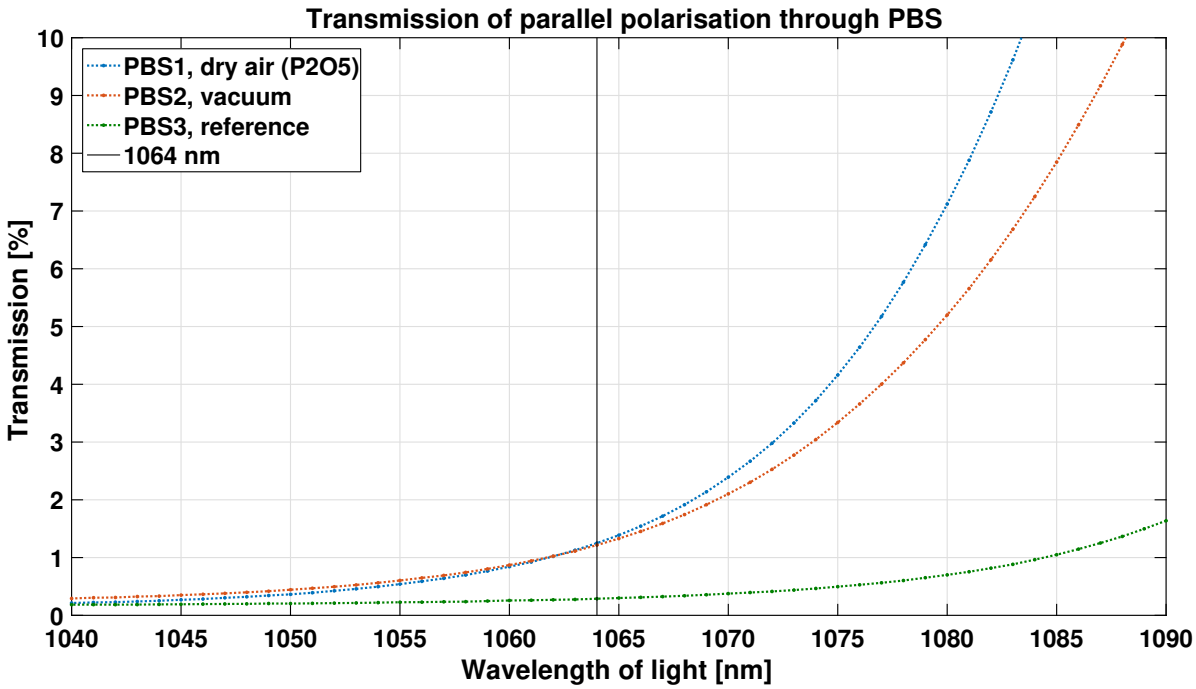

Figure 13.7.: Zoom in the spectral transmission of parallel polarised input light around the LPF laser frequency of 1064 nm.

edges of the gap between the two PBS prisms (measured with an optical telescope to be less than 30 μm wide), the effect could have still been increasing with longer exposure to space as during flight of LPF.

13.2. Describing the vacuum baking effect

The measured effect of vacuum baking or drying a PBS seems to be caused by a decrease of the polarisation extinction: The P-pol transmission for input light close to orthogonal polarisation (parallel to the PBS optical axis @ $0° + \varphi_{\mathrm{PBS}}$) is unaffected, whereas for increasing parallel polarisation in the input light, the transmission of P-pol increases, too.

Only around parallel input polarisation (orthogonal to the PBS optical axis @ $90° + \varphi_{\mathrm{PBS}}$), where all incoming light should be reflected by the PBS, the P-pol transmission decreases again to approximately zero, like before the PBS vacuum baking or drying.

To quantify the observed effect of the vacuum, a simple model is applied to the data of the reference PBS3 that was kept on air. Its PER is decreased by a factor, so that the resulting P-pol transmission fits the observed effect after the second vacuum baking of PBS2 (compare to Figure 13.5).
The model is given by the following equation:

$$\mathrm{fit}(P^{\parallel}_{\mathrm{out}}(\mathrm{vac})) = c^{\parallel}_{\mathrm{norm}} P^{\parallel}_{\mathrm{out}}(\mathrm{air}) + \kappa^{\parallel} \cdot P^{\parallel}_{\mathrm{in}}(\mathrm{air})\,, \tag{13.1}$$

with a factor $\kappa^{\parallel}$, describing the decrease in extinction of parallel input power $P_{\text{in}}^{\parallel}$.
Note that the normalisation $c_{\text{norm}}^{\parallel}$ accounts for the slightly lower transmission of P-pol through the vacuum baked PBS2 for an input close to orthogonal polarisation (at $0° + \varphi_{\text{PBS}}$). The deviation from the reference PBS3 is assumed to be induced by small deviations in the alignment of the PBS rotation below a degree. The coefficient was determined to $c_{\text{norm}} = \frac{P_{\text{out}}^{\parallel}(\text{PBS2})}{P_{\text{out}}^{\parallel}(\text{PBS3})} @ (\varphi = \varphi_{\text{PBS}}) \approx 1.3$.

Figure 13.8 shows the P-pol transmission through reference PBS3 and vacuum baked PBS2, together with the fit of the vacuum state, $\text{fit}(P_{\text{out}}^{\parallel}(\text{vac}))$.

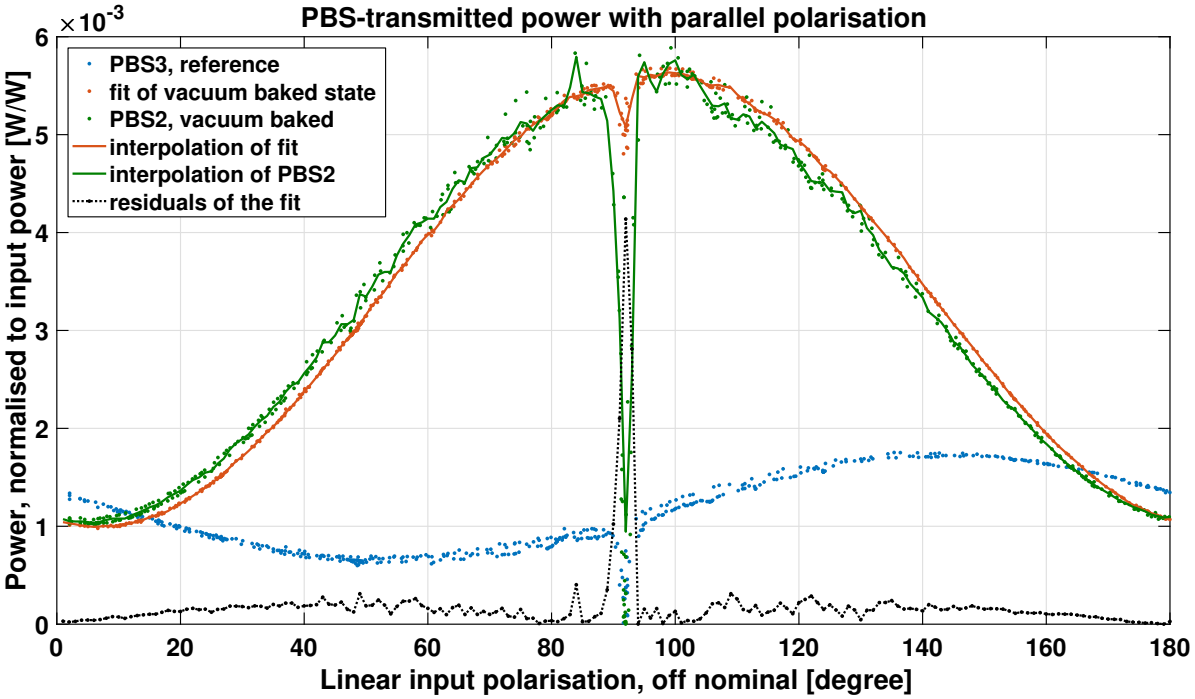

Figure 13.8.: Transmission of P-pol through the reference PBS3 and the vacuum baked PBS2. The red data points give a simple fit of the "after vacuum state", determined by the "reference state", following Equation 13.1 with $c_{\text{norm}} = 1.3$ and $\kappa^{\parallel} = 4.8 \cdot 10^{-3}$.

The correspondence between fit and vacuum baked output power is good with the exception of the dip at $@\,90° + \varphi_{\text{PBS}}$. Nevertheless, these values, close to parallel input polarisation, are of no interest with regard to LPF. Besides the dip, the vacuum state seems to be less asymmetric than the fit. This could again be a consequence of small deviations in PBS rotation alignment, already mentioned.

The coefficient describing the decrease in PER was found to be $\kappa^{\parallel} = 4.8 \cdot 10^{-3}$, giving an extra extinction ratio of $[4.8 : 1000]$, in addition to the previous P-pol transmission.

The spectral photometer data show that vacuum baking the PBS shifts the spectral properties towards shorter wavelengths. Of course, both polarisations are affected by the change in optical properties. Figure 13.9 therefore shows the transmission of both polarisations through the reference and the vacuum baked PBSs.

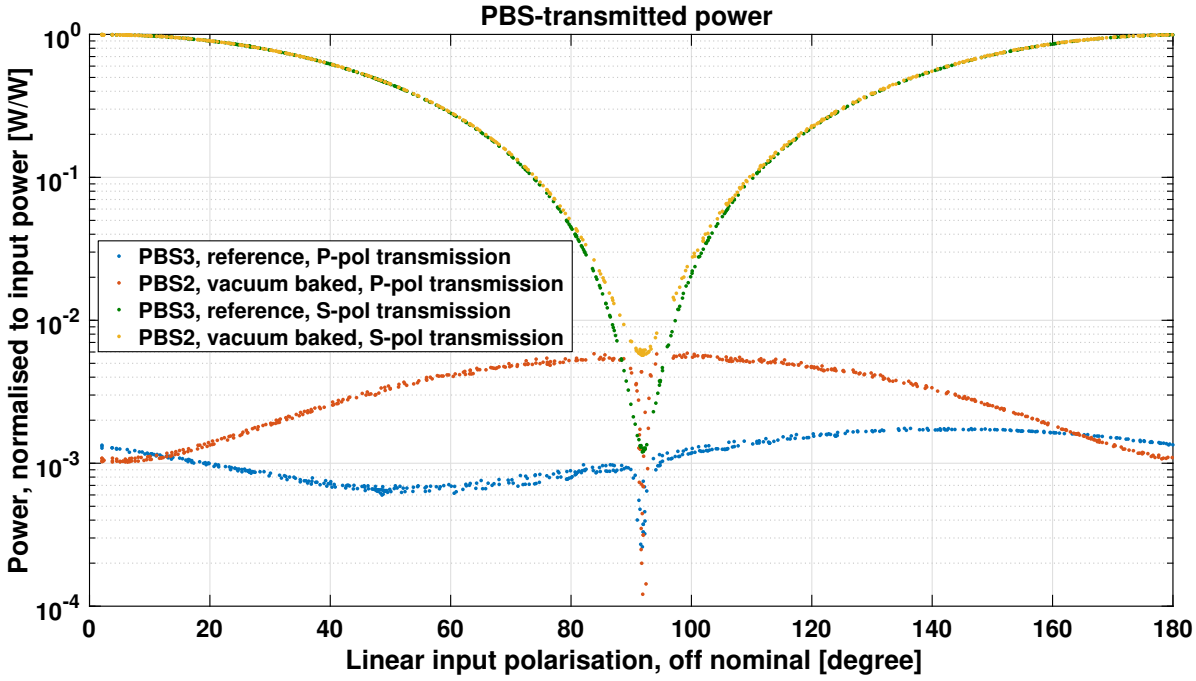

Figure 13.9.: Transmission of orthogonal and parallel polarisation through the reference PBS3 and the vacuum baked PBS2.

The transmission with orthogonal polarisation seems to be affected by the vacuum baking, as well.

For input light, parallel polarised to the PBS optical axis, orthogonal polarised light is transmitted with a power comparable to the parallel polarised transmission at the edges of the dip (around $\varphi_{\mathrm{pol}} = 90° + \varphi_{\mathrm{PBS}}$). This behaviour was already found for the transmission of orthogonal polarisation for P-pol input polarisation with PBS rotation, as shown in Figure11.4.

As a consequence, also for the S-pol transmission, a simple fit with increased PER is applied, as can be seen in Figure 13.10.

$$\mathrm{fit}(P^{\perp}_{\mathrm{out}}(\mathrm{vac})) = P^{\perp}_{\mathrm{out}}(\mathrm{air}) + \kappa^{\perp} \cdot P^{\perp}_{\mathrm{in}}(\mathrm{air}) \tag{13.2}$$

The simple model in Equation 13.2 fits the S-pol transmission quite well. The extinction ratio is computed to be $\kappa^{\perp} = 4.5$. The deviation from the P-pol extinction ratio with $\kappa^{\parallel} = 4.8$ may occur due to the missing normalisation coefficient of $c^{\perp}_{\mathrm{norm}} = 1$, which in case of the S-pol transmission vanishes by normalisation to input power (as described in Box 11.4.1).

The question is left, whether the observed vacuum effects are capable of explaining the observations from the flight OB.

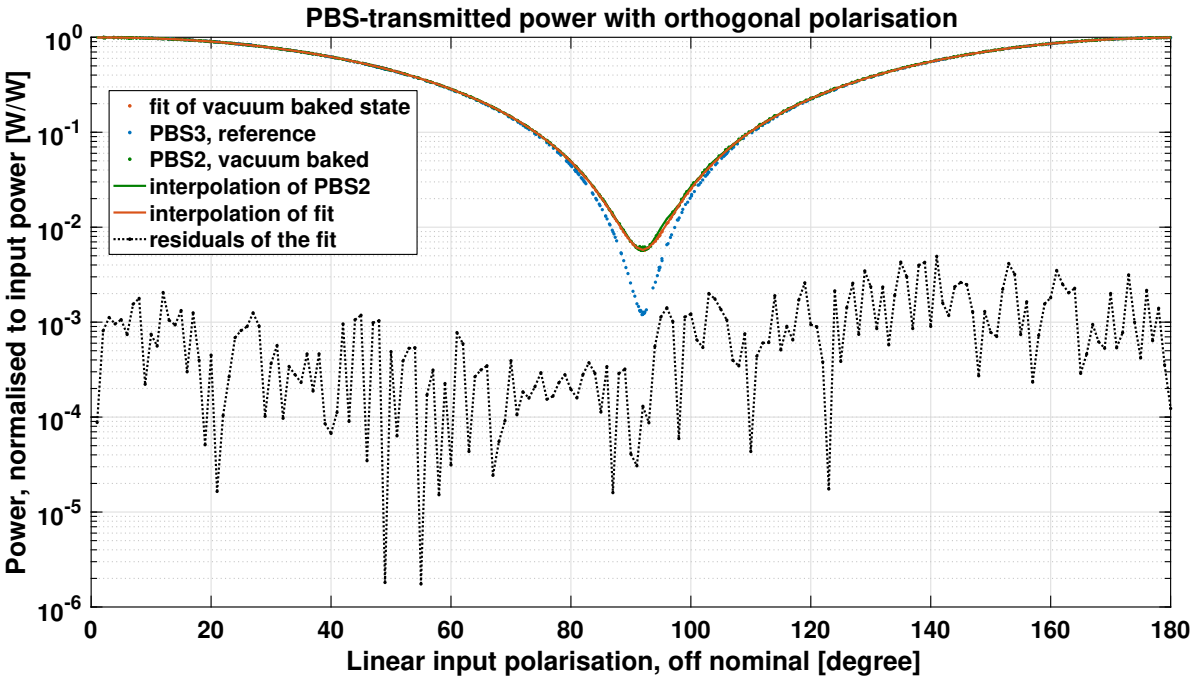

Figure 13.10.: Transmission of orthogonal polarisation through the reference PBS3 and the vacuum baking PBS2. The red data points give a simple fit of the "vacuum baked state", determined with Equation 13.2 with $\kappa^{\perp} = 4.5$, analogous to the model for P-pol.

13.3. Extrapolation of vacuum baking to the LPF OB

For the actual LPF OB, the ratio of parallel and orthogonal transmission was derived from the measured power data.
Subsequently, the same quantity is computed for the vacuum baked PBS, to compare the laboratory results with the data from the OB. The resulting ratio of S-pol and P-pol for the vacuum baked PBS2 (data from Figure 13.5) is shown in Figure 13.11.

Comparison of laboratory results with the P-pol during the thermal cycling, previous to flight:

During the pre-flight thermal cycling tests, the power detected on the OB was fluctuating in a range of up to 40 %. The derived fluctuations in the ratio of P-pol and S-pol for this data set came out with a range of approximately $P^{\parallel}_{\mathrm{RB}}/P^{\perp}_{\mathrm{RB}} \approx (6.1 \pm 0.4)\cdot 10^{-3}$ W/W for reference beam and $P^{\parallel}_{\mathrm{MB}}/P^{\perp}_{\mathrm{MB}} \approx (3.8 \pm 0.3)\cdot 10^{-3}$ W/W for the measurement beam (compare to Chapter 9).

Comparing these data to the PBS laboratory data in Figure 13.11, a loss of 40 % input power is reached at $\varphi_{\mathrm{pol}} = 143°$ or $\varphi_{\mathrm{pol}} = 41°$ input polarisation. The corresponding ratio of P-pol to S-pol is approximately $(5.6 \pm 0.3) \cdot 10^{-3}$. Subtraction of the lowest measured ratio of P-pol to S-pol at $\varphi_{\mathrm{pol}} = 0° + \varphi_{\mathrm{PBS}}$ of approximately 0.1 %, gives a resulting range of fluctuating P-pol to S-pol transmission of 0.44 %. This ratio fits the derived value for the measurement beam during the thermal cycling prior to flight. However, for the reference beam the transmitted P-pol is still 40 % stronger than observed in the lab.

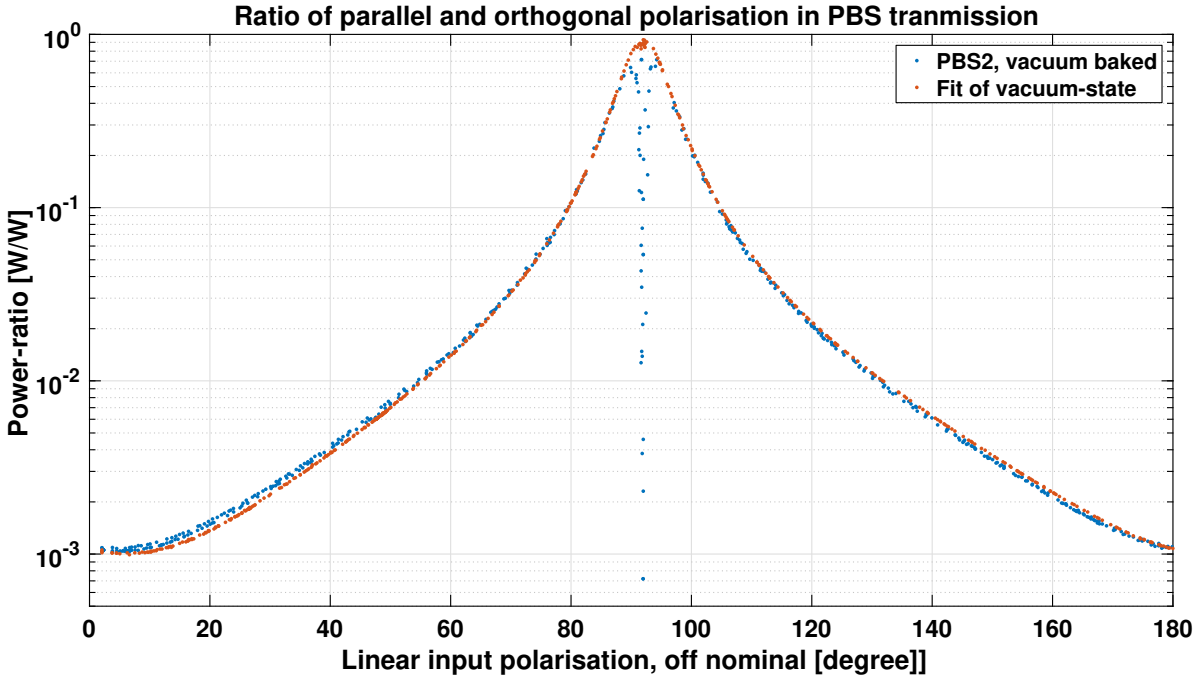

Figure 13.11.: Ratio of P-pol and S-pol transmission for the vacuum baked PBS2 and the corresponding fit from the reference PBS3.

Comparison of laboratory results with the P-pol on the OB during flight:

The derived values of P-pol during the flight of LPF are, as described before, even higher. For the vacuum baked PBS2, a transmission of $P^{\parallel}_{\mathrm{RB}}/P^{\perp}_{\mathrm{RB}} \approx (4.5 \pm 0.045) \cdot 10^{-2}\,\mathrm{W/W}$ at an input polarisation angle of $\varphi_2 \approx 147°$ (as derived for the reference beam) is not reached before a 69° off-nominal rotation of the input polarisation to 111°. At this angle, only 15 % of the input power are left in transmission to the OB. The maximum part of parallel polarised light in the measurement beam during flight was $P^{\parallel}_{\mathrm{MB}}/P^{\perp}_{\mathrm{MB}} \approx (1.74 \pm 0.017) \cdot 10^{-2}\,\mathrm{W/W}$. This ratio is reached for the vacuum baked PBS2 not before a 55° off-nominal rotation of the input polarisation to 122°, where 26 % of the power are transmitted through the PBS.
Such a huge loss in power was excluded already in the earlier analysis.

Therefore, the next question was again, if there could have been an additional effect that enhanced the detected ratio of P-pol and S-pol. A combination of three mechanisms was found to be possible.

Possible enhancing parameters for the transmission of P-pol to the OB:

At first, the PBS in the reference beam — transmitting more P-pol in-flight as well as in the thermal cycling on ground — could be of poor quality. Maybe it was from a batch with poorer quality or in a bad position during the coating process, leading to an even looser packing of the atoms in the coating layers. On the other hand, the measured offset angle of $\varphi_{\mathrm{PBS}} = 3°$ could have been greater within errors of ±2° for the reference FIOS.

A **second mechanism** could be found in the input polarisation. It is likely that at no time all input light was perfectly orthogonal polarised.

If the input polarisation varied between 5° and 10° off-nominal (for example), this would correspond to a smaller variation in the transmitted P-pol than a rotation between 15° and 20° would. However, also the change in transmitted S-pol would be different for the two cases. Although there is no information about the input polarisation to the PBS, there is little information on the variations in the transmitted power to the OB. For the pre-flight thermal cycling, a variation of $\approx 40\,\%$ of the transmitted power was measured. For the in-flight data, the control loop is compensating these fluctuations. However, the applied actuation to the RF power is known. In Appendix E it was found that within the used control range, the RF power amplification is not far off a linear correlation with the transmitted power to the OB (measured at the control loop sensor). For simplicity it is therefore assumed that the input power to the OB was fluctuating in a range of $\approx 15\,\%$, corresponding to the applied range of RF power.
Of course, these values are only a rough estimation. Nevertheless, they can be used to estimate an upper limit of the possible impact on the transmitted P-pol. Therefore, it is further assumed that all variations in the transmitted power to the OB result from the reflection of parallel polarised light at the PBS.

In the next step, the pair of input polarisation rotation angles — corresponding to a variation of 15 % or 40 % transmission to the OB — need to be derived.

For this, the transmitted S-pol through the PBS from Box 11.4.1 can be used (with the assumption of negligible P-pol at the power monitor diode).

$$P^{\perp}_{\text{PBS-out}}(\varphi) = P_{\text{in}} \cdot \cos^2(\varphi - \varphi_{\text{PBS}}) \cdot \cos^2(\varphi_{\text{PBS}})\,.$$

The input polarisation angles φ_1 and φ_2, corresponding to a range of ΔP in the transmitted power, are related as follows:

$$\begin{aligned}
\Delta P &= \frac{\max(P^{\perp}_{\text{PBS-out}}) - \min(P^{\perp}_{\text{PBS-out}})}{\text{mean}(P^{\perp}_{\text{PBS-out}})} \\
&= \frac{P^{\perp}_{\text{PBS-out}}(\varphi_2) - P^{\perp}_{\text{PBS-out}}(\varphi_1)}{0.5 \cdot (P^{\perp}_{\text{PBS-out}}(\varphi_1) + P^{\perp}_{\text{PBS-out}}(\varphi_2))} \qquad (13.3) \\
&= 2 \cdot \frac{\cos^2(\cos^2(\varphi_2 - \varphi_{\text{PBS}}) - \cos^2(\varphi_1 - \varphi_{\text{PBS}})}{\cos^2(\cos^2(\varphi_2 - \varphi_{\text{PBS}}) + \cos^2(\varphi_1 - \varphi_{\text{PBS}})} \\
\rightarrow \varphi_1 &= \arccos\left(\sqrt{\frac{1 - \frac{\Delta P}{2}}{1 + \frac{\Delta P}{2}}} \cdot \cos(\varphi_2 - \varphi_{\text{PBS}})\right) + \varphi_{\text{PBS}}\,. \qquad (13.4)
\end{aligned}$$

As stated above, in the worst case approximation, the range of fluctuations in the transmitted power during flight are given by $\Delta P \approx \Delta P^{\text{flight}}_{\text{RF}} = 15\,\%$ and during the ground tests by $\Delta P = \Delta P^{\text{ground}}_{\text{PBS-out}}{}^{\perp} \approx \Delta P^{\text{ground}}_{\text{PBS-out}} = 40\,\%$. The corresponding pairs of φ_1 and φ_2 are plotted in Figure 13.12.

The derived pairs, $[\varphi_1, \varphi_2]$, can now be adapted to the observed P-pol levels on the OB:

As a consequence, the reference beam power with off-nominal polarisation during the ground measurement can be described by the pair of input polarisation angles with $[\varphi_1, \varphi_2] \approx [161°, 142°]$. At the minimum off-nominal polarisation angle of $\varphi_1 = 161°$, the transmitted power through

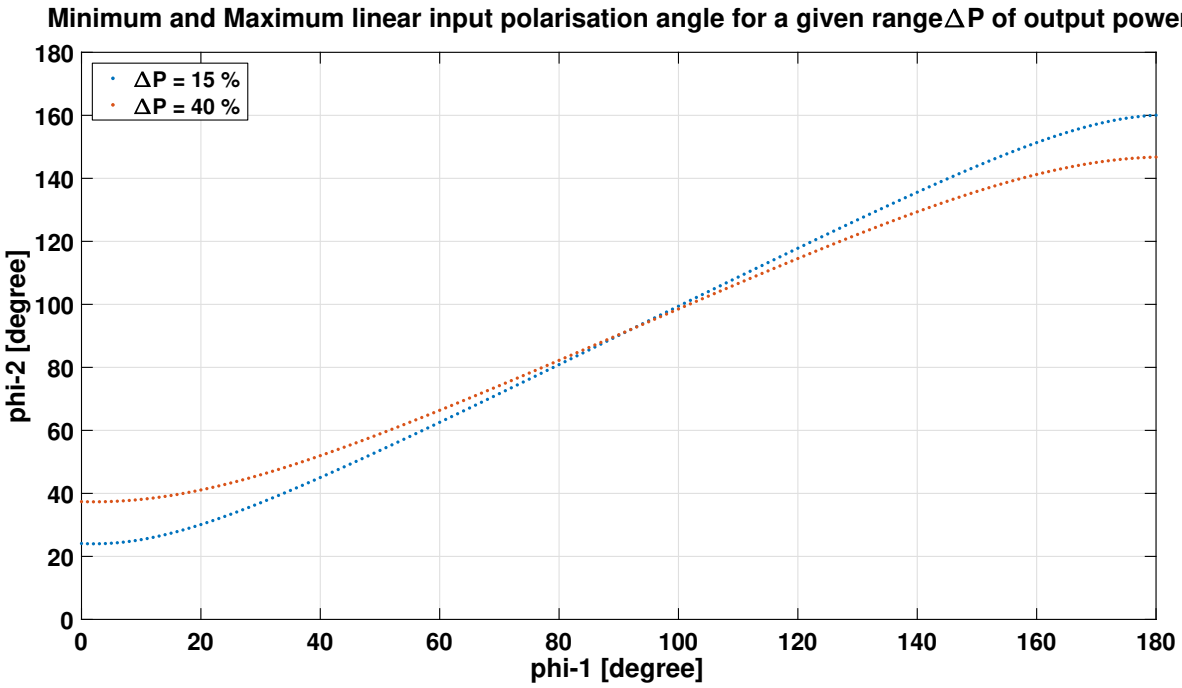

Figure 13.12.: Relation between minimum and maximum linear input polarisation angle $[\varphi_1, \varphi_2]$.

Relation between minimum and maximum linear input polarisation angle $[\varphi_1, \varphi_2]$, corresponding to an output power range of $\Delta P^{\text{flight}} = 15\,\%$ and $\Delta P^{\text{ground}} = 40\,\%$ in a simplified LPF power control scheme for predominant orthogonal input polarisation.

the PBS is 87 %, which might not be far off a realistic condition for the output polarisation of a fibre in a temperature-cycled environment.

For the in-flight observations, Equation 13.4 and Figure 13.12, however, can only be used to consider a realistic enhancing contribution of the input polarisation in combination with another effect that further increases the P-pol transmission during flight, as described in the following.

The **third enhancing effect** is a further degradation of the PER. Since the PBSs are exposed to the spacecraft environment for several months and the interaction surface of glue and the surrounding space is small, it is possible that the water out-gassing continued on a longer time scale than covered by the laboratory experiments described in this thesis.

A further decrease in extinction ratio, following the previously found description can be approached by an additional factor κ_{F}, as described in 13.5.

$$\frac{\text{fit}(P^{\parallel}_{\text{out}}(\text{vac}))}{\text{fit}(P^{\perp}_{\text{out}}(\text{vac}))} = \frac{P^{\parallel}_{\text{out}}(\text{air}) + \kappa_{\text{F}} \cdot \kappa^{\parallel} \cdot P^{\parallel}_{\text{in}}(\text{air})}{P^{\perp}_{\text{out}}(\text{air}) + \kappa_{\text{F}} \cdot \kappa^{\perp} \cdot P^{\perp}_{\text{in}}(\text{air})} \,. \tag{13.5}$$

Figure 13.13 shows the ratio of P-pol and S-pol, following Equation 13.5, for different long-term decreasing factors κ_{F}.

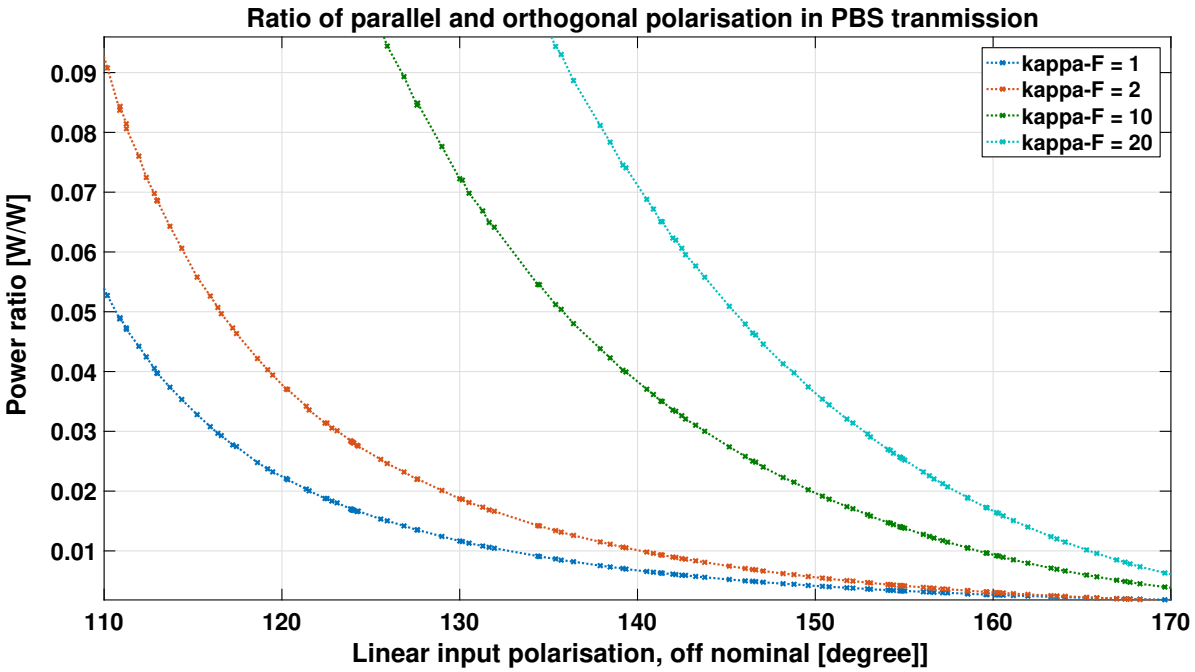

Figure 13.13.: Modelled ratio of P-pol and S-pol transmission for a further decrease of the PER by a factor κ_F, following Equation 13.5.

With a further decrease of a factor $\kappa_F = 2$, the ratio $\frac{P^{\parallel}}{P^{\perp}}$ for the reference beam during thermal cycling on ground would already be explainable with the observed output power fluctuations (for $\kappa_F = 2$, the ratio $P^{\parallel}_{RB}/P^{\perp}_{RB} \approx (6.1 \pm 0.4) \cdot 10^{-3}\,W/W$ is reached at $\varphi_2 = 149°$, with a transmission of 70 % of the input power through the PBS).

For the observed maximum ratio $\frac{P^{\parallel}}{P^{\perp}}$ in the measurement beam during flight, an enhancing factor $\kappa_F \approx 10$ would be needed. Then, the $P^{\parallel}_{MB}/P^{\perp}_{MB} \approx (1.74 \pm 0.017) \cdot 10^{-2}\,W/W$ would be reached at $\varphi_2 \approx 138°$. The corresponding minimum off-nominal input polarisation angle would be $\varphi_1 \approx 161°$. The two angles belong to a transmitted power through the PBS between 75 % and 87 %.

For the reference beam during flight, however, a stronger decreasing factor of $\kappa_F \approx 20$ would at least be needed to result in a level of $P^{\parallel}_{RB}/P^{\perp}_{RB} \approx (4.5 \pm 0.045) \cdot 10^{-2}\,W/W$ at an input polarisation angle of $\varphi_2 \approx 147°$. The corresponding angle $\varphi_1 \approx 154°$ would result in a transmitted power through the PBS of 67 % to 78 %.

Comment on the reasonability of the assumed enhancing mechanisms:
It needs to be noted that for the huge extrapolation of the vacuum effect, an error analysis is not reasonable. The derived values can therefore only be understood as a rough estimate to consider the in-flight observations.
The fact that the pre-flight thermal cycling experiments are explainable with the observed vacuum decrease and a level of up to 30 % P-pol in the input polarisation supports the theory of the PBS degradation as originator of the P-pol on the OB. The reference beam PBS had shown a worse performance in both available measurements, whereas the spare OB had shown a comparable performance of the two PBSs. The assumption of a poor component is therefore

likely. An increase by a factor 10 for the extrapolation of the vacuum effect to the flight case might also be reasonable within the several additional months. For clarification, the total decrease in the PER of spare PBSs could be measured in a long-term laboratory experiment. However, it remains debatable, if the input polarisation to the PBS was actually fluctuating as much as assumed and of course, why that happened. The linear correlation between P-pol on the OB and the power control signal (as estimated in Section 8.4.2), anyway, supports a theory with a fluctuating input polarisation in a range of more then 10 % in P-pol to S-pol for the flight case.

Box 13.3.1 | Summary: PBS vacuum baking

Vacuum baking decreases the PER at the used laser frequency

- The effect is induced by water out-gassing of the PBS coating:
  - → A dry environment led to a comparable decrease in PER.
  - → The spectral photometer data confirmed a strong wet-dry shift of the spectral properties.
- After 3 weeks of vacuum baking at 50 °C, an extra 0.48 % of the input P-pol are transmitted through the PBS.
- The observed P-pol during thermal cycling (ground testing) is reasonably explainable by the observed vacuum-induced PER decrease.
- For the in-flight observations the decrease in PER is still too small:
  - The P-pol in the measurement beam is reasonably explainable by a further decrease in PER due to a longer exposure to the spacecraft environment (about a factor 10 is needed).
  - **However,** the P-pol in the reference beam is still worse,

    → a further decrease of the measured PER by at least a factor 20 would be needed.

Open Questions:

- What is the PER after several months in vacuum?
- Is there another effect, enhancing the P-pol transmission in the reference beam?

→ Possible candidates are: initial bad PER, greater rotation angle of the PBS in the reference beam or mechanical stress effects.

14. Impact on LISA Pathfinder

In the previous chapter, the observation of unexpected low-frequency power noise and its description with fluctuations in polarisation were discussed. Also, the origin of the off-nominal polarisation on the OB was investigated experimentally.
Going ahead, the next step is, to investigate the impact of the polarisation fluctuations on the LPF metrology and the science results. At first, a direct cause of the observed low-frequency power noise comes to mind: The efficiency of balanced detection is affected by the differential power changes on A and B diode.

14.1. Balanced detection

The phasemeter effectively cancels intensity noise by demodulation of the signal at the heterodyne frequency. However, intensity noise around the heterodyne frequency appears as a signal and is therefore affecting the measurement. This noise contribution can be removed by combining the two ports, A and B, of an interferometer in the so-called balanced detection, as described in Section 2.3. If one of the two ports has more or less noise power than the other one, the noise cancellation gets imperfect and a part of the intensity noise at heterodyne frequency is present in the read-out, even with balanced detection.
In general, differential beam power variations do not lead to a different power in the A and B port, because both beams are nominally split by 50:50. Therefore, also the correlated intensity noise of beams with different average power cancels for a 50:50 BS. However, in the case of parallel polarisation this is not true any more, because of the asymmetric BS splitting ratio (compare to the BS splitting ratios in Table 8.1). In an example: If the P-pol of one beam is increasing, one diode measures about 79.5 % of this increase and the other one only 20.5 %. Therefore, 59 % of the P-pol power remains after subtracting the two ports.

The mismatch in balanced detection for the LPF interferometers is derived in the following with the available single beam power measurements. It is assumed that the relative intensity noise around the heterodyne frequency is correlated between the beams, for the orthogonal, as well as for the parallel polarised part of the beams.

The power mismatch in the balanced interferometer output $P_{i\mathrm{A}} - P_{i\mathrm{B}}$ can be written with the measured individual beam powers at the two diodes, $\mathrm{DC}_{ij,\,\mathrm{RB}}$ and $\mathrm{DC}_{ij,\,\mathrm{MB}}$, following Equation 2.2, as:

$$\mathrm{DC}_{i\mathrm{A}} - \mathrm{DC}_{i\mathrm{B}} = (\mathrm{DC}_{i\mathrm{A},\,\mathrm{RB}} - \mathrm{DC}_{iB,\,\mathrm{RB}}) + (\mathrm{DC}_{i\mathrm{A},\,\mathrm{MB}} - \mathrm{DC}_{iB,\,\mathrm{MB}}) \; . \tag{14.1}$$

The remaining power after subtraction also gives a contribution at the heterodyne frequency, ω_{het}, due to the RIN noise at that frequency. The RIN contributions from the single beam

powers add linearly and the remaining power noise in the balanced data stream can be written as:

$$\mathrm{IN}(@f_{\mathrm{het}}) = ((\mathrm{DC}_{i\mathrm{A},\ \mathrm{RB}} - \mathrm{DC}_{iB,\ \mathrm{RB}}) + (\mathrm{DC}_{i\mathrm{A},\ \mathrm{MB}} - \mathrm{DC}_{iB,\ \mathrm{MB}})) \cdot \mathrm{RIN}\,(@f_{\mathrm{het}})\ . \tag{14.2}$$

The contribution to the signal phase can be estimated by division with the root mean square of the carrier heterodyne amplitude a_{het}, as described in Reference [46]. The heterodyne amplitude needs to be estimated with the single beam powers, as follows:

$$a_{\mathrm{het}} = 2 \cdot \left(\sqrt{\eta_{i\mathrm{A}}^{\mathrm{het}} \cdot \mathrm{DC}_{i\mathrm{A},\ \mathrm{RB}} \cdot \mathrm{DC}_{i\mathrm{A},\ \mathrm{MB}}} + \sqrt{\eta_{i\mathrm{B}}^{\mathrm{het}} \cdot \mathrm{DC}_{iB,\ \mathrm{RB}} \cdot \mathrm{DC}_{iB,\ \mathrm{MB}}} \right)\ , \tag{14.3}$$

with the heterodyne efficiency, η^{het}.
The contribution of RIN to the signal phase follows as:

$$\begin{aligned} \Delta\phi_{\mathrm{RIN}} &= \frac{\mathrm{IN}(@f_{\mathrm{het}})}{\frac{1}{\sqrt{2}} \cdot a_{\mathrm{het}}} \\ &= \frac{((\mathrm{DC}_{i\mathrm{A},\ \mathrm{RB}} - \mathrm{DC}_{iB,\ \mathrm{RB}}) + (\mathrm{DC}_{i\mathrm{A},\ \mathrm{MB}} - \mathrm{DC}_{iB,\ \mathrm{MB}})) \cdot \mathrm{RIN}\,(@f_{\mathrm{het}})}{\sqrt{2} \cdot \left(\sqrt{\eta_{i\mathrm{A}}^{\mathrm{het}} \cdot \mathrm{DC}_{i\mathrm{A},\ \mathrm{RB}} \cdot \mathrm{DC}_{i\mathrm{A},\ \mathrm{MB}}} + \sqrt{\eta_{i\mathrm{B}}^{\mathrm{het}} \cdot \mathrm{DC}_{iB,\ \mathrm{RB}} \cdot \mathrm{DC}_{iB,\ \mathrm{MB}}} \right)} \\ &= \Delta c_{\text{bal-det}}^{\mathrm{phase}} \cdot \mathrm{RIN}(@f_{\mathrm{het}})\,. \end{aligned} \tag{14.4}$$

Assuming perfect heterodyne efficiencies of $\eta_{i\mathrm{A}}^{\mathrm{het}} = \eta_{i\mathrm{B}}^{\mathrm{het}} \approx 1$, the coupling coefficients for balanced detection in the different interferometers are shown in Figure 14.1.

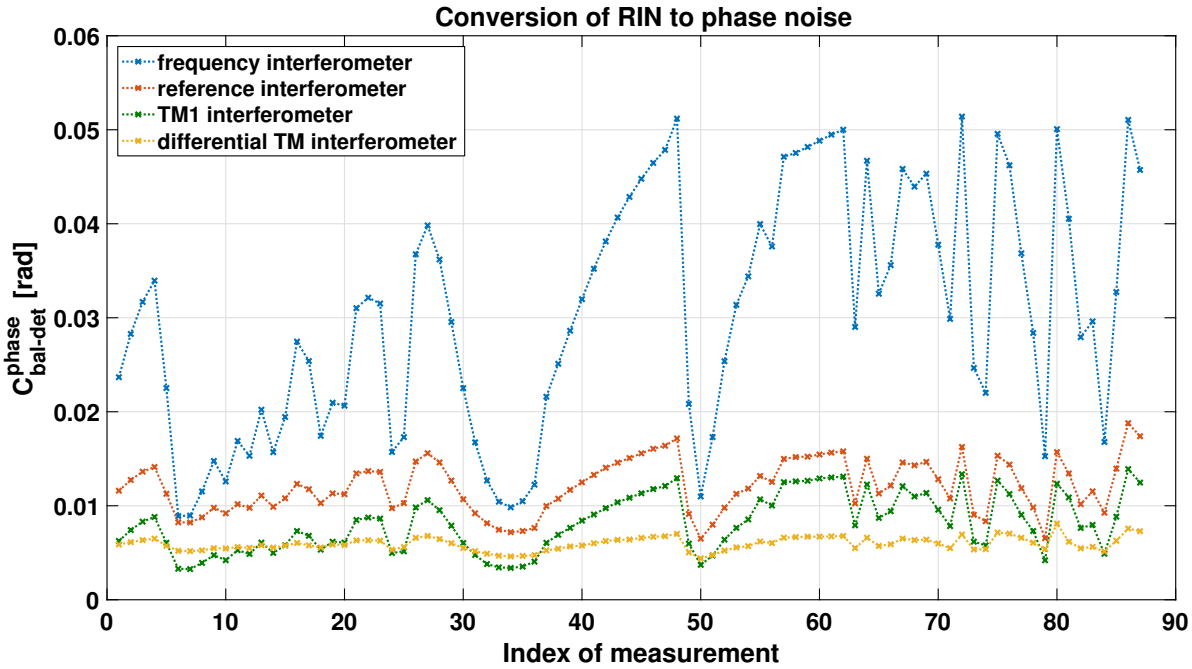

Figure 14.1.: Coupling coefficients of RIN to phase noise via Equation 14.4, due to parallel polarisation for the available polarisation data points.

$$\Delta s_{\mathrm{RIN}} = \frac{\lambda}{4\pi \cdot \cos 4.5^{\circ}} \cdot \Delta\phi_{\mathrm{RIN}} \,. \tag{14.5}$$

However, the differential TM displacement is computed by subtracting the reference from the differential TM interferometer. Therefore, the resulting displacement error is dependent on the relative phase between these two interferometers. The corresponding conversion factor is somewhere between $\Delta s_{\mathrm{RIN}}(\text{x12-ifo}) - \Delta s_{\mathrm{RIN}}(\text{ref-ifo})$ and $\Delta s_{\mathrm{RIN}}(\text{x12-ifo}) + \Delta s_{\mathrm{RIN}}(\text{ref-ifo})$.

The maximum error is $\Delta s_{\mathrm{RIN}}^{\text{diff-TM}} = 2 \cdot 10^{-9}\,\mathrm{m} \cdot \mathrm{RIN}(@f_{\mathrm{het}})$.

Taking into account that for LPF the RIN is small, leads to a resulting coupling to displacement noise in the order of a $\mathrm{fm}/\sqrt{\mathrm{Hz}}$ (for a RIN of $\mathrm{RIN}(@f_{\mathrm{het}}) \approx 10^{-6}\frac{1}{\sqrt{\mathrm{Hz}}}$, white around the heterodyne frequency [71]). The effect of the mismatch in balanced detection on the OMS performance can therefore be neglected [19].

However, besides balanced detection there are two other mechanisms, how the polarisation state fluctuations impact on the measurement of differential TM displacement on LPF, as described in the following:

1. direct force noise, via radiation pressure
2. read-out noise, via spurious interference of parallel polarised light

14.2. Radiation pressure

The beam, being reflected off the TMs, applies radiation pressure to them, as discussed in Section 3.3 of Chapter 3. Next to the nominal power in orthogonal polarisation (mainly controlled by the power control loop), the TMs are hit by a part of the parallel polarised light, fluctuating in power at low frequencies. This applies an extra force that is neither controlled by the power CLs, nor measurable by a single diode or interferometer.

The power monitor diodes can not be used to determine the radiation pressure, because they are the control loop sensors. Therefore, they neither sense the power noise in the nominal polarisation nor the amount of P-pol. Hence, the combined beam powers, the Σ parameters, measured at the interferometer ports, need to be used.

This leads to the difficulty of the radiation pressure estimation: The power with orthogonal and parallel polarisation of the measurement beam needs to be determined by combined beam power measurements, only. Furthermore, the low frequency noise in P-pol is not, or only partly, correlated between the two beams. Therefore, the current best solution is to use the knowledge of the single beam power measurements and the OB model, to give a best estimate on the applied radiation pressure.

In a first step, the measured Σ parameters are used to retrieve the power with nominal and off-nominal polarisation. In the next step the ratio between power in measurement and reference beam needs to be estimated, so that the right amount of power can be propagated to the TMs, of course with polarisation-dependent propagation factors. This step is particularly difficult for the parallel polarisation, for which the correlation of the power noise in the two beams is unclear.

For clarity, the Σ parameters are written here again, with the individual powers with nominal and off-nominal polarisations:

$$\Sigma_i = \left(P^{\perp}_{\mathrm{MB}} \cdot \lambda^{\perp}_{\Sigma_i,\,\mathrm{MB}} + P^{\perp}_{\mathrm{RB}} \cdot \lambda^{\perp}_{\Sigma_i,\,\mathrm{RB}} + P^{\parallel}_{\mathrm{MB}} \cdot \lambda^{\parallel}_{\Sigma_i,\,\mathrm{MB}} + P^{\parallel}_{\mathrm{RB}} \cdot \lambda^{\parallel}_{\Sigma_i,\,\mathrm{RB}}\right) \cdot \frac{1}{\mathrm{G}_i}\,, \tag{14.6}$$

$$P_{\mathrm{TM}} = P^{\perp}_{\mathrm{MB}} \cdot \lambda^{\perp}_{\mathrm{TM1,\,MB}} + P^{\parallel}_{\mathrm{MB}} \cdot \lambda^{\parallel}_{\mathrm{TM1,\,MB}}\,, \tag{14.7}$$

The conversion of the power noise in the Σ parameters to the differential TM acceleration, Δ_g, is derived in the following, separately for orthogonal - and parallel polarisation.
In the end the derived conversion is applied exemplarily to the longest LPF noise run in February 2017.

14.2.1. Conversion of intensity noise with nominal polarisation (S-pol) to Δ_g

To derive the S-pol, the Σ_{12} measurement is used, because it is the least sensitive one to parallel polarisation. Off-nominal polarised light is filtered out by 2 reflections at BSs in the beam path of Σ_{12}. For the measurement beam, one BS reflection is at an angle of 43° and the other one at an angle of 47° (compare to Section 2.2).

The remaining power fluctuations from parallel polarisation can be reduced by subtraction of the frequency interferometer, where the amount of P-pol is much higher. The ratio in Σ_{12} and Σ_{F} can be derived by using the propagation factors from Appendix B:

For the correction of Σ_{12}, the beam paths of reference and measurement beam are averaged for simplicity:

$$\begin{aligned}
\lambda^{\parallel}_{\Sigma_{12},\Sigma_F} &= \frac{1}{2} \cdot \left(\frac{\lambda^{\parallel}_{\Sigma_{\mathrm{F}},\,\mathrm{MB}}}{\lambda^{\parallel}_{\Sigma_{12},\,\mathrm{MB}}} + \frac{\lambda^{\parallel}_{\Sigma_{\mathrm{F}},\,\mathrm{RB}}}{\lambda^{\parallel}_{\Sigma_{12},\,\mathrm{RB}}} \right) \approx 16 \\
\lambda^{\perp}_{\Sigma_{12},\Sigma_F} &= \frac{1}{2} \cdot \left(\frac{\lambda^{\perp}_{\Sigma_{\mathrm{F}},\,\mathrm{MB}}}{\lambda^{\perp}_{\Sigma_{12},\,\mathrm{MB}}} + \frac{\lambda^{\perp}_{\Sigma_{\mathrm{F}},\,\mathrm{RB}}}{\lambda^{\perp}_{\Sigma_{12},\,\mathrm{RB}}} \right) \approx 0.92\,.
\end{aligned} \tag{14.8}$$

The corrected time series, $\Sigma^{\perp}_{12}$, can therefore be derived, using Equation 14.8 by:

$$\Sigma^{\parallel}_{\mathrm{F}} \approx \Sigma_{\mathrm{F}} - \Sigma_{12} \cdot \lambda^{\perp}_{\Sigma_{12},\Sigma_F} \tag{14.9}$$

$$\Sigma^{\perp}_{12} \approx \Sigma_{12} - \frac{\Sigma^{\parallel}_{\mathrm{F}}}{\lambda^{\parallel}_{\Sigma_{12},\Sigma_F}} \tag{14.10}$$

Annotation: The corrected time-series $\Sigma^{\perp}_{12}$ is noisier than the primary time series Σ_{12} (as can be seen exemplarily in Figure 14.4). This is plausible, since the beam power is controlled by a reflection from a glass-plate. This reflection already contains a share of P-pol, about $\frac{2}{3}$ of that in Σ_{12}. Therefore, the corrected $\Sigma^{\perp}_{12}$, ideally containing only orthogonal polarisation, shows higher noise than the raw data of Σ_{12}.

In the next step, the share of power noise from the measurement beam needs to be estimated. The ratio of average reference and measurement beam power is known from the single beam power measurements (compare to Figures 4.6 and 4.7).

Since the control loops mainly control S-pol and in addition the share of P-pol is below 5 %, the ratio of measurement and reference beam S-pol is assumed to be stable.
Furthermore, the intensity noise in the two beams is assumed to be correlated, so that the share of measurement beam power noise in $\Sigma_{12}^{\perp}$ can be retrieved by simple multiplication with the ratio of the single beam powers in Σ_{12}, measured during the several single beam power investigations (see Section 4.3). The ratio determines to:

$$P_{\mathrm{RB}} \cdot \lambda^{\perp}_{\Sigma_{12},\,\mathrm{RB}} = 1.21 \cdot P_{\mathrm{MB}} \cdot \lambda^{\perp}_{\Sigma_{12},\,\mathrm{MB}}, \tag{14.11}$$

with $\frac{\langle \mathrm{DC}_{12\mathrm{A},\,\mathrm{RB}} + \mathrm{DC}_{12\mathrm{B},\,\mathrm{RB}} \rangle}{\langle \mathrm{DC}_{12\mathrm{A},\,\mathrm{MB}} + \mathrm{DC}_{12\mathrm{B},\,\mathrm{MB}} \rangle} \approx (1.21 \pm 0.002)$ W/W, (mean and standard deviation).

Applying Equation 14.11 to Equations 14.6 and 14.7 , allows the derivation of the S-pol at the TMs from the Σ_{12} measurement:

$$\Sigma_{12}^{\perp} \approx (1 + 1.21) \cdot P_{\mathrm{MB}} \cdot \lambda^{\perp}_{\Sigma_{12},\,\mathrm{MB}} \cdot \frac{1}{\mathrm{G}_{12}}\,, \tag{14.12}$$

$$\begin{aligned} P^{\perp}_{\mathrm{TM1}} &= P^{\perp}_{\mathrm{MB}} \cdot \lambda^{\perp}_{\mathrm{TM1}}\,, \\ &\approx \Sigma_{12}^{\perp} \cdot \frac{0.45 \cdot \mathrm{G}_{12}}{\lambda^{\perp}_{\Sigma_{12},\,\mathrm{MB}}} \cdot \lambda^{\perp}_{\mathrm{TM1}}\,, \end{aligned} \tag{14.13}$$

$$P^{\perp}_{\mathrm{TM2}} \approx \Sigma_{12}^{\perp} \cdot \frac{0.45 \cdot \mathrm{G}_{12}}{\lambda^{\perp}_{\Sigma_{12},\,\mathrm{MB}}} \cdot \lambda^{\perp}_{\mathrm{TM1}} \cdot \lambda^{\perp}_{\mathrm{TM1\text{-}TM2}}\,. \tag{14.14}$$

The contribution of S-pol to Δ_g by radiation pressure is therefore given by:

$$\Delta_g^{\perp}(\mathrm{RP}) = \Sigma_{12}^{\perp} \cdot 0.45 \cdot \mathrm{G}_{12} \cdot \frac{\lambda^{\perp}_{\mathrm{TM1}}}{\lambda^{\perp}_{\Sigma_{12},\,\mathrm{MB}}} \cdot \left(\frac{1 + \mathrm{R}_{\mathrm{TM1}}}{\mathrm{c} \cdot \mathrm{m}_{\mathrm{TM1}}} + \frac{1 + \mathrm{R}_{\mathrm{TM2}}}{\mathrm{c} \cdot \mathrm{m}_{\mathrm{TM2}}} \cdot \lambda^{\perp}_{\mathrm{TM1\text{-}TM2}} \right)\,. \tag{14.15}$$

$\Delta_g^{\perp}(\mathrm{RP})$ can be computed with the corresponding losses in the beam paths from Appendix B and the G-coefficients from Equation 5.7.

14.2.2. Conversion of intensity noise with off-nominal polarisation (P-pol) to Δ_g

In Figure 14.2, the frequency interferometer, Σ_F, shows extra low-frequency power noise below 3 mHz, above the Σ_{12} level. This noise is clearly resulting from parallel polarised light (compare with the description in Box 7.0.1).
The frequency interferometer detects most of the parallel polarised light. Therefore, it is used for the estimation of a conversion factor from the Σ_{F} parameter to $\Delta_g^{\parallel}(\mathrm{RP})$, as described in the following.

The P-pol is not controlled by the power control loop. Therefore, the different average power levels of the two beams are of no interest, here. Instead, the low frequency power fluctuations below 3 mHz are the relevant parameter, describing the noise by the fluctuating amount of parallel polarisation in the particular interferometer. For the frequency interferometer they are referred to in the following, as $\Sigma_{\mathrm{F}}^{\parallel}|_{<3\mathrm{mHz}} \stackrel{!}{=} \Delta(\Sigma_{\mathrm{F}})$.
The low frequency power fluctuations from reference and measurement beam, however, are known to be not (or only partly) correlated. Therefore, the challenge is to retrieve the P-pol power fluctuations in the measurement beam from the fluctuations in the combined beam

power.
Of course, there is also a small constant share of parallel polarisation in both beams, which is not accounted for by the low frequency power fluctuations, $\Delta(\Sigma_\mathrm{F})$. However, this small power is neglected here, because it is contributing to radiation pressure like the S-pol only by RIN (from the laser or the AOMs), but with much lower power than the nominal polarisation.

Therefore, in the following, the propagation coefficients between the low frequency power noise (P-pol, below 3 mHz) in the frequency interferometer, $\Delta(\Sigma_\mathrm{F})$, to the measurement beam P-pol at the TMs, $\Delta(P^{\parallel}_{\mathrm{TM}})$, are estimated with the best available measurement — the single beam powers (as described in Section 8.2).

Fir this, the reference and measurement beam powers on both frequency interferometer diodes for all single beam power measurements are summed. The resulting parameter, analogously processed to the Σ parameter, has an average power fluctuation, of which the contribution from the measurement beam is known. As a consequence, this knowledge is transferable to the observed fluctuations in the frequency interferometer, $\Delta(\Sigma_\mathrm{F})$, to give the best estimate of the average P-pol contribution from the measurement beam.

The sum of all single beam power measurements at the frequency interferometer diodes is given by:

$$\begin{aligned} \mathrm{DC}_{\mathrm{FA,\,MB}} + \mathrm{DC}_{\mathrm{FB,\,MB}} &= \langle P_\mathrm{MB}\rangle \cdot \lambda^{\parallel}_{\Sigma_\mathrm{F},\,\mathrm{MB}} \pm \Delta(P_\mathrm{MB}) \cdot \lambda^{\parallel}_{\Sigma_\mathrm{F},\,\mathrm{MB}} \\ \mathrm{DC}_{\mathrm{FA,\,RB}} + \mathrm{DC}_{\mathrm{FB,\,RB}} &= \langle P_\mathrm{RB}\rangle \cdot \lambda^{\perp}_{\Sigma_\mathrm{F},\,\mathrm{RB}} \pm \Delta(P_\mathrm{RB}) \cdot \lambda^{\parallel}_{\Sigma_\mathrm{F},\,\mathrm{RB}}\,, \end{aligned} \tag{14.16}$$

with the average power $\langle P_m\rangle$ of the two beams and the important quantity — their average fluctuation $\Delta(P_m)$.

These single beam powers can then be summed to the combined beam power, equivalent to Σ_F of the frequency interferometer:

$$\begin{aligned} &\mathrm{DC}_{\mathrm{FA,\,MB}} + \mathrm{DC}_{\mathrm{FB,\,MB}} + \mathrm{DC}_{\mathrm{FA,\,RB}} + \mathrm{DC}_{\mathrm{FB,\,RB}} \\ &= \langle P_\mathrm{MB}\rangle \cdot \lambda^{\perp}_{\Sigma_\mathrm{F},\,\mathrm{MB}} \pm \Delta(P_\mathrm{MB}) \cdot \lambda^{\parallel}_{\Sigma_\mathrm{F},\,\mathrm{MB}} + \langle P_\mathrm{RB}\rangle \cdot \lambda^{\perp}_{\Sigma_\mathrm{F},\,\mathrm{RB}} \pm \Delta(P_\mathrm{RB}) \cdot \lambda^{\parallel}_{\Sigma_\mathrm{F},\,\mathrm{RB}} \\ &\overset{!}{=} \langle \Sigma_\mathrm{F}\rangle \pm \Delta(\Sigma_\mathrm{F})\,. \end{aligned} \tag{14.17}$$

The sum of the two single beam noise contributions $\Delta(\Sigma_\mathrm{F})$ depends on their correlation:

For positive correlation, $\Delta\phi = 0°$:

$$\langle \Sigma_\mathrm{F}\rangle + \Delta(\Sigma_\mathrm{F}) = \langle \Sigma_\mathrm{F}\rangle \pm \left(\Delta(P_\mathrm{MB}) \cdot \lambda^{\parallel}_{\Sigma_\mathrm{F},\,\mathrm{MB}} + \Delta(P_\mathrm{RB}) \cdot \lambda^{\parallel}_{\Sigma_\mathrm{F},\,\mathrm{RB}}\right)\,, \tag{14.18}$$

for uncorrelated noise without phase relation:

$$\langle \Sigma_\mathrm{F}\rangle + \Delta(\Sigma_\mathrm{F}) = \langle \Sigma_\mathrm{F}\rangle \pm \sqrt{\left(\Delta(P_\mathrm{MB}) \cdot \lambda^{\parallel}_{\Sigma_\mathrm{F},\,\mathrm{MB}}\right)^2 + \left(\Delta(P_\mathrm{RB})\lambda^{\parallel}_{\Sigma_\mathrm{F},\,\mathrm{RB}}\right)^2}\,, \tag{14.19}$$

for negative correlation, $\Delta\phi = 180°$:

$$\langle \Sigma_\mathrm{F}\rangle + \Delta(\Sigma_\mathrm{F}) = \langle \Sigma_\mathrm{F}\rangle \pm \left(\Delta(P_\mathrm{MB}) \cdot \lambda^{\parallel}_{\Sigma_\mathrm{F},\,\mathrm{MB}} - \Delta(P_\mathrm{RB}) \cdot \lambda^{\parallel}_{\Sigma_\mathrm{F},\,\mathrm{RB}}\right)\,, \tag{14.20}$$

with $\langle \Sigma_\mathrm{F}\rangle = \langle P_\mathrm{MB}\rangle \cdot \lambda^{\perp}_{\Sigma_\mathrm{F},\,\mathrm{MB}} + \langle P_\mathrm{RB}\rangle \cdot \lambda^{\perp}_{\Sigma_\mathrm{F},\,\mathrm{RB}}$.

The average ratio of the P-pol power fluctuations from the individual beams in the frequency interferometer is known from the single beam power measurements. It comes out as $\Delta(P_{\mathrm{RB}}) \cdot \lambda^{\parallel}_{\Sigma_{\mathrm{F}},\,\mathrm{RB}} = 3.18 \cdot \Delta(P_{\mathrm{MB}}) \cdot \lambda^{\parallel}_{\Sigma_{\mathrm{F}},\,\mathrm{MB}}$.
Note again that the share of P-pol from the measurement beam in the combined beam power can only be computed on average to give the best available estimate. Since the beam correlation is unclear, the actual fraction of the power fluctuations from the measurement beam is not determinable with the combined beam power, only.

With the ratio of power fluctuations between measurement and reference beam the final propagation factors between the measured fluctuations in combined beam power, $\langle\Sigma_{\mathrm{F}}\rangle$, and the corresponding P-pol power fluctuations from the measurement beam, $P^{\parallel}_{\mathrm{MB}}\lambda^{\parallel}_{\Sigma_{\mathrm{F}},\,\mathrm{MB}}$, in the frequency interferometer can be derived to be:

$$P^{\parallel}_{\mathrm{MB}} \cdot \lambda^{\parallel}_{\Sigma_{\mathrm{F}},\,\mathrm{MB}} \stackrel{!}{=} \Delta(P_{\mathrm{MB}}) \cdot \lambda^{\parallel}_{\Sigma_{\mathrm{F}},\,\mathrm{MB}} \approx \Delta(\Sigma_{\mathrm{F}}) \cdot \mathrm{G_F} \cdot \begin{cases} 0.24 & \text{positive correaltion} \\ 0.3 & \text{uncorrelated} \\ 0.46 & \text{negative correaltion} \end{cases} . \tag{14.21}$$

Multiplication with $\mathrm{G_F}$, converts the Σ_{F} parameter to real beam power in Watts.

For the further propagation to the TMs, the different BS splitting ratio's for P-pol need to be taken into account, as listed in Appendix B.

The P-pol at TM1 can then be written with Σ_{F}, as follows:

$$\Delta(P^{\parallel}_{\mathrm{TM}}) \approx \frac{\lambda^{\parallel}_{\mathrm{TM1}}}{\lambda^{\parallel}_{\Sigma_{\mathrm{F}},\,\mathrm{MB}}} \cdot \Delta(\Sigma_{\mathrm{F}}) \cdot \mathrm{G_F} \cdot \begin{cases} 0.24 & \text{positive correaltion} \\ 0.3 & \text{uncorrelated} \\ 0.46 & \text{negative correaltion} \end{cases} . \tag{14.22}$$

The contribution to Δ_g can further be derived by:

$$\begin{aligned} \Delta^{\parallel}_{g}(\mathrm{RP}) =& P^{\parallel}_{\mathrm{TM}} \cdot \left(\frac{1+\mathrm{R_{TM1}}}{\mathrm{c}\cdot\mathrm{m_{TM1}}} + \lambda^{\parallel}_{\mathrm{TM1\text{-}TM2}} \cdot \frac{1+\mathrm{R_{TM2}}}{\mathrm{c}\cdot\mathrm{m_{TM2}}} \right) \\ \approx& \left(\frac{1+\mathrm{R_{TM1}}}{\mathrm{c}\cdot\mathrm{m_{TM1}}} + \lambda^{\parallel}_{\mathrm{TM1\text{-}TM2}} \cdot \frac{1+\mathrm{R_{TM2}}}{\mathrm{c}\cdot\mathrm{m_{TM2}}} \right) \\ & \cdot \frac{\lambda^{\parallel}_{\mathrm{TM1}}}{\lambda^{\parallel}_{\Sigma_{\mathrm{F}},\,\mathrm{MB}}} \cdot \Delta(\Sigma_{\mathrm{F}}) \cdot \mathrm{G_F} \cdot \begin{cases} 0.24 & \text{positive correaltion} \\ 0.3 & \text{uncorrelated} \\ 0.46 & \text{negative correaltion} \end{cases} . \end{aligned} \tag{14.23}$$

In Section 8.2, the Pearson factor of linear correlation for parallel polarised light in the reference and measurement beams was computed to be $c = -0.348$. This indicates that the actual contribution is higher than the uncorrelated case.

Besides the correlation of parallel polarised light between the two beams, the correlation of orthogonal polarisation to the parallel polarised contribution at low frequencies also needs to be considered.

14.2.3. Radiation pressure contribution for the long noise run in February 2017

In the following, the radiation pressure contribution from orthogonal and parallel polarised light is exemplarily computed for the longest noise run in February 2017.

The amplitude spectra of the Σs are shown in Figure 14.2. Below $5 \cdot 10^{-3}$ Hz, the individual interferometers have different noise levels. The noise levels at low frequencies correspond to polarisation fluctuations, detected mostly by the frequency interferometer.

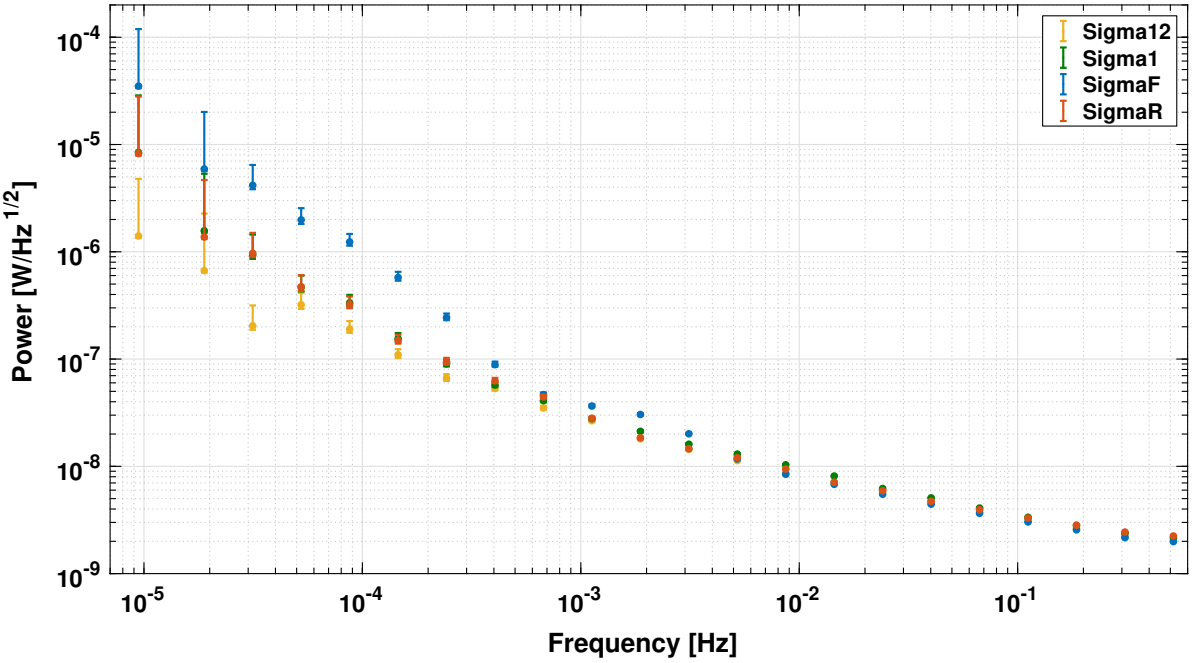

Figure 14.2.: ASD of the combined beam powers Σ in all four interferometers during long noise run in February 2017. The influence of polarisation fluctuations is visible at low frequencies, in particular for the frequency interferometer.

Above $5 \cdot 10^{-3}$ Hz, the power noise is comparable in the four interferometers. However, a closer look to the time series of Σ_{12} and Σ_{F} in Figure 14.3 shows that at higher frequencies, the power measurements are limited by the least significant bit of the ADC.

A conversion of the estimated noise in nominal polarisation to radiation pressure therefore overestimates the contribution to Δ_g at higher frequencies.

To derive an upper limit for the radiation pressure contribution from orthogonal polarisation, the strategy from Section 14.2.1 is changed for the higher frequencies. Instead of the Σ_{12} parameter, the average of all four Σ parameters is used. In contrast to the intensity noise of S-pol, the ADC noise is uncorrelated between the four interferometers. Therefore, the SNR should get better by a factor of 2 for the average power of the four Σ-parameters.

$$\Sigma_{\mathrm{average}} = \frac{1}{4} \cdot (\Sigma_{12} + \Sigma_1 + \Sigma_{\mathrm{R}} + \Sigma_{\mathrm{F}}) \tag{14.24}$$

However, the addition of the other three interferometers to Σ_{12}, also adds P-pol at the low frequencies.

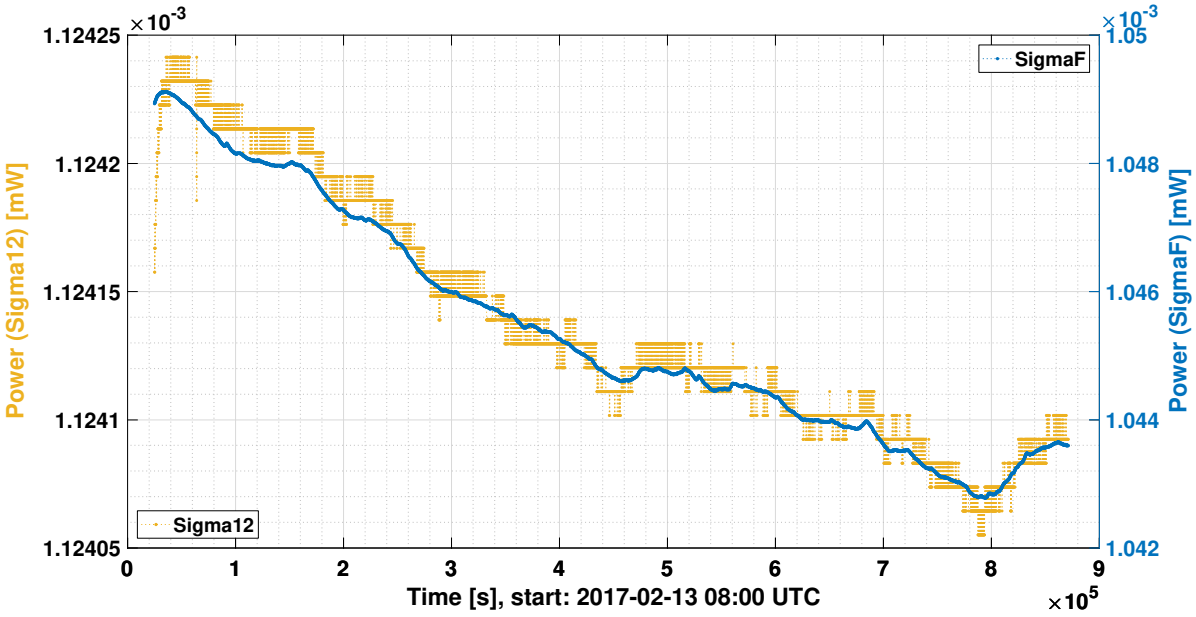

Figure 14.3.: Time series of the combined beam power in the x12 - and the frequency interferometer during long noise run in February 2017. The low frequency fluctuations from parallel polarisation are visible for both interferometers, but much stronger in the frequency one. At high frequencies, the interferometer power is limited by the least significant bit of the ADC, as visible for the Σ_{12} parameter.

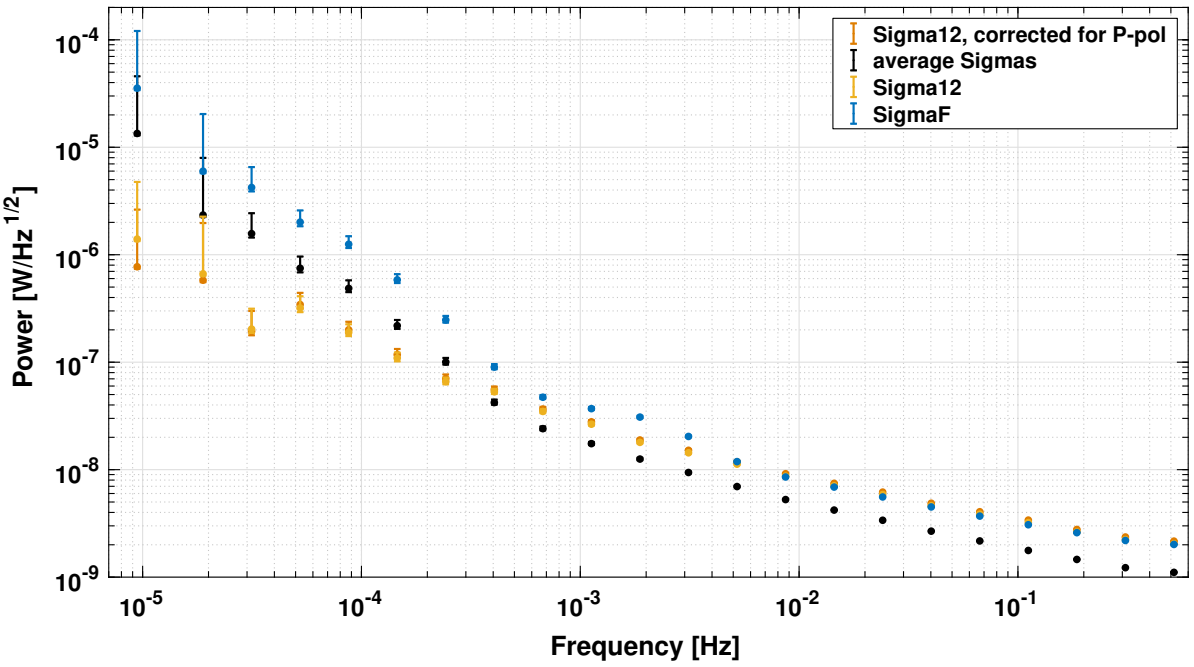

Figure 14.4.: ASD of Σ_{12} and $\Sigma_{12}^{\perp}$ with reduced P-pol by subtraction of Σ_F (see Equation 14.10), during the long noise run in February 2017.

Figure 14.4 shows the average power, Σ_{average}, and the P-pol corrected power, $\Sigma_{12}^{\perp}$, together with Σ_{12} and Σ_{F}.
At frequencies above $4 \cdot 10^{-4}$ Hz, the ADC noise is reduced by averaging of all powers.

To give the best estimate for an upper limit of the radiation pressure contribution from orthogonal polarisation, the P-pol corrected power, $\Sigma_{12}^{\perp}$, is used for frequencies below $4 \cdot 10^{-4}$ Hz, and the average power Σ_{average} in all four interferometers, for frequencies above.

For the final conversion to Δ_g, the power propagation factor for the average power needs to be adapted, too. Therefore, the share of the measurement beam power at the front of the OB is determined by the ratio of the constant control points, C_{RB} and C_{MB} for the reference and measurement beam power, from the fit of the OB model, described in Section 8.2. It comes out as $\frac{\text{C}_{\text{MB}}}{\text{C}_{\text{MB}}+\text{C}_{\text{RB}}} \approx 0.47$. The conversion of Σ_{average} to Δ_g is therefore given by:

$$\begin{aligned}\Delta_g^{\perp}(\text{RP})|_{f>0.4\text{mHz}} = &8 \cdot \Sigma_{\text{average}} \cdot \text{G}_{\text{average}} \cdot 0.47 \cdot \lambda_{\text{TM1}}^{\perp} \\ &\cdot \left(\frac{1+\text{R}_{\text{TM1}}}{\text{c} \cdot \text{m}_{\text{TM1}}} + \frac{1+\text{R}_{\text{TM2}}}{\text{c} \cdot \text{m}_{\text{TM2}}} \cdot \lambda_{\text{TM1-TM2, MB}}^{\perp} \right) . \end{aligned} \tag{14.25}$$

Here, the factor 8 converts the average power, Σ_{average}, to the average power at the front of the OB, P_{OB}, which is split by 0.47 into the share of the measurement beam (with the assumption of correlated power noise for orthogonal polarisation between the beams) and with $\lambda_{\text{TM1}}^{\perp}$ converted to TM1:

$$P_{\text{OB}} \approx 2 \cdot (\Sigma_{12} + \Sigma_1 + \Sigma_{\text{R}} + \Sigma_{\text{F}}) . \tag{14.26}$$

Furthermore, $\text{G}_{\text{average}}$ describes the average of the four measured G-coefficients, which are listed in Equation 5.7.

The contribution of parallel and orthogonal polarisation to Δ_g can therefore be finally computed by Equations 14.15, 14.25 and 14.23. The ASDs of the upper and lower limit of the P-pol contribution, together with the upper limit for S-pol is shown in Figure 14.5. Below 0.1 mHz, the P-pol contributes significantly to the overall radiation pressure. Below 50 µHz the P-pol even applies more force noise to the TMs than the nominal polarisation, although it is about two orders of magnitude weaker in the measurement beam.

As discussed throughout this Section, the estimation of radiation pressure has limitations due to the insufficient knowledge about the polarisation states in the two beams. On the one hand, the detected low frequency noise, clearly corresponds to fluctuations in P-pol. On the other hand, it is unknown, which part of these fluctuations belongs to the measurement beam. The conversion factor is only known on average for the single beam power measurements.
The power control loop mechanism implies a negative correlation between S-pol and P-pol at low frequencies, where the polarisation fluctuations dominate the noise. At higher frequencies, however, a positive correlation is more likely, because the two beams originate from the same laser. However, the actual correlation of intensity noise in S-pol and P-pol remains inaccessible. Therefore, the computed upper limit for the total radiation pressure is the best estimate for the share of power modulations from the measurement beam together with the assumption of negative correlation in P-pol between the two beams and positive correlation between noise in S-pol and P-pol.

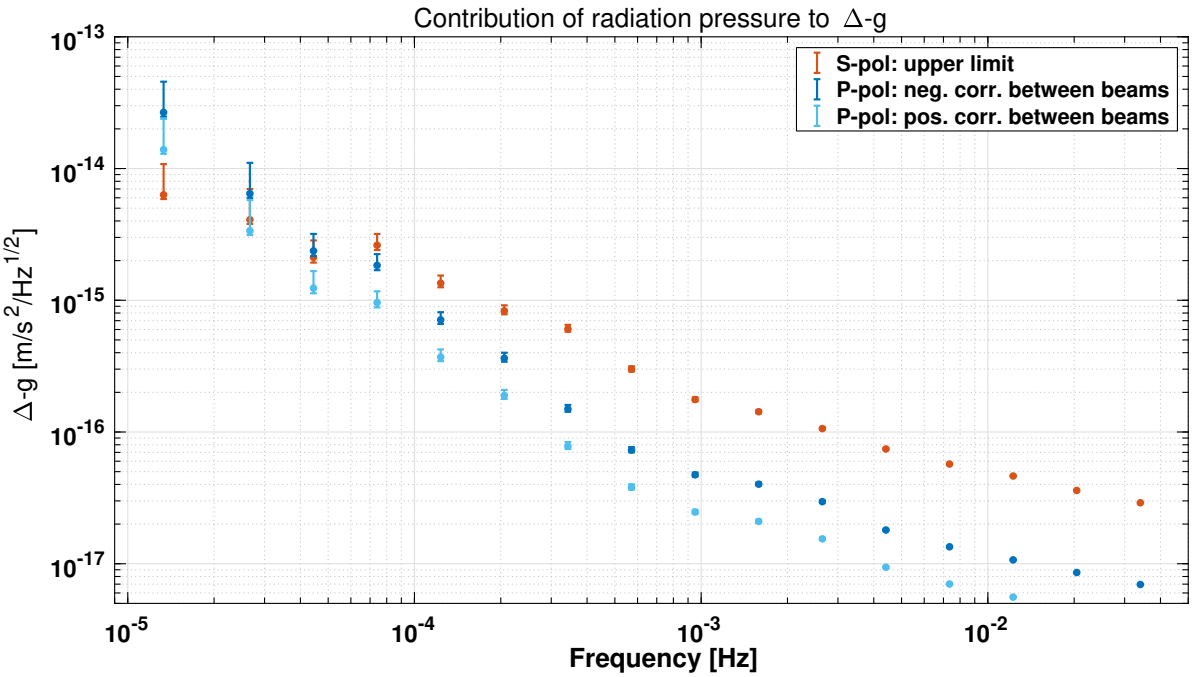

Figure 14.5.: Contribution (as ASD) of radiation pressure from parallel and orthogonal polarised light to Δ_g during the long noise run in February 2017.

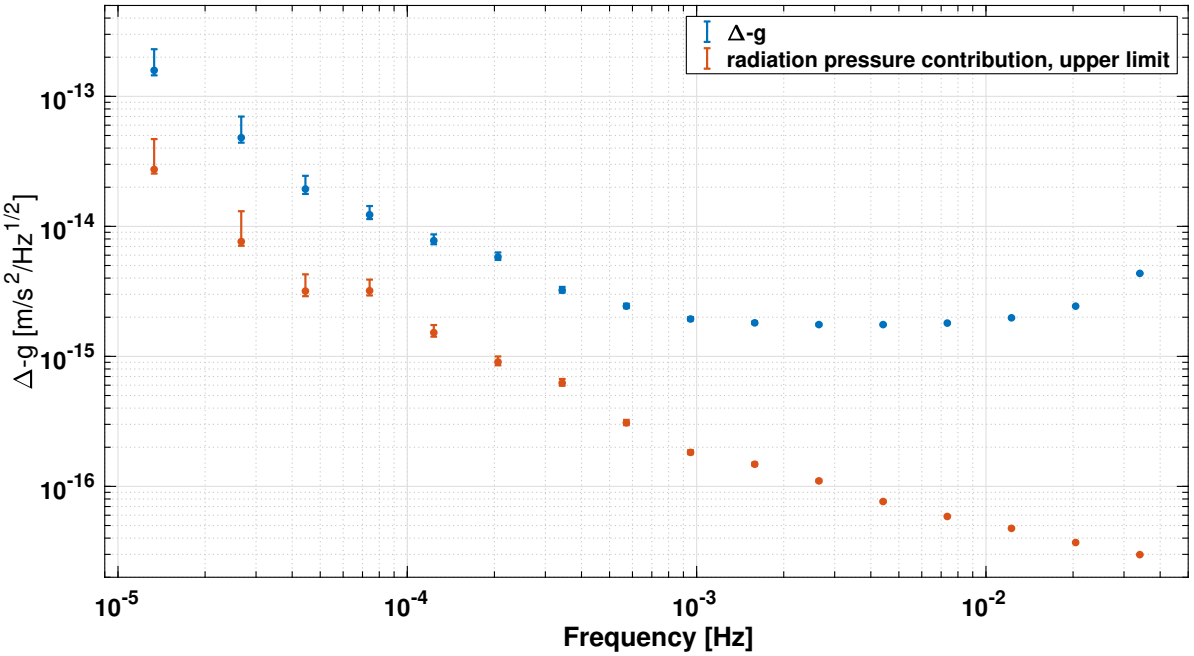

Figure 14.6.: Upper limit of radiation pressure contribution (as ASD) to Δ_g together with Δ_g, during the long noise run in February 2017.

The resulting upper limit of radiation pressure contribution, together with the corresponding Δ_g, is shown in Figure 14.6. The maximum contribution to the ASD of the relative differential TM acceleration, Δ_g, noise was found to be $26\,(+6-2)\,\%$ at $74\,\mu$Hz,corresponding to the best estimate of the radiation pressure contribution of $3.2\,(+0.7-2.6)\,\mathrm{fm/s^2/\sqrt{Hz}}$.

14.3. Read-out noise

In the previous section, the P-pol at the TMs was analysed. At the end of the interferometers, the off-nominal polarised light is hitting the PDs, which at first glance is harmless, because it is not interfering with the nominal S-pol. However, as it was found with the OB model (compare to Section 8.2), the reference beam is also carrying light with parallel polarisation that is able to interfere with the measurement beam P-pol. It even has about 3 times more P-pol power and therefore acts as a local oscillator for the weak measurement beam P-pol power. To estimate this effect, the power measurements from Equation 2.2 are written in a more general form, using the polarisation-dependent reflectance, ρ, and transmittance, τ, of the recombination BS:

$$\begin{aligned} P_{i\mathrm{A}} =& {\rho^{\parallel}}^2 \cdot \frac{P^{\parallel}_{i,\,\mathrm{RB}}}{2} + {\tau^{\parallel}}^2 \cdot \frac{P^{\parallel}_{i,\,\mathrm{MB}}}{2} + {\rho^{\perp}}^2 \cdot \frac{P^{\perp}_{i,\,\mathrm{RB}}}{2} + {\tau^{\perp}}^2 \cdot \frac{P^{\perp}_{i,\,\mathrm{MB}}}{2} \\ & \pm 2 \cdot \rho^{\parallel} \cdot \tau^{\parallel} \cdot \sqrt{\eta \cdot P^{\parallel}_{i,\,\mathrm{RB}} \cdot P^{\parallel}_{i,\,\mathrm{MB}}} \cdot \cos(\omega \cdot t - \phi_{\mathrm{P}}) \\ & \pm 2 \cdot \rho^{\perp} \cdot \tau^{\perp} \cdot \sqrt{\eta \cdot P^{\perp}_{i,\,\mathrm{RB}} \cdot P^{\perp}_{i,\,\mathrm{MB}}} \cdot \cos(\omega \cdot t - \phi_{\mathrm{S}}) + \mathcal{O}^2\,, \end{aligned} \tag{14.27}$$

with reference and measurement beam powers $P_{i,m}$ before the recombination BS in P-pol $P^{\parallel}_{\mathrm{RB/MB}}$ and S-pol $P^{\perp}_{\mathrm{RB/MB}}$. Here, $\mathcal{O}^2$ describes higher order and fast oscillating terms that are neglected in the further analysis.
For the B diode, the reflectance and transmittance coefficients in Equation 14.27 are just inverted.
Since the beam paths are not affected by the polarisation state (no birefringence on the OB components), the spatial overlap and correspondingly, the heterodyne efficiency, η, of the reference and measurement beam can be assumed to agree between nominal and parallel polarisation. With $P^{\perp}_{\mathrm{MB}} \approx P^{\perp}_{\mathrm{RB}} = P^{\perp}$, the subtraction of A and B diode therefore gives:

$$\begin{aligned} P_{\mathrm{A}} - P_{\mathrm{B}} =& ({\tau^{\parallel}}^2 - {\rho^{\parallel}}^2) \cdot P^{\parallel}_{i,\,\mathrm{RB}} + (\rho_{\mathrm{P}}^2 - {\tau^{\parallel}}^2) \cdot P^{\parallel}_{i,\,\mathrm{MB}} \\ & + 4 \cdot \left(\rho^{\parallel} \cdot \tau^{\parallel} \cdot \sqrt{\eta \cdot P^{\parallel}_{i,\,\mathrm{RB}} \cdot P^{\parallel}_{i,\,\mathrm{MB}}} \cdot \cos(\omega \cdot t - \phi_{\mathrm{P}}) \right. \\ & \left. + \rho^{\perp} \cdot \tau^{\perp} \cdot \sqrt{\eta \cdot {P^{\perp}}^2} \cdot \cos(\omega \cdot t - \phi_{\mathrm{S}}) \right)\,. \end{aligned} \tag{14.28}$$

The stationary part in Equation 14.28 gives the mismatch in balanced detection by polarisation noise, as described in Section 14.1. The oscillating part in Equation 14.28 however describes the heterodyne interference from the two polarisations. Depending on the phase offset between S-pol and P-pol heterodyne amplitude $\Delta\phi = \phi_{\mathrm{S}} - \phi_{\mathrm{P}}$, the power in parallel polarisation adds a spurious phase to the nominal one from S-pol. The corresponding phasors are shown in Figure 14.7 (in a rotating coordinate-system at the heterodyne frequency).

The measured phase error is given by the phase difference of the sum of both phasors and the phase of the desired S-pol phasor to be derived (with the assumption of a much smaller heterodyne amplitude from P-pol compared to S-pol). It can easily be seen that for $\Delta\phi = 0°$ (first case in Figure 14.7), there is no effect on the nominal phase and for $\Delta\phi = \frac{\pi}{2}$ it becomes largest. A non-stationary P-pol phasor with a time-dependent phase offset to the S-pol one, therefore, produces noise at the corresponding frequency (third case in Figure 14.7). But it should be mentioned that for a constant offset $\Delta\phi \neq 0°$, the phase of the measured heterodyne amplitude is also affected by the non-stationary P-pol, as shown by the second case in 14.7 (a change in the length of the red P-pol phasor changes the phase of the resulting sum of both phasors). Nevertheless, this contribution is expected to be at very low frequencies (compare with Figure 14.3).

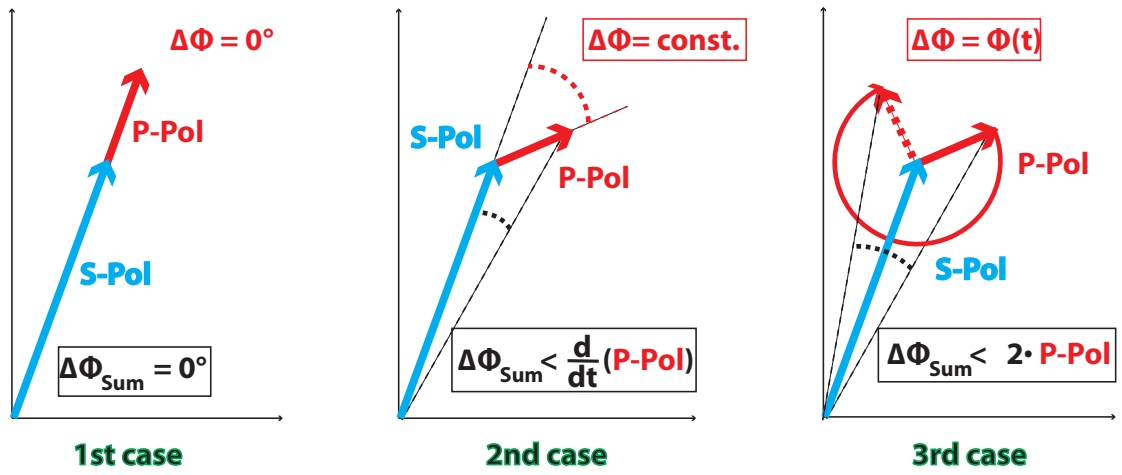

Figure 14.7.: Phase error from spurious P-pol interference: vector summation of heterodyne phase from S-pol and P-pol, dependent on relative phase relation.

The maximum phase error at $\Delta\phi = \frac{\pi}{2}$ can be approximated by the small-angle approximation:

$$\begin{aligned}\phi_{\max} &= \tan^{-1}\left(\frac{\rho^{\parallel}\cdot\tau^{\parallel}\cdot\sqrt{P^{\parallel}_{i,\,\mathrm{RB}}\cdot P^{\parallel}_{i,\,\mathrm{MB}}}}{\rho^{\perp}\cdot\tau^{\perp}\cdot\sqrt{P^{\perp\,2}}}\right)\\ &\approx \sqrt{\frac{\rho^{\parallel\,2}\cdot\tau^{\parallel\,2}\cdot P^{\parallel}_{i,\,\mathrm{RB}}\cdot P^{\parallel}_{i,\,\mathrm{MB}}}{\rho^{\perp\,2}\cdot\tau^{\perp\,2}\cdot P^{\perp\,2}}} \approx 0.81\cdot\sqrt{\frac{P^{\parallel}_{i,\,\mathrm{RB}}\cdot P^{\parallel}_{i,\,\mathrm{MB}}}{P^{\perp\,2}}},\end{aligned} \tag{14.29}$$

with the BS splitting ratios from Table 8.1. The propagation of a systematic error in the BS splitting ratios of up to 1 % leads to a systematic error of ≈ 3 % for $\phi_{\max}$.

In the design of LPF, phase noise, common to all interferometers is subtracted via the reference interferometer. However, due to the differing BS splitting-ratio, the polarisation noise is higher in the reference interferometer. Therefore, the correction adds phase-noise to the science variable instead of subtracting it.

The P-pol before the recombination BS of the differential TM and the reference interferometer (neglecting the losses at mirrors, TMs and optical windows and the different angles of the BSs) can be written with the measurement and reference beam power at the front of the OB, P_m, as follows:

$$P^{\parallel}_{\mathrm{R},\,m} = P^{\parallel}_{m} \cdot \rho^2 \cdot \tau^2 \,, \tag{14.30}$$

$$P^{\parallel}_{12,\,m} = P^{\parallel}_{m} \cdot \rho^4 \,. \tag{14.31}$$

Therefore, the maximum phase error can be written with the P-pol power at the beginning of the OB, as derived in Section 8.2:

$$\phi_{\max}(\text{x12-Ifo}) - \phi_{\max}(\text{ref-Ifo}) = \sqrt{\frac{P^{\parallel}_{\mathrm{RB}}(\mathrm{OB}) \cdot P^{\parallel}_{\mathrm{MB}}(\mathrm{OB})}{P^{\perp\,2}(\mathrm{OB})}} \cdot \left(\frac{\rho^{\parallel\,5} \cdot \tau^{\parallel}}{\rho^{\perp\,5} \cdot \tau^{\perp}} - \frac{\rho^{\parallel\,3} \cdot \tau^{\parallel\,3}}{\rho^{\perp\,3} \cdot \tau^{\perp\,3}} \right) \tag{14.32}$$

$$\approx -0.4 \cdot \sqrt{\frac{P^{\parallel}_{\mathrm{RB}}(\mathrm{OB}) \cdot P^{\parallel}_{\mathrm{MB}}(\mathrm{OB})}{P^{\perp\,2}(\mathrm{OB})}} \tag{14.33}$$

Here, the propagation of a systematic error from the BS splitting ratios leads to a prominent systematic error of about $\approx 5\,\%$ in $\phi_{\max}(\text{x12-Ifo}) - \phi_{\max}(\text{ref-Ifo})$.
The phase error converts with $x_{12} = \phi \cdot \frac{\lambda}{4 \cdot \pi \cdot cos(4.5°)}$ to TM displacement.
Using Equation 14.33, the maximum phase error during the several single beam power measurements is computed and shown in Figure 14.8.

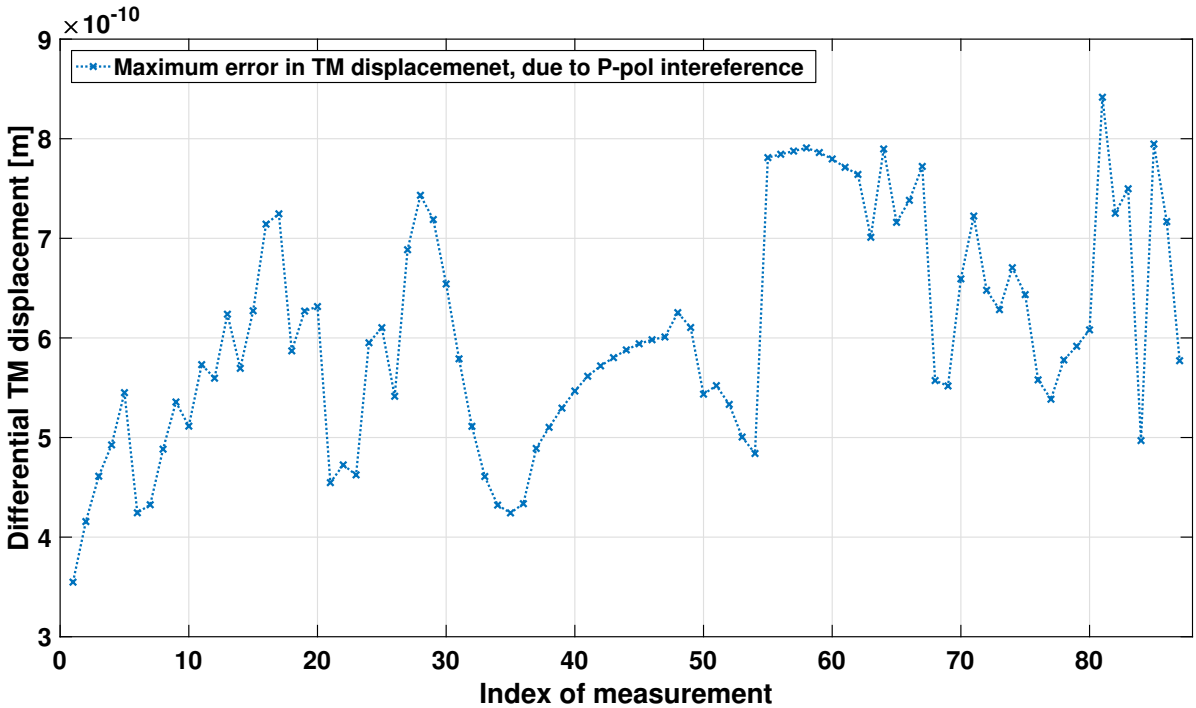

Figure 14.8.: Maximum phase error from spurious P-pol interference, converted to TM displacement during the spot position measurements. A systematic error of 5 %, propagated from the maximum deviation in the fit of the BS splitting ratios needs to be considered.

However, retrieving the maximum phase offset during science mode is more difficult, since only the superposition of reference and measurement beam power in any polarisation is measured. At least a rough estimation can be done by use of the frequency interferometer power, which is most sensitive to P-pol. The reference beam acts as a local oscillator and therefore dominates the P-pol power measured in the frequency interferometer, as well as the P-pol heterodyne amplitude that produces the phase error.

Even if the maximum phase offset during science mode would be known, the crucial information of the dynamics in differential phase is missing. Therefore, an estimation of possible coupling frequencies with a deterministic signal as an upper limit, is done in the following.

A continuous rotation of the P-pol phasor with respect to the S-pol one would result in a sinusoidal displacement signal at the particular frequency with a peak-to-peak amplitude of the maximum displacement error (which is up to 800 pm). This spurious displacement signal further converts to acceleration by multiplication with ω^2.

If the P-pol phasor would rotate quickly with respect to S-pol the resulting contribution to acceleration would be huge. At a frequency of $f = 10\,\mathrm{mHz}$ and the maximum displacement error of about 800 pm (see Figure 14.8), the signal would convert into an acceleration with an amplitude of $800\,\mathrm{pm} \cdot \omega^2 \approx 3.16\,\frac{\mathrm{pm}}{\mathrm{s}^2}$. This signal would be high above the noise of the OMS [15, 16].

Since the OMS performance on LPF in the measurement band is furthermore well-understood [19], a significant contribution of the read-out noise at theses frequencies down to 0.1 mHz can be excluded (because it would have been a limiting noise source). Therefore, with 0.1 mHz an upper limit for the frequencies at which the read-out noise is possibly significantly contributing, is found.

At frequencies below 0.1 mHz, however the conversion of a displacement error to acceleration is very small. Even for the maximum displacement error, the induced acceleration of a sinusoidal displacement at 0.1 mHz converts to an acceleration of only $800\,\mathrm{pm} \cdot \omega^2 \approx 0.316\,\frac{\mathrm{fm}}{\mathrm{s}^2}$. Such a small acceleration signal is below the acceleration noise performance at these frequencies [16]. Therefore, the impact of the read-out noise on the OMS system performance and the LPF residual acceleration is assumed to be negligible.

Nevertheless, the most likely origin of the P-pol that is transmitted to the OB, are the fibres. Therefore, the assumption is still that the differential phase between S-pol and P-pol changes with environmental influences like temperature or vibrations. However, the corresponding frequencies remain inaccessible for the given data set.

Box 14.3.1 | Summary: Low-frequency polarisation noise, impact on LPF science

The polarisation fluctuations impact on the LPF science via three different mechanisms:

- By unbalancing the power on a pair of A and B diodes.
- A direct impact on differential TM acceleration by radiation pressure.
- Read-out noise due to a spurious interference from parallel polarised light.

Effects on balanced detection:

- Parallel polarised light is split with an asymmetric ratio at the recombination BS.

  → The power mismatch increases the relative intensity noise coupling.

- The maximum coupling to the differential TM displacement is:

  $\Delta s_{\mathrm{RIN}}^{\text{diff-TM}} = 2 \cdot 10^{-9} \cdot \mathrm{RIN}(@f_{\mathrm{het}})$.

- However, the RIN on LPF was very small: $\mathrm{RIN}(@f_{\mathrm{het}}) \approx 10^{-6} \frac{1}{\sqrt{\mathrm{Hz}}}$.

  → The effect on the OMS performance is therefore negligible.

Effects on radiation pressure:

- A fluctuating amount of P-pol hits the TMs.

  → For an estimation of the coupling to radiation pressure, the power needs to be propagated adequately for the different polarisations.

- Difficulties:
  - The correlation of parallel power noise between the beams is unknown.
  - The measurement of power with nominal polarisation is limited by the ADC resolution.
  - Also, the correlation of power noise for the two polarisations is unclear.

→ Therefore, only an **upper limit for the radiation pressure contribution to** Δ_g can be determined.

→ For the longest LPF noise measurement, the **parallel polarised light significantly contributed to the fluctuations in radiation pressure at least below frequencies of 0.1 mHz.**

Induced read-out noise:

- The light with parallel polarisation from the two beams interferes at the interferometer output.
- However, the reference and the differential TM interferometer have a different share of P-pol.

  → Therefore, the resulting heterodyne amplitude from P-pol is not fully subtracted.

- The impact of the P-pol heterodyne phase on the total measured phase is dependent on the phase difference to the heterodyne phase from nominal polarisation.

  → A constant relative phase between the two results in a constant read-out error.

  → A changing relative phase results in a spurious signal at the corresponding frequencies.

- The off-nominal polarised light is assumed to originate mainly in the fibres.
  → Therefore, the phase between S-pol and P-pol is presumed to be non-stationary.

→ However: the measured LPF noise restricts **possible coupling frequencies for the read-out noise to be lower than mHz.**

Part III.

Outlook

In Chapter 15 of Part III, the findings of this thesis are applied to LISA. An adapted radiation pressure experiment for LISA is proposed. Furthermore, the impact of possible polarisation imperfections in the current LISA OB design is outlined to discuss the possibilities for a prevention of their origin or to mitigate the corresponding effects.
In Chapter 16, the results of this thesis are summarised and discussed. A conclusion states the answers to the overall research questions and discusses their relevance for LISA.

15. Impact on LISA

An extrapolation of the in-flight stability of the PD responsivities and TM reflectivities to the planned LISA mission duration was already derived in Part I, as described in Sections 4.3 and 5.3. The monitoring investigations, however, led to further knowledge beyond the parameter stability that is applicable to the LISA mission.

In Section 15.1, an independent force calibration for the TMs on LISA, using radiation pressure, is outlined. In contrast to the LPF experiment design, however, a power reference measurement from the temperature of a beam dump is proposed here. The evidence for a ghost beam interference signal is used for a draft of a ghost beam identification experiment during the build process of the LISA OBs, as described in Section 15.2.

Furthermore, the findings about polarisation on LPF from Part II are applied to LISA. The possible impact of polarisation imperfections on the LISA OB is discussed in Section 15.3. The advantage of a subsequent experimental investigation on the output polarisation of the optical fibres on LPF is discussed in Section 15.4. Finally, an idea for minor changes to the OB design, in order to detect and clean the polarisation and avoid the synthesis of ghost beams, is detailed in Section 15.5. In the end, the plausibility of possible polarisation control mechanisms in the LISA OB design is discussed.

15.1. An Independent force calibration for LISA using radiation pressure

The main science measurement on LISA is the differential displacement of two free-falling TMs, separated by millions of kilometres. In the split interferometer design, one measurement is the differential displacement of one TM with respect to the OB. Besides the interferometric measurement, a model of the non-gravitational forces and stiffness parameters is required to retrieve the purely gravitational TM accelerations. This model was optimized for LPF and will be adapted for LISA. However, it is possible that an in-flight calibration for the LISA satellite environment is needed. In such a calibration experiment, a known signal force would need to be applied to the TM and compared with the measured acceleration. The known signal force could be generated by the capacitive actuators of the GRS along the sensitive axis. However, if for any reason a further in-flight calibration of the capacitive actuation is desired, a different independent method for the application of a force along the sensitive axis would be needed.

Such an independent force could be applied by radiation pressure from the laser beam, reflected off the TM. The corresponding radiation pressure measurement for LPF was described in Chapter 3. However, the experiment was designed with the opposite logical direction: The TM force — assumed to be a well-calibrated ultra-precise measurement — was used to determine the applied beam power and in a next step, was used for the calibration of the PDs. Therefore,

the question is, how this chain of argument could be turned around so that the TM force can be calibrated by a known power modulation. The easiest option is to measure the observable of the LPF experiment — the PD responsivity — separately, so that the applied beam power is known.

For LISA, there could be an option to calibrate the beam power independently of any PD measurement and, furthermore, independently of the applied radiation pressure: A well-defined part of the laser beam is clipped and blocked with a beam dump. As a black body (in good approximation), the temperature of the beam dump could be used to retrieve the absorbed beam power. To do this, the difference between the environmental temperature and the beam dump surface, as well as the ratio between clipped and transmitted beam power need to be known, as described in Box 15.1.1.

Box 15.1.1: Basic concept of a reference power measurement by the temperature of a beam dump:

A beam dump is designed as a cavity with a hole. The incident light passes through the hole inside the cavity where it is reflected many times. Ideally, no reflection of the incident beam escapes the beam dump, so that all beam power is absorbed in the end. As a consequence, the power is converted to heat at the surface of the beam dump. The emitted radiation, therefore, corresponds to that of a black body.
If the beam dump continuously absorbs a beam, a thermal state of equilibrium will be reached after a while. A measurement of the equilibrium temperature can then be used to retrieve the power that is dumped.

The total incident and emitted power, P_{in} and P_{out}, of the beam dump can be written as:

$$P_{\mathrm{in}} = P_{\mathrm{beam}} + P_{\mathrm{SB}}\left(T_{\mathrm{env.}},\, \mathrm{A_{BD}}\right) \tag{15.1}$$

$$P_{\mathrm{out}} = P_{\mathrm{SB}}\left(T_{\mathrm{equi.}},\, \mathrm{A_{BD}}\right)\,, \tag{15.2}$$

with the radiated power, P_{SB}, given by the Stefan-Boltzmann law ([72], pages 72 to 78) at environmental temperature, $T_{\mathrm{env.}}$, and temperature $T_{\mathrm{equi.}}$ of the state of equilibrium and the beam dump surface, A_{BD}. During equilibrium, the emitted and absorbed total power are balanced.

$$P_{\mathrm{in}} = P_{\mathrm{out}} \tag{15.3}$$

$$P_{\mathrm{beam}} = P_{\mathrm{SB}}\left(T_{\mathrm{equi.}},\, \mathrm{A_{BD}}\right) - P_{\mathrm{SB}}\left(T_{\mathrm{env.}},\, \mathrm{A_{BD}}\right) \tag{15.4}$$

$$= \sigma_{\mathrm{SB}} \cdot A_{\mathrm{BD}} \cdot \left(T_{\mathrm{equi.}}^4 - T_{\mathrm{env.}}^4\right)\,, \tag{15.5}$$

with the Stefan-Boltzmann constant, σ_{SB}.
Hence, the beam power can be derived from the temperature difference between the environmental temperature and the temperature of the beam dump surface.
In an example with $T_{\mathrm{env.}} = 20\,^{\circ}\mathrm{C}$ and a beam dump surface of $5\,\mathrm{cm} \times 5\,\mathrm{cm}$, a beam power of 1 mW leads to a heating of $T_{\mathrm{equi.}} - T_{\mathrm{env.}} = 0.077\,^{\circ}\mathrm{C}$ of the beam dump surface.

The measurement accuracy could be improved by a smaller beam dump surface, since the resulting temperature difference is thus increased. However, a high temperature object radiating on the OB is undesired. The radiated power would therefore need to be blocked by another surface with a size comparable to that of the original beam dump.
The resulting design then basically consists of a small beam dump, with surface A_A and temperature T_A within a larger one with surface A_B and temperature T_B, as depicted in Figure 15.1. The two beam dumps should be mounted with a thermally isolating material, so that radiation dominates the heat transfer.

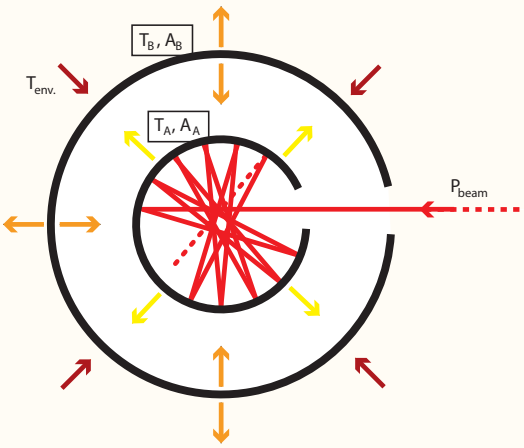

Figure 15.1.: Basic idea for an assembly of a small beam dump, A, and a bigger one, B, to block a laser beam and retrieve its power, P_{beam}, with the surface temperature.

If the equilibrium temperature of both surfaces is measured, their difference can directly be used to determine the dumped beam power in the inner, smaller beam dump.

$$\sigma_{\text{SB}} \cdot A_B \cdot T_B^4 = \sigma_{\text{SB}} \cdot A_B \cdot T_{\text{env.}}^4 + \sigma_{\text{SB}} \cdot A_A \cdot T_A^4 \tag{15.6}$$

$$\sigma_{\text{SB}} \cdot A_A \cdot T_A^4 = \sigma_{\text{SB}} \cdot A_A \cdot T_B^4 + P_{\text{beam}} \tag{15.7}$$

$$\rightarrow P_{\text{beam}} = \sigma_{\text{SB}} \cdot A_A \cdot \left(T_A^4 - T_B^4\right) . \tag{15.8}$$

Here, the surface of the outer beam dump is not relevant and only the inner beam dump surface needs to be known.

There are several advantages of this design for the measurement of the dumped beam power: The most important one is that the temperature difference between outer and inner surface is larger and the observable signal is increased. The corresponding measurement accuracy for a given temperature sensor, therefore, increases. Furthermore, the radiation environment of the inner beam dump is in good agreement with the black body radiation, because it is surrounded by another beam dump. Since the surface of the outer beam dump does not need to be known for this measurement, it would also be possible to guide the power off of the OB by a thermal bridge. For one single beam dump and a heat transfer bridge, the beam power could not be retrieved since the beam dump surface is not easily computable any more.

Of course, a setup like the one depicted in Figure 15.1 would need to be prototyped first and tested in the laboratory to estimate the actual feasibility and accuracy of such a measurement. In particular, the stable mounting of the inner beam dump with a low thermal conductivity might be challenging. Furthermore, the initial functionality must be maintained, so that no stray light escapes the beam dump.

The dedicated beam dump is the so-called TX clip that clips the beam to the input diameter of the telescope, as can be seen in the current LISA OB design in Figure 15.2. Since the transmitted beam to the other satellite needs to have high power ($\approx 2\,\mathrm{W}$), the clipped beam power is also of significant intensity. The temperature of the beam dump could therefore be high enough to give a reasonable signal, especially if a two-beam-dump design could be realised. Furthermore, a slow square wave power modulation could be used to estimate the propagation factors between different diodes and the beam dump in-flight. However, the frequency of the modulation would need to be small enough, so that the time — needed for the beam dump to reach an equilibrium state — is negligible in comparison to the period length of the power modulation.

Before the TX beam is clipped, a low power reflection is picked off and guided to the TM. Therefore, the derived TX beam power could be used to calibrate the PDs, measuring the power at the TM. In the final step, the applied power to the TM could be derived with the calibrated PDs, so that the induced radiation pressure could be used as an independent force to the TM.

However, at the current status, there is no need for an independent force calibration, since the capacitive actuation is well-calibrated. Furthermore, it is unclear, if there will be a possibility to modulate the laser power during flight.

Nevertheless, the measurement of the beam dump temperature could still be useful for the estimation of the actual radiation pressure at the TM. Since the power is controlled by PDs, a decrease in their responsivity would lead to more applied radiation pressure. The beam dump temperature could therefore be used as a long-term monitor for changes of the PD responsivity.

In a first step, the current model of the TX clip could be used to estimate the equilibrium state temperatures and the corresponding measurement accuracies for different designs, so that the actual usefulness of the experiment can be discussed.

15.2. Ghost beam analysis via single beam power measurement

During the single beam power measurements on LPF, a sinusoidal signal could be observed that is assumed to be the homodyne interference of the beam with a subsequent ghost beam (as described in Section 4.2). The in-mode power of the ghost and main beam was determined to be below 10^{-8} parts of the main beam.

A comparable measurement with the LISA OB could be used to identify the presence of ghost beams in the LISA OB interferometers, which would be particularly useful during the build process.

On LPF the observed sinusoidal signals were assumed to be drifts of the differential phase from ghost and main beam, likely driven by temperature.
The laboratory environment during the build process is expected to be less stable than the flight environment of LPF. Therefore, a deterministic signal would need to be applied to the interferometer of ghost and main beam. One option to insert such a signal is a frequency modulation of the single beam.

A ghost beam is expected to travel a different path than the original one. Therefore, the arms of the ghost beam interferometer (which means the distance between the origin of the ghost beam and the recombination with its main beam) are generally of unequal length. As a consequence, a frequency modulation would couple into the phase of the ghost beam interferometer with a signal at the modulation frequency [73]. A demodulation at the modulation frequency would therefore give a tiny coupling coefficient relative to the intensity and path length difference to the ghost beam. For a QPD, the intensity of the coupling at the single quadrants could furthermore be used to retrieve spatial information about the ghost beam on the diode. The effect of selective blocking of surface regions at optical components where ghost beams may occur, could be monitored by the analysis of the frequency modulation coupling. The results could be used to identify critical components and help to improve the design.
Of course, this idea can easily be tested with the LPF engineering model.

The described coupling of a frequency modulation to the relative phase of a ghost beam interferometer might also be an explanation for the observed DWS signals during frequency modulation on LPF [74]. The corresponding signal would be a multi beam interference from one or more ghost beams, its main beam and the other beam, shifted by the heterodyne frequency. The interference between ghost beam and the frequency shifted beam gives a contribution at the heterodyne frequency. The spatial distribution of the ghost beam on the QPD furthermore leads to a stronger signal at one side of the diode, which would appear as a DWS signal.

15.3. Polarisation in the LISA OB design

For LPF the laser beam polarisation was fluctuating much more than expected. The origin of the unstable polarisation state on the OB could be identified, as described in Chapter 10. The PER of the PBS that was used for polarisation cleaning decreased due to out-gassing of water during transport of the satellite to its orbit around L1. Although the magnitude of the observed decrease during flight could still not be reproduced with flight spare hardware in the laboratory, it is assumed that the PBS is the only responsible component for the decreased PER. The much longer transport to L1 is likely to be responsible for the worse PER, in comparison to the short laboratory experiments. However, it can not be ruled out that there are other parameters besides the out-gassing of water that further decreased the PER of the PBS during flight.

As a consequence, the observed issues with polarisation on LPF are easily avoidable in the LISA OB design by using different PBSs for polarisation cleaning. For selection of the particular component the following properties could be considered:

- The optical coating should have a small wet-dry shift: A manufacturing method with high kinetic energy (like ion beam sputtering) should be used to ensure a dense packing of the atoms in the coating where no water can accumulate.

- The band of wavelengths with the desired properties should have enough space towards higher frequencies, to be insensitive to a shift of the spectral transmission and reflection curves towards lower frequencies.

- The active layer should not be sealed. On LPF, the cement between the two prisms lead to a slow evaporation of the water outside the optical layers. Therefore, only a weak effect was observed during thermal tests on ground.
- Of course, the long-term stability of critical components could also be tested in vacuum.

On LPF it was not possible to identify the origin of the parallel polarisation out of the optical fibres, incident to the OB. However, for reliably working polarisation cleaners on LISA, all polarisation fluctuations out of the fibres would be cleaned. Therefore, the parallel polarisation within the LISA OB interferometers should, in contrast to LPF, be negligible.

Nevertheless, the impact of possible polarisation imperfections reaching the LISA OB (even though they are expected to be negligible) can be studied in preparation of the mission, to assess possible risks.
The analysis could furthermore help to identify possible issues with polarisation during the build and characterisation process of the LISA OBs.

In general, a fluctuating polarisation state in a LISA-like interferometer could cause the following problems:

- polarisation ghost beams,
- a decrease in balanced detection,
- radiation pressure fluctuations,
- or a spurious phase at the interferometer output.

15.3.1. Polarisation ghost beams

For LISA the angle of incidence to the TM is normal to the TM surface. Therefore, the reflected beam off the TM is separated by polarisation from the incident one. The beam that is guided to the TM, is a low power pick-off of the one that is transmitted to the other spacecraft. It is called the TX beam, as can be seen in the CAD drawing, Figure 15.2, with the current design for the OB, from Reference [75].

The low-power pick-off of the TX beam has linear orthogonal polarisation and is therefore reflected at the polarising BS with the number PBS2. The reflected beam is then phase-shifted by a quarter wave plate to circular polarisation before it is guided off the plane to the TM. After reflection at the TM, the beam passes through the quarter wave plate again and is further shifted to linear parallel polarisation. Therefore, on the way back, the parallel polarised beam is transmitted through PBS2 and thus separated from the incoming one.

However, if the beam experiences any additional differential phase shift between orthogonal and parallel polarisation on its way between PBS2 and TM, the beam is not perfectly parallel polarised in the end. Therefore, a small part of the power (the projected beam power onto the S-pol axis) would be reflected back at PBS2 into the incident beam path. This back-reflection can be referred to as polarisation ghost beam, although it has the same polarisation as the incident main beam.

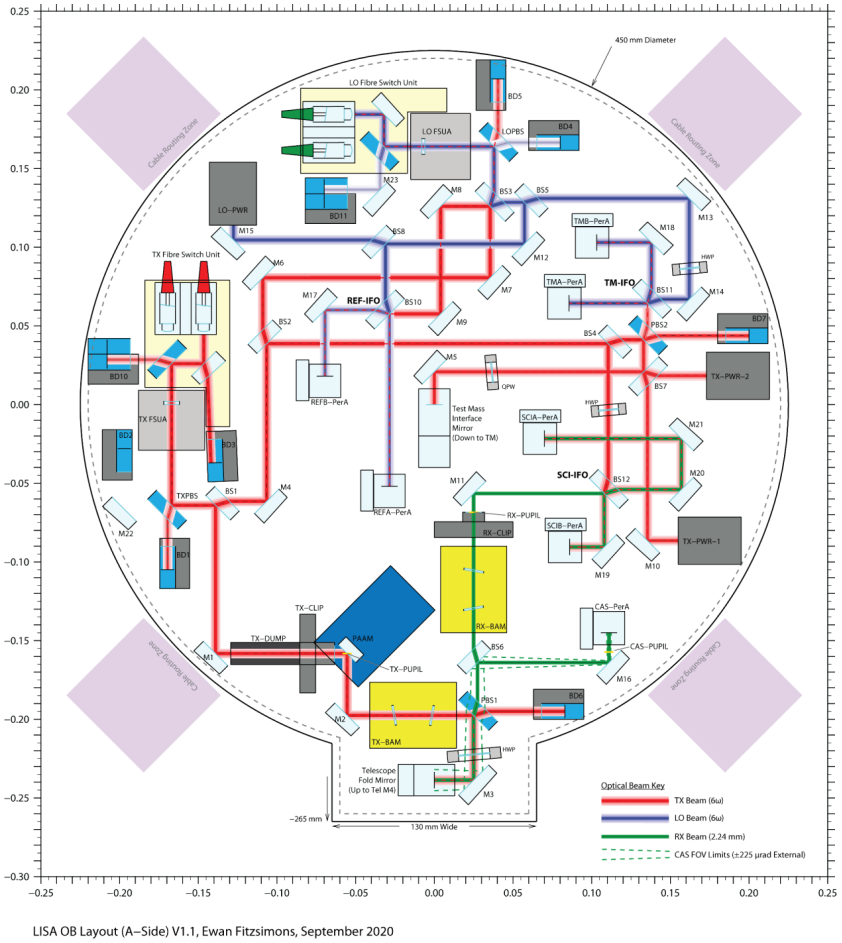

Figure 15.2.: Layout of the LISA OB, 2 dimensional CAD drawing, reprint from Reference [75].

In the current OB design, it would travel the beam path backwards and reflect at BS4, out of the nominal beam path. The reflection can be blocked with a beam dump. The transmitted part of the polarisation ghost beam through BS4 further travels within the beam path of the TX beam back to BS2. At BS2 a part of the beam is again transmitted out off the nominal beam path. The transmission could also be dumped. The reflected part of the beam would further travel within the TX beam path back to BS1, where it is reflected out off the beam path. Since BS1 has a highly asymmetric splitting ratio (with R = 99.6%), almost no light will be transmitted through BS1 back into the Fibre Switching Unit (FSU) of the TX beam.

The origin of a possible polarisation ghost — a differential phase shift between S-pol and P-pol at the path between PBS2 and TM — could be induced by birefringence in a transmitted bulk material (like the optical window to the TM) or reflection at an optical component.

The received beam from the other spacecraft, the so-called Rx beam (collected by the telescope), is also separated by polarisation from the transmitted beam (TX). However, the received beam has such little power that a possible polarisation ghost is negligible. For the high power transmitted beam the correspondingly prominent polarisation ghost is already dumped in the current OB design (see PBS1 in Figure 15.2).

15.3.2. Balanced detection

In general, the transmission and reflection coefficients at a surface between two media with different refractive indices depend on the polarisation of the incoming beam, as described by the Fresnel Formulas. The polarisation, parallel to the plane of incidence, has a different ratio of transmitted to reflected power than the one orthogonal to this plane. This difference only vanishes for normal incidence, where the definition of the plane of incidence is ambiguous (all electrical field vectors are parallel to the surface between two media) and of course for the region of total reflection.
Optical coatings consist of a superposition of several thin layers of two or more media. The thickness of the layers is designed in such a way that the resulting superposition of all reflected and transmitted beams has the desired properties. For example, for a 50:50 BS such a property is an equivalent power of the two beams. However, the desired power ratio is typically reached only for a specific polarisation. For other polarisations the splitting ratio can be quite different. For example, the splitting ratio of LPF's 50:50 BSs is about 20:80 for parallel polarisation, as can be seen in Table 8.1.

If, for any reason, the polarisation state of a beam on the OB changes, the splitting of power at the BSs will change, as well. As a consequence, the balancing of beam powers on the pair of A and B diodes is not fully matched any more. The balancing could be matched synthetically in the post-processing or directly in the phasemeter (the matching factor could be dynamically adjusted).
However, a synthetic matching of the beam powers only removes correlated noise of the two interfering beams. For uncorrelated noise, the recombination at a BS with a splitting ratio different from 50:50 always leads to a remaining coupling of RIN in the nominal balanced detection scheme, even if the beam powers and the power levels at the PDs are matched.

A possible impact of off-nominal polarised power could therefore be mitigated by the use of BSs with a similar splitting ratio of 50:50 for orthogonal and parallel polarisation. However, the decision on a specific optic component is a trade-off of many requirements. The sensitivity to polarisation might therefore be of lower priority.

15.3.3. Radiation pressure

Another effect that could be induced by polarisation fluctuations is based on the power control mechanism. Typically, the beam power is controlled by picking off a small part of the beam with a BS and detecting it for the control scheme. However, the pick-off is likely to be polarisation-dependent, as well. If the incident polarisation is fluctuating, then the power ratio between the picked power and the transmitted beam is also changing. The resulting power fluctuations would lead to a modulation of the applied radiation pressure to the TM and therefore induce direct force noise. Besides the control of the input polarisation, this effect could be mitigated by the use of a pick-off with similar splitting ratio for S-pol and P-pol.

15.3.4. Spurious phase

If both beams of an interferometer have a non-negligible power with off-nominal polarisation, the resulting spurious interference signal may induce a read-out error. Besides the heterodyne amplitude from the off-nominal polarisation, the relative phase between P-pol and S-pol is the relevant parameter, as described for the LPF data in Section 14.3.
A dynamic phase relation could possibly originate in optical fibres. By design, the polarisation out of the fibre is cleaned. Therefore, no significant spurious phase noise is expected for the LISA OB interferometers. Nevertheless, since the cleaning efficiency was degraded already once on LPF, it might be of interest, to further investigate the origin of the polarisation fluctuations incident to the LPF OB.

15.4. Investigation of fibre output polarisation on LPF

On LPF, the power control loop actuators used a range of approximately 15% (see Section8.4.2). A significant amount of the control signal was correlated to the polarisation fluctuations in the OB interferometers. Therefore, it is likely that the power fluctuations of the transmitted power to the OB are induced by polarisation fluctuation coming out of the fibre, leading to more reflection at the PBS.

Polarisation maintaining fibres are designed for two specific orthogonal linear input polarisations which they transmit with a PER of typically better than 20 dB [76]. Hence, the polarisation of the light coming out of the LPF fibres was worse than expected for the LPF fibres and a nominal input polarisation state [76, 71]. A possible disturbed input polarisation might have caused an elliptical output polarisation. In particular, the fibre connectors that were used to directly connect two fibres, are under suspicion. The input polarisation to the second fibre is likely to be rotated, because the optical axes of the two fibres at the connector are unlikely to be perfectly aligned.
Furthermore, mechanical stress in the fibres, induced for example by a temperature gradient or vibrations, could have caused additional birefringence that might have influenced the output polarisation.

Although an analysis of the actual input and output polarisation of the fibres on LPF is not possible, because the data is missing, the impact of a fibre connector in combination with stress could be studied in the laboratory. As a possible noise source, the phase relation between parallel and orthogonal part in the fibre output could be measured with a polarimeter. An alternative setup, using the LPF engineering model, can be found in Appendix F.

15.5. Polarisation detection

On LPF there was no detector, sensitive to the beam polarisation. Therefore, the off-nominal polarised power could only be retrieved from the available single beam power measurements with a corresponding model of the OB. As a consequence, the power with off-nominal polarisation could only be determined after the mission itself. Hence, it would be an advancement for LISA, to have a polarisation-sensitive detection scheme, in particular, because the LISA

OB design has a rotatable wave-plate implemented. Therefore, the polarisation could actually be adjusted (with limited ability) if serious changes occurred.

However, for LISA there are more laser beams from different sources than on LPF. On one of the six OBs there are at least three beams from three different lasers (one local Ultra-Stable Oscillator (USO), one from the adjacent OB and one from the distant SC) combined by at least three interferometers (one science, one TM and one reference interferometer). It is possible that another laser source or a frequency shifted beam and another interferometer are needed, to remove the non-reciprocity in the back link As a consequence, there are several beams that need to be monitored.

The incident off-nominal polarised power to the LISA OB (at the different FSUs) could be monitored by the transmitted power (or reflected power in case of the redundant optical fibre) through the PBS that is used to clean the polarisation. In the current design, this power is dumped. On the one hand, the power could be detected with a PD instead of the beam dump. However, the use of this signal is likely to be too little to justify the additional payload. Furthermore, a PD will introduce additional stray light which is known to be a relevant noise source that needs to be limited. On the other hand, without changing the current design, and therefore, without adding stray light, the dumped power could also be detected by a simple temperature sensor at the beam dump. Here, the designed similarity between a beam dump and a black body is used, as described in Box 15.1.1.

However, monitoring the incident P-pol to the OB only describes what happened in and before the fibres. The polarisation being present in the OB interferometers needs to be monitored on the OB itself. One major difference is, whether or not the polarisation is analysed before or after the recombination BS of an interferometer.

Before the recombination BS, the individual beam power with off-nominal polarisation can be detected. For the TM interferometer, the detection of the P-pol could help to estimate the radiation pressure to the TM, if the polarisation is disturbed more than expected.

One simple solution is to retrieve the power in the post-processing, as it was done with the single beam power measurements on LPF. The advantages in the LISA design are the out-of-loop power monitors with redundant PDs. The BS between the nominal and the redundant PD is likely to have a different splitting ratio for S-pol and P-pol. Therefore, the differential power between these two diodes could be used to monitor the off-nominal polarised power hitting the TMs during nominal science mode. A difficulty could be to distinguish a differential power change from a change in PD responsivity.

The P-pol could also be detected directly. Such a measurement could be done by another PBS which would furthermore act as a second polarisation filter stage. To avoid additional optical components in the beam path, the polarisation-sensitive coating could also be applied to one (or more) of the 50:50 BSs instead of the anti reflection coating at the backside. For the nominal polarisation, the PBS coating would still be anti-reflective. The off-nominal polarised beam instead would be reflected and could be monitored. However, to separate the reflected beam and avoid the synthesis of a ghost beam, travelling parallel with the main one, the BS design would need to be adapted. An edge at the lateral surface, as illustrated in sketch 15.3, could be an option. The reflected parallel polarised beam would travel through the BS, to the edge, coated with an anti-reflection coating for parallel polarisation. The beam is then

transmitted with an angle to the main beam and can be detected at a PD or a beam dump with a temperature sensor (principle described in Box 15.1.1).

Of course, such a design would need to be optimised in geometry and tested experimentally to trade-off the actual benefits in polarisation cleaning and ghost beam reduction with possible drawbacks like beam clipping or an increased temperature-to-phase coupling due to a greater BS thickness and extra cost.

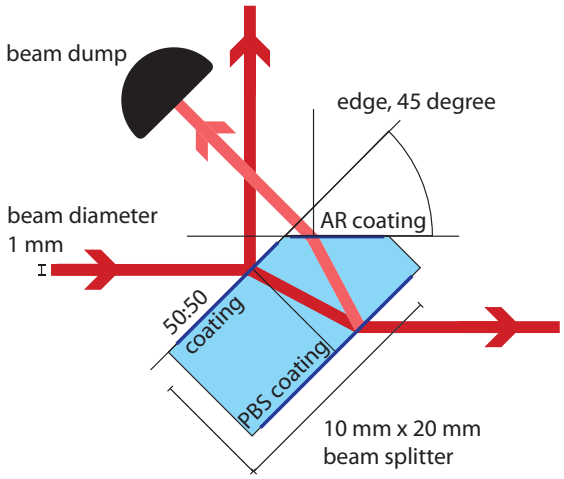

Figure 15.3.: Proposal for a design of a beam splitter with a polarising coating at the backside. The reflected off-nominal polarised beam is transmitted through a cut edge to avoid the synthesis of ghost beams parallel to the main one.

At the recombination BS the off-nominal polarised power of the two individual beams interferes and contributes to the heterodyne phase. This spurious interference signal is indistinguishable from the nominal interference signal in the data post-processing. However, the interference signal could also be detected separately for the two polarisations. Therefore, a PBS and another PD would need to be adapted to one of the interferometer ports. The separate detection of the P-pol interference could actually provide additional information: Besides the heterodyne efficiency in off-nominal polarisation, also the relative phase between the two heterodyne signals could be retrieved. Both bits of information would be necessary to estimate the impact of possible polarisation disturbances to the interferometric measurement.

The sum of the reflected and transmitted beam at the PBS corresponds to the nominal A or B port of the interferometer and therefore allows for the nominal balanced detection scheme.

In case of serious issues with polarisation, the interferometer measurement could be used for subtraction of these effects. However, additional knowledge of the OB component properties for P-pol would be required then.

15.6. Polarisation control

On LISA, the polarisation is controlled passively as it was implemented on LPF. The laser output polarisation is nominally in a linear polarisation state that is furthermore cleaned by a PBS.

To ensure the polarisation cleanliness, another redundant filter stage could be implemented as described in the previous section.

In the current design, the beam polarisation is adjustable with a rotatable half wave plate, located directly behind the FSU. Since the plate has to be rotated with a step motor, the polarisation cannot be rotated during science measurements, because of the corresponding

noise. Therefore, the plate can only be used for a calibration but not for an active control mechanism.

For an active polarisation control mechanism, the design of the OB would need to be changed in different places. The control actuator could conveniently be implemented within the fibres. There are all-fibre, piezo-driven controllers available. However, besides the actuators, polarisation sensors would also be needed. An ordinary polarimeter has fast rotating components which would induce vibrations and torques to the satellite. Since only the parallel polarised power needs to be minimised, a control mechanism could be realised that simply uses the detected amount of P-pol behind the fibre as a sensor (without information of the phase to the nominal polarisation).

However, the LISA OB is designed to maintain a stable linear polarisation state. Therefore, it is most likely that no active stabilisation is needed and the passive polarisation filter, as realised in the current design, remains the most stable and suitable method.

16. Summary and Conclusion

The main research question of this thesis was the stability of the PDs during flight of LPF, as described in Section 1.5. Within the experimental investigation, however, an unexpected yet significant noise source was observed that had to be removed before the initial research question could be answered.

Therefore, the thesis had two leading research questions, which are the topics of Part I and Part II.
The investigations on the unexpected noise source, described in Part II, led to a long path with several steps, where many investigations were a direct consequence of the previous results. For clarity, a short summary of the main findings and conclusions on the further proceeding could already be found at the end of each investigation, typically at the end of a chapter. Furthermore, an overview of Part II can be found in Figure 6.13.
In Section 16.1 the relevant results of both parts of this thesis are summarised and discussed. A conclusion can be found in Section 16.2.

16.1. Results of this thesis

Part I dealt with the long-term monitoring of the PD responsivities on LPF. For that, a radiation pressure modulation experiment was used. In a second experiment, the reflectivity of the TMs was monitored, to derive the applied power from the measured radiation pressure and calibrate the PDs.
The design of the two entangled experiments was summarised in **Chapter 3**.

Chapter 4 described the in-flight monitoring of changes in the TM reflectivity. The measurement principle was a combination of single beam power measurements that cancelled the PD responsivities and the laser power noise, but kept the reflectivity of the TMs. As a consequence, only the uncorrelated read-out noise affected the in-flight monitoring. However, a significant systematic error prevented the measurement of the absolute reflectivity.
During the mission, 87 single beam power investigations were collected, covering a time span of 392 days. The measurements had to be corrected for off-nominal polarisation in preparation of the analysis.
The measurement uncertainty was estimated with a reference of equivalent single beam power combinations that further cancelled the TM reflectivity. The relative maximum deviation in all possible reference combinations for all 87 investigations was $\pm 4.5 \cdot 10^{-3}$ [W/W] (deviation from the average value of all investigations for a particular reference combination). For most of the investigations, however, a deviation in the order of $\pm 1 \cdot 10^{-3}$ [W/W] was found.
A comparison between TM reflectivity and reference combinations showed that there was no

change in reflectivity of both TMs within those errors during the whole monitoring duration of 392 days. The TM reflectivity therefore decreased by less than $2 \cdot 10^{-3}$ [W/W] over a year.

In **Chapter 5**, the in-flight PD responsivity monitoring was described. The applied optical power to the PDs was derived by the radiation pressure that the laser beam induced at the TMs. For this, the radiation pressure was modulated by a square wave power modulation of the measurement beam that induces a differential TM displacement. The resulting modulation depth was measured with the PDs and with the interferometric read-out of differential TM displacement. The propagation from the optical power at the TMs to the PDs finally allowed the retrieval of the responsivity.
In total, three investigations were performed, covering a time span of 389 days. It was found that the responsivity of the PDs in all four interferometers (for the virtually combined responsivity of A and B QPD) had not changed within the full monitoring period, within statistical errors of ±1%. In a simplified linear extrapolation to a 6-years LISA mission, a degradation of more than 12% can therefore be excluded. This corresponds to a decrease of less than 6% in sensitivity of a shot noise limited antenna.
The average responsivity of all four interferometer PDs during flight was given by $\langle \eta^{\text{flight}} \rangle = 0.821\,\text{A/W}$ with a statistical error of $u_{\eta^{\text{flight}}} = 0.01\,\text{A/W}$. A comparison to responsivity measurements before flight [49] showed an average PD degradation of less than 4% for the whole mission duration including the launch and transit to the final orbit. However, systematic errors of up to 3% had to be considered for the in-flight measurements.
Nevertheless, this result was of significant interest even within the systematic error, because PD radiation tests (flight preparation) had predicted an average degradation of 17.5% responsivity for the expected mission dose [20, 21]. A lower actual fluence of particles during flight, as well as a different particle energy spectrum may have been the to cause of the overestimation.
For the radiation pressure modulation, several characterisation measurements were performed. They showed a linear coupling between the measured power at a PD and the measured TM acceleration, as well as no spurious couplings at the nominal modulation depth.
However, within the characterisation measurements at higher modulation depth a tiny unexpected power-to-phase coupling was identified.

Therefore, in **Chapter 6**, further analysis of the power-to-phase coupling was described. During the square wave power modulations it was found that a step in the power of one beam led to a step in the longitudinal and the DWS phase signals. A correlation of the induced DWS step size to the DWS offset angles, given by the average DWS angles that are measured for the optimally aligned TMs, was found.
The effect was further analysed during another LPF experiment, the so-called contrast experiment. Here, the reference beam power was reduced in constant power steps to less than 10% and afterwards stepped up again. The DWS angles, as well as the longitudinal phase, showed steps, correlated with the power steps, without a delay, with equivalent sign and of equivalent length, as was observed for the square wave power modulations. However, the phase step sizes were decreasing towards lower reference beam powers, although the power step size was constant.
The observations were used to trace the origin of the effect back to the processing of the phase signals. However, no simple coupling mechanism was found that agreed with all observed properties of the effect. The normalisation of the phasemeter variables with the so-called C-coefficients in combination with a non-linearity in the digitized heterodyne signal was suspected to be relevant. However, the investigations on the origin of the mechanism could not

be conclusively identified in the scope of this thesis.
The biggest DWS step was observed in φ_1, which had the greatest offset angle of $\approx -60\,\mu\text{rad}$ (in units of a TM angle). A reference beam power step of 10% led to a DWS step of $\Delta\varphi_1 \approx 166\,\text{nrad}$ (in units of a TM angle). The same power step induced a longitudinal step in x_{12} of 6.8 pm. With the assumption of a frequency-independent linear coupling between power and phase, the observed effect could be applied to the measured RIN on LPF. As a consequence, the effect was found to be below the OMS performance by at least a factor 50 and therefore negligible.

Besides the power-to-phase coupling, another unexpected effect was observed that led to further investigations, as detailed in **Part II** of this thesis.

The chronological path was described in **Chapter 7**. The single beam powers were affected by low frequency noise. This noise was different for the two beams, but correlated for different PDs. The intensity of the power fluctuations, however, varied between different PD measurements on the OB. The range between the minimum and maximum measured power differed between 1% and 14% for the different diodes at the OB. This special distribution of noise power led to the conclusion that polarisation fluctuations are the origin of the power noise, although the input polarisation to the OB was nominally cleaned with a PBS.

A dedicated model of the OB was derived in **Chapter 8**. A fit of the single beam powers to the derived model retrieved the off-nominal polarised power in the two beams for each investigation. Accordingly, the reference beam showed a fluctuating share of off-nominal polarised power of up to $P^{\parallel}_{\text{RB}}/P^{\perp}_{\text{RB}} \leq (4.5 \pm 0.045) \cdot 10^{-2}\,\text{W/W}$. For the measurement beam, a lower value of $P^{\parallel}_{\text{MB}}/P^{\perp}_{\text{MB}} \leq (1.74 \pm 0.017) \cdot 10^{-2}\,\text{W/W}$ could be found. These values were significantly higher than the expected transmission through the PBS with a PER better than 1:1000. However, the applicability of the model could be verified by laboratory measurements with the spare OB. Furthermore, experimentally determined splitting ratios of flight spare 50:50 BS and responsivity temperature coefficients of identically constructed PDs agreed with the corresponding parameter estimates.
The P-pol in the two beams was found to have a low,significant, negative, linear correlation. Furthermore, the actuation of the single beam power control loops showed moderate, significant, positive, linear correlations with the P-pol of the individual beams. Both power control loop actuators used a range of $\approx$ 15%. However, the coupling strength between actuator control signal and P-pol was more than 5 times stronger for the reference beam.

The reanalysis of pre-flight single beam power measurements with the OB was described in **Chapter 9**. The analysis showed an increased level in off-nominal polarisation, but with a lower amplitude than in-flight. The reference beam showed fluctuating levels in the off-nominal polarised power of up to $P^{\parallel}_{\text{RB}}/P^{\perp}_{\text{RB}} \leq (6.1 \pm 0.4) \cdot 10^{-3}\,\text{W/W}$. For the measurement beam, again, a lower value of $P^{\parallel}_{\text{MB}}/P^{\perp}_{\text{MB}} \leq (3.8 \pm 0.3) \cdot 10^{-3}\,\text{W/W}$ was found. Furthermore, a slow periodic correlation with the environmental temperature was apparent in the much greater amount of data, compared to the flight data set.

Possible theories for the origin of the polarisation fluctuations were discussed in **Chapter 10**. For this, the effect of the constant vertical rotation of the PBSs on LPF by an angle of up to $\varphi_{\text{PBS}} = 3^\circ \pm 2^\circ$ was considered. The corresponding best theory at that time was that mechanical stress induced changes to the PBS optical properties, resulting in a rotation of the PBS optical axis.

To verify this, a flight spare PBS was investigated experimentally for its sensitivity to mechanical stress, as was described in **Chapter 11**. At first, the influence of a PBS rotation around its vertical axis was measured, without application of mechanical stress. The transmitted off-nominal polarised power for a nominally linear input polarisation agreed with the prediction of a simplified geometrical model for PBS rotation angles below $\varphi_{\mathrm{PBS}} < 10°$. Afterwards, constant mechanical stress was applied by the gravity force of weights, corresponding to a homogenous pressure at the upper PBS surface of up to (736 ± 10) kPa. Repeating the measurement of transmitted power through a rotated PBS with mechanical stress, however, showed only weak effects with a high statistical variation for small PBS rotation angles with $\varphi_{\mathrm{PBS}} < 10°$. The measurement was subsequently repeated with an increased PBS temperature of about $T_{\mathrm{PBS}} \approx 50\,°\mathrm{C}$ (without a temperature monitoring), without a significant effect on the transmitted power with off-nominal polarisation. As a consequence, the first theory of mechanical stress as the source of the P-pol on the OB was rejected.
Therefore, a second measurement series investigating the PER of the PBS in combination with a PBS rotation was performed. In general, the cleaning efficiency for nominal parameters was found to agree with the specifications. For parallel input polarisation the transmitted P-pol was found to be dominated by the coating efficiency, for PBS rotation angles below $\varphi_{\mathrm{PBS}} < 10°$. As a consequence, a change of the input polarisation had a higher impact on the transmitted power with S-pol than on the one with P-pol. This effect was found to be greatest for a PBS rotation of $\varphi_{\mathrm{PBS}} = 3°$. The ratio of parallel and orthogonal polarisation in the transmitted light was determined to be $P^{\parallel}_{\mathrm{out}}/P^{\perp}_{\mathrm{out}}\,(\varphi_{\mathrm{PBS}} = 3°) \approx 1.5 \cdot 10^{-3}\,\mathrm{W/W}$ for orthogonal input polarisation. However, for parallel input polarisation the ratio was determined to at least $P^{\parallel}_{\mathrm{out}}/P^{\perp}_{\mathrm{out}}\,(\varphi_{\mathrm{PBS}} = 3°) \approx 0.5\,\mathrm{W/W}$.
This finding was of particular interest, because the LPF power control loops were more sensitive to the nominal polarisation. As a consequence, the transmitted P-pol was further enhanced for an off-nominal polarised input polarisation.
Subsequently, the transmission through three flight spare PBSs was measured for a constant PBS rotation of $\varphi_{\mathrm{PBS}} = 3°$ and a continuous rotation of a linear input polarisation state. The transmitted powers were normalised equivalent to the LPF control loop (assuming perfect control and infinite laser power). It could be found that for a linear input polarisation of $\varphi_{\mathrm{pol}} = 76°$ off-nominal, the transmitted light had a share of 4.6% parallel polarisation, corresponding to the in-flight observations. However, this highly off-nominal input polarisation corresponded to a small amount of overall transmitted power of 4.1%, which was thought to be unrealistic for the LPF setup.
Overall, the first set of laboratory investigations could not reproduce the in-flight observations with reasonable assumptions on the input polarisation to the PBS. Therefore, as the next step, the most similar setup — the flight spare OB — was investigated.

In **Chapter 12** the spare OB was used for experimental investigation of the single beam powers with a known rotation of the linear polarisation state by a polarisation filter. The polarisation on the spare OB showed nominal performance for a reasonable rotation of the linear input polarisation to the PBS, of up to 41° off-nominal. A rotation of the linear polarisation angle behind the PBS, up to 37° off-nominal, however, agreed with the predicted beam powers from the OB model. The only difference between the two flight OB measurements and the spare OB measurement was the duration of exposure to a vacuum or satellite atmosphere. As a consequence, the impact of the environment was investigated in subsequent laboratory investigations.

In **Chapter 13** the effect of a vacuum on the PER of an LPF PBS was investigated. For that purpose, one flight spare PBS was vacuum baked at 50 °C for 2 weeks. After one further week in the vacuum environment at room temperature, the PBS was immediately moved to the current setup and analysed for a rotation of 3°. The PER was found to have decreased by a factor of 4.8, corresponding to a fit of the transmitted P-pol with a maximum deviation to the measurement of 8%. A comparable decrease was found for a PBS that was stored in a highly humidity reduced atmosphere for three weeks at room temperature.
A spectral photometer analysis of both PBSs and a reference sample could identify a strong so-called wet-dry shift as the reason for the decreased PER. The out-gassing of water from the active coating shifted the spectral properties towards shorter wavelengths, so that the PER at 1064 nm was reduced. Since the coated surface in the cubic PBS was sealed with glue (that combines the two prisms, forming the cube), the water needed to dissolve in the glue first, before it could evaporate into the surroundings from the interaction surface at the edges of the cube. Therefore, it remained unclear if all embedded water was out-gassed after the applied vacuum baking or drying process.
The transmission through the vacuum baked PBS was compared with the levels of P-pol on the OB:
The observed P-pol in the measurement beam of $P^{\parallel}_{\mathrm{MB}}/P^{\perp}_{\mathrm{MB}} \leq (3.8 \pm 0.3) \cdot 10^{-3}\,\mathrm{W/W}$ during the pre-flight measurements with the flight OB could directly be explained with the measured vacuum-induced decrease in the PER, under the assumption that the 40% fluctuations in transmitted power to the OB result from reflection of off-nominal polarised input light at the PBS. For the reference beam, however, a minimum off-nominal polarised input power to the PBS of approximately 11% was additionally needed to explain the share of parallel polarisation, $P^{\parallel}_{\mathrm{RB}}/P^{\perp}_{\mathrm{RB}} \leq (6.1 \pm 0.4) \cdot 10^{-3}\,\mathrm{W/W}$, by the vacuum-induced effect.
For the in-flight observations, in contrast, the input polarisation to the PBS was still unreasonably far off-nominal, even when considering the measured decrease in the vacuum.
Since it was unclear whether the vacuum out-gassing was complete after 3 weeks, a further decrease in the PER was modelled. As for the pre-flight data, it was further assumed that the control loop range of $\approx 15\%$ was mainly used to compensate off-nominal polarisation, incident to the PBS. The in-flight P-pol in the measurement beam of $P^{\parallel}_{\mathrm{MB}}/P^{\perp}_{\mathrm{MB}} \leq (1.74 \pm 0.017) \cdot 10^{-2}\,\mathrm{W/W}$, was then reasonably explainable with a further decrease in the PER by a factor of 10 and a minimum loss of power at the PBS due to polarisation of 9%. For the reference beam, however, the further decrease of the PER would have needed to be at least a factor 20 to explain the significant share of P-pol during flight of $P^{\parallel}_{\mathrm{RB}}/P^{\perp}_{\mathrm{RB}} \leq (4.5 \pm 0.045) \cdot 10^{-2}\,\mathrm{W/W}$.
Since the out-gassing of water from the PBS coating is assumed to be slow, a further decrease of the PER was reasonable. However, a factor of 20 was still thought to be unreasonably high. Therefore, a further degrading mechanism of the reference beam PBS, such as a greater PBS rotation angle, an initial bad PER, or more mechanical stress, was assumed to be relevant.
Furthermore, it was unknown how much P-pol was actually incident to the PBS. The correlation with the power CL gives a hint on the fluctuations to be in the magnitude of 10%, but not on the average parallel input polarisation to the PBS.
For clarification, the presented measurements in this thesis could be repeated with the three flight spare PBSs, or the spare OB after an LPF equivalent exposure to an ultra-dry atmosphere of several months.

The discovery of polarisation noise led to the analysis of subsequent effects on the science observables of LPF that were described in **Chapter 14**. There were three coupling mechanisms

identified: a mismatch in balanced detection, an additional contribution to radiation pressure and a spurious interference signal.

The polarisation-dependent splitting ratios of the recombination BS for parallel polarisation, led to different power levels at the A and B diodes in the interferometer output. As a consequence, the removal of intensity noise by the balanced detection scheme decreased, as was described in **Section 14.1**. For the measurement of differential TM displacement, the maximum coupling of relative intensity noise was found to be: $\Delta s_{\mathrm{RIN}}^{\text{diff-TM}} \leq 2 \cdot 10^{-9}\,\mathrm{m} \cdot \mathrm{RIN}(@f_{\mathrm{het}})$. For LPF ($\mathrm{RIN}(@f_{\mathrm{het}}) \approx 10^{-6}\frac{1}{\sqrt{\mathrm{Hz}}}$), the effect was with $\Delta s_{\mathrm{RIN}}^{\text{diff-TM}} \leq 2 \cdot 10^{-15}\frac{\mathrm{m}}{\sqrt{\mathrm{Hz}}}$ found to be at least an order of magnitude below the OMS performance of $s_{\mathrm{disp.}}^{1/2} = (34.8 \pm 0.3)\,\mathrm{fm}/\sqrt{\mathrm{Hz}}$ at frequencies above 30 mHz [16, 19].

The polarisation fluctuations induced low frequency power fluctuations, as were initially observed in the data. The resulting radiation pressure led to low frequency TM acceleration noise, as described in **Section 14.2**.
On LPF there was no out-of-loop sensor for the measurement beam that was reflected off the TMs. Therefore, the combined beam powers had to be used to estimate the share of parallel polarisation, incident to the TMs.
For the long February noise run, the polarisation-dependent contributions to radiation pressure were estimated at frequencies below 10 mHz. The measurement of power with nominal polarisation was found to be limited by the resolution of the ADC. Therefore, an upper limit was estimated by the use of all interferometer power measurements.
For the parallel polarisation, the average ratio of P-pol between measurement and reference beam during all single beam power measurements was used to derive the best estimate of the P-pol at the TMs from the frequency interferometer during the noise run. The resulting contribution to radiation pressure was a band between negative and positive correlation of the P-pol from reference and measurement beam. For the single beam power measurements a significant negative correlation between the P-pol in the measurement and reference beam was found. Therefore, an actual coupling within the upper half of the derived band was assumed to be more likely.
Below 1 mHz, the upper limit of the derived radiation pressure contribution to the ASD of residual differential TM acceleration noise became relevant with a share of up to $26\,(+6-2)\,\%$ at 74 µHz. It could be found that the P-pol significantly contributed to that allocation at frequencies below 0.1 mHz. Below 50 µHz the parallel polarised light was even dominating the radiation pressure to the TM.
However, the average ratio between the P-pol parts of reference and measurement beam had to be estimated by the single beam power measurements. Therefore, it would have been possible that in this specific experiment, the fluctuations in the measurement beam were higher than the ones from the reference beam. As a consequence, even the upper limit of the band could have underestimated the actual radiation pressure at the TMs. The individual parallel polarised beam powers, however, remained inaccessible with the LPF data set.

The third identified coupling mechanism of polarisation to the LPF metrology was a spurious heterodyne signal from the interference of parallel polarised light in the reference and measurement beams, as described in **Section 14.3**. Because of the different P-pol levels in the interferometers, the subtraction of the reference interferometer was not cancelling the spurious phase signal.
The maximum error in the differential TM displacement, for a relative phase of $\frac{\pi}{2}$ between

heterodyne interference from nominal and off-nominal polarisation, was derived to be 800 pm, within a systematic error of up to 5%.
Since there is no information about the phase relation between nominal and off-nominal polarisation and its dynamics, it was not possible to estimate a spectral contribution. However, a comparison with the measured acceleration noise and the OMS performance indicated that the impact of the read-out noise, within the measurement band of LPF, is negligible.

16.2. Conclusion

The main research question, focused in Part I of this thesis, was the long-term stability of LPFs PDs. It was found that the actual decrease in PD responsivity was significantly lower than expected. In a simplified linear extrapolation to a 6-years LISA mission duration, the sensitivity of a shot noise limited observatory would therefore be reduced by at most 6%. However, although the LPF satellite was a comparable functional environment of the PDs for LISA, the radiation environment will be different. LPF was operated during a period with low solar activity. The much longer LISA mission, in contrast, will have to cope with at least one period of higher solar activity, due to the solar cycle of about 11 years. Therefore, a linear extrapolation of the LPF results underestimates the radiation environment for LISA. As a consequence, the estimate needs to be adapted for the expected radiation environment and equivalent shielding, when available. Since the initial radiation tests for LPF overestimated the actual displacement damage it might furthermore be recommended to use more realistic particle energies for application of an equivalent fluence, if possible.

The PD responsivities were monitored with a radiation pressure modulation. This experiment design could be adapted for LISA not only for a calibration of the PDs, but also for the possibility of an independent force application to the TM. The temperature of the beam dump, that is clipping the high power transmitted beam, could be used to estimate the applied optical power to to the PDs, as well as to the TM.

Part II of this thesis dealt with a mostly unrelated research question — the origin of the polarisation fluctuations on the OB of LPF.
It was found that the beam polarisation fluctuated significantly more than designed, with an off-nominal polarised part of the beam power up to 4.5%. A decreased cleaning efficiency of the PBSs due to out-gassing of water could be identified as the reason. An intentional rotation of the PBS and the influence of the power CLs significantly enhanced the effect. However, it was not possible to completely conclude on the origin of the highest observed polarisation fluctuations in the reference beam during flight.
The applied power control actuation further indicated a significant incidence of off-nominal polarised power to the PBS, of which the origin is unclear. Since functionally similar components will be used in LISA, a further investigation on the origin of the incident off-nominal polarisation to the LPF OB could be useful for the identification of polarisation sensitive elements in the LISA design.

The impact of the polarisation fluctuations on the LPF metrology was found to be negligible with the exception of the contribution to radiation pressure. Here, the polarisation fluctuations significantly enhanced the low frequency contribution to the differential TM acceleration and, furthermore, disabled the possibility of a noise subtraction, because of the unknown correlation

of the off-nominal polarised power in the two beams.
Furthermore, it should be considered that on LPF the polarisation noise at the TMs was actually low in comparison to the overall polarisation noise on the OB. The measurement beam was more than three times less affected by power fluctuations from off-nominal polarisation than the reference beam. Furthermore, the applied off-nominal polarised power at the TMs was further reduced by reflection at the 50:50 BSs that reflect only 20.5% of the incident parallel polarisation. If reference and measurement beam would have been switched, and the BS transmitted beams would have been guided to the TMs, the polarisation-induced power noise at the TMs would have been more than 17 times stronger. Therefore, the low frequency acceleration noise would have been limited by polarisation.
As a consequence, the design of the LISA OB should be analysed on the impact of possible polarisation imperfections. A first analysis of the main expectable effects from polarisation was outlined in Chapter 15.
It was found that most of the possible effects could be reduced by the choice of the optical coatings of the BSs. The optical properties should be as similar as possible for parallel and orthogonal polarisation. Especially the optical components, that are used for reflection to a power monitor diode, should be considered with regard to polarisation to avoid the conversion of polarisation to power noise.
Furthermore, the optics specifications should be verified for a vacuum or dry environment to exclude effects on the performance by out-gassing of water.
A second polarisation filter step could be implemented as redundancy. Such an extra filter step could possibly be combined with a reduction of ghost beams at critical components, as proposed in Section 15.5.

A. Phasemeter and Processing

In general, a phasemeter is a processing unit that computes the average phase in a sampled signal time series at a given frequency. The time segment is chosen such that it covers some multiple cycles of the desired signal frequency. The output frequency is therefore given by the length of the chosen segment of which the average phase is determined. The average phase in one time segment is estimated by a single-bin discrete Fourier transformation giving the sine and cosine transformation of that segment. In the following, the parameter calibration within the LPF phasemeter is described. More details can be found in Reference [77].

Note that the normalisation of the phasemeter parameters with the so-called C-coefficients is described in further detail, because of its relevance for the power-to-phase coupling effect, described in Chapter 6.

On LPF, the input to the phasemeter is the ADC sampled optical signal from an interferometer PD quadrant $x_n(t)$. It has a sampling frequency of 50 kHz. The desired frequency to analyse is the heterodyne frequency of 1 kHz. The length of the time segment is chosen such that 10 full cycles fit inside. Therefore, the DFT is applied on $\mathrm{N_{fft}} = 500$ samples, giving the cosine transformed signal z, the sine-transformed signal y and the DC component d.

$$z = \sum_{n=0}^{\mathrm{N_{fft}}-1} c_n \cdot x_n(t)\,, \tag{A.1}$$

$$y = \sum_{n=0}^{\mathrm{N_{fft}}-1} s_n \cdot x_n(t)\,, \tag{A.2}$$

$$d = \sum_{n=0}^{\mathrm{N_{fft}}-1} x_n(t)\,. \tag{A.3}$$

The parameters for the transformation are given by:

$$\begin{aligned} s_n &= round\left(\mathrm{A_{SC}} \cdot (1 + \omega_n \cdot \sin_n)\right)\,, \\ c_n &= round\left(\mathrm{A_{SC}} \cdot (1 + \omega_n \cdot \cos_n)\right)\,, \end{aligned} \tag{A.4}$$

with $\sin_n = \sin\left(\frac{2\pi \cdot 10}{\mathrm{N_{fft}}} n\right)$ or $\cos_n = \cos\left(\frac{2\pi \cdot 10}{\mathrm{N_{fft}}} n\right)$. The constant $\mathrm{A_{SC}}$ refers to the range of a 16 bit integer and ω_n describes a window function that can be applied to the time segment to improve boundary conditions.
The additional 1 in equation A.4 accounts for an unsigned integer operation, keeping all values positive. Of course this offset needs to be removed again in the data-processing.

The sampled signal itself can be reduced to a DC component, x_n^{dc} , and an oscillatory component, x_n^{het}, at the heterodyne frequency, since all other frequencies are disregarded by the transformation.

$$x_n(t) = \mathrm{A}_{\mathrm{range}}(x_n^{\mathrm{dc}} + x_n^{\mathrm{het}})\,. \tag{A.5}$$

$\mathrm{A}_{\mathrm{range}}$ describes the range of the ADC, converting the analogue time series $x(t)$ from the PD into a sampled signal series $x_n(t)$. Applied to Equations A.1 to A.3, the phasemeter parameters are given by:

$$\begin{aligned} z = &\sum_{n=0}^{\mathrm{N_{fft}}-1} round\left(\mathrm{A_{SC}}\cdot(1+\omega_n\cdot\cos_n)\right)\cdot\mathrm{A_{range}}\cdot x_n^{\mathrm{dc}} \\ &+\sum_{n=0}^{\mathrm{N_{fft}}-1} round\left(\mathrm{A_{SC}}\cdot(1+\omega_n\cdot\cos_n)\right)\cdot\mathrm{A_{range}}\cdot x_n^{\mathrm{het}}\,, \end{aligned} \tag{A.6}$$

$$\begin{aligned} y = &\sum_{n=0}^{\mathrm{N_{fft}}-1} round\left(\mathrm{A_{SC}}\cdot(1+\omega_n\cdot\sin_n)\right)\cdot\mathrm{A_{range}}\cdot x_n^{\mathrm{dc}} \\ &+\sum_{n=0}^{\mathrm{N_{fft}}-1} round\left(\mathrm{A_{SC}}\cdot(1+\omega_n\cdot\sin_n)\right)\cdot\mathrm{A_{range}}\cdot x_n^{\mathrm{het}}\,, \end{aligned} \tag{A.7}$$

$$d = \sum_{n=0}^{\mathrm{N_{fft}}-1} \mathrm{A}_{\mathrm{range}}(x_n^{\mathrm{dc}} + x_n^{\mathrm{het}})\,. \tag{A.8}$$

The oscillatory part of the DC component x_n^{het} averages out for a full cycle:

$$d \approx \sum_{n=0}^{\mathrm{N_{fft}}-1} \mathrm{A_{range}} x_n^{\mathrm{dc}} = \mathrm{N_{fft}}\mathrm{A_{range}} x_n^{\mathrm{dc}}\,. \tag{A.9}$$

On the other hand, for the purely oscillatory summand, the 1 vanishes for the same reason. So Equation A.6 and A.7 reduce to:

$$\begin{aligned} z = &\sum_{n=0}^{\mathrm{N_{fft}}-1} round\left(\mathrm{A_{SC}}\cdot(1+\omega_n\cdot\cos_n)\right)\cdot\frac{d}{\mathrm{N_{fft}}} \\ &+\sum_{n=0}^{\mathrm{N_{fft}}-1} round\left(\mathrm{A_{SC}}\cdot\omega_n\cdot\cos_n\right)\cdot\mathrm{A_{range}}\cdot x_n^{\mathrm{het}}\,, \end{aligned} \tag{A.10}$$

$$\begin{aligned} y = &\sum_{n=0}^{\mathrm{N_{fft}}-1} round\left(\mathrm{A_{SC}}\cdot(1+\omega_n\cdot\sin_n)\right)\cdot\frac{d}{\mathrm{N_{fft}}} \\ &+\sum_{n=0}^{\mathrm{N_{fft}}-1} round\left(\mathrm{A_{SC}}\cdot\omega_n\cdot\sin_n\right)\cdot\mathrm{A_{range}}\cdot x_n^{\mathrm{het}}\,. \end{aligned} \tag{A.11}$$

By subtraction of the DC-summand, the purely oscillatory components of the complex vector $\vec{F}_{\mathrm{raw}}$ (containing the amplitude and phase of the heterodyne signal) can be retrieved:

$$
\begin{aligned}
Re\{\vec{F}_{\mathrm{raw}}\} &= \sum_{n=0}^{\mathrm{N_{fft}}-1} round\left(\mathrm{A_{SC}}\cdot\omega_n\cdot\cos_n\right)\cdot\mathrm{A_{range}}\cdot x_n^{\mathrm{het}} \\
&= z - \sum_{n=0}^{\mathrm{N_{fft}}-1} round\left(\mathrm{A_{SC}}\cdot(1+\omega_n\cdot\cos_n)\right)\cdot\frac{d}{\mathrm{N_{fft}}}\,, \qquad \text{(A.12)} \\
Im\{\vec{F}_{\mathrm{raw}}\} &= \sum_{n=0}^{\mathrm{N_{fft}}-1} round\left(\mathrm{A_{SC}}\cdot\omega_n\cdot\sin_n\right)\cdot\mathrm{A_{range}}\cdot x_n^{\mathrm{het}} \\
&= y - \sum_{n=0}^{\mathrm{N_{fft}}-1} round\left(\mathrm{A_{SC}}\cdot(1+\omega_n\cdot\sin_n)\right)\cdot\frac{d}{\mathrm{N_{fft}}}\,. \qquad \text{(A.13)}
\end{aligned}
$$

The last step in processing is a normalisation of $\vec{F}_{\mathrm{raw}}$, which still has the unit of ADC counts. The oscillatory parts of the sampled PD time series are a cosine or sine wave with an amplitude smaller than one: $x_n^{\mathrm{het}} < 1$ (compare to Equation A.5). Therefore, a cosine or sine with an amplitude of one is used for normalisation:

$$
Re\{\vec{F}\} = \frac{Re\{\vec{F}_{\mathrm{raw}}\}}{\sum_{n=0}^{\mathrm{N_{fft}}-1} round\left(\mathrm{A_{SC}}\cdot(1+\omega_n\cdot\cos_n)\right)\cdot\mathrm{A_{range}}\cdot\cos_n} = \mathrm{C}^{Rz}\cdot z + \mathrm{C}^{Rd}\cdot d\,, \qquad \text{(A.14)}
$$

$$
Im\{\vec{F}\} = \frac{Im\{\vec{F}_{\mathrm{raw}}\}}{\sum_{n=0}^{\mathrm{N_{fft}}-1} round\left(\mathrm{A_{SC}}\cdot(1+\omega_n\cdot\sin_n)\right)\cdot\mathrm{A_{range}}\cdot\sin_n} = \mathrm{C}^{Iz}\cdot z + \mathrm{C}^{Id}\cdot d\,. \qquad \text{(A.15)}
$$

.

The C-coefficients derive to:

$$
\mathrm{C}^{Rz} = \frac{1}{\sum_{n=0}^{\mathrm{N_{fft}}-1} round\left(\mathrm{A_{SC}}\cdot(1+\omega_n\cdot\cos_n)\right)\cdot\mathrm{A_{range}}\cdot\cos_n}\,, \qquad \text{(A.16)}
$$

$$
\mathrm{C}^{Iy} = \frac{1}{\sum_{n=0}^{\mathrm{N_{fft}}-1} round\left(\mathrm{A_{SC}}\cdot(1+\omega_n\cdot\sin_n)\right)\cdot\mathrm{A_{range}}\cdot x_n^{\mathrm{het}}}\,, \qquad \text{(A.17)}
$$

$$
\mathrm{C}^{Rd} = -\frac{\mathrm{C}^{Rz}}{\mathrm{N_{fft}}}\cdot\sum_{n=0}^{\mathrm{N_{fft}}-1} round\left(\mathrm{A_{SC}}\cdot(1+\omega_n\cdot\cos_n)\right)\,, \qquad \text{(A.18)}
$$

$$
\mathrm{C}^{Id} = -\frac{\mathrm{C}^{Iy}}{\mathrm{N_{fft}}}\cdot\sum_{n=0}^{\mathrm{N_{fft}}-1} round\left(\mathrm{A_{SC}}\cdot(1+\omega_n\cdot\sin_n)\right)\,. \qquad \text{(A.19)}
$$

Note that the above derivation is simplified for perfect alignment of the diodes. The off-diagonal components c^{Iz} and c^{Ry} are assumed to be zero.

$$
\vec{F} = \begin{pmatrix} Re\{\vec{F}\} \\ Im\{\vec{F}\} \end{pmatrix} = \begin{pmatrix} \mathrm{C}^{Rz} & \mathrm{C}^{Iz} \\ \mathrm{C}^{Ry} & \mathrm{C}^{Iy} \end{pmatrix}\cdot\begin{pmatrix} z \\ y \end{pmatrix} + \begin{pmatrix} \mathrm{C}^{Rd} \\ \mathrm{C}^{Id} \end{pmatrix}\cdot d\,. \qquad \text{(A.20)}
$$

In general, they can be used to cancel quadrant channel phase-shifts as described in further detail in Reference [77].

Of course, the DC component d also needs to be normalised with a corresponding C-coefficient, given by:

$$\mathrm{DC} = \mathrm{C}^{\mathrm{DC}} \cdot d\,, \tag{A.21}$$

$$\mathrm{C}^{\mathrm{DC}} = \frac{1}{\mathrm{N}_{\mathrm{fft}} \cdot \mathrm{A}_{\mathrm{range}}}\,. \tag{A.22}$$

B. OB power propagations

For the estimation of the radiation pressure at the TMs, the powers need to be propagated between the TMs and the PD power measurements, given by the Σ parameters. Therefore, the reflection and transmission coefficients of the particular optical components in the beam path need to be regarded.
The propagation factors, λ_i, were therefore estimated with the most accurate available values, listed and described in the following:

$$
\begin{aligned}
T^{\perp}_{BS-45^\circ} &= 0.484\,,\\
T^{\parallel}_{BS-45^\circ} &= 0.795\,,\\
T^{\perp}_{BS-43^\circ} &= 0.5\,,\\
T^{\parallel}_{BS-43^\circ} &= 0.78\,,\\
T^{\perp}_{BS-47^\circ} &= 0.466\,,\\
T^{\parallel}_{BS-47^\circ} &= 0.81\,,\\
R^{p}_{BS} &= 1 - T_{BS}\,,\\
R_{M} &= 0.997\,,\\
R_{TM} &= 0.99\,,\\
T_{OW} &= 0.98\,.
\end{aligned}
$$

For the 50:50 BSs, the most accurate available values are the result of a fit of the single beam power measurements to the OB model, described in Part II, in Section 8.2. The maximum deviation of the BS transmission best parameter estimate is about 1% for the orthogonal polarisation and less than 0.5% for the parallel polarisation.
The reflectivity of the OB mirrors, R_M, and the optical window transmittance, T_{OW}, are used from pre-flight measurements (mirrors from Reference [42] and optical windows from [78]).
The TM reflectivity was found to be stable over the mission duration within errors below $\pm 2.5 \cdot 10^{-3}$ (see Chapter 4). Therefore it is further assumed that no major decrease in reflectivity occurred during transmission to the Lagrange-point L1. As a consequence, the reflectivity of polished pure gold for $\lambda = 1064\,\mathrm{nm}$ and $\varphi_{\mathrm{inc.}} = 4.5^\circ$ was used as TM reflectivity with $R_{TM} = 0.99$, as found in Reference [79]).

Note that in general all of these coefficients are polarisation-dependent. However, in the LPF design this difference is only relevant for the BSs.

For simplicity, all powers are propagated back to a shared point in the beam path — at the front of the OB, before the beam is split up into the different interferometers.

B.1. Measurement beam propagation to the TMs and Σ parameters

The propagation factors from the front of the OB to the Σ-parameters are given by:

$$\begin{aligned}
\lambda^p_{\Sigma_{12},\,\mathrm{MB}} &= \frac{1}{2}\cdot\lambda^p_{\mathrm{TM2}}\cdot \mathrm{R_{TM}}\cdot \mathrm{T_{OW}}\cdot \mathrm{R_M}\,,\\
\lambda^p_{\Sigma_1,\,\mathrm{MB}} &= \frac{1}{2}\cdot\lambda^p_{\mathrm{TM1}}\cdot \mathrm{R_{TM}}\cdot \mathrm{T_{OW}}\cdot \mathrm{T}^p_{\mathrm{BS-45^\circ}}\cdot \mathrm{R_M}\,,\\
\lambda^p_{\Sigma_\mathrm{R},\,\mathrm{MB}} &= \frac{1}{2}\cdot\mathrm{T}^p_{\mathrm{BS-47^\circ}}\cdot \mathrm{R}^p_{\mathrm{BS-45^\circ}}\cdot \mathrm{R}^3_{\mathrm{M}}\,,\\
\lambda^p_{\Sigma_\mathrm{F},\,\mathrm{MB}} &= \frac{1}{2}\cdot\mathrm{T}^p_{\mathrm{BS-47^\circ}}\cdot \mathrm{T}^p_{\mathrm{BS-45^\circ}}\cdot
\end{aligned} \tag{B.1}$$

The propagation factors to the TM are given by:

$$\begin{aligned}
\lambda^p_{\mathrm{TM1}} &= \mathrm{R}^p_{\mathrm{BS-47^\circ}}\cdot \mathrm{T_{OW}}\,,\\
\lambda^p_{\mathrm{TM2}} &= \mathrm{R}^p_{\mathrm{BS-47^\circ}}\cdot \mathrm{R}^p_{\mathrm{BS-43^\circ}}\cdot \mathrm{T}^3_{\mathrm{OW}}\cdot \mathrm{R_{TM}}\cdot \mathrm{R_M}\,,\\
\lambda^p_{\mathrm{TM1\text{-}TM2}} &= \mathrm{R}^p_{\mathrm{BS-43^\circ}}\cdot \mathrm{T}^2_{\mathrm{OW}}\cdot \mathrm{R_{TM}}\cdot \mathrm{R_M}\,.
\end{aligned} \tag{B.2}$$

The propagation between the two TMs and between a diode and the TMs are given as follows:

$$\begin{aligned}
\lambda^p_{\mathrm{TM1\ to\ TM2,\,MB}} &= \frac{\lambda^p_{\mathrm{TM2}}}{\lambda^p_{\mathrm{TM1}}} = \mathrm{R}^p_{\mathrm{BS-43^\circ}}\cdot \mathrm{T}^2_{\mathrm{OW}}\cdot \mathrm{R_{TM}}\cdot \mathrm{R_M}\,,\\
\lambda^p_{\Sigma_{12}\text{-}\mathrm{TM1},\,\mathrm{MB}} &= \frac{\lambda^p_{\mathrm{TM1}}}{\lambda^p_{\Sigma_{12},\,\mathrm{MB}}} = \left(\frac{1}{2}\cdot \mathrm{R}^p_{\mathrm{BS-43^\circ}}\cdot \mathrm{T}^3_{\mathrm{OW}}\cdot \mathrm{R}^2_{\mathrm{TM}}\cdot \mathrm{R}^2_{\mathrm{M}}\right)^{-1}\,,\\
\lambda^p_{\Sigma_1\text{-}\mathrm{TM1},\,\mathrm{MB}} &= \frac{\lambda^p_{\mathrm{TM1}}}{\lambda^p_{\Sigma_1,\,\mathrm{MB}}} = \left(\frac{1}{2}\cdot \mathrm{R_{TM}}\cdot \mathrm{T_{OW}}\cdot \mathrm{T}^p_{\mathrm{BS-45^\circ}}\cdot \mathrm{R_M}\right)^{-1}\,,\\
\lambda^p_{\Sigma_\mathrm{R}\text{-}\mathrm{TM1},\,\mathrm{MB}} &= \frac{\lambda^p_{\mathrm{TM1}}}{\lambda^p_{\Sigma_\mathrm{R},\,\mathrm{MB}}} = 2\cdot\frac{\mathrm{R}^p_{\mathrm{BS-47^\circ}}\cdot \mathrm{T_{OW}}}{\mathrm{T}^p_{\mathrm{BS-47^\circ}}\cdot \mathrm{R}^p_{\mathrm{BS-45^\circ}}\cdot \mathrm{R}^3_{\mathrm{M}}}\,,\\
\lambda^p_{\Sigma_\mathrm{F}\text{-}\mathrm{TM1},\,\mathrm{MB}} &= \frac{\lambda^p_{\mathrm{TM1}}}{\lambda^p_{\Sigma_\mathrm{F},\,\mathrm{MB}}} = 2\cdot\frac{\mathrm{R}^p_{\mathrm{BS-47^\circ}}\cdot \mathrm{T_{OW}}}{\mathrm{T}^p_{\mathrm{BS-47^\circ}}\cdot \mathrm{T}^p_{\mathrm{BS-45^\circ}}}\,.
\end{aligned} \tag{B.3}$$

B.2. Reference beam propagation to the Σ parameters

For the estimation of the radiation pressure contribution during LPF's longest noise run (see Section 14.2), the propagation factors for the reference beam to the Σ parameters are also used. They are given by:

$$\begin{aligned}
\lambda^{p}_{\Sigma_{12},\,\mathrm{RB}} &= \frac{1}{2}\cdot\left(\mathrm{R}^{p}_{\mathrm{BS}-45^\circ}\right)^2\cdot\mathrm{R}^{3}_{\mathrm{M}}\,,\\
\lambda^{p}_{\Sigma_{1},\,\mathrm{RB}} &= \frac{1}{2}\cdot\mathrm{R}^{p}_{\mathrm{BS}-45^\circ}\cdot\mathrm{T}^{p}_{\mathrm{BS}-45^\circ}\,,\\
\lambda^{p}_{\Sigma_{\mathrm{R}},\,\mathrm{RB}} &= \frac{1}{2}\cdot\mathrm{R}^{p}_{\mathrm{BS}-45^\circ}\cdot\mathrm{T}^{p}_{\mathrm{BS}-45^\circ}\,,\\
\lambda^{p}_{\Sigma_{\mathrm{F}},\,\mathrm{RB}} &= \frac{1}{2}\cdot\left(\mathrm{T}^{p}_{\mathrm{BS}-45^\circ}\right)^2\cdot\mathrm{R}_{\mathrm{M}}\,.
\end{aligned} \tag{B.4}$$

B.3. Propagation of both beams to the individual PDs

Furthermore, for the full model of the OB, the coefficients for the individual diodes are needed. The reference beam propagates between the front the OB and the different diodes by the following parameters:

$$\begin{aligned}
\lambda^{p}_{12\mathrm{A},\,\mathrm{RB}} &= \mathrm{T}^{p}_{\mathrm{BS}-45^\circ}\cdot\left(\mathrm{R}^{p}_{\mathrm{BS}-45^\circ}\right)^2\cdot\mathrm{R}^{3}_{\mathrm{M}}\,,\\
\lambda^{p}_{12\mathrm{B},\,\mathrm{RB}} &= \left(\mathrm{R}^{p}_{\mathrm{BS}-45^\circ}\right)^3\cdot\mathrm{R}^{3}_{\mathrm{M}}\,,\\
\lambda^{p}_{1\mathrm{A},\,\mathrm{RB}} &= \mathrm{R}^{p}_{\mathrm{BS}-45^\circ}\cdot\left(\mathrm{T}^{p}_{\mathrm{BS}-45^\circ}\right)^2\,,\\
\lambda^{p}_{1\mathrm{B},\,\mathrm{RB}} &= \left(\mathrm{R}^{p}_{\mathrm{BS}-45^\circ}\right)^2\cdot\mathrm{T}^{p}_{\mathrm{BS}-45^\circ}\,,\\
\lambda^{p}_{\mathrm{RA},\,\mathrm{RB}} &= \mathrm{R}^{p}_{\mathrm{BS}-45^\circ}\cdot\left(\mathrm{T}^{p}_{\mathrm{BS}-45^\circ}\right)^2\,,\\
\lambda^{p}_{\mathrm{RB},\,\mathrm{RB}} &= \left(\mathrm{R}^{p}_{\mathrm{BS}-45^\circ}\right)^2\cdot\mathrm{T}^{p}_{\mathrm{BS}-45^\circ}\,,\\
\lambda^{p}_{\mathrm{FA},\,\mathrm{RB}} &= \left(\mathrm{T}^{p}_{\mathrm{BS}-45^\circ}\right)^3\cdot\mathrm{R}_{\mathrm{M}}\,,\\
\lambda^{p}_{\mathrm{FB},\,\mathrm{RB}} &= \mathrm{R}^{p}_{\mathrm{BS}-45^\circ}\cdot\left(\mathrm{T}^{p}_{\mathrm{BS}-45^\circ}\right)^2\cdot\mathrm{R}_{\mathrm{M}}
\end{aligned} \tag{B.5}$$

For the measurement, the propagation factors are:

$$
\begin{aligned}
\lambda^{p}_{\text{12A, MB}} &= \mathrm{R}^{p}_{\text{BS}-45^\circ} \cdot \lambda^{p}_{\text{TM2}} \cdot \mathrm{R}_{\text{TM}} \cdot \mathrm{T}_{\text{OW}} \cdot \mathrm{R}_{\text{M}}\,, \\
&= \mathrm{R}^{p}_{\text{BS}-45^\circ} \cdot \mathrm{R}^{p}_{\text{BS}-47^\circ} \cdot \mathrm{R}^{p}_{\text{BS}-43^\circ} \cdot \mathrm{T}^{4}_{\text{OW}} \cdot \mathrm{R}^{2}_{\text{TM}} \cdot \mathrm{R}^{2}_{\text{M}}\,, \\
\lambda^{p}_{\text{12B, MB}} &= \mathrm{T}^{p}_{\text{BS}-45^\circ} \cdot \lambda^{p}_{\text{TM2}} \cdot \mathrm{R}_{\text{TM}} \cdot \mathrm{T}_{\text{OW}} \cdot \mathrm{R}_{\text{M}}\,, \\
&= \mathrm{T}^{p}_{\text{BS}-45^\circ} \cdot \mathrm{R}^{p}_{\text{BS}-47^\circ} \cdot \mathrm{R}^{p}_{\text{BS}-43^\circ} \cdot \mathrm{T}^{4}_{\text{OW}} \cdot \mathrm{R}^{2}_{\text{TM}} \cdot \mathrm{R}^{2}_{\text{M}}, \\
\lambda^{p}_{\text{1A, MB}} &= \mathrm{R}^{p}_{\text{BS}-45^\circ} \cdot \lambda^{p}_{\text{TM1}} \cdot \mathrm{R}_{\text{TM}} \cdot \mathrm{T}_{\text{OW}} \cdot \mathrm{T}^{p}_{\text{BS}-45^\circ} \cdot \mathrm{R}_{\text{M}}\,, \\
&= \mathrm{R}^{p}_{\text{BS}-45^\circ} \cdot \mathrm{R}^{p}_{\text{BS}-47^\circ} \cdot \mathrm{T}^{p}_{\text{BS}-45^\circ} \cdot \mathrm{T}_{\text{OW}} \cdot \mathrm{R}_{\text{TM}} \cdot \mathrm{T}_{\text{OW}} \cdot \mathrm{R}_{\text{M}}\,, \\
\lambda^{p}_{\text{1B, MB}} &= \left(\mathrm{T}^{p}_{\text{BS}-45^\circ}\right)^{2} \cdot \lambda^{p}_{\text{TM1}} \cdot \mathrm{R}_{\text{TM}} \cdot \mathrm{T}_{\text{OW}} \cdot \mathrm{R}_{\text{M}}\,, \\
&= \left(\mathrm{T}^{p}_{\text{BS}-45^\circ}\right)^{2} \cdot \mathrm{R}^{p}_{\text{BS}-47^\circ} \cdot \mathrm{T}_{\text{OW}} \cdot \mathrm{R}_{\text{TM}} \cdot \mathrm{T}_{\text{OW}} \cdot \mathrm{R}_{\text{M}}\,, \\
\lambda^{p}_{\text{RA, MB}} &= \left(\mathrm{R}^{p}_{\text{BS}-45^\circ}\right)^{2} \cdot \mathrm{T}^{p}_{\text{BS}-47^\circ} \cdot \mathrm{R}^{3}_{\text{M}}\,, \\
\lambda^{p}_{\text{RB, MB}} &= \mathrm{T}^{p}_{\text{BS}-45^\circ} \cdot \mathrm{T}^{p}_{\text{BS}-47^\circ} \cdot \mathrm{R}^{p}_{\text{BS}-45^\circ} \cdot \mathrm{R}^{3}_{\text{M}}\,, \\
\lambda^{p}_{\text{FA, MB}} &= \mathrm{R}^{p}_{\text{BS}-45^\circ} \cdot \mathrm{T}^{p}_{\text{BS}-47^\circ} \cdot \mathrm{T}^{p}_{\text{BS}-45^\circ}\,, \\
\lambda^{p}_{\text{FB, MB}} &= \left(\mathrm{T}^{p}_{\text{BS}-45^\circ}\right)^{2} \cdot \mathrm{T}^{p}_{\text{BS}-47^\circ}
\end{aligned}
\tag{B.6}
$$

C. OB model implementation and parameter initialisation

The transmission of parallel and orthogonal polarisation for the individual interferometer beam paths of the LPF OB can be described by Equation 8.18.
For fitting the P-pol in the reference and measurement beam, an offset needs to be derived separately, as described in Appendix C.1.
Furthermore, the laboratory measured coefficients of flight spare BS splitting ratios led to the decision of dependent fitting of the splitting ratios for BS that are used with a different angle of incidence.
The implemented code that was used to derive the results in Section 8.2 is printed in Appendix C.3.

C.1. Offsets in parallel polarisation

Looking at the full model in Equation 8.18, variations in power can clearly be assigned to variations in polarisation. However, a constant offset in P-pol, or in other words, the minimum measured P-pol, is indistinguishable from spurious losses, equivalently distributed to the P-pol transmissivity in the particular beam path. Therefore, the minimum P-pol power was estimated first and set as a constraint in the fit.

The power CL mainly controls the orthogonal polarised power (see Equation 8.7). Hence, a fluctuating polarisation leads to a fluctuation of the overall power on the OB. For pure S-pol, the OB power becomes smallest. Therefore, the minimum measured overall power is also the measurement with minimum power in P-pol. For the reference beam, the overall power is smallest at sample $k = 6$. The estimation of the P-pol offset is described in the following, exemplarily for the reference beam.

The basic idea for retrieving the minimum P-pol power is the use of the different splitting at the recombination BS. A and B diodes of one interferometer share their beam path, up to the recombination BS and the PD. The PD responsivity is neglected for this purpose, so that the two channels are only different by reflection or transmission at the recombination BS. For the P-pol, this splitting is unequal, resulting in a differential power between A and B diode. Since the P-pol power is different in the four interferometers, their differential powers $\mathrm{DC}_{i\mathrm{A,\,RB}} - \mathrm{DC}_{i\mathrm{B,\,RB}}$ are different, too.

For sample $k = 6$ (with minimum overall reference beam power), the normalised differential power of A and B diode in the frequency interferometer — being most sensitive to parallel polarisation — is given by:

$$\mathrm{DC}_{\text{F-diff, RB}}(\text{measured}) = \frac{\mathrm{DC}_{\text{FA, RB}}(6) - \mathrm{DC}_{\text{FB, RB}}(6)}{0.5 \cdot (\mathrm{DC}_{\text{FA, RB}}(6) + \mathrm{DC}_{\text{FB, RB}}(6))}\,. \tag{C.1}$$

To retrieve the minimum power in P-pol from Equation C.1, the power splitting at the recombination BS needs to be modelled.

For the fit, the BS splitting ratios are a parameter to be fit. In contrast to this, the measured splitting ratios of three flight spare BSs (see Table 8.1) are used for this purpose of offset estimation:

$$\begin{aligned} \text{for S-pol: } \mathrm{T}^{\perp} &= 0.487 \\ \mathrm{R}^{\perp} &= 1 - \mathrm{T}^{\perp} = 0.513 \\ \text{for P-pol: } T^{\parallel} &= 0.785 \\ \mathrm{R}R^{\parallel} &= 1 - \mathrm{T}^{\parallel} = 0.215\,. \end{aligned} \tag{C.2}$$

With these splitting ratios, the normalised differential power of A and B diode can be modelled:

$$\begin{aligned} &\mathrm{DC}_{\text{F-diff, RB}}(\text{theo.}) \\ &= 2 \cdot \frac{({T^{\perp}}^3 - {T^{\perp}}^2 \cdot {R^{\perp}}^1) \cdot P^{\perp}_{\text{RB}} + ({T^{\parallel}}^3 - {T^{\parallel}}^2 \cdot {R^{\parallel}}^1) \cdot P^{\parallel}_{\text{RB, min.}}}{({T^{\perp}}^3 + {T^{\perp}}^2 \cdot {R^{\perp}}^1) \cdot P^{\perp}_{\text{RB}} + ({T^{\parallel}}^3 + {T^{\parallel}}^2 \cdot {R^{\parallel}}^1) \cdot P^{\parallel}_{\text{RB, min.}}} \end{aligned} \tag{C.3}$$

Since the orthogonal polarised power is much higher than the minimum parallel polarised one, the P-pol contribution in the denominator can be neglected.
With the same argument, the contribution from orthogonal polarisation in the numerator is not negligible, although the splitting ratio is much more similar than for parallel polarisation. Fortunately, for orthogonal polarisation, the differential power of A and B diode is comparable for the four interferometers (in contrast to the differential P-pol).

Therefore, the S-pol contribution in the numerator of Equation C.3 can approximately be removed by subtraction of the differential power $\mathrm{DC}_{i-\text{diff, RB}}(\text{theo.})$ from the reference interferometer (or the TM1 interferometer having an identical beam path for the reference beam in theory):

$$\begin{aligned} &\mathrm{DC}_{\text{F-diff, RB}}(\text{theo.}) - \mathrm{DC}_{\text{R-diff, RB}}(\text{theo.}) = \mathrm{DC}_{\text{F-diff, RB}}(\text{theo.}) - \mathrm{DC}_{\text{TM1-diff, RB}}(\text{theo.}) \\ &= 2 \cdot \frac{({T^{\parallel}}^3 - {T^{\parallel}}^2 \cdot {R^{\parallel}}^1) \cdot P^{\parallel}_{\text{RB, min.}}}{({T^{\perp}}^3 + {T^{\perp}}^2 \cdot {R^{\perp}}^1) \cdot P^{\perp}_{\text{RB}}} - 2 \cdot \frac{({T^{\parallel}}^2 \cdot {R^{\parallel}}^1 - {T^{\parallel}}^1 \cdot {R^{\parallel}}^2) \cdot P^{\parallel}_{\text{RB, min.}}}{({T^{\perp}}^2 \cdot {R^{\perp}}^1 + {T^{\perp}}^1 \cdot {R^{\perp}}^2) \cdot P^{\perp}_{\text{RB}}} \\ &= c_{\text{theo}} \cdot \frac{P^{\parallel}_{\text{RB, min.}}}{P^{\perp}_{\text{RB}}}\,. \end{aligned} \tag{C.4}$$

Comparison of the measured differential powers, following Equation C.1 to the corresponding model from Equation C.4 leads to the desired minimum ratio between parallel and orthogonal polarised power for the reference beam:

$$\begin{aligned} & \mathrm{DC}_{\text{F-diff, RB}}(\text{theo.}) - \mathrm{DC}_{\text{R-diff, RB}}(\text{theo.}) \\ & \stackrel{!}{=} \mathrm{DC}_{\text{F-diff, RB}}(\text{meas.}) - 0.5 \cdot (\mathrm{DC}_{\text{R-diff, RB}}(\text{meas.}) + \mathrm{DC}_{\text{TM1-diff, RB}}(\text{meas.})) \\ \rightarrow \frac{P^{\parallel}_{\text{RB, min.}}}{P^{\perp}_{\text{RB}}} &= \frac{\mathrm{DC}_{\text{F-diff, RB}} - 0.5 \cdot (\mathrm{DC}_{\text{R-diff, RB}} + \mathrm{DC}_{\text{TM1-diff, RB}})}{c_{\text{theo}}} . \end{aligned} \tag{C.5}$$

For the measurement beam, the procedure works analogously with the different beam paths.

As a result, the minimum P-pol of the reference beam is determined to be 1.27%. For the measurement beam, the minimum power is a bit smaller with 0.63%.
In comparison to the derived variations of P-pol, as described in the following section, the offsets are small. Nevertheless, they are still greater than the theoretical prediction of 0.13% for a 3° rotated PBS, as it was built on LPF.

C.2. Dependent fitting of splitting ratios for BS off-nominal angles

The experimentally determined BS splitting ratios showed that the relation of splitting ratios between the three angles 45°, 42.75° and 47.25° is very similar for the three flight spare samples. In comparison to that, the splitting ratio of one and the same angle has higher variation between the different samples. Therefore, the splitting ratios for the two off-nominal angles are fit depending on the nominal 45° angle with their measured linear correlation factor.

By this, the average splitting ratio of all eight OB BSs is determined. A possible deviation in the splitting ratio of a rotated BS then contributes to the fit of the average value with the same weight, as the nominal angled BSs do.

C.3. Implementation of the OB model in the least square optimiser, the *minimizer*

The model from Equation 8.18 was solved with the minimizer function from the IfoCAD library [54]. The program code is printed in the following:

```
#include <iomanip>
#include <stdlib.h>
#include <fstream>
#include <iostream>
#include <sstream>
#include <stdio.h>
#include <string.h>
#include <cmath>
#include <cassert>

// declare minimizer
#ifdef __cplusplus
extern "C"
{
#endif
  struct param_t
  {
    char name[30];
    int fit;          /* 0=No, 1=Regular, 2=Same, 3=proportional, 4=inv.prop. */
```

```
    double init;      /* initial value */
    double min, max; /* limits */
    int log;          /* 0=linear, 1=log */
    int mother;       /* index of mother parameter for fit=2,3,4 */
    double dep_fac;  /* factor for fit=3,4 */
    char unit[30];
    double val; /* actual value */
  };
  typedef struct param_t param;
  extern double minimizer(void (*f)(double *, double *, void *),
                          int np, param *ppa, void *extra_iter,
                          void *extra_final, void *extra_interm,
                          char *options, FILE *logfp_parm);
#ifdef __cplusplus
}
#endif

#define N 215 // number of parameters

// Define the model for:
// Transmission of refernce and measurement beam powers
// for the individual interferometer beam paths

void func(double *p, double *y, void *extra)
{
  static int data_loaded = 0;
  int NN = 17;
  int MM = 87;
  static double x_data[17][87];

  // Load the data: normalised single beam powers and normalised OB temperature

  if (data_loaded == 0)
  {
    std::ifstream read_file("input_corr.txt");
    assert(read_file.is_open());

    for (int i = 0; i < NN; i++)
    {
      for (int j = 0; j < MM; j++)
      {
        read_file >> x_data[i][j];
      }
    }

    read_file.close();
    data_loaded = 1;
  }

  double model_ref, model_meas, diff_ref, diff_meas, fom = 0;
  int i;
  int j;

  // Number of BS transmissions and reflections
  // in the individual interferometer beam paths

  int kR_45_T[8] = {3, 2, 2, 1, 2, 1, 1, 0};
  int kM_45_T[8] = {1, 2, 0, 1, 0, 1, 0, 1};
  int kM_45_R[8] = {1, 0, 2, 1, 1, 0, 1, 0};
  int kM_43_T[8] = {0, 0, 0, 0, 1, 1, 0, 0};
  int kM_43_R[8] = {0, 0, 0, 0, 0, 0, 1, 1};
  int kM_47_T[8] = {1, 1, 1, 1, 0, 0, 0, 0};
  int kM_47_R[8] = {0, 0, 0, 0, 1, 1, 1, 1};

  // Interferometer beam paths:
  // scaling parameters (0.1, 0.01 and pow(0.5,-3)) are used here to keep
```

```
  // the initialisation and range of all parameters close to one
  // they are re-scaled  in post processing.

  for (i = 0; i < 8; i++)
  {
    for (j = 0; j < 87; j++)
    {
      model_ref = ((p[7] - 0.1 * p[6] * 0.1 * p[33 + j]) *
        pow(0.5, -3) * pow(p[0], kR_45_T[i]) * pow((1 - p[0]), 3 - kR_45_T[i]) +
        pow(0.5, -3) * pow(p[3], kR_45_T[i]) * pow((1 - p[3]), 3 - kR_45_T[i]) *
        0.1 * p[33 + j]) * (p[9 + i] + p[25 + i] * 0.01 * (x_data[16][j] + 0.1)) +
        0.005 * p[207 + i]; // optional offset (was set to 0)

      model_meas = ((p[8] - 0.1 * p[6] * 0.1 * p[120 + j]) *
        pow(0.5, -3) * pow(p[0], kM_45_T[i]) * pow(p[1], kM_43_T[i]) *
        pow(p[2], kM_47_T[i]) * pow((1 - p[0]), kM_45_R[i]) *
        pow(1 - p[1], kM_43_R[i]) * pow(1 - p[2], kM_47_R[i]) +
        pow(0.5, -3) * pow(p[3], kM_45_T[i]) * pow(p[4], kM_43_T[i]) *
        pow(p[5], kM_47_T[i]) * pow((1 - p[3]), kM_45_R[i]) *
        pow(1 - p[4], kM_43_R[i]) * pow(1 - p[5], kM_47_R[i]) * 0.1 * p[120 + j]) *
        (p[17 + i] + p[25 + i] * 0.01 * (x_data[16][j] + 0.1)) +
        0.005 * p[207 + i]; // optional offset (was set to 0)

      diff_ref = model_ref - x_data[i][j];
      diff_meas = model_meas - x_data[i + 8][j];
      fom += diff_ref * diff_ref + diff_meas * diff_meas;

      y[0] = fom;
    }
  }
}

int main(void)
{

  // Initialisation of parameters:

  param p[N];
  double ymin;
  int i;
  char options[256];

  std::cout << "main: S_pol_splitting" << '\n';

  // Read external file with starting values

  int NNN = 6;
  int MMM = 87;
  double x_init[NNN][MMM];

  std::ifstream read_file("init_r.txt");
  assert(read_file.is_open());

  for (int i = 0; i < NNN; i++)
  {
    for (int j = 0; j < MMM; j++)
    {
      read_file >> x_init[i][j];
    }
  }

  read_file.close();

  std::cout << "initial guess for Splitting ratios" << '\n';

  sprintf(p[0].name, "S-pol, division ratio 45");
```

```
sprintf(p[0].unit, "a.u.");
p[0].init = x_init[4][0];
std::cout << "S-pol, division ratio 45 degrees: "
          << p[0].init << '\n';
p[0].min = 0.4;
p[0].max = 0.6;
p[0].fit = 1;
p[0].log = 0;

sprintf(p[1].name, "S-pol, division ratio 43");
sprintf(p[1].unit, "a.u.");
p[1].init = x_init[4][1];
std::cout << "S-pol, division ratio 43 degrees: "
          << p[1].init << '\n';
p[1].min = 0.4;
p[1].max = 0.6;
p[1].fit = 3;
p[1].mother = 0;
p[1].dep_fac = 1.034;
p[1].log = 0;

sprintf(p[2].name, "S-pol, division ratio 47");
sprintf(p[2].unit, "a.u.");
p[2].init = x_init[4][2];
std::cout << "S-pol, division ratio 47 degrees: "
          << p[2].init << '\n';
p[2].min = 0.4;
p[2].max = 0.6;
p[2].fit = 3;
p[2].mother = 0;
p[2].dep_fac = 0.964;
p[2].log = 0;

sprintf(p[3].name, "P-pol, division ratio 45");
sprintf(p[3].unit, "a.u.");
p[3].init = x_init[4][3];
std::cout << "P-pol, division ratio 45 degrees: "
          << p[3].init << '\n';
p[3].min = 0.7;
p[3].max = 0.9;
p[3].fit = 1;
p[3].log = 0;

sprintf(p[4].name, "P-pol, division ratio 43");
sprintf(p[4].unit, "a.u.");
p[4].init = x_init[4][4];
std::cout << "P-pol, division ratio 43 degrees: "
          << p[4].init << '\n';
p[4].min = 0.7;
p[4].max = 0.9;
p[4].fit = 3;
p[4].mother = 3;
p[4].dep_fac = 0.98;
p[4].log = 0;

sprintf(p[5].name, "P-pol, division ratio 47");
sprintf(p[5].unit, "a.u.");
p[5].init = x_init[4][5];
std::cout << "P-pol, division ratio 47 degrees: "
          << p[5].init << '\n';
p[5].min = 0.7;
p[5].max = 0.9;
p[5].fit = 3;
p[5].mother = 3;
p[5].dep_fac = 1.018;
p[5].log = 0;
```

```
sprintf(p[6].name, "Reflectivity␣GP");
sprintf(p[6].unit, "a.u.");
p[6].init = x_init[4][6];
std::cout << "Reflectivity␣GP:␣" << p[6].init << '\n';
p[6].min = 0.8;
p[6].max = 1.3;
p[6].fit = 1;
p[6].log = 0;

std::cout << "initial␣guess␣for␣ampl-control␣level" << '\n';

sprintf(p[7].name, "ampl-control␣level␣ref-beam");
sprintf(p[7].unit, "a.u.");
p[7].init = x_init[5][0];
std::cout << "ampl-control␣level␣ref-beam:␣"
          << p[7].init << '\n';
p[7].min = 0.8;
p[7].max = 1.3;
p[7].fit = 1;
p[7].log = 0;

sprintf(p[8].name, "ampl-control␣level␣meas-beam");
sprintf(p[8].unit, "a.u.");
p[8].init = x_init[5][1];
std::cout << "ampl-control␣level␣meas-beam:␣"
          << p[8].init << '\n';
p[8].min = 0.8;
p[8].max = 1.3;
p[8].fit = 1;
p[8].log = 0;

std::cout << "initial␣guess␣for␣losses*PD_0" << '\n';

for (i = 9; i < 17; i++)
{
  sprintf(p[i].name, "1␣-␣losses*PD_0,␣ref-beam␣ifo␣%d", i - 9);
  sprintf(p[i].unit, "a.u.");
  p[i].init = x_init[2][i - 9];
  p[9].init = 1;
  std::cout << p[i].name << ":␣" << p[i].init << '\n';
  p[i].min = 0.8;
  p[i].max = 1.2;
  p[i].fit = 1;
  p[9].fit = 0;
  p[i].log = 0;
}

for (i = 17; i < 25; i++)
{
  sprintf(p[i].name, "1␣-␣losses*PD_0,␣meas-beam␣ifo␣%d", i - 17);
  sprintf(p[i].unit, "a.u.");
  p[18].init = 1;
  p[i].init = x_init[2][i - 9];
  std::cout << p[i].name << ":␣" << p[i].init << '\n';
  p[i].min = 0.8;
  p[i].max = 1.2;
  p[i].fit = 1;
  p[18].fit = 0;
  p[i].log = 0;
}

std::cout << "initial␣guess␣for␣PD_T" << '\n';

for (i = 25; i < 33; i++)
{
```

```
    sprintf(p[i].name, "PD_T %d", i - 25);
    sprintf(p[i].unit, "a.u.");
    p[i].init = x_init[3][i - 25];
    std::cout << p[i].name << ": " << p[i].init << '\n';
    p[i].min = -2;
    p[i].max = 2;
    p[i].fit = 1;
    p[i].log = 0;
  }

  std::cout << "initial guess for P_pol ref-beam" << '\n';

  for (i = 33; i < 120; i++)
  {
    sprintf(p[i].name, "P_pol ref-beam, index %d", i - 33);
    sprintf(p[i].unit, "a.u.");
    p[i].init = x_init[0][i - 33];
    std::cout << p[i].name << ": " << p[i].init << '\n';
    p[i].min = 0;
    p[i].max = 1;
    p[i].fit = 1;
    p[i].log = 0;
    // 1.2% offset in P-pol, *10 for parameter size in the see model
    p[38].init = 0.12;
    p[38].fit = 0; // decouple linear dependency
  }

  std::cout << "initial guess for P_pol meas-beam" << '\n';

  for (i = 120; i < 207; i++)
  {
    sprintf(p[i].name, "P_pol meas-beam, index %d", i - 120);
    sprintf(p[i].unit, "a.u.");
    // p[i].init= 0;
    p[i].init = x_init[1][i - 120];
    std::cout << p[i].name << ": " << p[i].init << '\n';
    p[i].min = 0;
    p[i].max = 1;
    p[i].fit = 1;
    p[i].log = 0;
    // 0.6% offset in P-pol, *10 for parameter size in the see model
    p[120].init = 0.06;
    p[120].fit = 0; // decouple liner dependency
  }

  std::cout << "Offsets" << '\n';

  for (i = 207; i < 215; i++)
  {
    sprintf(p[i].name, "Offset , PD %d", i - 207);
    sprintf(p[i].unit, "a.u.");
    p[i].init = 0; // offsets were set to zero
    std::cout << p[i].name << ": " << p[i].init << '\n';
    p[i].min = -10;
    p[i].max = 10;
    p[i].fit = 0;
    p[i].log = 0;
  }

  strcpy(options, "pso"); // use particle swarm optimization algorythm

  // start fitting
  ymin = minimizer(func, N, p, NULL, (void *)1, NULL, options, stdout);

  // print results
```

```
  printf("\n␣result␣:␣f␣=␣%g\n", ymin);

  printf("\n␣splitting_ratios␣=[");
  for (i = 0; i < 7; i++)
  {
    printf("%g%s", p[i].val, (i == 7 - 1) ? "" : ",␣");
  }
  printf("];\n");

  printf("\n␣amp_control_level␣=[");
  for (i = 7; i < 9; i++)
  {
    printf("%g%s", p[i].val, (i == 9 - 1) ? "" : ",␣");
  }
  printf("];\n");

  printf("\n␣losses_PD␣=[");
  for (i = 9; i < 25; i++)
  {
    printf("%g%s", p[i].val, (i == 25 - 1) ? "" : ",␣");
  }
  printf("];\n");

  printf("\n␣PD_Temp_dep␣=[");
  for (i = 25; i < 33; i++)
  {
    printf("%g%s", p[i].val, (i == 33 - 1) ? "" : ",␣");
  }
  printf("];\n");

  printf("\n␣P_pol_1␣=[");
  for (i = 33; i < 120; i++)
  {
    printf("%g%s", p[i].val, (i == 120 - 1) ? "" : ",␣");
  }
  printf("];\n");

  printf("\n␣P_pol_2␣=[");
  for (i = 120; i < 207; i++)
  {
    printf("%g%s", p[i].val, (i == 207 - 1) ? "" : ",␣");
  }
  printf("];\n");

  printf("\n␣offsets␣=[");
  for (i = 207; i < 215; i++)
  {
    printf("%g%s", p[i].val, (i == 215 - 1) ? "" : ",␣");
  }
  printf("];\n");

  return 0;
}
```

D. Power-to-phase coupling: Additional figures

D.1. DC angles during power modulations

Figure D.1 shows the φ_1^{DC} and φ_2^{DC} angles together with φ_1^{DWS} and φ_2^{DWS} during the power modulation sequence with highest modulation depth (compare to Figure 5.4).
The η^{DC} and η^{DWS} angles are shown in Figure D.2.

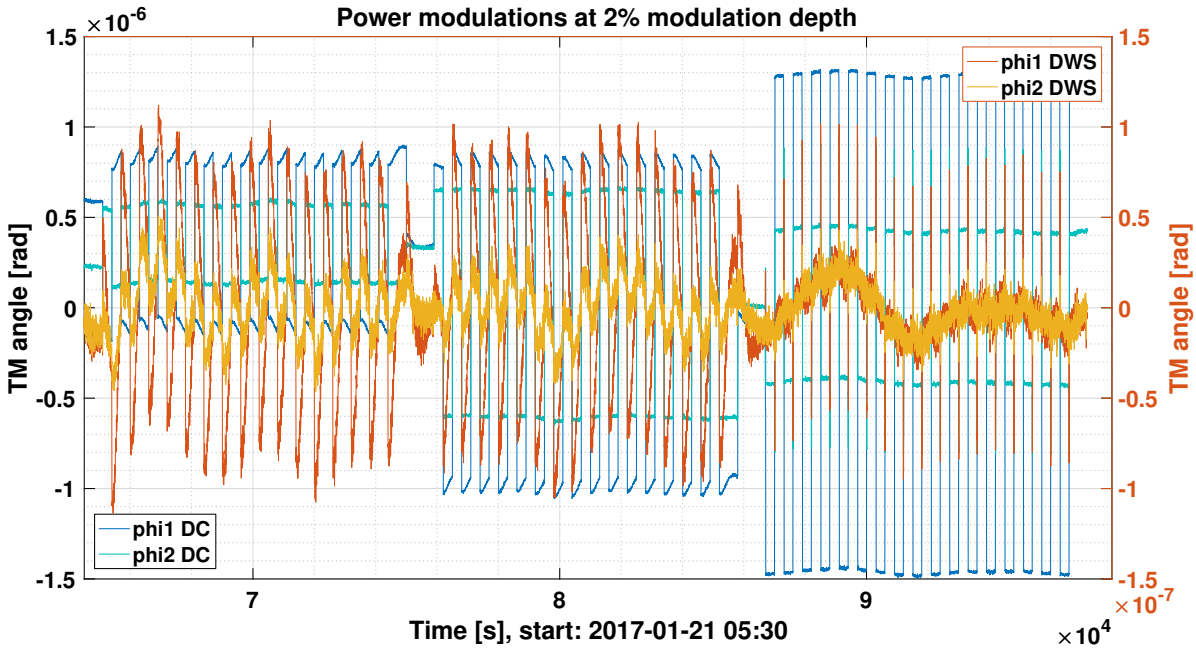

Figure D.1.: φ angle of TM1 and TM2 angles, derived by the DC signals and the DWS signals during the beam modulation experiments with 2% modulation depth. At first, the measurement beam is modulated, afterwards the reference beam and in the end both beams with opposite sign (compare to Figure 5.4).

All four DC angles show a signal in correlation with the power modulations. This coupling, however, can easily be explained by the centre of mass of the combined beam powers. The spot positions of the two beams are slightly different. A modulation of one beam, therefore, couples into a displacement of the centre of mass of the total power at the diode.
The coupling of beam power into the DC angles appears to be much stronger than the ones in DWS and of comparable magnitude for all four angles. However, the coupling is different for the measurement and reference beams, dependent on the particular angle. The counter modulation is worse for φ_1 than φ_2. The η_2 angle, however, seems to couple stronger than η_1.

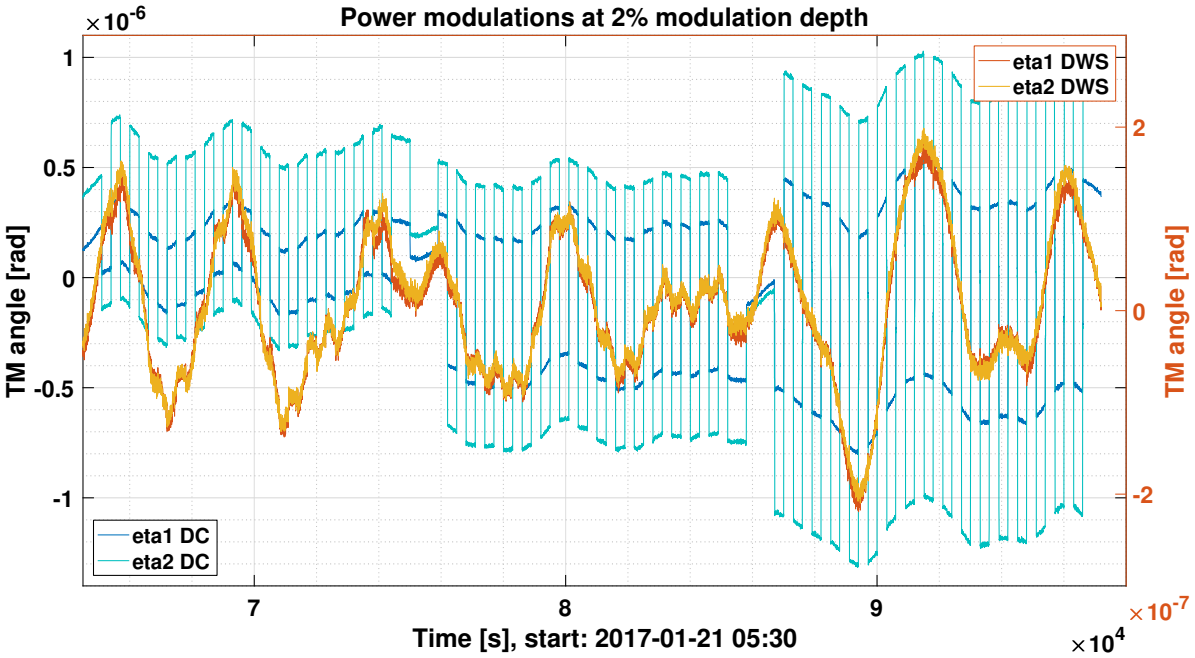

Figure D.2.: η angle of TM1 and TM2 angles, derived by the DC signals and the DWS signals during the beam modulation experiments with 2% modulation depth. At first, the measurement beam is modulated, afterwards the reference beam and in the end both beams with opposite sign (compare to 5.4).

In summary, there seems to be no logical connection to the steps that are measured for the DWS angles.

D.2. DWS angles during contrast experiment

The time series of the DWS angles during the contrast experiment were high-pass filtered to visualise the steps in the different parameters. The corresponding plot is shown in Figure D.3.

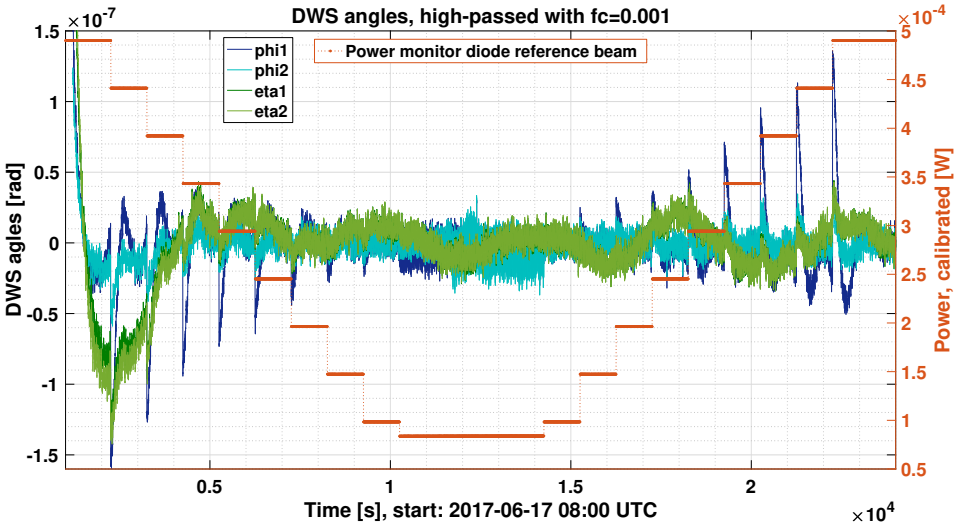

Figure D.3.: High-pass filtered DWS angles together with the reference beam power during the contrast experiment.

E. Linearity of amplitude CL in the operated range

The control action of the fast amplitude CL during flight of LPF is relevant in this theses. Therefore, the relation between the applied RF power actuation and the transmitted power through the AOM shall be checked.

Figure E.1 shows the time series of a single beam power measurement. At first, the reference beam is turned off for one minute. Afterwards the measurement beam and in the end both beams together. Before the beams are turned off, the power control loop of the particular beam is opened and a constant RF power is applied. This step can be seen by a short peak in the measured power before the RF power amplification is commanded to zero.

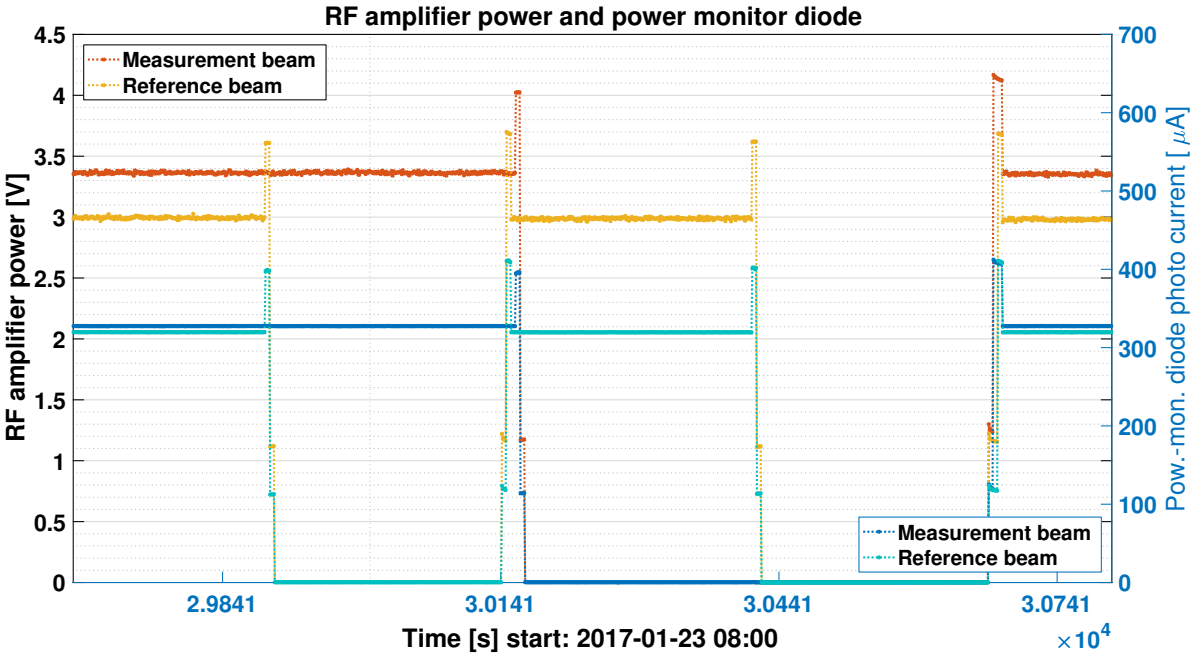

Figure E.1.: Zoom to one single beam power measurement. It can be seen that, before shutting the beams off, a short period with open loop power control is measured.

The open loop step only lasts for a few samples, since it was not meant to be analysed. The samples close to the edges may contain transients from the switch in power. Therefore, the central sample of power during the open loop state was selected for each single beam power measurement. As a consequence, the open loop state is affected by more read-out noise than the closed loop state

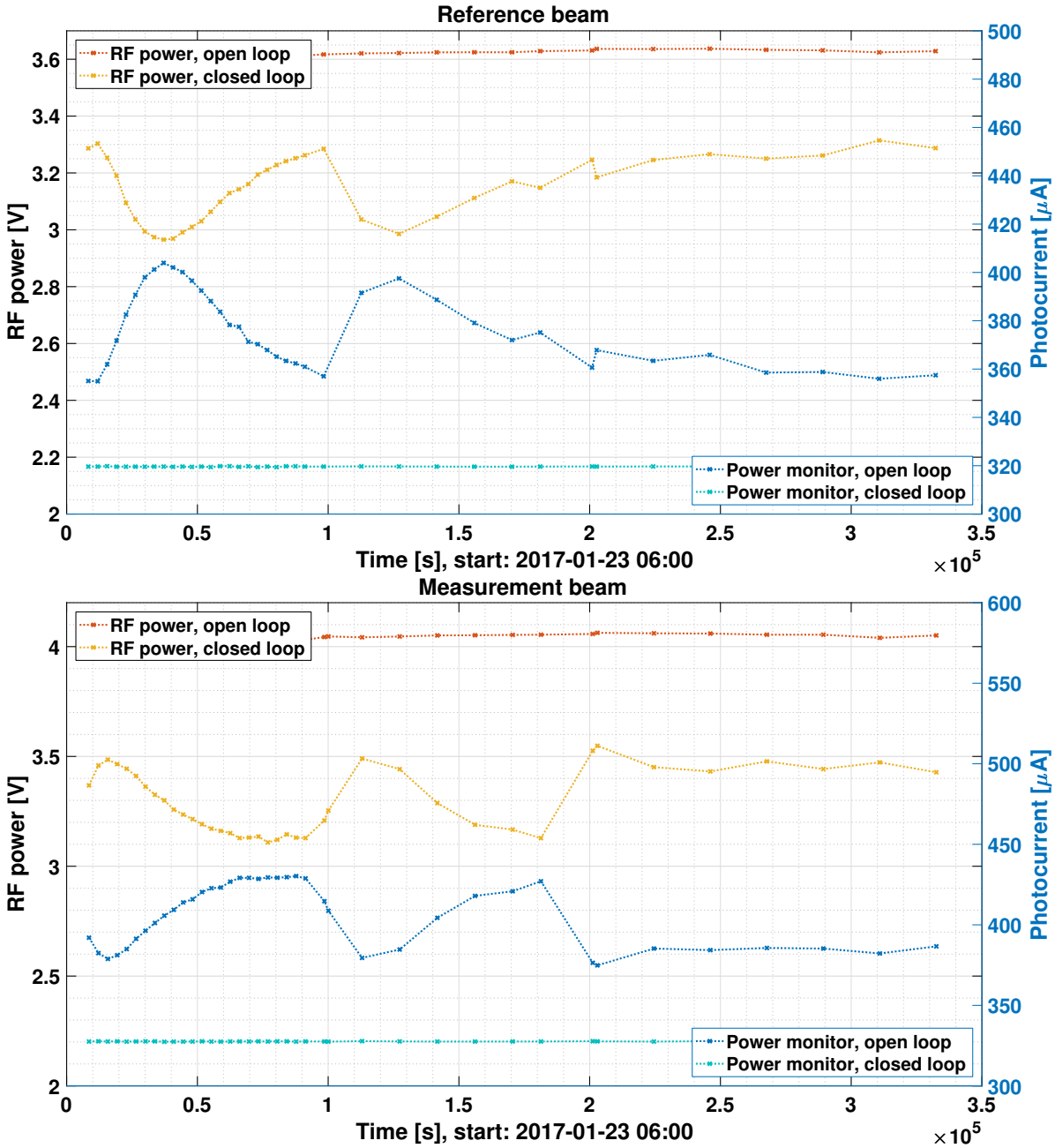

Figure E.2.: Comparison of open loop and closed loop states for the RF power and the power monitor diode. Upper figure: Reference beam, lower figure: measurement beam.

Figure E.2 shows the open loop and closed loop powers of the RF amplifier and the power monitor diode, for the reference and the measurement beam, respectively. As expected, the open loop power monitor diodes show an inverse shape to the closed loop RF powers.

To compare the step in power between the two parameters, the difference between open loop and closed loop state is computed and normalised to the average power:

$$\Delta P_{\mathrm{RF}} = \left(P_{\mathrm{RF}}^{\mathrm{OL}} - P_{\mathrm{RF}}^{\mathrm{CL}}\right) \cdot \left(P_{\mathrm{RF}}^{\mathrm{OL}} + P_{\mathrm{RF}}^{\mathrm{CL}}\right)^{-1} \tag{E.1}$$

$$\Delta P_{\mathrm{Pwr\text{-}mon}} = \left(P_{\mathrm{Pwr\text{-}mon}}^{\mathrm{OL}} - P_{\mathrm{Pwr\text{-}mon}}^{\mathrm{CL}}\right) \cdot \left(P_{\mathrm{Pwr\text{-}mon}}^{\mathrm{OL}} + P_{\mathrm{Pwr\text{-}mon}}^{\mathrm{CL}}\right)^{-1} . \tag{E.2}$$

The resulting time series for the measurement and reference beams are shown in Figure E.4.

Furthermore, Figure E.3 shows a scatter plot of ΔP_{RF} and $\Delta P_{\mathrm{Pwr\text{-}mon}}$ for the two beams. A linear fit of the RF power and the power monitor diode power is shown, as well. A small offset and a linear correlation factor between 1.1 and 1.2 an be observed.

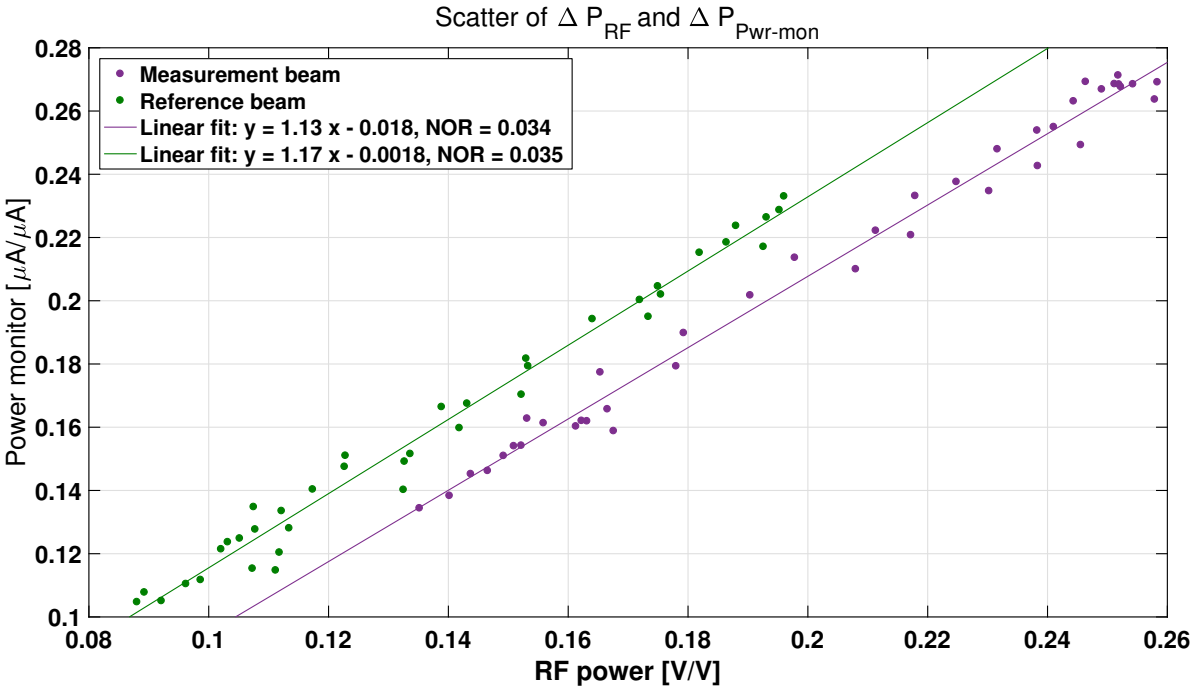

Figure E.3.: Scatter of ΔP_{RF} and $\Delta P_{\mathrm{Pwr\text{-}mon}}$, normalised to the average power, for both beams, together with a linear fit.

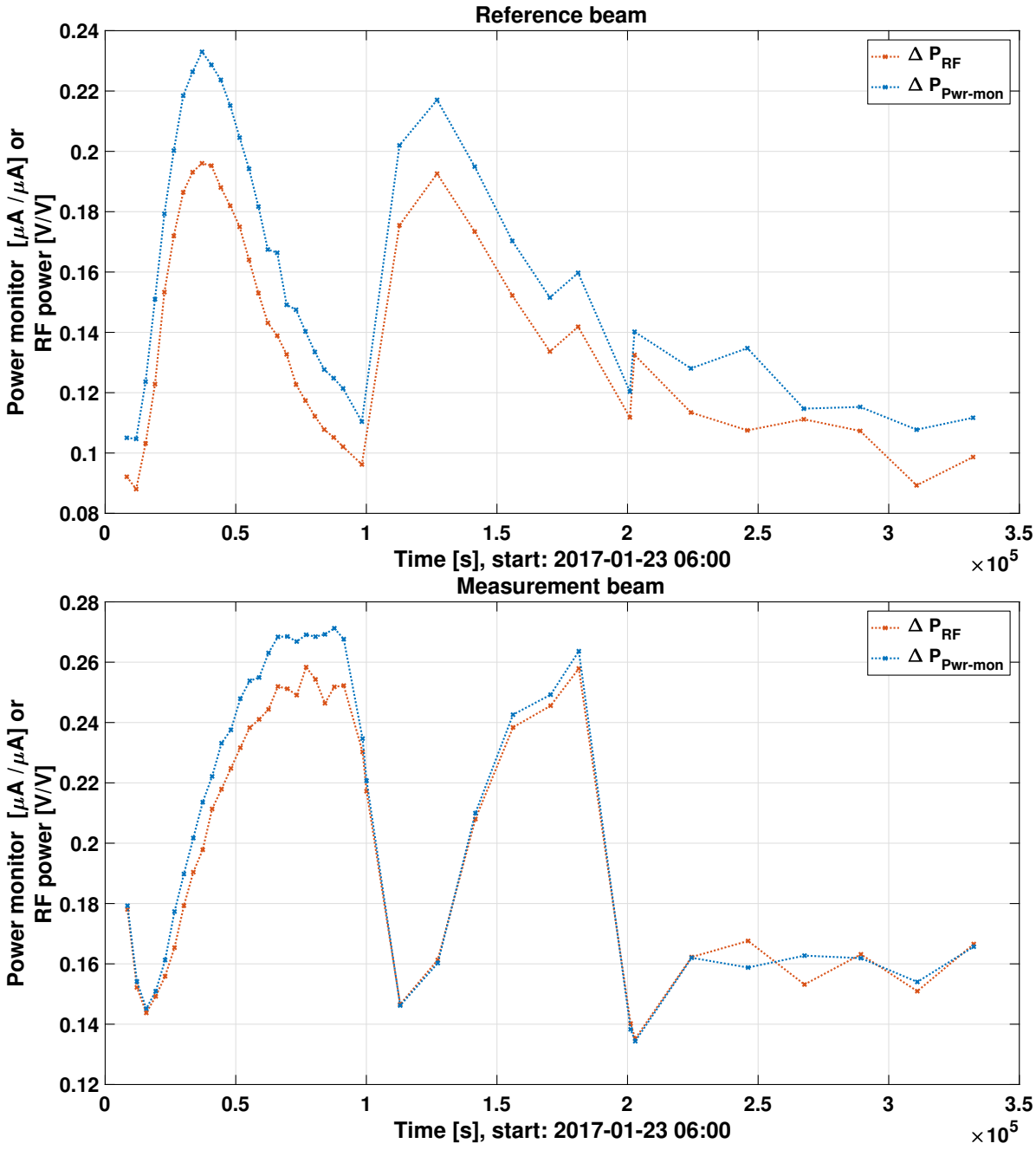

Figure E.4.: Steps in the RF power, ΔP_{RF}, and the power monitor diode, $\Delta P_{\mathrm{Pwr\text{-}mon}}$, normalised to the average power.

F. Measurement of the differential phase between S-pol and P-pol with the LPF engineering model

In the following, a draft of an experiment for the analysis of parallel polarisation at the output of a polarisation-maintaining fibre with the LPF engineering model is presented.

For investigating the phase between S-pol and P-pol out of a fibre, a simple solution for an experiment could be the use of the engineering model of LPF's OMS, currently operated in the AEI laboratories. The OB could be exchanged with a simple interferometer and a polarisation sensitive detector, as shown in Figure F.1.

At the engineering model MB, a laser beam is split, shifted in frequency (with a differential frequency shift of the heterodyne frequency) and coupled into two polarisation maintaining fibres. The two fibre outputs are nominally routed to the engineering model OB. For polarisation analysis, the fibres could be routed to a separate, simpler setup instead, with a 50:50 BS and a polarisation sensitive detection scheme. In a very simple solution, the two recombination BS output ports are split again by two PBSs to achieve an interference signal from parallel polarisation and one from orthogonal components of the beam. The resulting four output ports of the two PBSs could then be detected with four PDs, to allow a balanced readout of the S-pol and P-pol interferometers. For the phase retrieval, the engineering model architecture could be used again.

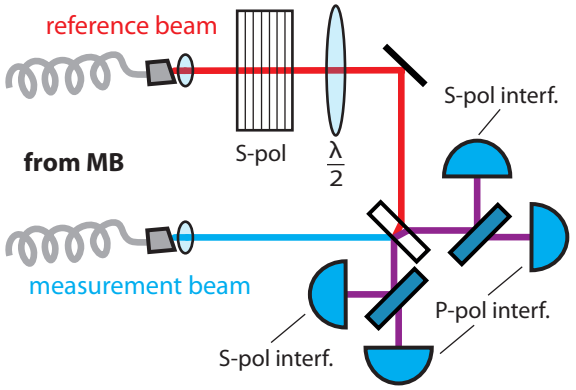

Figure F.1.: Proposed setup for a fibre output polarisation analysis with the LPF engineering model.

In this simple setup, the two polarisation components travel the same geometrical path until detection. The differential phase of the orthogonal and the parallel interference therefore provides the desired signal of the differential optical path-lengths in a setup, comparable to the LPF in-flight case.

However, the P-pol interference for a well-aligned setup is expected to be very small. Therefore, the setup could be extended so that only the effect of one fibre is measured with the option to increase the interference by the off-nominal polarised power of the other beam. The extension consists of a polarisation filter and a half wave plate that are placed directly after the other reference fibre output. The polarisation cleaner removes the undesired parallel polarisation

from one fibre (with a spurious phase) and leaves a linear polarised beam with the phase of the orthogonal polarisation. This beam is then used as reference beam for the interference with the S-pol and P-pol from the measurement beam. The S-pol interference signal functions as the reference interferometer. It can be used as an input signal for the OPD controller of the engineering model. Furthermore, to provide enough power for the interference with the parallel polarised component of the measurement beam, the polarisation of the reference beam needs to be rotated by use of a half wave plate, as can be seen in Figure F.1). The off-nominal polarised reference beam power then acts as a local oscillator for the measurement beam P-pol. In the end, the differential phase of the S-pol and P-pol interference yields the desired signal of the differential phase between the S-pol and P-pol coming out of the measurement beam fibre.

Within this simple setup would allow to estimate the impact of a rotated input polarisation to the measurement beam fibre, which mimics the undesired misalignment of a fibre connector. Also the effect of stress application to the fibre, in combination with a misaligned input polarisation state, can be investigated in power and phase of the off-nominal output polarisation.

Bibliography

[1] B. S. Sathyaprakash and Bernard F. Schutz. Physics, Astrophysics and Cosmology with Gravitational Waves. *Living Reviews in Relativity*, 12(2), 2009.

[2] B. P. Abbott et al. (LIGO Scientific Collaboration). LIGO: the laser interferometer gravitational-wave observatory. *Reports on Progress in Physics*, 72(7), June 2009.

[3] S. Barke, Y. Wang, J. J. Esteban Delgado, M. Tröbs, G. Heinzel, and K. Danzmann. Towards a gravitational wave observatory designer: sensitivity limits of spaceborne detectors. *Classical and Quantum Gravity*, 32(9):095004, April 2015.

[4] J. H. Taylor, L. A. Fowler, and P. M. McCulloch. Measurement of general relativistic effects in the binary pulsar PSR1913+16. *Nature*, 277:437–440, 1979.

[5] B. P. Abbott et al. (LIGO Scientific Collaboration and Virgo Collaboration). GW170814: A Three-Detector Observation of Gravitational Waves from a Binary Black Hole Coalescence. *Physical Review Letters*, 119(14), October 2017.

[6] T. Akutsu, KAGRA Collaboration, et al. Overview of KAGRA: KAGRA science, 2020.

[7] C. Bond, D. Brown, A. Freise, et al. Interferometer techniques for gravitational-wave detection. *Living Reviews in Relativity*, 19(3), 2016.

[8] Giles Hammond, Stefan Hild, and Matthew Pitkin. Advanced technologies for future ground-based, laser-interferometric gravitational wave detectors. *Journal of Modern Optics*, 61(sup1):S10–S45, June 2014.

[9] B. P. Abbott et al. (LIGO Scientific Collaboration). Advanced LIGO. *Classical and Quantum Gravity*, 32(7):074001, March 2015.

[10] D. V. Martynov, E. D. Hall, B. P. Abbott, R. Abbott, T. D. Abbott, C. Adams, R. X. Adhikari, R. A. Anderson, S. B. Anderson, K. Arai, et al. Sensitivity of the Advanced LIGO detectors at the beginning of gravitational wave astronomy. *Physical Review D*, 93(11), June 2016.

[11] Pau Amaro-Seoane et al. Laser Interferometer Space Antenna, 2017.

[12] LISA Instrument Group. LISA Payload Description Document - ESA-L3-EST-INST-DD-001 1.1. Technical report, European Space Agency, December 2017.

[13] M. Otto. *Time-delay interferometry simulations for the laser interferometer space antenna*. Ph. D. thesis, Leibniz Universität Hannover, 2016.

[14] M. Hewitson, E. Fitzsimons, B. Weber (LISA Instrument Group). LISA Performance Model and Error Budget - LISA-LCST-INST-TN-003. Technical report, LISA Consortium, June 2018.

[15] M. Armano et al. (The LISA Pathfinder Collaboration). Sub-Femto-g Free Fall for Space-Based Gravitational Wave Observatories: LISA Pathfinder Results. *PHYSICAL REVIEW LETTERS*, 116(23), June 2016.

[16] M. Armano et al. (The LISA Pathfinder Collaboration). Beyond the Required LISA Free-Fall Performance: New LISA Pathfinder Results down to 20 μHz. *PHYSICAL REVIEW LETTERS*, 120(6), February 2018.

[17] Karsten Danzmann, Gerhard Heinzel, Martin Hewitson, Jens Reiche, Michael Tröbs, Gudrun Wanner, Michael Born, Heather Audley, Nikos Karnesis, Andreas Wittchen, Sarah Paczkowski, Brigitte Kaune, and Lennart Wissel. LPF final report for the german contribution to the nominal mission. *Max Planck Institute for Gravitational Physics (Albert Einstein Institute)*, 2018.

[18] P. McNamara and G. Racca. Introduction to LISA Pathfinder - LISA-LPF-RP-0002. Technical report, European Space Agency, 2009.

[19] M. Armano et al. (The LISA Pathfinder Collaboration). Sensor Noise in LISA Pathfinder: In-Flight Performance of the Optical Test Mass Readout. *PHYSICAL REVIEW LETTERS*. to be published soon.

[20] D. Hoyland. Photodiode Displacement Damage Test Report - S2-UBI-TR-3084. Technical report, University of Birmingham, 2012.

[21] R. Flatscher. Selection and Justification of Fast Power Control Gain in LME - S2-ASD-TN-3193. Technical report, EADS Astrium, 2013.

[22] M. Armano et al. (The LISA Pathfinder Collaboration). The LISA Pathfinder Mission. *Journal of Physics: Conference Series*, 610:012005, May 2015.

[23] G. Anderson et al. (The ST7 Team) and M. Armano et al. (The LISA Pathfinder Collaboration). Experimental results from the ST7 mission on LISA Pathfinder. *Physical Review D*, 98(10), November 2018.

[24] H. Audley. *Preparing for LISA Pathfinder operations: characterisation of the optical metrology system*. Ph.D. thesis, Leibniz Universität Hannover, 2014.

[25] W. Demtröder. *Experimentalphysik 2: Elektrizität und Optik*, volume 2. Springer-Verlag, 6, illustrated edition, 2014.

[26] F. Herzog. LM Loop Performance and Stability - S2-CSZ-TN-3053. Technical report, Oerlikon Space AG, 2009.

[27] Claus Braxmaier, Gerhard Heinzel, Kevin Middleton, Martin Caldwell, W. Konrad, H. Stockburger, Stefano Lucarelli, Maurice Plate, Vinzenz Wand, A. Garcia, F. Draaisma, and Joep Pijnenburg. LISA pathfinder optical interferometry. September 2004.

[28] E. J. Elliffe, J. Bogenstahl, A. Deshpande, J. Hough, C. Killow, S. Reid, D. Robertson, S. Rowan, H. Ward, and G. Cagnoli. Hydroxide-catalysis bonding for stable optical systems for space. *Classical and Quantum Gravity*, 22(10):S257–S267, April 2005.

[29] H. Ward. Optical Bench Interferometer Detailed Design - S2-UGL-DDD-3003. Technical report, Institute for Gravitational Research, University of Glasgow, 2007.

[30] H. Ward. OBI - Revised Fibre Injector Design - S2-UGL-DDD-3004. Technical report, Institute for Gravitational Research, University of Glasgow, 2008.

[31] J. Bogenstahl. FIOS Proto-flight models OPT - S2-UGL-RP-3020. Technical report, Institute for Gravitational Research, University of Glasgow, 2013.

[32] M. Perreur-Lloyd. 3OB As-built Configuration List (ABCL) - S2-UGL-LI-3013. Technical report, Institute for Gravitational Research, University of Glasgow, 2013.

[33] D. Robertson. 3OB As Built OptoCAD Model - S2-UGL-TN-3045. Technical report, University of Glasgow, 2013.

[34] Euan Morrison, Brian J. Meers, David I. Robertson, and Henry Ward. Automatic alignment of optical interferometers. *Appl. Opt.*, 33(22):5041–5049, August 1994.

[35] G. Wanner. *Complex optical systems in space: numerical modelling of the heterodyne interferometry of LISA Pathfinder and LISA*. Ph.D. thesis, Leibniz Universität Hannover, 2010.

[36] Lennart Wissel. In-orbit performance and behaviour of the LISA Pathfinder Optical Metrology System. Master's thesis, Leibniz Universität Hannover, 2017.

[37] Daniele Vetrugno and Nikolaos Karnesis and. Calibrating LISA Pathfinder raw data into femto-g differential accelerometry. *Journal of Physics: Conference Series*, 840:012002, May 2017.

[38] Stefano Vitale. Measurement of LTP dynamical coefficients by system identification - S2-UTN-TN-3045. Technical report, Department of Physics, University of Trento, and Trento Institute for Fundamental Physics and Applications, INFN, 2015.

[39] E. El Allam, C. Inguimbert, S. Addarkaoui, A. Meulenberg, A. Jorio, and I. Zorkani. NIEL calculations for estimating the displacement damage introduced in GaAs irradiated with charged particles. *IOP Conference Series: Materials Science and Engineering*, 186:012005, March 2017.

[40] D. Hoyland. Photodiode Radiation Test Procedure - S2-UBI-TP-3016. Technical report, University of Birmingham, 2008.

[41] D. Hoyland. Photodiode TID Radiation Test Report - S2-UBI-TR-3081. Technical report, University of Birmingham, 2010.

[42] E. Fitzsimons. Optical Components - Test Report. Technical report S2-UGL-TR-3010, University of Glasgow, 2008.

[43] M. Hewitson and A. Garcia. Laser Amplitude Noise Characterisation for LTP - S2-AEI-TN-3055. Technical report, Max Planck Institute for Gravitational Physics (Albert-Einstein-Institute), 2014.

[44] David Robertson. OMS Beam Positions on Photodiodes - S2-UGL-RP-3301. Technical report, University of Glasgow, 2016.

[45] F. Guzmán Cervantes. S2-UGL-TN-3017 Stray light analysis. Technical report, University of Glasgow, 2006.

[46] G. Heinzel. LISA interferometer noise. Technical note LISA-AEI-TN, AEI Hannover, 2016.

[47] I.S. Amiri, Fatma Mohammed Aref Mahmoud Houssien, Ahmed Nabih Zaki Rashed, and Abd El-Naser A. Mohammed. Temperature effects on characteristics and performance of near-infrared wide bandwidth for different avalanche photodiodes structures. *Results in Physics*, 14:102399, 2019.

[48] G. Heinzel, A. Rüdiger, and R. Schilling. Spectrum and spectral density estimation by the Discrete Fourier transform (DFT), including a comprehensive list of window functions and some new flat-top windows. Technical report LISA-AEI-TN, AEI Hannover, 2002.

[49] E. Fitzsimons. Optical characterisation of 3OB. Technical note S2-UGL-TN-3039, University of Glasgow, 2013.

[50] M. Armano et al. (The LISA Pathfinder Collaboration). Measuring the Galactic Cosmic Ray flux with the LISA Pathfinder radiation monitor. *Astroparticle Physics*, 98:28 – 37, 2018.

[51] The LISA Pathfinder Team. General Design and Interface Requirements Specification - S2-ASU-RS-2031. Technical report, EADS Astrium, 2006.

[52] J. Sanjuán Munõz. *Development and validation of the thermal diagnostics instrumentation in LISA Pathfinder*. Ph. D. thesis, Polytechnic University of Catalonia, 2009.

[53] M. Armano et al. (The LISA Pathfinder Collaboration). In-flight performance of the LISA Pathfinder Optical Metrology System. to be published.

[54] G. Heinzel et al. IfoCAD software library. https://gitlab.aei.uni-hannover.de/ifocad/ifocad_cpp.

[55] K. Pearson. Notes on regression and inheritance in the case of two parents. 58, June 1895.

[56] John I. Marden. Hypothesis Testing: From p Values to Bayes Factors. *Journal of the American Statistical Association*, 95(452):1316–1320, 2000.

[57] L. Müller. Polarisationseffekte auf der optischen Bank von LISA-Pathfinder. Bachelor thesis, Leibniz Universität Hannover, 2018.

[58] Michael Tröbs and Gerhard Heinzel. Improved spectrum estimation from digitized time series on a logarithmic frequency axis. *Measurement*, 39:120–129, February 2006.

[59] R. Paschotta, article on 'Polarization of Light' in the RP Photonics Encyclopedia. https://www.rp-photonics.com/polarization_of_light.html. Accessed: 2020-11-27.

[60] R. Gross. Kapitel 3: Die Polarisation von Licht,. https://www.wmi.badw.de/teaching/Lecturenotes/Physik3/Gross_Physik_III_Kap_3.pdf. Accessed: 2020-11-27.

[61] Thorlabs: 'Broadband Polarizing Beamsplitter Cubes'. https://www.thorlabs.de/newgrouppage9.cfm?objectgroup_id=739. Accessed: 2020-11-27.

[62] T Toyoda and M Yabe. The temperature dependence of the refractive indices of fused silica and crystal quartz. *Journal of Physics D: Applied Physics*, 16(5):L97–L100, May 1983.

[63] H Audley, K Danzmann, A García Marín, and G Heinzel et. al. The LISA Pathfinder interferometry — hardware and system testing. *Classical and Quantum Gravity*, 28(9):094003, April 2011.

[64] A. Wittchen. *Noise Investigation on the LISA-Pathfinder Optical Bench Ground Setup*. Master's thesis, Leibniz Universität Hannover, 2014.

[65] Thorlabs. PAX1000 Operation Manual - Compact Polarimeter. https://www.thorlabs.com/newgrouppage9.cfm?objectgroup_id=1564. Accessed: 2020-11-27.

[66] University of Glasgow. *Operation manual for multi-channel DC beam position readout kit*, 2013.

[67] Jeffrey O. White, Aaron Z. Chan, and Carl E. Mungan. The Effect of Moisture and Temperature on Optical Coatings Used in Eye-safer Lasers - ARL-TN-0408. Technical report, Army Research Laboratory, September 2010.

[68] R. J. Crase and M. Hamel, article on 'Optical Thin-Film Coating Methods' in Photonics Media. https://www.photonics.com/Articles/Optical_Thin-Film_Coating_Methods/a35232. Accessed: 2020-11-27.

[69] C. J. Stolz, J. R. Taylor, W. K. Eickelberg, and J. D. Lindh. Effects of vacuum exposure on stress and spectral shift of high reflective coatings. *Appl. Opt.*, 32(28):5666–5672, October 1993.

[70] Samuel F. Pellicori and Herbert L. Hettich. Reversible spectral shift in coatings. *Appl. Opt.*, 27(15):3061–3062, August 1988.

[71] H. Alexander. LTP Laser Assembly: LA PFM Function and Performance Test Report, "Hanover-Tests" - S2-KTM-RP-3075. Technical report, Kaiser-Threde, March 2010.

[72] W. Demtröder. *Experimentalphysik 3: Atome, Moleküule und Festkörper*, volume 2. Springer-Verlag, 5, illustrated edition, 2015.

[73] G. Heinzel. SMART-2 interferometer - S2-AEI-TN-3010. Technical report, Albert Einstein Institut, 2002.

[74] S. K. Paczkowski. *Laser Frequency Stabilisation and Interferometer Path Length Differences during the LISA Pathfinder Satellite Mission*. Ph.D. thesis, Leibniz Universität Hannover, 2020.

[75] E. Fitzsimons. Optical Bench Requirement Specification - LISA-UKOB-INST-RS-001. Technical report, UK Astronomy Technology Centre and University of Glasgow's Institute for Gravitational Research, October 2020.

[76] 'Polarization-Maintaining Fiber (PM Fiber, PMF) ' in FiberLabs Glossary. https://www.fiberlabs.com/glossary/polarization-maintaining-fiber/. Accessed: 2020-11-27.

[77] G. Hechenblaikner. OMS calibration parameters and procedures - S2-ASD-TN-3085. Technical report, EADS Astrium, 2009.

[78] J. Bogenstahl. *Interferometry for the space mission LISA Pathfinder*. Ph. D. thesis, University of Glasgow, 2010.

[79] Kevin M. McPeak, Sriharsha V. Jayanti, Stephan J. P. Kress, Stefan Meyer, Stelio Iotti, Aurelio Rossinelli, and David J. Norris. Plasmonic Films Can Easily Be Better: Rules and Recipes. *ACS Photonics*, 2(3):326–333, 2015. PMID: 25950012.

Acknowledgements

Bevor ich meinen Dank an die vielen Personen richte, die mich im Laufe meiner Promotion unterstützt haben, möchte ich zunächst meinen Dank an LISA Pathfinder und all die Wissenschaftler ausdrücken, die den hervorragenden Erfolg dieser Mission ausgemacht haben. Mit großem Glück durfte ich die Mission miterleben und spannende Phänomene untersuchen.

An erster Stelle möchte ich Herrn Prof. Dr. Karsten Danzmann danken. Bereits in meinem ersten Semester haben Sie mich mit Ihrer Begeisterung für Physik und LISA angesteckt. Durch die Annahme als Promotionsstudentin und die fortwährende Unterstützung haben Sie mir die Möglichkeit gegeben ein kleines St$\breve{}$ck in diesem unglaublich spannenden Projekt mitzugestalten. Ganz besonders möchte ich mich an dieser Stelle auch für Ihren Einsatz um Ihre Studenten bedanken — ich kann mir keine bessere Umgebung für einen Promovierenden vorstellen.

Meinen größten Dank möchte ich an Herrn Prof. Gerhard Heinzel aussprechen. Vielen Dank für die Inspiration, die ständige Unterstützung und die viele Zeit, die Du neben den vielen Aufgaben für Deine Studenten bereit hältst.

Dieser Dank gebürt auch Herrn Dr. Martin Hewitson. Thank you so much for your support, the many discussions and also the great fun we had in the LISA Pathfinder meetings.

Des weiteren möchte ich mich bei Herrn Prof. Benno Willke für die Uebernahme der Korrektur meienr Arbeit bedanken.
And I want to thank Prof. William Weber for agreeing to correct my thesis. I know that a thesis correction is a huge effort, so thank you for the time you are spending on it.
Auch an Herrn Prof. Klemens Hammerer möchte ich meinen Dank richten für die Übernahme des Vorsitzes der Promotionskommission.
Furthermore I want to thank Dr. David Robertson for being my ancillary supervisor.

A special thanks belongs to our colleagues from the research team at the University of Glasgow for the support with flight spare hardware.
In particular, I want to thank Dr. Alasdair Taylor for the effort you spend on the LPF spare OB measurements.
Furthermore, I want to thank the *Airbus Defence and Space GmbH* for the loan of the multi-channel DC beam-position read-out kit and Dr. Rüdiger Gerndt and Dr. Jens Reiche for organising the transport to Glasgow.
The data that was generated helped a lot for understanding the polarisation effects on LPF.

Des weiteren möchte ich Herrn Tobias Gross und der *Laseroptic GmbH* für die freundliche und umfangreiche Unterstützung durch Ssektralphotometrische Aufnahmen der LPF PBSs danken. Die entstandenen Messungen waren sehr hilfreich für die Identifikation des zugrunde liegenden Effektes.

Auch bei Laura Müller mochte ich mich für die gemeinsame Arbei bedanken. Es hat eine Menge Spaß gemacht!

Besonders wichtig ist mir der Dank an meine Kollegen aus dem Albert Einstein Institut. Der Austausch, die Diskussionen und auch die direkte Hilfsbereitschaft und Unterstützung machen unser Institut für mich zu so einem besonderen Ort und haben mir persönlich sehr geholfen. An erster Stelle möchte ich hier unser LPF team nennen: Danke Dr. Sarah Paczkowski, Lennart Wissel, Andi Wittchen, Dr. Gudrun Wanner, Dr. Michael Born und Dr. Nikos Karnesis für die fantastische gemeinsame Zeit im Büro und auf Dienstreisen. Außerdem möchte ich Karsten Wiesner und Ingo Diepholz für die Büro-Nachbarschaft danken, ohne die die Promotion nur halb so spaßig gewewsen wäre. Vielen Dank auch an Dr. Sönke Schuster, Max Rohr, Dr. Markus Otto und Daniel Penkert, für eure Ideen und das Teilen eures beeindruckenden Wissens!

Auch für die Arbeitsgruppen übergreifende Hilfsbereitschaft möchte ich mich herzlich bedanken: Danke Phillip Koch für die Messungen mit eurer Vakuumtestkammer und danke Harald Lück für Diskussionen und das Teilen von Wissen.

Ein persönliches Dankeschön mochte ich an meine Mentorin Dr. Uta Weiland richten. Die gemeinsame Arbeit hat mir neue und sopannende Einblicke mitgegeben. Auch bei Frau Prof. Dr. Michèle Heurs möchte ich mich herzlich für die Zeit und das Engagement bedanken.

Zu guter Letzt möchte ich mich bei meiner Familie und meinen Freunden bedanken, die mich in jeder einzelnen Phase und Krise dieser Jahre unterstützt haben. Danke an Daniel, für den aller besten Freund der Welt! Danke an meine Mutter für die ständige Unterstützung. Danke Tim für Deine Geduld und Unterstützung. Danke an meine Tochter, für die viele Geduld, das Verständnis und den Ansporn. Das letzte Wort gebührt Dir: LUISE.